Microstructural evolution of Dual Phase steel. Improvement of damage resistance

Irina Pushkareva

Institut National Polytechnique de Lorraine

Ecole des Mines de Nancy

Ecole doctorale Energie, Mécanique et Matériaux (ED409)

Laboratoire de Science et Génie des Surfaces – UMR CNRS 7570

Docteur de l'INPL

Science et Ingénierie des Matériaux

Irina PUSHKAREVA

Evolution microstructurale d'un acier Dual Phase. Optimisation de la résistance à l'endommagement.

Thèse dirigée par Abdelkrim REDJAÏMIA

Soutenue publiquement le 13 Novembre 2009 devant la commission d'examen
Jury :

Anna Fraczkiewicz	Directeur de recherche, ENSM St Etienne	Rapporteur
Alexandre Legris	Professeur, UST Lille	Rapporteur
Sabine Denis	Professeur, Nancy-Université-INPL	Examinateur
Mohamed Gouné	Ingénieur, ArcelorMittal, Maizières-lès-Metz	Examinateur
Antoine Moulin	Ingénieur, ArcelorMittal, Maizières-lès-Metz	Examinateur
Abdelkrim Redjaïmia	Professeur, Nancy-Université-INPL	Examinateur

Acknowledgments

The present work is a result of collaboration between ArcelorMittal R&D center, Maizières-lès-Metz and National School of Mines of Nancy, France. The experiments were carried out at the ArcelorMittal R&D center Maizières-lès-Metz, except where indicated. I am indebted to ArcelorMittal group for financial support of this project.

I am grateful to my university supervisor A. Redjaïmia for advice and useful comments, especially during the reviewing of this manuscript.

I would like to express my thanks to my industrial supervisor A. Moulin for his great encouragement and support throughout this work.

I acknowledge the support, help and interest that I receive from G. Metauer.

I am grateful to O. Bouaziz, S. Allain and C. Scott for many inspiring discussions on the subject of the damage behaviour of the steels. I am also grateful to C. Scott who carefully reviewed the script and made very useful comments. In addition, I acknowledge C. Scott for EELS measurements and TEM observations.

I would like to express my appreciation to M. Gouné for numerous discussions which contributed to the development of this work and permitted understanding the experimental observations.

I wish to thank J. Drillet for so many advices in the microstructural characterization.

I would like to thank C. Landron for in-situ tensile test data.

All the help from N. Valle with the NanoSIMS characterization is gratefully acknowledged.

I would like to thank A. Perlade and S. Cobo for useful suggestions.

I would like to thank the Documentation department staff for help in the literature research and particularly S. Fogel.

I would like to thank the technicians of the Auto Center for their kind help with the experimental work.

I would like to express my appreciation to all the members of the Auto Center for their help and friendship.

I would like to thank A. Fraczkiewicz and A. Legris for accepting to judge my PhD work. Other members of jury are also gratefully acknowledged.

In everything I seek to grasp
The fundamental:
The daily choice, the daily task,
The sentimental.

To plumb the essence of the past,
The first foundations,
The crux, the roots, the inmost hearts,
The explanations.[*]

Boris Pasternak, 1956

[*] Translation from Russian www.friends-partners.org

Table of contents

Introduction

High-strength steels in automobiles

Steels are amongst the most important and useful of all engineering materials because of their wide range of mechanical properties and low cost. High strength steels are commonly used in automotive body in white (BIW) to increase the impact safety (Figure 1). Steel crashworthiness is then an important property, which depends on the steel mechanical properties. For example the absorbed energy in a crash test is proportional to the area under the stress-strain tensile curve (Figure 2).

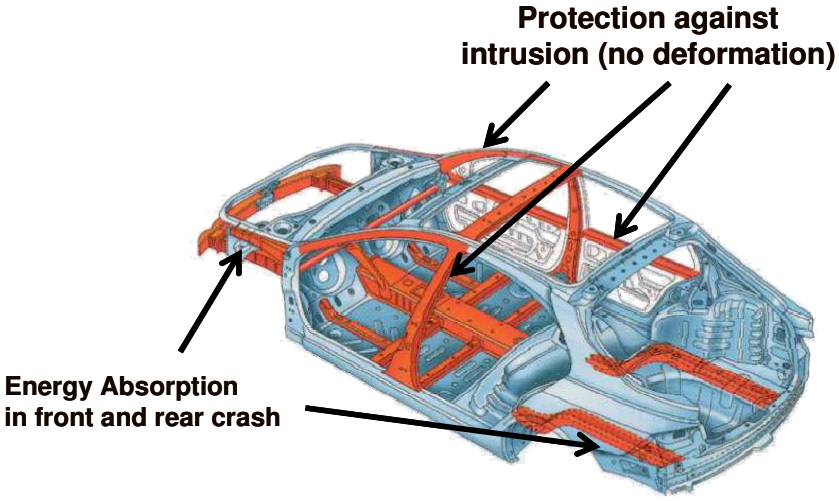

Figure 1. Typical applications of high strength steels for crash resistance (ArcelorMittal credit).

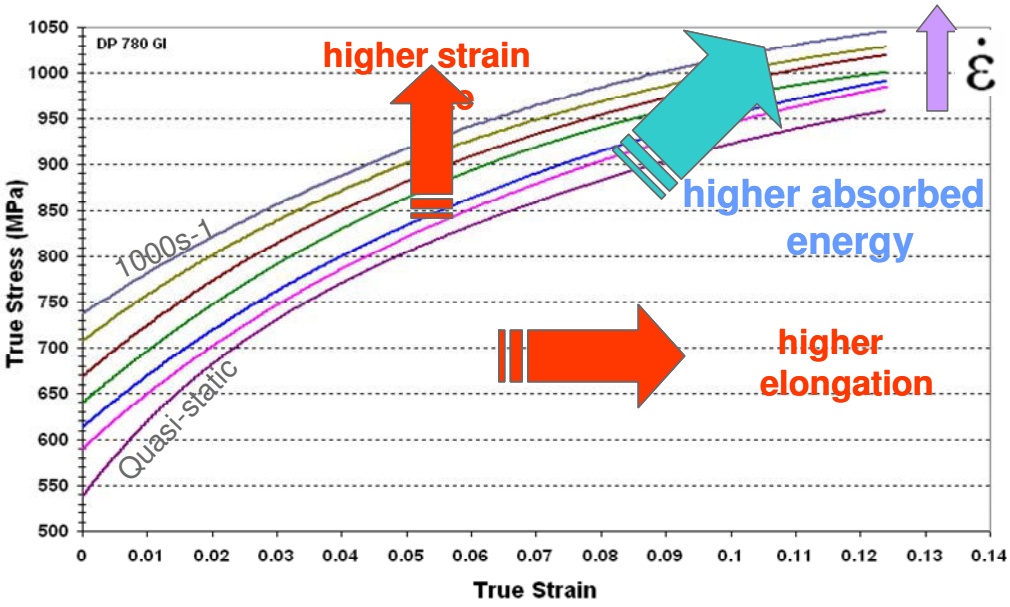

Figure 2. Factors affecting absorbed energy (ArcelorMittal credit).

In the automotive industry current environmental concerns require that the vehicle fuel consumption and CO_2 emissions should be reduced as much as possible. It is therefore advantageous to reduce the weight of BIW components by replacing existing parts with higher strength, thinner gauge alternatives with equivalent or improved functional properties.

Dual Phase (DP) steels are a class of high-strength low-alloy steels characterized by a microstructure consisting of martensite and ferrite. Figure 3 shows DP steel position in a diagram ultimate tensile strength (UTS)-elongation. Dual Phase steels combine high strength levels with good ductility. Thus, DP steels are potentially very attractive for the automobile industry.

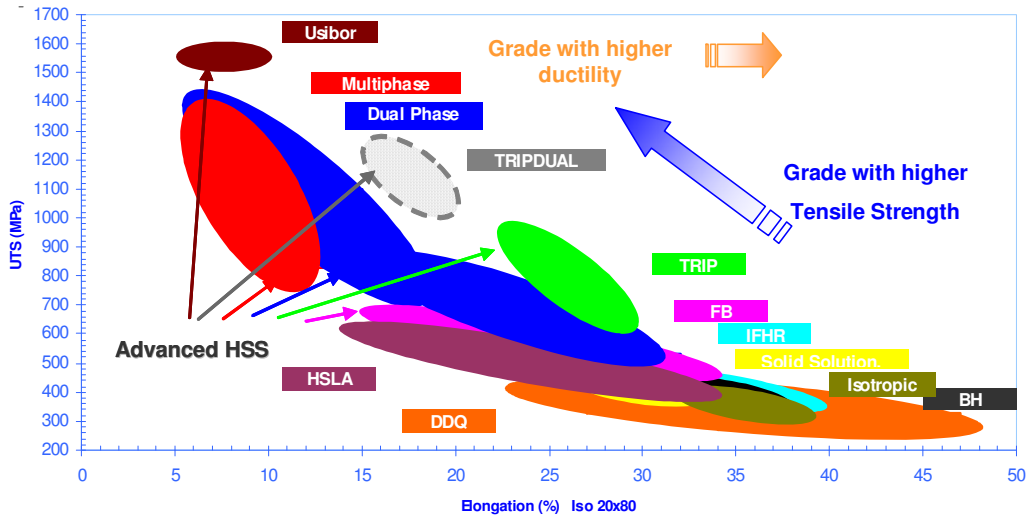

Figure 3. Comparison of tensile properties of various steels. UTS and elongation values are measured during tensile test (ArcelorMittal credit).

Typical DP steel properties are as follows:

- Continuous yielding behavior (no defined yield point),
- A low 0.2 percent offset yield strength,
- A high tensile strength,
- A high work-hardening rate,
- High uniform and total elongations.

The industrial production of DP steels

A unique method of DP steel production is exploited at the ArcelorMittal continuous annealing line of Kessales plant in Liège, Belgium. Here, Hot Water Quenching equipment (HOWAQ) and Turbulent Water Injection Cooling equipment (TWICE) are installed after the soaking furnace (Figure 4). HOWAQ and TWICE equipments are used for quenching operations.

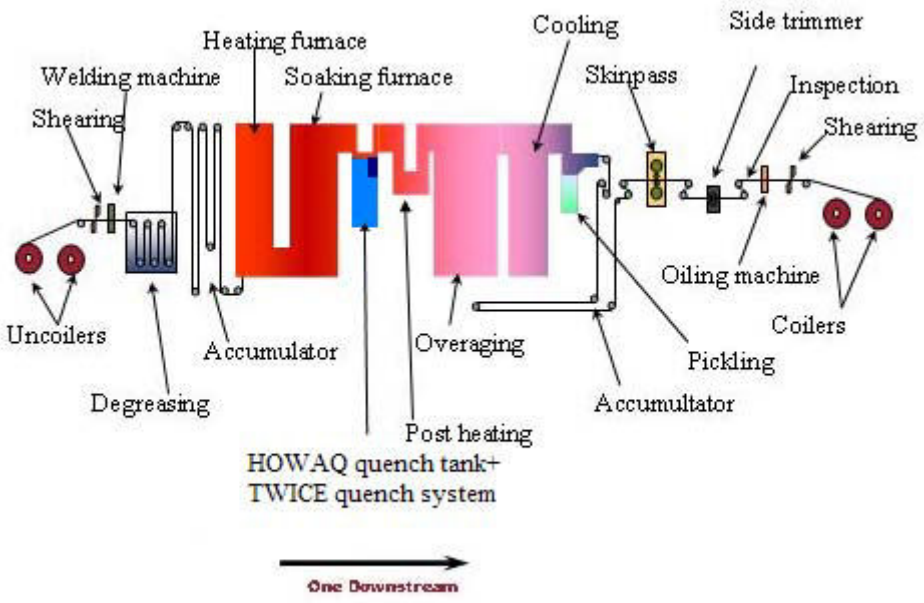

Figure 4. Schematic diagram of the HOWAQ-TWICE installation on the Kessales continuous annealing line (ArcelorMittal credit).

After holding at required isothermal annealing temperature the steel sheet goes first through the HOWAQ equipment (Figure 5) where the steel is cooled by boiling water. Then it is directed to the TWICE equipment (Figure 5) where the quenching operation is carried out by turbulent cold water. The main characteristics of these installations are given in Table 1.

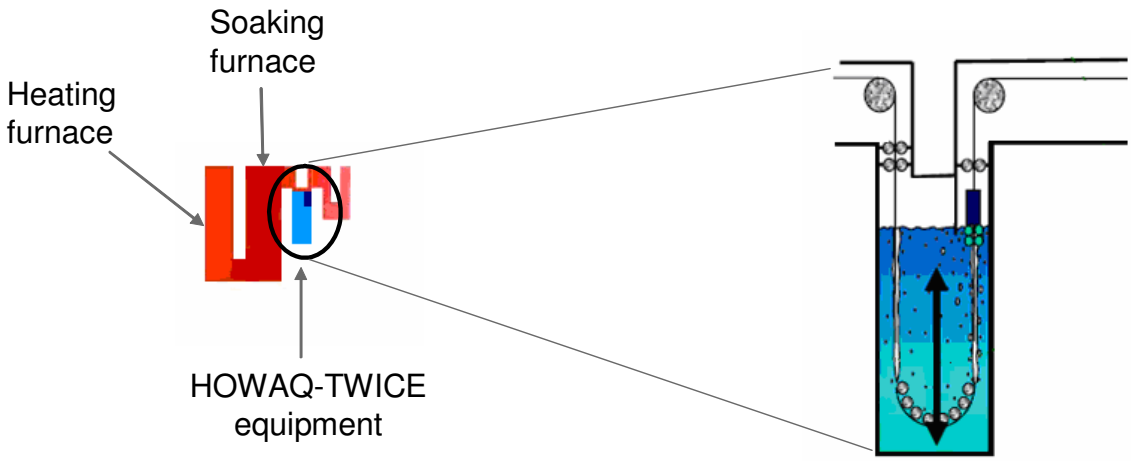

Figure 5. HOWAQ-TWICE quenching equipment (ArcelorMittal credit).

Equipment	HOWAQ	TWICE
Cooling rate	55°C/sec for 1 mm strip thickness	>1000°C/sec

Table 1. HOWAQ-TWICE equipment characteristics.

HOWAQ quenching provides homogeneous heat transfer and accurate quenching with precise end temperature regulation.

Scope of the research

This work is concerned with the study of microstructural evolution and damage mechanisms in DP steels.

In addition to the required high strength and ductility, DP steel has to be cold formed into complex shapes. The steel formability depends on its microstructure, which is controlled by the applied thermo-mechanical treatment. There are many papers on formability in the literature, but these seem to focus mainly on the relationship between the standard mechanical properties and formability, which has little physical meaning. Connecting steel formability with standard mechanical properties seems insufficient, and the significance of many relationships is not obvious. This makes it difficult to design microstructures which are good for forming operations.

Research on DP steels indicates that two factors seem to control the damage mechanisms: the volume fraction of the ductile phase (ferrite) and the hardness gradient between the martensite and ferrite. It is reported that steel formability improves with increasing percent of the ferrite phase. However, for a given steel chemical composition (carbon content is fixed) increase in the volume fraction of the ferrite phase leads to increase of the martensite carbon content (according to the lever rule) and then the hardness gradient increases.

The aim of this work is to identify the important damage mechanisms in DP steel and to clarify the influence of different microstructural parameters on the steel formability.

The first chapter is devoted to a literature overview of the available research on DP steels: the microstructure formation, the phase structure and properties, the effects of different alloying elements, the tempering reactions, and finally the mechanical properties and damage behaviour.

The second chapter is concerned with the microstructural and mechanical characterization of the studied DP steel. This chapter should be regarded as a start point for the understanding of DP steel damage behaviour.

Chapter 3 is concerned with extending our knowledge of DP steel microstructure and microstructure evolution with tempering; the fine analysis is carried out by *FEG-SEM* and electron beam microprobe analysis (*EBMA*).

The role of the local martensite carbon content in the damage behaviour of DP steel is central. The fine-scale analysis of the carbon distribution in the as-quenched and tempered microstructure is investigated using the powerful *NanoSIMS* technique and presented in chapter 4.

The study of the steel damage resistance through the Hole Expansion test is presented in chapter 5. The damage mechanisms are investigated in Chapter 6 by *FEG-SEM* and on the basis of this chapter a simple model of the damage behaviour is proposed in Chapter 7.

Finally, the general conclusions and suggestions for the future work are presented.

Chapter I

Literature review

Different aspects of DP steels are considered in this chapter: a microstructure formation, an influence of different alloying elements on the microstructure and mechanical properties, effects of tempering on the microstructure and the mechanical properties. The important part represents the state of the art in the understanding Dual Phase steels mechanical and damage behaviour. This knowledge is a foundation for the experimental work and it furthers the understanding and interpretation of the obtained results.

I.1 Dual Phase steel microstructure formation

DP sheet steels can be produced by intercritical heat treatment with either continuous-annealing or box annealing techniques. In the continuous annealing technique, the steel sheet with ferrite-pearlite microstructure is heated for a short time into the intercritical temperature range to form ferrite-austenite mixtures, followed by accelerated cooling to transform the austenite phase into martensite. The carbon content of these steels is generally low to be sure that the steels are weldable.

I.1.1 Austenite formation during intercritical annealing

Figure I.1 is a schematic Fe-C diagram showing the annealing temperature field for a given chemical composition of the steel.

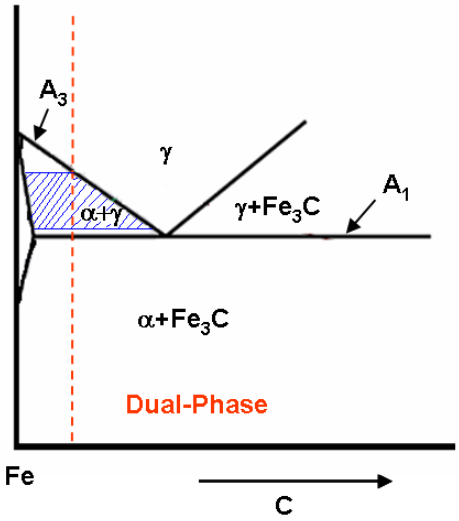

Figure I.1. Schematic Fe-C diagram showing the annealing temperature field for a given chemical composition of the steel.

From the lever rule it can be seen that for any given carbon content, the amount of austenite will increase with increasing intercritical temperature, becoming equal to 100% at the A_3 temperature. Similarly, for any given intercritical temperature, the amount of austenite will increase with increasing carbon content, becoming equal to 100% at a carbon content corresponding to the $\gamma/\gamma+\alpha$ boundary (Figure I.1).

Austenite formation from ferrite-pearlite microstructure during intercritical annealing can be separated into several steps [SPEI81]:

- Almost instantaneous nucleation of austenite at pearlite particles followed by the very rapid growth of austenite until the carbide phase is dissolved,

- Slower growth of austenite into ferrite at a rate that is controlled by carbon diffusion in austenite at high temperatures (850°C) and by manganese diffusion in austenite at low temperatures (750°C),

- Very slow final equilibration of ferrite and austenite at a rate that is controlled by manganese diffusion in austenite.

The first step consists of pearlite dissolution and growth of austenite into the pearlite at the rate controlled primarily by carbon diffusion in the austenite, with the diffusion path lying along the pearlite-austenite interface, and with a diffusion distance about equal to the interlamellar spacing of the pearlite (Figure I.2 (1)).

At the end of the first step, a high-carbon austenite is generated which is not in equilibrium with the ferrite. Subsequent growth of this austenite into ferrite to achieve partial equilibrium with the ferrite constitutes the second step. The slower growth of the austenite in this second step may be controlled either by carbon diffusion in the austenite, or by manganese diffusion in the ferrite (Figure I.2 (2a and 2b)).

In the third step very slow final equilibration of the ferrite and austenite is achieved by manganese diffusion through the austenite (Figure I.2 (3)) (the diffusion rate of Mn in austenite is three orders of magnitude slower than in ferrite) [SPEI81].

The kinetics of austenite formation during the intercritical annealing is influenced by the ferrite grain size. The effect of the ferrite grain size in accelerating the first step is due to the increase of the nucleation sites of austenite at the intersections of ferrite grains with pearlite. Also, the finer the ferrite grains are, the easier it is for substitutional alloying elements (for example, Mn) to diffuse along the ferrite grains during the second step of austenite growth [ELSE90].

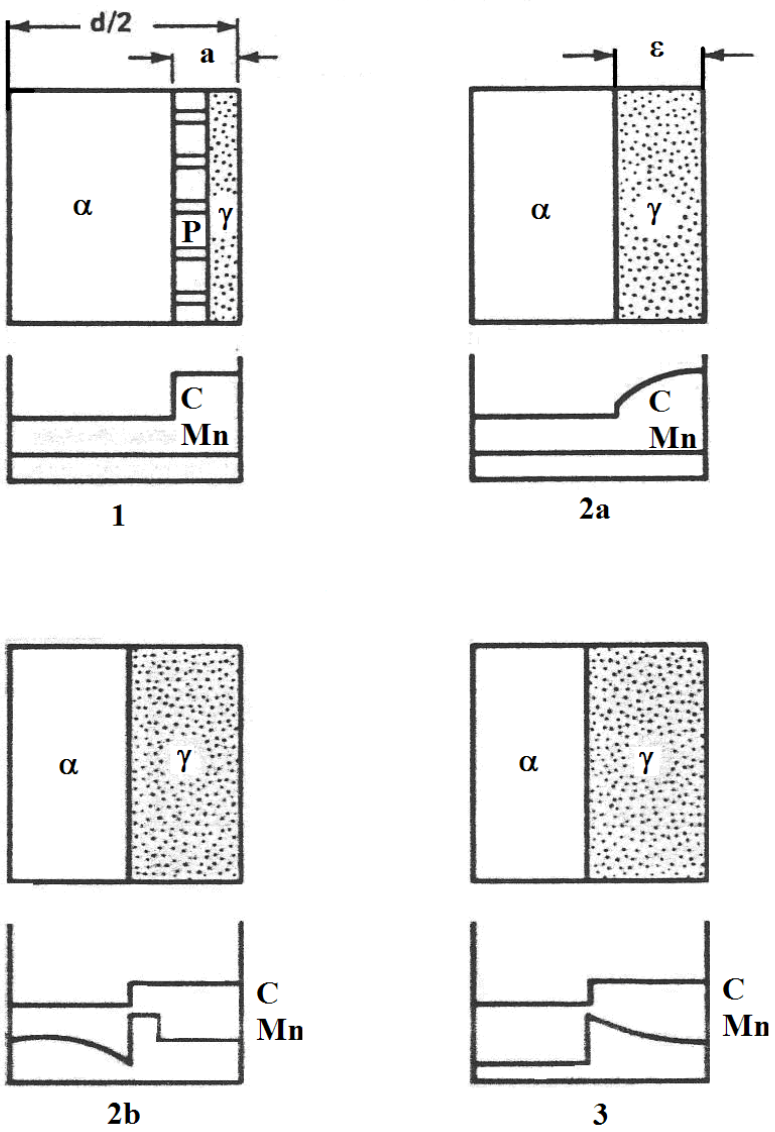

Figure I.2. Scheme of three steps in austenitic growth during intercritical annealing of ferrite-pearlite steels: 1 - dissolution of pearlite, 2a - austenite growth with carbon diffusion in austenite, 2b - austenite growth with manganese diffusion in ferrite, 3 - final equilibration with manganese diffusion in austenite [SPEI81].

The austenite appears to form most rapidly from the cold-rolled structure. Figure I.3 is the isothermal reaction curves for the austenite formation from the hot-rolled, the 25% and the 50% cold deformed states at 735°C. As can be seen, tp shifts to smaller values by increasing the extent of cold rolling from 0% to 50%. The possible effect of the cold-deformation on the kinetics of austenite formation is to accelerate the austenitizing process up to time of complete pearlite dissolution, tp, owing to the higher driving force or lower activation energy [ELSE90].

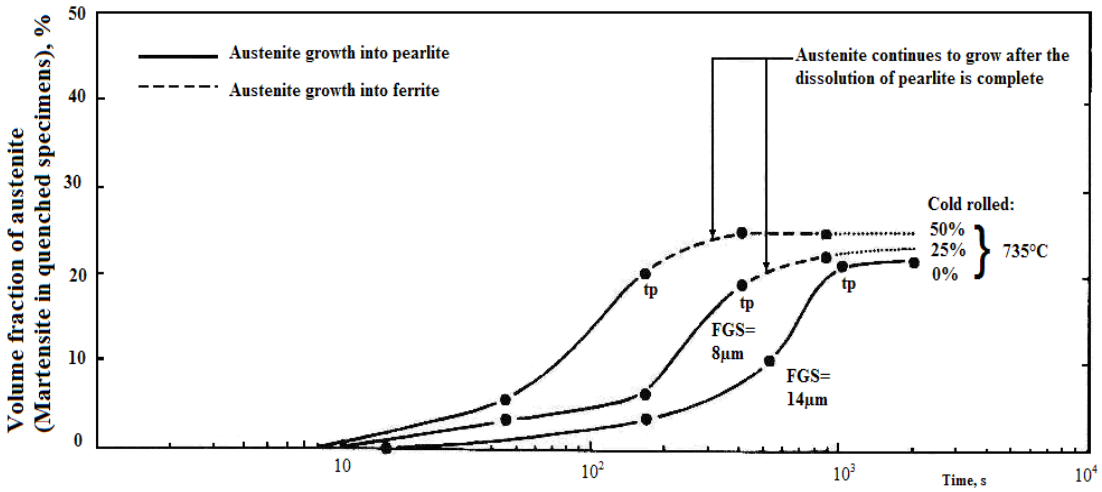

Figure I.3. Effect of cold deformation on the kinetics of austenite formation in 0.11C-1.58Mn-0.4Si steel at 735°C, FGS is the ferrite grain size; tp is the time of complete pearlite dissolution [ELSE90].

I.1.2 Transformation of austenite after intercritical annealing

Although the transformation of austenite in DP steel after intercritical annealing is similar to the transformation of austenite after normal austenitizing, two features make this transformation process unique:

First, because the carbon content of the austenite is fixed by the intercritical temperature, the hardenability of the austenite phase varies with intercritical temperature. Thus, at low temperatures where the carbon content of the austenite is high, the hardenability of austenite is high. Similarly, at high temperatures where the carbon content of the austenite is low, the hardenability of the austenite is low.

Second, because the ferrite already pre-exists, transformation $\gamma \rightarrow \alpha$ can proceed by epitaxial growth of this old ferrite into austenite with no nucleation step required [SPEI81A].

A whole range of morphologies and a whole range of transformation products can be formed from the austenite phase after intercritical annealing, depending on the annealing temperature, time and cooling rate. The hardenability of intercritically formed austenite is also affected by alloying elements present in DP steels [SPEI81A].

The transformation of the austenite phase into martensite in DP steels occurs at low temperatures so that the ferrite phase must plastically deform to accommodate the volume expansion (2 to 4 percent) arising from the austenite to martensite transformation. As a result, both a *high dislocation density and residual stresses* are generated in the ferrite phase immediately surrounding the martensite particle. The residual stress patterns are too small a scale to be directly measured, but a theoretical analysis indicates that their maximum value would be of the order of the yield strength of the ferrite (at the Ms temperature) and decay exponentially away from the martensite-ferrite interface [SPEI81A].

The martensite carbon content of the most common DP steels is in the 0.4-0.7 wt. % range, thus either a lath or mixed type martensite can be expected. These changes in morphology reflect the effect of intercritical annealing temperature on the carbon content of the austenite phase and in turn its effect on the Ms temperature [SPEI81A].

I.1.3 Changes in ferrite phase during intercritical annealing and cooling

In cold-rolled steels, recrystallization of the ferrite will occur rapidly and is generally complete before the steel reaches the intercritical annealling temperature, even during the rapid heating encountered on most continuous-annealing lines. Grain growth of the ferrite phase after recrystallization is generally restricted because of the pinning action of the second phase austenite particles.

Changes in the carbon content of the ferrite phase may occur during intercritical annealing:

- The solubility of carbon in the ferrite may be lower at the intercritical temperature than that originally present in the ferrite phase of the as-received material. The solubility of carbon in the ferrite decreases with increasing intercritical temperature, but may also be markedly decreased by increasing the total alloy content of the steel,

- Variations in the cooling rate from the intercritical temperature can also affect the carbon content of the ferrite phase. As the cooling rate is lowered, cementite may precipitate in the ferrite resulting in lower ferrite carbon content [SPEI81A].

Two different types of ferrite may be identified in most intercritically annealed DP steels: the ferrite which is present at the intercritical annealing temperature, “retained ferrite”, and the ferrite which forms from austenite during cooling, “epitaxial ferrite” (Figure I.4). It was shown that there is no structural interface between the two types of ferrite, and that the epitaxial ferrite is an extension of the retained ferrite grains [KORZ82].

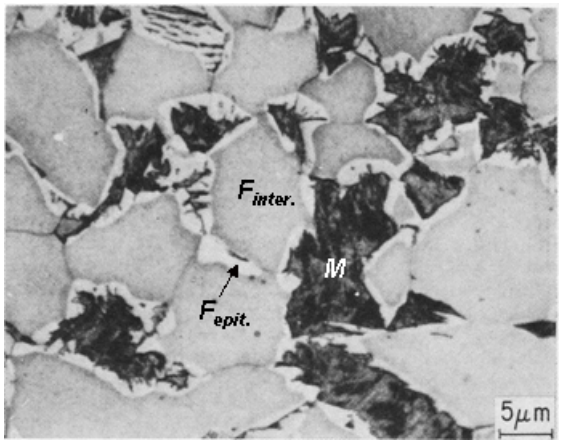

Figure I.4. Types of ferrite in a DP steel: gray- retained ferrite, white - epitaxial ferrite; black – martensite [SPEI81A].

I.1.4 Dual Phase steel microstructure

The pure dual phase microstructure consists of ferrite and martensite (Figure I.5). The ferrite near martensite phase has a high dislocation density (Figure I.6), which was created during plastic accommodation of the martensite in the ferrite [MAND85].

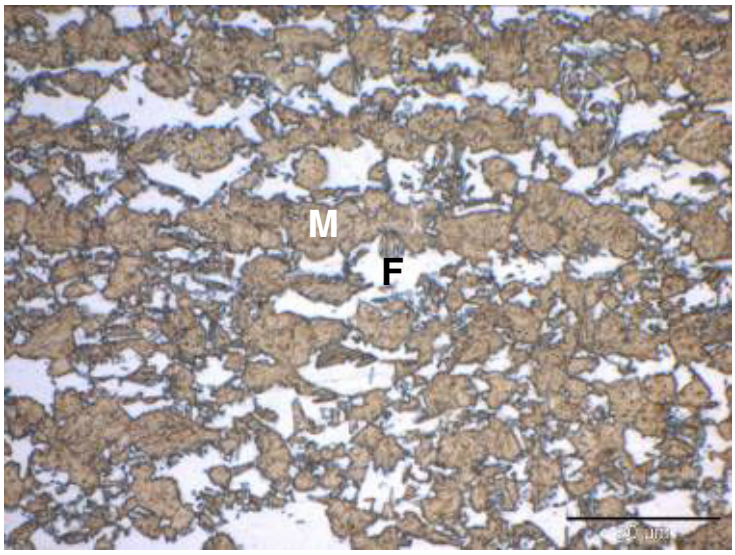

Figure I.5. Light microscope micrograph showing DP steel microstructure.

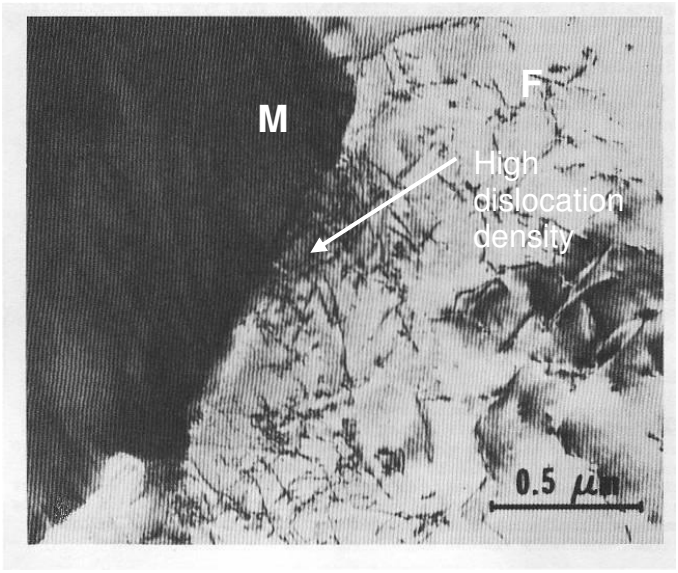

Figure I.6. TEM micrograph showing martensite/ferrite interface with high dislocation density in the ferrite region [MAND85].

For most industrially processed DP steels, the presence of small amounts of other phases, such as bainite and pearlite can be accepted. They do not significantly change the specific DP properties as long as sufficient amount of low-temperature martensite has been formed. The ensemble of the stronger phases, martensite, bainite and pearlite, is often referred to as “second phase”.

Retained austenite is also generally present in DP steels due to uncompleted austenite to martensite transformation. The amount of retained austenite varies from 2 to 9 % with composition, tending to be more prevalent in steels with high carbon content and other alloying elements [SPEI81A].

The important microstructural phenomena in DP steels can be summarized as follows:

- The DP steel obtains its particular properties from the low temperature transformation of intercritical austenite to martensite. This transformation results in a non-uniform dislocation distribution and internal stresses in the material,

- Factors that may influence the mechanical properties of DP steels are:

  - ferrite grain size,
  - ferrite strength,
  - solid-solution alloy additions,
  - dispersed-phase strengthening,
  - martensite nature,
  - martensite morphology,
  - amount of bainite,
  - hardness gradient between ferrite and martensite,

- Alloying elements may lead to more complex consequences on DP steel microstructure formation.

I.2 Martensite structure

The martensite phase is an important component of the DP steel microstructure. It is of value then to expand our knowledge of the martensite phase formation and morphology. This is the aim of the present chapter.

I.2.1 Martensitic transformation

Martensite is a supersaturated solid solution in which the interstitial solutes interact strongly with dislocations [BHAD99].

The martensite transformation is a diffusionless, solid state shear. The martensitic transformation can be defined as a mechanism for changing crystallographic structure that does not require atomic diffusion. It takes place very rapidly at a temperature lower than a critical value called M_S. The fraction transformed depends on the temperature to which the sample is cooled, not on the time spent at this temperature. The transformation ceases at certain temperature denominated M_f. Transformation rarely goes completely to 100% [WAYM85].

The carbon atoms are trapped in octahedral interstitial sites, producing a tetragonal bcc structure (carbon atoms occupy preferentially Oc sites in the lattice, Figure I.7). The martensite carbon content determines the $c_{\alpha M}/a_{\alpha M}$ ratio, the proportion between the elongated axis and the base plane lattice parameter, of the bct unit cell when C>0.2 wt. %.

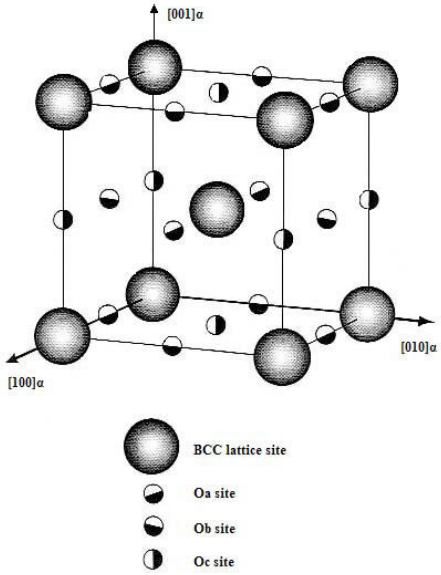

Figure I.7. Schematic representation of a bcc unit cell showing the octahedral interstitial sites [SPEI92].

The *volume expansion* that occurs when fcc austenite transforms to bct martensite and the lattice invariant deformation, accomplished by slip or twinning introduce a high density of dislocation and/or fine twins [MAND85, WAYM85].

The transformation creates *residual stresses and strains* related to the specific volume change in addition to the strains due to the misfit of the interstitial solute atoms [KRAU01, KRAU99].

In carbon steels with high M_S temperatures, because of the high mobility of carbon atoms, carbon diffusion cannot be suppressed during quenching, room-temperature storage, or room-temperature testing. Thus, the evaluation of a pure, as-quenched, untempered martensite is impossible in carbon steels [KRAU01, KRAU99].

I.2.2 Martensite morphology

Depending of the C content of the austenite, different types of martensite may be formed. Crystals of martensite may be arranged in one of two major morphologies: *lath or plate*. Figure I.8 illustrates the volume fraction of lath martensite in Fe-C alloys as a function of the carbon content in the parent austenite phase [KRAU01, WATE03].

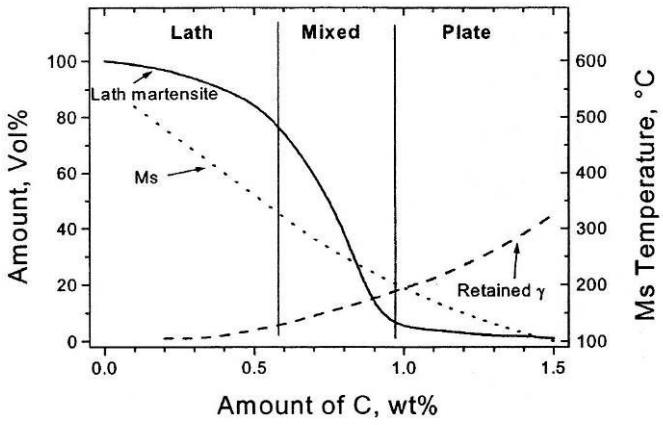

Figure I.8. Effect of C content on relative volume percent of lath and plate martensite, Ms temperature and volume percent of retained austenite in Fe-C alloys [WATE03].

Lath martensite

In the martensite that forms in dilute alloys of iron, the basic transformation unit takes the shape of a lath, and hence the term lath martensite is appropriate for identifying this morphology (Figure I.9). Each lath is a result of a homogeneous shear, and successive shears produce a packet of parallel laths containing a high density of tangled dislocations. Two important structural characteristics, the shape of individual units and the association of the units on a microstructural scale, justify the consideration of martensite that forms in dilute alloys of iron as a distinct morphological type. Basic units are generally aligned parallel to one another in groups that have been termed packets, blocks, or sheaves.

Several packets could be found within a prior austenite grain. Adjacent units may be separated by low- or high-angle boundaries. The widths of the units which make up a packet of martensite range from less than 0.1µm to several microns, with the most frequently occurring width being between 0.1 and 0.2 µm.

The substructure of lath martensite consists predominantly of a high density of tangled dislocations. The dislocation density is shown (by electrical resistivity measurements) to be between 0.3 and 0.9×10^{12} cm/cm^3.

The adjacent laths may be separated be either high- or low-angle boundaries, and may be twin related. Fine internal twins are frequently observed in the lath martensite of Fe-C alloys and steels.

The density of twins in lath martensites is quite low and many laths are in fact devoid of twins [KRAU71].

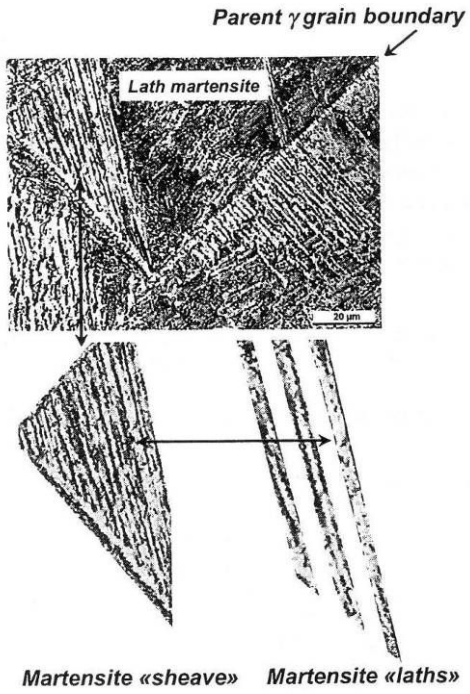

Figure I.9. Structure of lath martensite [WATE03].

Plate martensite

The other type, plate martensite, differs in the shape taken by a transformation unit and its transformation sequence is characterized by nonparallel plate formation (Figure I.10).
Alloy composition and the transformation temperature influence the transition from lath to plate martensite.

Plate martensite is found in high-carbon binary iron alloys. This structure differs from that of a lath martensite in that adjacent plates do not form parallel to one another. The plates which are the first to form tend to span their parent austenite grains and effectively partition the austenite grains, thus limiting the size of plates that subsequently form. The effect of this partitioning is to produce a large range of plate sizes in this type of martensite.

The fact that the units of plate martensite form at angles to one another results in accommodation effects at the sites of impingement.

The fine structure of plate martensite consists in part of fine parallel twins [KRAU71].

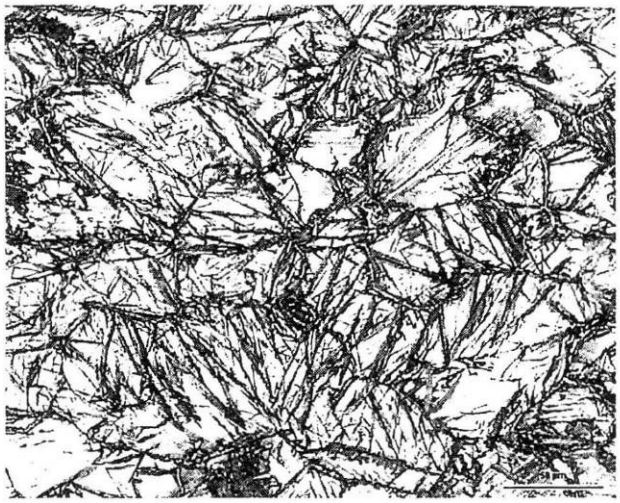

Figure I.10. Structure of plate martensite [WATE03].

The important differences between plate and lath martensite:

- *the nonparallel formation of plates and the large size differences in plates because of the continuing partitioning of austenite through the transformation,*

- *the parallel lath formation and rather uniform size of laths within a packet. The growth of plate martensite may occur as a result of new plate formation or the continued growth of existing plates, whereas lath martensite apparently growth only by new plate formation* [KRAU71].

Medium-carbon steels may contain a mixture of lath and plate martensite so their structure is particularly complex.

Retained austenite is present in all as-quenched martensitic microstructures. The amount of the retained austenite increases as Ms temperature decreases with increasing carbon content. The martensite morphology establishes the distribution of retained austenite, from thin interlath locations in lath martensite to large multifaceted regions between non parallel plates in high carbon steels [KRAU01, WATE03,KRAU99].

In the as-quenched structure the hardness is provided by strengthening effects of substructure and of carbon. Substructural strengthening results from the finely spaced cell walls and lath boundaries and a high dislocation density. The strengthening effect of carbon results from the segregation to cell walls and to dislocations and by solid-solution strengthening [KRAU99].

I.3 The effect of the alloying elements

One of the reasons of adding alloying elements to steels is to *increase their hardenability*, this is, to delay the time required for the austenite decomposition into ferrite and pearlite (transformations that occur by diffusion). This allows slower cooling rates to produce fully martensitic structures.

In general, the alloying elements that are added to control hardenability do not markedly improve the mechanical properties obtainable in tempered martensite. It has been found that there is a strong dependence of the mechanical properties on the carbon content, whereas variations in the substitutional alloying elements (Cr, Ni, Mo) have apparently a much lower effect on the mechanical properties of steels. For high tempering temperatures, however, they may serve to retard the rates of softening [MEYR01].

Basically there are two ways in which alloying elements can reduce the rate of austenite decomposition. They can reduce either the growth rate or the nucleation rate of ferrite, pearlite or bainite [PORT92].

The main factor limiting hardenability is the rate of formation of pearlite at the nose of the C curve in the TTT diagram. To discuss the effects of alloy elements on pearlite growth it is necessary to distinguish between austenite stabilizers (Mn, Ni, Cu) and ferrite stabilizers (Cr, Mo, Si). Austenite stabilizers depress the A_1 temperature (Figure I.1), while ferrite stabilizers have the opposite effect. All of these elements are substitutionally dissolved in the austenite and ferrite.

At equilibrium an alloy element X will have different concentrations in cementite and ferrite, i.e. it will partition between the two phases. Carbide-forming elements, such as Cr, Mo, Mn will concentrate in the carbide, while elements like Si will concentrate in the ferrite. When pearlite forms close to the A_1 temperature the driving force for growth will only be positive if the equilibrium partitioning occurs. Since X will be homogeneously distributed within the austenite, the pearlite will only be able to grow as fast as substitutional diffusion of X allows partitioning to occur. The most likely diffusion route for substitutional elements is through the γ/α and γ/cementite interfaces. However, it will be much slower than the interstitial diffusion of carbon and will therefore reduce the pearlite growth rate.

- When *X is a ferrite stabilizer* there are thermodynamic considerations that suggest that X will partition even at large undercooling close to nose of the C curve. Thus, Si, for example, will increase the hardenability by diffusing along the austenite/ferrite interface into the ferrite.

- When *X is an austenite stabilizer* such as Ni, it is possible, at sufficiently high undercooling, for pearlite to grow without partitioning. The ferrite and cementite simply inherit the Ni content of the austenite and there is no need for substitutional diffusion. Pearlite can then grow as fast as diffusion of carbon allows. However, the growth rate will still be lower than in binary Fe-C alloys since the non-equilibrium concentration of X in the ferrite and the cementite will raise their free energies, thereby lowering the eutectoid temperature, and reducing the total driving force.

- When *X is a strong carbide-forming* element such as Mo or Cr, it has been suggested that it can reduce the rate of growth of pearlite, as well as proeutectoid ferrite, by a solute-drag effect on the mowing γ/α interface. These elements also partition to cementite [PORT92].

I.3.1 Influence of alloying elements on Continuous Cooling Transformation (CCT) diagram

Figures I.11 and I.12 give a selection of CCT diagrams [BERA96] showing the effect of carbon and manganese on the transformation kinetics during continuous cooling and on the volume fractions of the various microstructural constituents. In general, increased amounts of alloying elements lower the temperature for the start of the different transformations and reduce the reaction rates. These effects are related to the influence of the solutes on both the nucleation and growth processes.

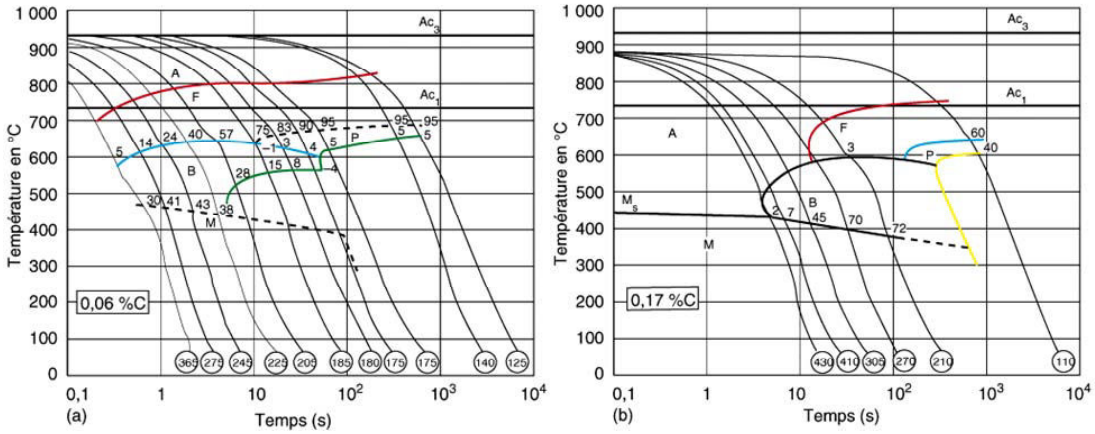

Figure I.11. Effect of C on CCT diagram [BERA96].

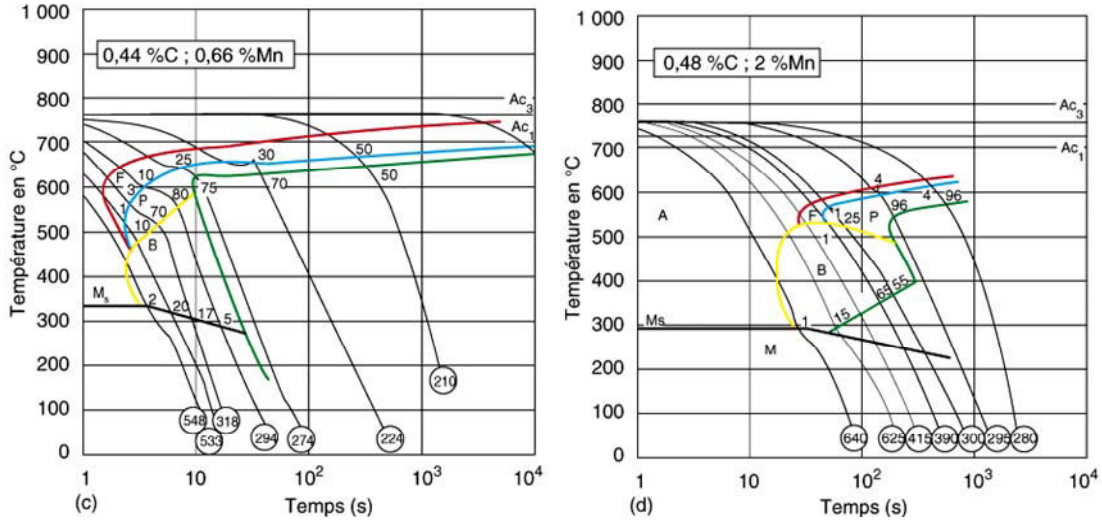

Figure I.12. Effect of Mn on CCT diagrams [BERA96].

The numbers on the cooling curves represent the volume fractions transformed in the corresponding range, while the circled numbers at the bottom of these curves are the final Vickers hardness values measured on the specimens concerned.

It can be seen that ferrite and pearlite start temperatures are shifted down and to the right for both carbon an Mn alloying elements. Carbon and Mn alloying elements improve steel hardenability.

I.3.2 The role of different alloying elements

CMnSiCr chemical composition is typical for DP steels [THOM79, GRAN77]. Table I.1 summarizes the effects of these alloying elements.

Alloying element	Influence
C	Determines the amount of second phase (at a given temperature)
	Strong hardenability agent
Mn	Austenite forming element, decreases C solubility in ferrite
	Retards pearlite and bainite formation, increases the transformation temperatures
	Regular solid solution hardening
	Increases the hardness of tempered martensite by retarding the coalescence of carbides, and thus provides a resistance to grain growth in the ferrite matrix
Si	Increases the slope of the A_3 line, thus allowing more flexibility in heat treatment.
	Raises transformation temperatures
	Increases the activity of carbon and hence promotes the ductility of ferrite
	Inhibits carbide formation, particularly Fe_3C at the ferrite-martensite interface
	May also contribute to the solid solution strengthening
	Negligible effect on hardenability
	Refines microstructure
	Increases the hardness of tempered martensite by inhibiting the conversion of epsilon carbide to cementite
Cr	Austenite forming element, decreases C solubility in ferrite
	Strong carbide-forming element
	Retards pearlite and bainite formation, increases the transformation temperatures
	Increases hardenability
	Increases connectivity of martensite
	Increases hardness of tempered martensite through alloy carbides formation
	Retards the tempering of martensite by retarding the carbides coalescence

Table I.1.The influence of different alloying elements [GRAN77, MARG81, POTT06, WATE03].

During intercritical annealing Mn partitioning between the ferrite and the austenite can take place, resulting in a higher Mn content in the austenite and providing the further enhancement of the hardenability [WATE03].

Mn and Si have a significant influence on the aging behavior of ferrite. Mn reduces the activity of carbon in iron and thus reduces the driving force for precipitation relative to binary Fe-C alloys. Mn also suppresses the formation of the metastable ε-carbide, which is more easily nucleated than the cementite. Si has the opposite effect, raising the activity of C and promoting the formation of the metastable carbide [KORZ82].

The demand for the highest strength in the steel can be met by increasing the carbon concentration, however these higher carbon levels introduce serious weldability problems. Precipitation hardening by microalloying additions (TI, Nb, V) is an interesting alternative to increasing the carbon concentration and has the major advantage that weldability and hot rolling parameters are not degraded [PERR07].

Microalloying elements (Nb, Ti, V, Zr, B) change the recristallization behaviour of the steel (Figure I.13). The precipitation of these elements delays the recrisrallization (increases the recristallization temperature) by pinning the grain boundaries which prevent the grain growth.

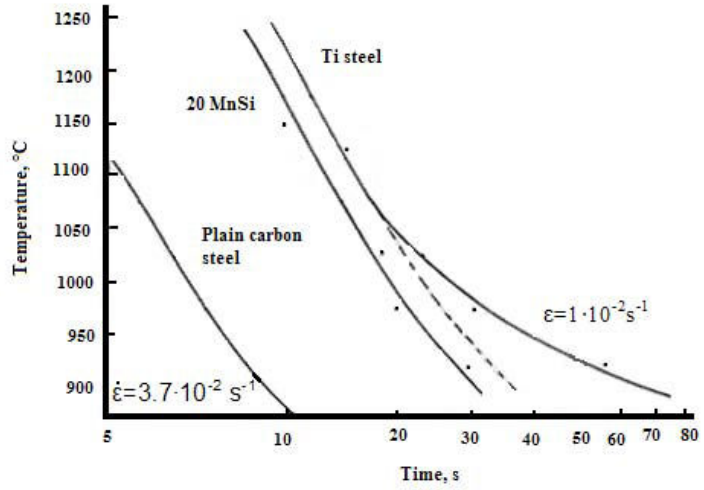

Figure I.13. Time-Temperature recristallization curves: for C-Mn steel and C-Mn-Ti steel [WEIY88].

I.3.3 The effects of alloying elements on austenitising

There are three main consequences of alloying elements:

1. When alloying elements are present, both ferrite stabilizer and moderate or strong carbide formers, austenitising temperature may have to rise,

2. When alloy or mixed carbides are present, longer austenitising times are required. Cementite dissolution is obtained in a short time, but alloy carbides especially of Mo take much longer so they must be austenitised at higher temperatures,

3. When very strong carbide formers present (Nb, V, Ti) the same occurs but these elements are not primarily added for hardenability increase, but for the effect of their carbides.

If steel, with fine VC, is austenitised, without dissolving the carbides, then the effect of V is to reduce hardenability not only because of carbon intake, but also because the migration of the austenite grain boundaries is resisted by the carbides leading to a finer grain size which would then favor formation of diffusive transformation phases [MEYR01]. This can be extended for all microalloying elements.

I.3.4 The effects of alloying elements on ferrite formation

The kinetics of the transformation of austenite to proeutectoide ferrite is retarded in general by the presence of both austenite stabilizers and ferrite stabilizers probably due to effects such as solute drag on migrating interphase boundaries and the rate of diffusion of carbon.

For instance, Mo retards the transformation and it has been suggested that Mo interacts with carbon and reduces the rate at which it can diffuse away into the austenite. Another possible contribution may be done by Mo segregations to ferrite/austenite interphase [RENG85].

The beneficial effect of B occurs, when it is in solid solution in the austenite. B delays the start of ferrite and pearlite transformations. It does not seem to affect the time to complete them, so apparently B has an interaction with austenite grain boundaries. It has been suggested that B segregates at grain boundaries, because it is able to reduce the grain boundary energy, so grain boundary became less effective as nucleation's sites. B increases hardenability without lowering the Ms temperature. This is valuable, because lowering the Ms causes an increase of the amount of retained austenite [RENG85].

I.3.5 The effects of alloying elements on martensite formation

The quantity of martensite formed depends on the temperature, chemical composition and the nature, degree and rate of deformation. The elements that increase hardenability are Cr, Mo, Ni, Mn and B.

The alloying elements change the martensite transformation start temperature, M_S. Andrew's formula gives the effect of alloying elements on M_S temperature in steels [LAFR99]:

$$M_S = 539 - 423C - 30.4Mn - 12.1Cr - 17.7Ni - 7.5Mo - 11Si,$$

M_S temperature is in °C, concentrations are in wt%.

If the steel is quenched rapidly enough from the annealing temperature, there is no time for the diffusion-controlled decompositions processes to occur, and the austenite transforms to martensite [PORT92]. The cooling rate required to suppress diffusional transformations is called the critical cooling rate. Alloying elements change the critical cooling rate. The critical cooling rate, necessary for the DP steel formation, decreases in a linear manner with increasing equivalent Mn content (Table I.2).

Critical cooling rate (CCR)	Reference
$\log(CCR) = -1.73Mn_{eq} + 3.95$ $Mn_{eq} = Mn + 1.3Cr + 2.67Mo$	[TANA79]
$\log(CCR) = -1.46Mn_{eq} + 3.84$ $Mn_{eq} = Mn + 1.24Cr + 3.43Mo + 0.30Si + 2.40P + 78.4B$	[WATE03]

Table I.2. Influence of the alloying elements on CCR to produce DP microstructure (CCR is in °C/s, manganese equivalent Mn_{eq} and concentrations are in wt. %)

I.3.6 Segregations in Ingots and Castings

During the solidification of liquid steel the segregations of alloying element can be formed. This may change damage behaviour of the steel and the mechanical properties of the finished product eventually [BERA96].

Two types of segregation can be distinguished in solidified structures.

1) *Macrosegregation:* composition changes over large distances, on the scale of the ingot.

This type of segregation is caused by the overall enrichment of the liquid in solute elements as the volume fraction of solid increases. As a result the slab centre is enriched in alloying elements (Figure I.14a). Figure I.14b shows the P, S, C and Mn distribution in the ingot. The highest impurity concentration is found in the middle of the ingot. The S has the strongest segregation, Mn – the lowest [LIVC90, BERA96].

2) Microsegregation occurs on the scale of the secondary dendrite arm spacing (Figure I.15a). The dendrite axes, which solidify first, contain fewer impurities (S, P), than inter axes spaces [LIVC90, BERA96]. Deformation of this structure leads to the banded structure formation (Figure I.15b).

The degree of microsegregation of an element in an alloy is greater the lower the values of its partition and diffusion coefficients. Microsegregation is therefore inexistent for the interstitial elements, but relatively high for the metallic alloying elements. It is extremely marked for certain residuals, such as sulphur and phosphorus.

In general, segregation is undesirable as it has marked deleterious effects on mechanical properties. The effects of microsegregation can be mitigated by subsequent homogenization heat treatment (high temperature soaking before the hot rolling), but diffusion in the solid is far too slow to be able to remove macrosegregation which can only be combated by good control of the solidification process [PORT92, BERA96].

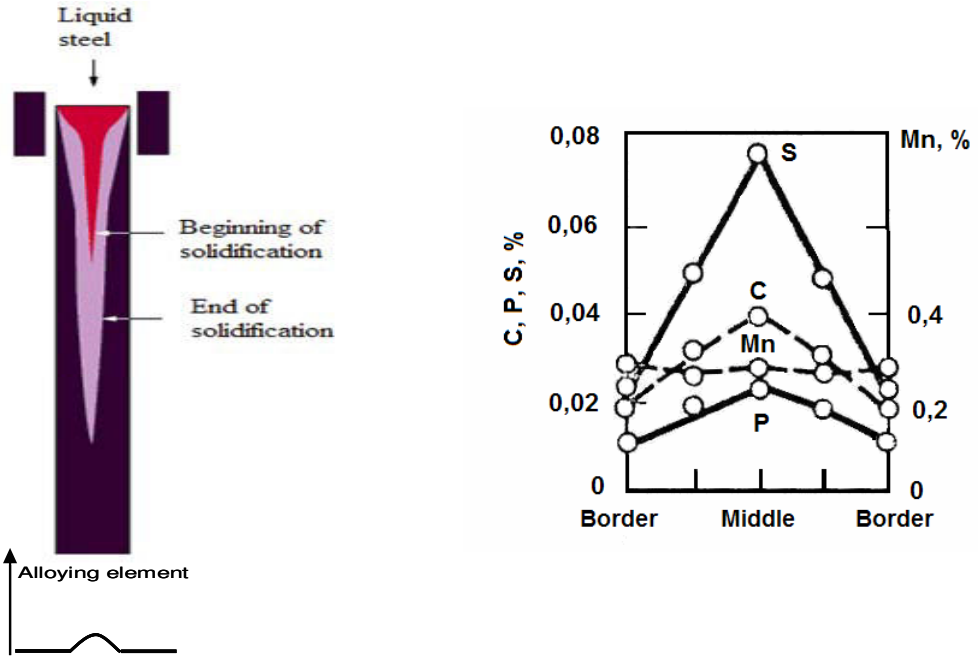

Figure I.14. The macrosegregation formation (a) and impurities distribution in the diameter of steel ingot (b) [BERA96, LIVC90].

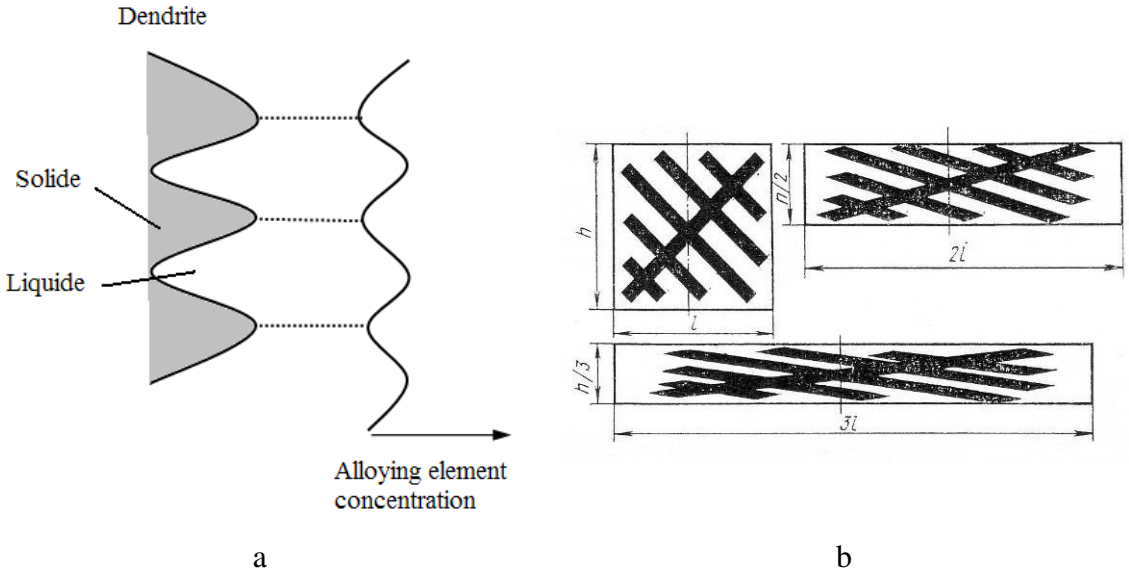

Figure I.15. a-schematic microsegregation formation due to the dendritic solidification, b-schematic banded microstructure formation due to deformation of microstructure [BERA96, LIVC90].

DP steels can be produced by a wide variety of chemical compositions from low C to relatively high alloy steels associated with adequate heat treatment parameters. The alloying elements can increase flexibility and stability of processing in controlling volume fraction, compositions of the two phases and mechanical property variations.

I.4 Tempering

After quenching the DP steel is subjected to tempering in order to improve its mechanical properties and formability. Different changes occur in the microstructure, which has a significant impact on its damage behaviour. In the present chapter the tempering reactions in the martensite phase and in the DP steel are reviewed.

I.4.1 Tempering of ferrous martensites

Tempering* is the process in which the microstructure approaches equilibrium under the influence of thermal activation.

The tendency to temper depends on how far the starting microstructure deviates from the equilibrium. It can be demonstrated that excess carbon which is forced into solution in martensite is the major contributor to the stored energy of martensite.

There is a strong repulsion between carbon atoms in nearest neighbor sites. This means that carbon atoms almost always have an adjacent interstitial site vacant, leading to a very high diffusion coefficient when compared with the diffusion of substitional solutes. Given that carbon is able to migrate in martensite even at ambient temperature, it is likely that some of it redistributes, for example by migrating to defects or by rearranging in the lattice such that the overall free energy is minimized [BHAD04].

I.4.2 Stages of tempering

The decomposition processes are complex and involve many overlapping phenomena. The classical scheme (Figure I.16) of tempering behavior is divided in four stages [SPEI92]:

- precipitation of epsilon transition carbide, T1,
- decomposition of retained austenite, T2,
- formation of cementite, T3,
- precipitation of alloy carbides, T4.

In addition to these four stages, pre-precipitation clustering of carbon atoms, segregation of carbon atoms to lattice defects, the formation of other transition carbides, recovery and recristallization of the martensitic substructure must be taken into account [SPEI92]. These processes are summarized in Figure I.16.

In lath martensite carbon tends to diffuse to sites close to dislocations in order to lower its chemical potential. In plate martensite, however, the martensite is internally twinned and there are relatively few dislocations. In this case carbon-rich clusters or zones tend to form instead [PORT92].

* In general, tempering and strain aging are the different terms to designate the same processes occurred during the post-heating.

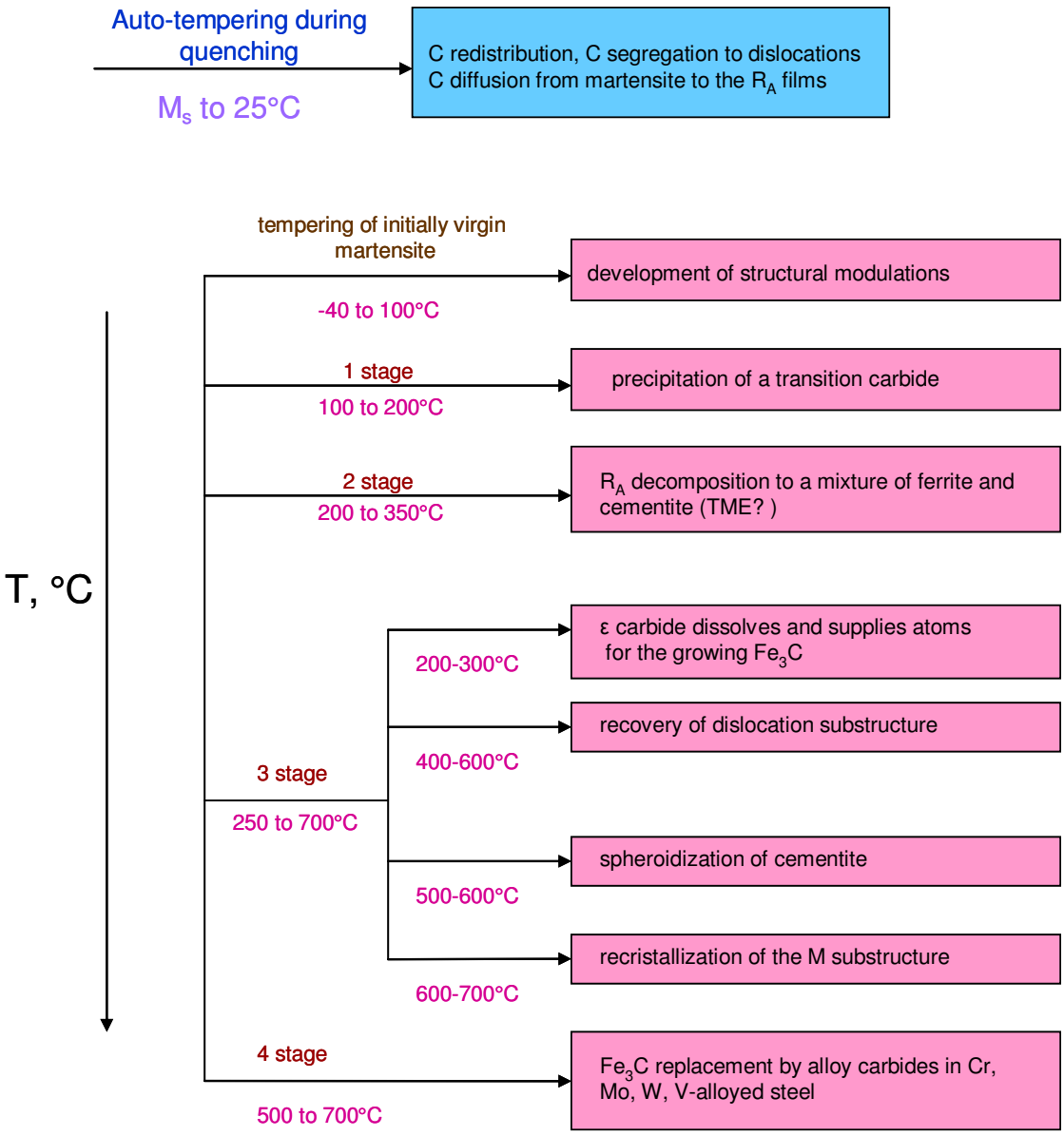

Figure I.16. Scheme of tempering reactions in ferrous martensites.

Autotempering

Segregation of carbon atoms during quenching (M_s to 25°C)

Most commercial quenched and tempered steels have M_s temperatures that are considerably above room temperature (200-400°C). Many products manufactured from these steels have appreciable dimensions and cooling through the M_s-M_f region is sufficiently slow that extensive redistribution of C atoms may occur after transformation. As a result the as-quenched martensite in these steels is referred to be "auto-tempered".

In low-carbon, low-alloy steels, appreciable carbon segregation to dislocation sites occurs during quenching. Also, segregation of carbon from the martensite to interlath austenite films may occur during quenching. As a result the initial carbon distribution is very complex [SPEI92].

Segregation of carbon atoms to dislocations (S1)

In low-carbon martensites, it was postulated on the basis of electrical resistivity results that carbon atoms were segregated to dislocations and to subboundaries in very rapidly quenched thin samples, even though no carbide precipitation was observed.

The calculations indicate that the first stage of tempering would be absent in lath martensites with less than 0.2%C, because all the carbon atoms would be segregated to dislocations with a higher binding energy than in epsilon carbide.

When the carbon content exceeds 0,2%C, most of the low energy dislocation sites are occupied and much of the additional carbon will enter the normal interstitial positions located far from defects (dislocations and lath boundaries).

It is interesting to note that 0,2%C is also about the carbon content at which tetragonality of Fe-C martensite is first detected. It has been suggested that the segregation of carbon to defects in martensitre during quenching explains the lack of tetragonality of Fe-C martensites with carbon content less than 0,2%C [SPEI69, SPEI92].

Segregation of carbon atoms to interlath austenite films (S2)

The films of retained austenite have been detected in many high-Ms lath martensites by careful electron microscopy.

Carbon diffusion from the martensite to the austenite films offers another possible mode of carbon redistribution during quenching (Figure I.17).

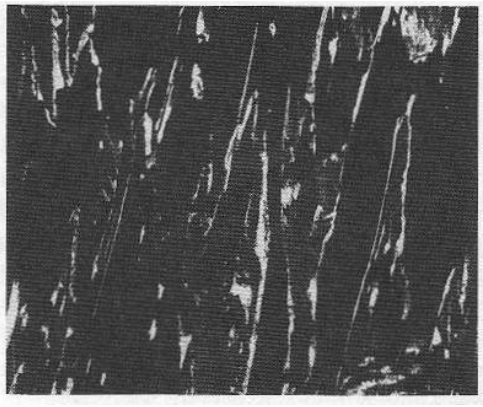

Figure I.17. Dark-field TEM of thin films of interlath retained austenite in water-quenched steel [SPEI92].

Such carbon redistribution has been detected in lath martensites (Ms between 400 and 250°C) even during very rapid water quenching.

For the steel contained 0.26%C with Ms=320°C, after oil quenching, the carbon content in the austenite at the austenite/martensite interface was found to be enriched to levels as high as 2.1wt% [SPEI92].

Aging of initially virgin martensite (-40 to 100°C)

The martensites with M_S temperature below room temperature (thus carbon atom redistribution prior to deliberate tempering is minimal) are generally referred to as "*virgin martensites*".

The diffusionless nature of the martensitic transformation in the Fe-C alloys has important implications regarding the structure of the martensite phase.

The Bain distortion which converts the face-centered cubic (fcc) parent austenite into the body-centered martensite phase transfers the carbon atoms on octahedral interstitial sites (OIS) of the austenite into OIS in the martensite.

The hardness and electrical resistivity in Fe-Ni-C martensites passed through a maximum at temperatures below 100°C, i.e. before the precipitation during the first stage of tempering. This indicates that the kinetics of the early stages of aging are controlled by carbon diffusion.

The first evidence of structural changes preceding T1 came from the selected-area electron-diffraction results from high-carbon martensite aged at room temperature. Peculiar sets of diffuse streaks were observed along directions near the four <012> reciprocal lattice distortion. Diffraction patterns displaying this diffuse scattering also exhibit a tetragonal distortion, indicating that carbon atoms continue to preferentially occupy Oc sites during aging. The dark field transmission electron micrograph reveals that the diffuse scattering is associated with fine striations spaced approximately 1.5 nm. The absence of reflections other than the normal body-centered tetragonal reflections in diffraction patterns indicates the development of *coherent structural modulations.*

Mechanism of phase separation

Atom-probe field-ion microscopy data from Fe-15Ni-1C martensite has revealed periodic variations in carbon concentration (alternating carbon-reach and carbon-free bands) with a wavelength comparable to that of the modulated structure detected by TEM. The composition amplitude increases continuously with time.

The aligned nature of the modulated structure and the graduate increase in carbon concentration amplitude with aging time are both consistent with decomposition by a spinodal mechanism influenced by elastic anisotropy.

First stage of tempering (100-200°C, T1)

This stage is associated with the appearance of transition carbide, which precipitates uniformly throughout the martensite phase. Although the precipitation of the transition carbide proceeds in a few minutes in the tempering range of 100 to 200°C, precipitation has been detected at temperatures as low as room temperature after several months of aging.

Tempering leads to a dispersion of coarse particles in a matrix of low-carbon martensite. Above 200°C the transition carbide is rapidly replaced by the more stable M_3C carbide, cementite.

Some results indicate that the nucleation of transition carbide is heterogeneous, at least in martensites that undergo spinodal decomposition prior to T1 carbide precipitation. The decomposition of virgin martensite, which occurs uniformly throughout the martensite phase, provides a fine, uniform distribution of sites for subsequent carbide nucleation.

Structure and morphology of the stage 1 carbide.

Detailed electron investigation of the Fe-C and Fe-Ni-C martensites indicated that carbon atoms may be ordered in the transition carbide, reducing the lattice symmetry from hexagonal to orthorhombic.

A variety of morphologies have been reported for the stage 1 carbide: plate-like carbide, rod-like. The disparity among the above observations suggests that alloy composition might exert an important influence on the carbide morphology.

Second stage of tempering (200 to 350°C, T2)

This stage of tempering (200-350°C) involves the transformation of retained austenite, usually in the temperature range of 200 to 300°C. The product is a mixture of ferrite and cementite.

Dark-field electron microscopy has shown that long interlath ribbons of cementite form during the austenite decomposition. These interlath carbide films are apparently associated with "tempered martensite embrittlement".

Several investigators have concluded that the kinetics of retained austenite decomposition is controlled by the rate of carbon atom diffusion in the austenite.

Third stage of tempering (250 to 700°C, T3)

The third stage of tempering (250-700°C) is associated with precipitation in the martensite phase of the Fe_3C carbide, the most stable of the various iron carbides. In addition, several other transition carbides have been observed in the regime of T3. Also a number of thermally activated processes such as recovery, recristallization, grain growth and spheroidization of cementite occur at higher temperatures in this region.

Precipitation of cementite generally begins in the temperature range of 200 to 300°C; at the same time, the transition carbide dissolves and supplies carbon atoms for the growing cementite particles.

At higher temperatures of 400-600°C recovery of the dislocation substructure occurs. At 500-600°C spheroidization of the cementite particles becomes important. Finally, at 600-700°C recristallization of the martensitic substructure may occur, depending on the carbon content and impurity level. The final product is an equiaxed ferrite containing a coarse dispersion of spheroidal cementite particles.

During tempering, recovery, recristallization, grain growth are occurring simultaneously with the precipitation of cementite.

Fourth stage of tempering (500 to 700°C, T4)

If strong carbide formers are present (Cr, Mo, W, V) a fourth stage of tempering may occur. In this stage the cementite particles dissolve and are replaced by more stable alloy carbides. The formation of these carbides is controlled by the diffusion of substitutional elements, hence, the alloy carbides are formed only in the 500-700°C temperature range and in a much finer dispersion than the cementite dispersion which they replace. As a result, hardness may increase during tempering at these higher temperatures, resulting in a "secondary hardening".

I.4.3 Tempering reactions in DP steels

Tempering in DP steel is complex in nature, as a result of its composite two phase microstructure and strain partitioning. The tempering behavior can be influenced by the interstitial carbon, the carbon in the grain boundaries, the specific distribution of dislocations and residual stresses, and probably by carbon liberated from the martensite as a result of tempering phenomena. Moreover, the volume decrease due to martensite tempering can impact the yielding behavior [WATE03].

Usually, tempering reactions in DP steels are a combination of those effects expected for each of the individual phases. There are synergistic effects that can be attributed to the presence of both phases [WATE03].

Pre-precipitation clustering of carbon can be expected to occur during cooling after the martensitic transformation, because of the high Ms-temperature of low carbon martensite [WATE03].

Stages of tempering

The schematic overview of different aging phenomena in DP steels is shown in Figure I.18. Tempering reactions are determined as a function of the yield stress increase $\Delta\sigma_{0.5}$.

The aging process can be divided in three main stages [WATE03]:

1. Pinning of dislocations in the ferrite by interstitial carbon atoms,

2. The precipitation stage: the excess interstitial carbon, not used to pinning, starts to form carbon clusters or low-temperature transition carbides, such as ε-carbide,

3. The martensite tempering stage: due to the formation of transition-carbides in the martensite, the volume of the martensite decreases. The internal stresses, introduced in the ferrite due to the martensitic transformation, are reduced.

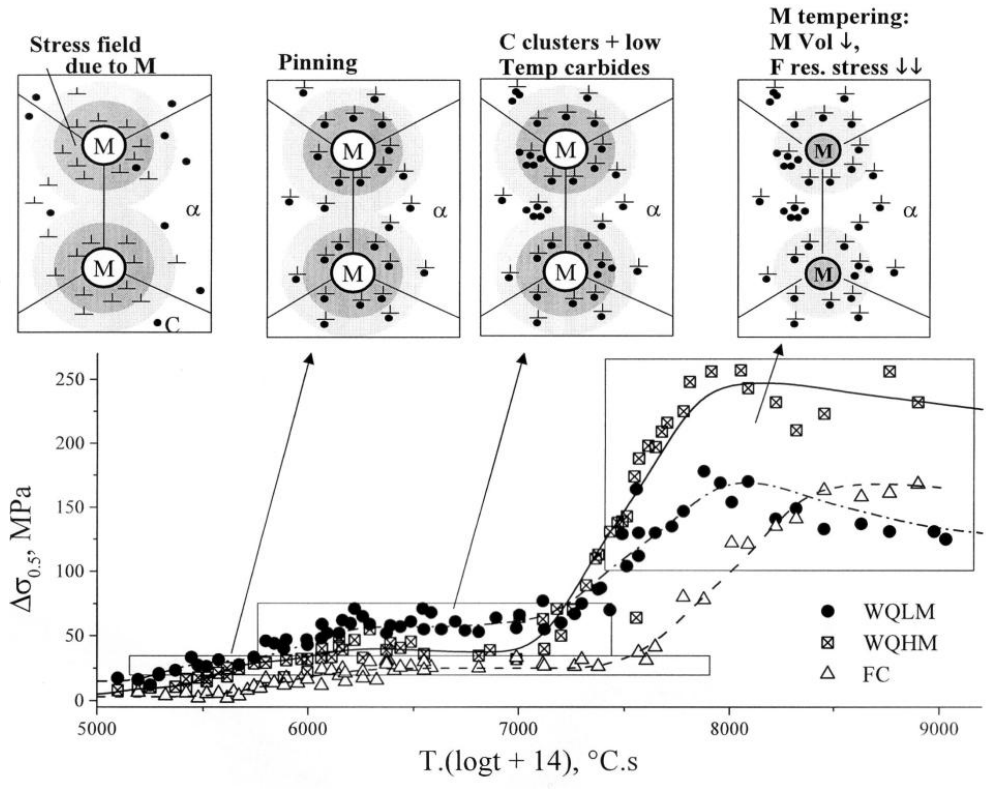

Figure I.18. Scematic overview of the processes involved in the tempering of DP steels as a function of the Hollomon-Jaffe parameter (T: Temperature, K, and t: time, sec.) [WATE03].

Thus, the effects of tempering can be summarized as follows:

- In high M_S martensites, carbon redistribution may take place during quenching by segregation of carbon atoms to dislocations, by carbon diffusion to interlath retained austenite films, or under very slow quenching conditions by carbide precipitation ("autotempering"). As a result, the first stage of tempering can be absent in these steels,

- The first stage of tempering involves the formation of transition carbide, which morphology varies from plates to rods and may be composition dependent,

- The second stage of tempering implicates the decomposition of retained austenite to form cementite and ferrite. In low-carbon steels, retained austenite is present as interlath films, and the cementite films, formed during austenite decomposition play an important role in TME,

- The third stage comprises a number of competing processes: transition carbide dissolution, which supplies atoms for the growing Fe_3C, recovery of dislocation substructure, spheroidization of cementite, recristallization of the martensite substructure,

- In steels with strong-carbide formers elements (Cr, Mo, V, W) a forth stage of tempering is present, in which cementite is replaced with more stable alloy carbides, this may result in secondary hardening.

I.5 The DP steel deformation behaviour

I.5.1 Mechanical behaviour

Microstructural factors, such as the volume fraction of martensite, the carbon content of the martensite and the substructure of ferrite grains and the effects of tempering influence the distribution of strain between the ferrite and martensite of DP steels.

The distribution of strains between the ferrite and the martensite phases, as well as among the different grains of each phase, was observed to be inhomogeneous upon mechanical loading. The macroscopic strain of the specimen at which the martensite begins to deform was also found to be dependent on the microstructural parameters [SHEN86].

It was confirmed that plastic deformation of martensite should not be neglected in some microstructure configurations. As a consequence, martensite should be considered as a ductile phase after an elastic regime [KRAU01, RACH77]. Figure I.19 presents the estimated (by averaging equations) stress-strain curves for ferrite and martensite in DP steel together with the macroscopic curve for a DP steel [JACQ07].

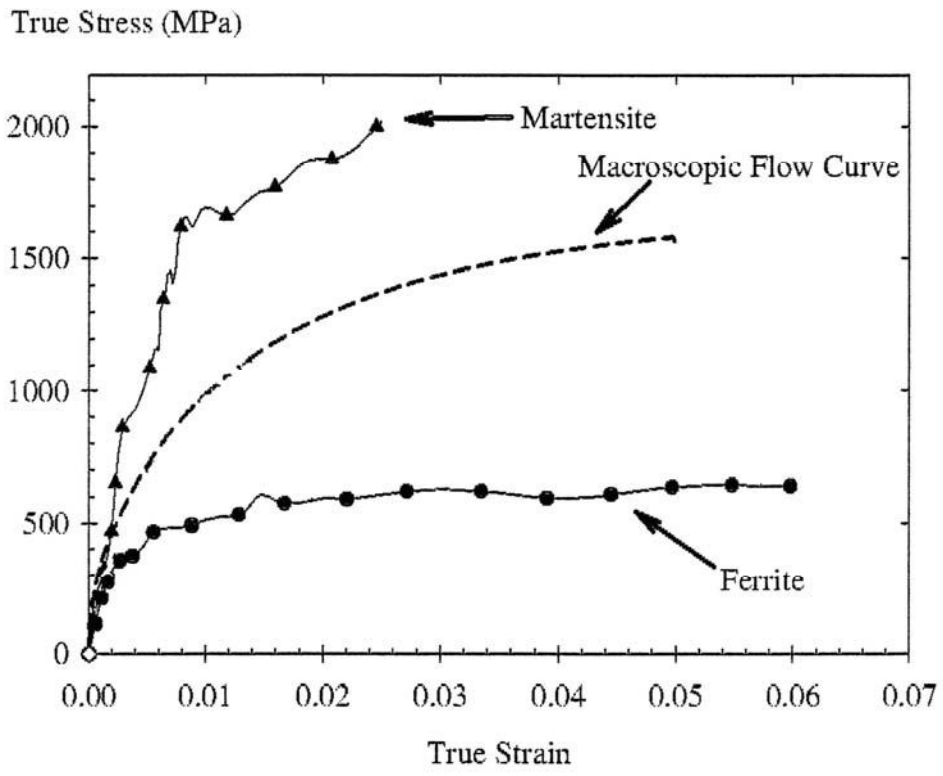

Figure I.19. Flow curves of ferrite and martensite phases, macroscopic stress-strain curve for DP steel (Fe-0.29C-1.42Mn-1.41Si) with 50% martensite - 50% ferrite microstructure [JACQ07].

The stages of deformation are as follows [ABBA03]:

- Both component phases are elastic,
- The softer phase (ferrite) is deformed plastically, while the harder phase (martensite) only elastically,
- Both components deform plastically.

The macroscopic strains at which the martensite islands begin to deform is very important. It is obvious that the start of martensite deformation depends on the microstructural parameters of the steels. A decrease of martensite carbon content (i.e. decrease of martensite hardness) results in earlier deformation of martensite. Tempering at various temperatures decrease the martensite hardness, which also causes earlier deformation of martensite [SHEN86].

I.5.2 Continuous yielding behaviour

In general, DP steels show a continuous yielding behaviour without a yield point. The combination of mobile dislocations introduced by the low temperature martensite transformation and the residual stresses developed during the transformation causes plastic flow to occur easily at low plastic strains. Plastic flow begins simultaneously at many sites throughout the specimen and discontinuous yielding is suppressed [SPEI81A].

Role of dislocations

Hansen and Pradhan have reported that two conditions must be satisfied for DP steel to exhibit the continuous yielding [HANS81]:

1. There must be a sufficient density of mobile dislocations: the mobile dislocation density must exceed the critical density of approximately 10^6-10^8 cm^{-2} required for continuous yielding*,
2. The dislocations produced during the austenite to martensite transformation must remain mobile at room temperature.

In the DP steel the austenite to martensite transformation during quenching involves a volume expansion which creates the dislocations in the ferrite immediately adjacent to martensite. Figure I.20 shows the TEM images with heavily dislocated ferrite regions which lie in close proximity to the martensite particles. Since the martensitic transformation occurs at relatively low temperatures, the dislocations generated in the ferrite will not be solute pinned and thus mobile.

**Although 10^6-10^8 $1/cm^2$ dislocation densities are typical of hot-rolled or annealed steels, the majority of these dislocations are pinned by interstitial atoms and thus immobile.*

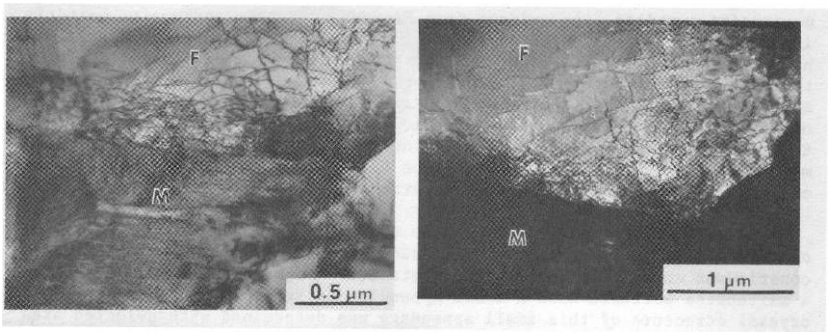

a b

Figure I.20. TEM examination of variation in dislocation density in ferrite (F) adjacent to a martensite (M) particle: (a) bright field, (b) dark-field [RIGS77].

The motion of the already present and mobile transformation induced dislocations can occur at a low level of stress and explains the characteristic low yield stress of DP steels [RIGS77].

Role of residual stresses

Residual stresses generated in the ferrite by the volume expansion accompanying the austenite to martensite transformation during quenching are another contributing factor in the yielding behaviour. Because the transformation occurs at low temperatures, the transformation induced stresses will be only partially relieved by the generation of dislocations in the ferrite and the residual stresses can assist in the initiation of yielding at low stress levels [RIGS77].

Thus, DP steels show decreased yield strength and a continuous yielding behaviour due to dislocations and residual stresses concentrated at ferrite/martensite interface.

I.5.3 Tensile strength

Devies reported that the tensile stress (TS) and the yield stress are linear functions of the martensite fraction in DP steel. The TS and YS were only functions of the percentage of martensite in the alloy and did not depend upon the martensite carbon content (Figure I.21) [DAVI78].

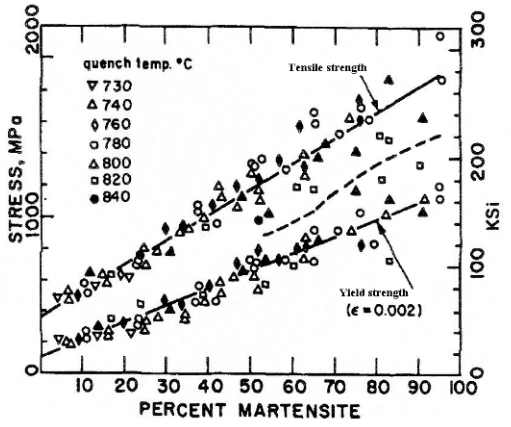

Figure I.21. Evolution of TS and YS with martensite fraction for the Fe-Mn-C steels [DAVI78].

However, strength of full martensitic steels is very sensitive to changes in carbon content. Krauss reviewed hardness measured as a function of carbon content for a variety of carbon and low alloy martensitic steels by a number of investigators (Figure I.22). Despite the scattering which reflects differences in microstructure, the martensite hardness is carbon-dependent [KRAU99].

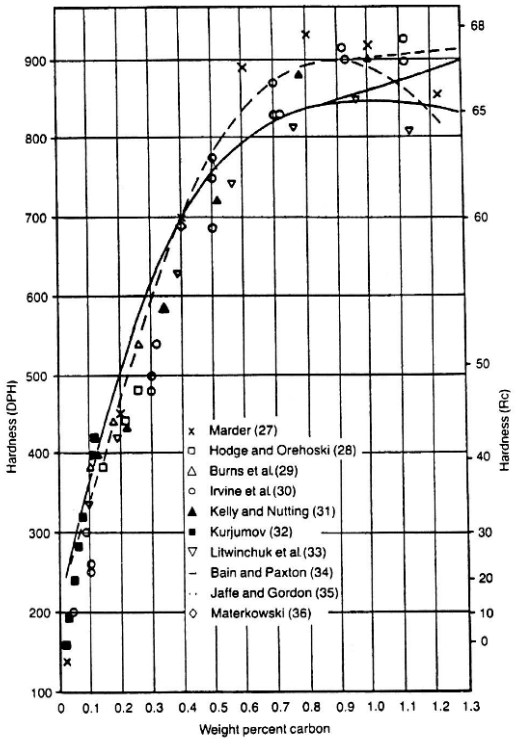

Figure I.22. Hardness of martensitic microstructures as a function of steel carbon content [KRAU99].

I.5.4 Ductility

It is indicated that uniform elongation decreases in a non-linear manner with increasing percent martensite. The total elongation of ferrite-martensite steels also decreases with increasing percent martensite. Also, total elongation was found to depend not only on the volume fraction of martensite, but also on the carbon content of the martensite phase, decreasing as the carbon content (hardness) of the martensite phase increased.

Distribution of the martensite phase influences ductility. For any given percent martensite, a set of widely spaced, small particles is desired. Chains of martensite particles that are linked up may be detrimental to ductility because they may offer an easy crack-propagation path through the matrix, although such effects are sensitive to the nature of the distribution and to the manner in which the sheet is stressed. Because the distribution of the martensite phase is determined by the nucleation of austenite particles at the cementite or pearlite phases present in the starting microstructure, it is important in intercritically annealed DP steels that this microstructure be as uniform and fine as possible [BECK79, HAYA77].

Lowering the carbon content of the ferrite phase by decreasing the cooling rate after continuous annealing, has also been reported to be critical in obtaining the highest possible ductility in DP steels. The ductility obtained after water quenching is much inferior to that obtained with a mild cooling rate, because of the lower carbon content of the ferrite in the slower cooled material [RACH77].

The amount of epitaxial ferrite formed upon cooling has an important effect on ductility. The ductility is improved as the amount of epitaxial ferrite was increased [SPEI81A].

Arguments about the effect of retained austenite in DP steels are complex and still not resolved. When large amounts of retained austenite are present and when the stability of the austenite is sufficient that the transformation of the retained austenite occurs late in the plastic-straining process, then large effects on UE can be expected [SPEI81A].

The factors that can influence the elongation value can be summarized as follows:

- volume fraction, carbon content of ferrite, amount of epitaxial ferrite,
- volume fraction, carbon content, distribution of martensite,
- amount of retained austenite.

I.6 The damage mechanisms in DP steel during the ductile fracture process

The ductile fracture process is generally considered to occur in three sequential stages: void nucleation, void growth and void coalescence.

I.6.1 Void nucleation

Two types of void nucleation can be distinguished:

1) Homogeneous nucleation – not associated with inclusions,

2) Heterogeneous nucleation – associated with structure heterogeneity.

In the ductile fracture process of the DP steel the important role is played by the second phase. Heterogeneous nucleation is observed in DP steels. It is shown that the voids nucleate both by cracking of the second phase island and by decohesion of second phase/ferrite interfaces [STEI88, STEV77, BALL82]. It was reported that in a given sample large inclusions appear to produce cavities sooner than small ones [ARGO75, BALL82].

Criteria for inclusion separation: energy criteria, local stress criteria and local strain criteria [ARGO75]:

- Cracks at interfaces could form when the locally concentrated elastic strain energy which could be released upon decohesion becomes comparable to the energy of the surfaces to be generated. This is only a necessary condition for inclusion separation,

- Separation requires reaching the interfacial strength at the interface, at least in some points, to provide a nucleus of separation,

- Cavity formation at interfaces may obey a critical local strain criterion.

Argon criterion for decohesion.

Argon criterion for decohesion is based on interfacial critical stress, σ_C. Interface decohesion occurs, when local stresses (at the interface) reach the interface strength. Interfacial stresses are described by equation [ARGO75]:

$$\sigma_C = \sigma_{eq} + \sigma_h$$

Where σ_{eq} is an equivalent stress, σ_h is a hydrostatic stress. The stress triaxiality $T = \sigma_h / \sigma_{eq}$ appears in Argon's criterion:

$$\sigma_C = \sigma_{eq}(1+T)$$

Brittle fracture criterion: Griffith cracks

The theoretical fracture strength of a solid is of the order of E/10, but the strengths of crystals in practice tend to be lower than this value by some two orders of magnitude. Griffith supposed that a macroscopically homogeneous test sample might contain small defects which enable the stress to be concentrated sufficiently for the ideal fracture stress to be attained in small localized regions of the sample.

Griffith equation gives an approximate value of critical stress σ_f for brittle fracture of particle [GRIF20]:

$$\sigma_f = A\sqrt{\frac{2E\gamma}{\pi a}}$$

Where A is a constant, E- Young modulus, γ - surface energy and a - defects size in material.

I.6.2 Void growth

Once voids have nucleated, they grow mainly in the tensile direction. Rice and Tracey proposed a model to describe the void growth process. Rice and Tracey characterized the plastic flow field in an elastically rigid, perfectly plastic material containing an isolated spherical void and treated the growth of voids for a remotely uniform stress and strain-rate field. The following equation permits to determine the average void radius [RICE69]:

$$\frac{dR}{R} = K \exp(\frac{3}{2}T)d\varepsilon$$

Where K=0,283, R - an average void radius, T- stress triaxiality, ε – plastic deformation.

This approach shows that void growth increases as a function of applied strain and that the rate of void growth is greatly increased by elevations in the triaxial stress [RICE69].

I.6.3 Void coalescence

Void coalescence takes place when ligaments between them are ruptured. Two types of coalescence can be observed: internal necking and formation of secondary voids between existing voids. Internal necking can occur by two mechanisms: localization of plastic deformation in ligament or by microscopic shear. Tomason's model can be used to describe void coalescence. It is based on internal necking between cavities.

I.7 Microscopic fracture appearance in DP steel

It is reported that DP steels can exhibit brittleness in the as-quenched condition necking after tempering (Figure I.23). SEM examination reveals patches of cleavage in some of the freshly quenched samples, while only ductile dimpling is found in the tempered specimens.

During tempering the carbon distribution occurs and the martensite and ferrite properties are modified. Thus, post-heating ameliorates the ductility [DAVI81, TANA79].

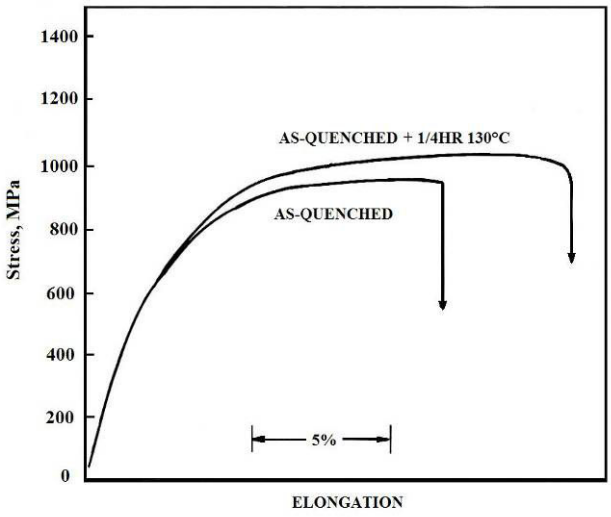

Figure I.23. Stress-strain curves for the DP steel [DAVI81].

TEM examination of carbon replicas of fracture surfaces shows that many of the cusps are of the classical type, being associated with individual inclusions, many cusps are not. The later type of cusps which has not nucleated on inclusions differs because they are 'rough bottomed'. In many cases, the bases of these cusps resembles cleavage facets, their diameters being of similar size to the mean second phase island diameter. It is explained that the rough bottomed cusps has nucleated by brittle cleavage of second phase islands [BALL82].

It is demonstrated that tempering change the crack initiation and crack propagation mode in DP steel (Figure I.24). It improves martensite toughness and thus increases the martensite fracture stress. The material's ability to distribute strain improves after tempering: a blunted crack is observed in tempered state as opposed to a sharp-shape crack in the as-quenched state [STEV77].

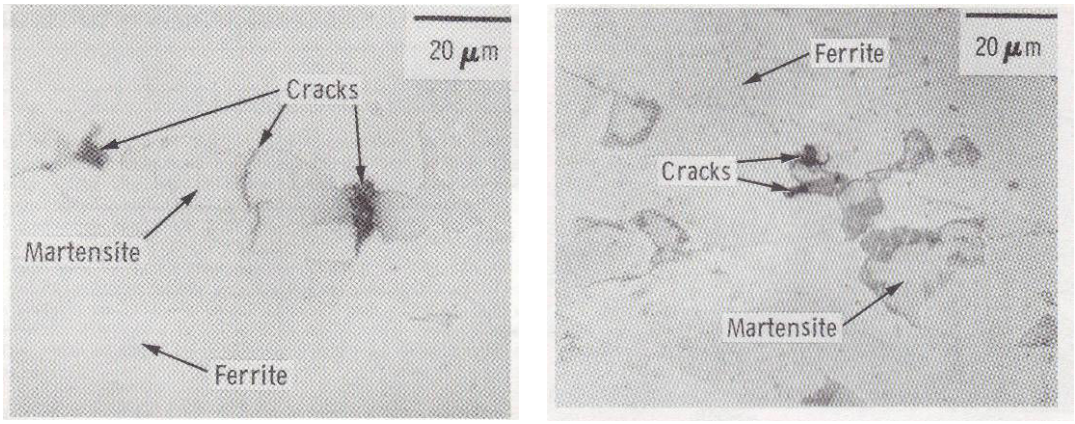

As-quenched sample: sharp cracks Tempered sample: blunted cracks

Figure I.24. Fracture observations in DP steel [STEV77].

I.8 Damage resistance of DP steel through Hole Expansion (HE)

In the automotive industry the steel sheets formability is described through various test methods including the hole expansion (HE) testing. The procedure for HE test is presented in A.1.

It is reported that the good formability of DP steels is determined mainly by the ferrite constituent, which is normally highly ductile. Ferrite is also plastic because of the "fresh" dislocations created by the transformation stresses resulting from the quench from $\alpha+\gamma$ region.

An increase in martensite volume fraction leads to a decrease in the HE ratio. When the difference in the hardness between ferrite and martensite is large, formation of the micro-cracks during punching will be promoted and the hard martensite phase in the vicinity of the micro-cracks will cause a stress concentration, leading to an acceleration of the crack propagation. Tempering provides martensite softening and this reduces the above tendencies [NISH81, FANG03].

Chapter II

Microstructures and mechanical properties

II.A Microstructure formation

The steel microstructure controls its mechanical properties, which in turn will govern the possible application of the material in vehicle parts.

The aim of this chapter is to understand the influence of the heat treatment parameters on the microstructure formation in a reference DP steel.

Firstly, the initial data necessary in understanding the microstructure formation in studied DP steel is presented: the chemical composition of the steel, the continuous cooling transformation diagram, and the applied heat treatments. Secondly, the microstructures obtained after these heat treatments are analyzed and a quantitative analysis of the phase compositions in these microstructures is carried out.

II.A.1 Chemical composition and initial microstructures

An industrial DP780 steel is used as reference material for the observations in this work. This steel was provided in the cold rolled condition without coating. The sheet thickness is 1.2 mm and the chemical composition is shown in Table II.1. This chemical composition (CMnSiCr) is typical for DP steels.

C	Si	Mn	Cr
0.15	0.215	1.9	0.195

Table II.1. Chemical composition of the reference DP steel (in wt. %).

The cold rolled sample issued from the 2.73 mm hot rolled sheet. The metal temperature after hot rolling is 889°C and the coiling temperature is 562°C.

Figure II.1 shows the steel microstructure after hot (a) and cold (b) rolling. The hot rolled microstructure consists of ferrite and pearlite. The pearlite fraction determined by image analysis is 26.5±4.2 %. The pearlite fraction assessed by Ceqcsi® is 29 %, which is in accordance with experimental value.

After the cold rolling the microstructure is heavily deformed and banded. The grains and the non-metallic inclusions are elongated and deformed respectively in the rolling direction.

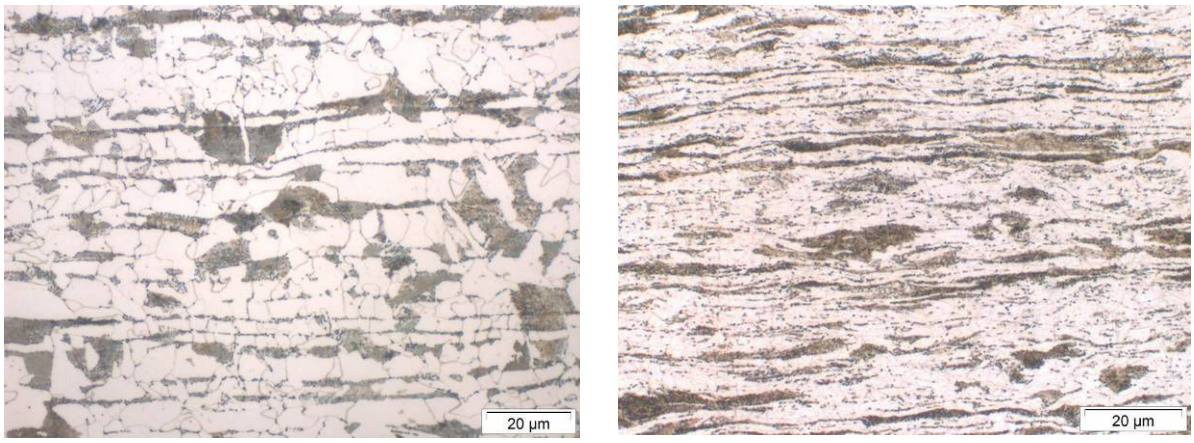

a b

Figure II.1. The hot (a) and cold-rolled (b) microstructures (Nital etching).

II.A.2 Continuous Cooling Transformation (CCT) diagram for studied DP steel

Figure II.2 is a continuous cooling transformation (CCT) diagram taken from a previous study on a similar DP steel [DELB03]. The steel was annealed at two temperatures: 800°C in the intercritical region and 900°C in the fully austenitic region. The diagram is characterized by an elongated C-curve for the ferrite reaction and by delayed pearlite formation. The long ferrite nose provides a simple ferrite formation during slow cooling.

It can be seen that bainite appears in microstructure for a cooling rate of about 15°C/s for both annealing temperatures while pearlite formation occurs at cooling rate less than 1°C/s for the 800°C-annealing temperature.

For this DP steel, when a lower, 800°C annealing temperature is used the ferrite formation is easier because ferrite continues to grow on already present intercritical ferrite. So the ferrite nose is shifted to the left for 800°C compared to 900°C on this diagram. As a consequence, pearlite formation is easier in the 800°C-annealed steel, because of the higher carbon concentration of intercritical austenite. Thus, the pearlite nose is more on the left for the 800°C-annealed steel.

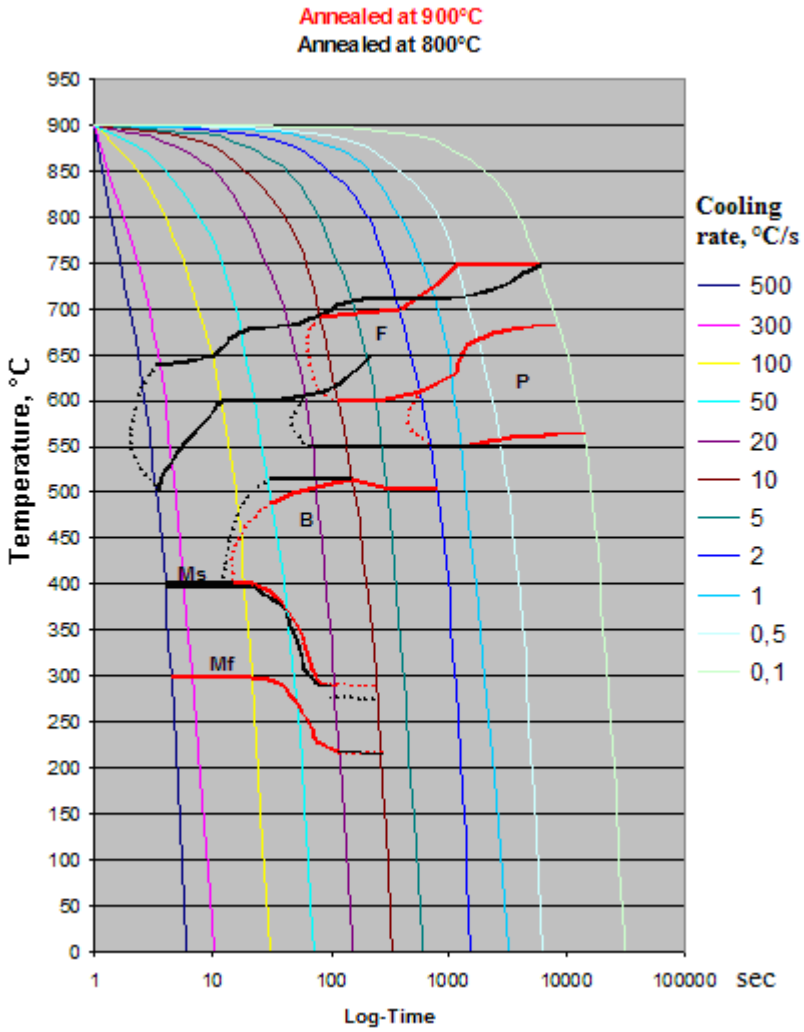

Figure II.2. The CCT diagram for DP steel (Fe-0.15C-1.9Mn-0.2Si-0.2Cr).

II.A.3 Determination of intercritical region temperatures

In order to determine the intercritical interval limits (i.e. A_{C1} and A_{C3} temperatures) an experiment is carried out using a dilatometer. The temperatures are determined for the heating. The cold rolled sample is heated in dilatometer at 2.7°C/sec to 1000°C. The change of a dilatometric curve slope (Figure II.3) gives value of A_{C1} and A_{C3} temperatures on heating.

Therefore, austenite transformation region is between 746°C and 845°C.

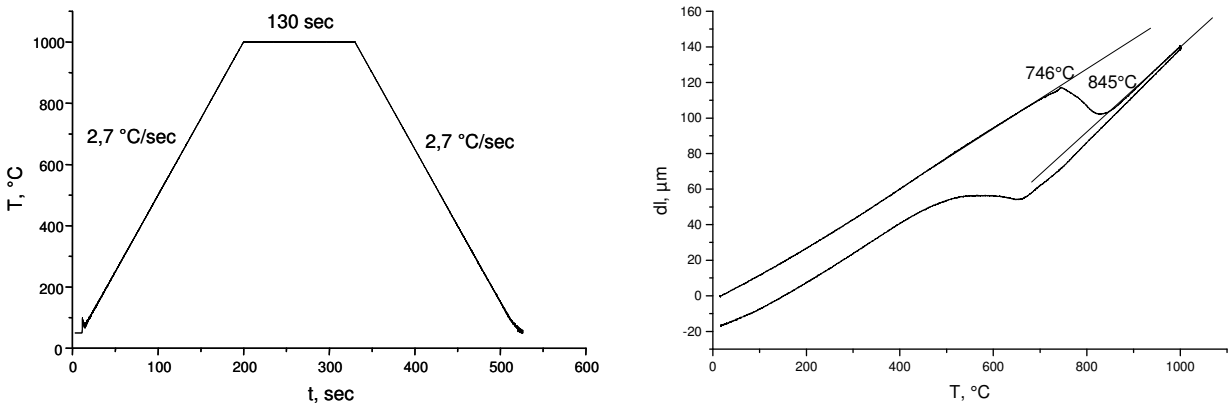

Thermal cycle Dilatometric curve

Figure II.3. Dilatometric analysis.

II.A.4 Heat treatments

Heat treatments, used to obtain Dual Phase microstructures, are presented in this section.

II.A.4.1 Thermal treatment cycles

The steel microstructure is varied through the different heat treatment parameters as described below. Two kinds of thermal cycles are used: direct quenching from isothermal annealing temperature (DQ) and rapid cooling followed by quenching (RCQ) both followed by a tempering treatment (Figure II.4.).

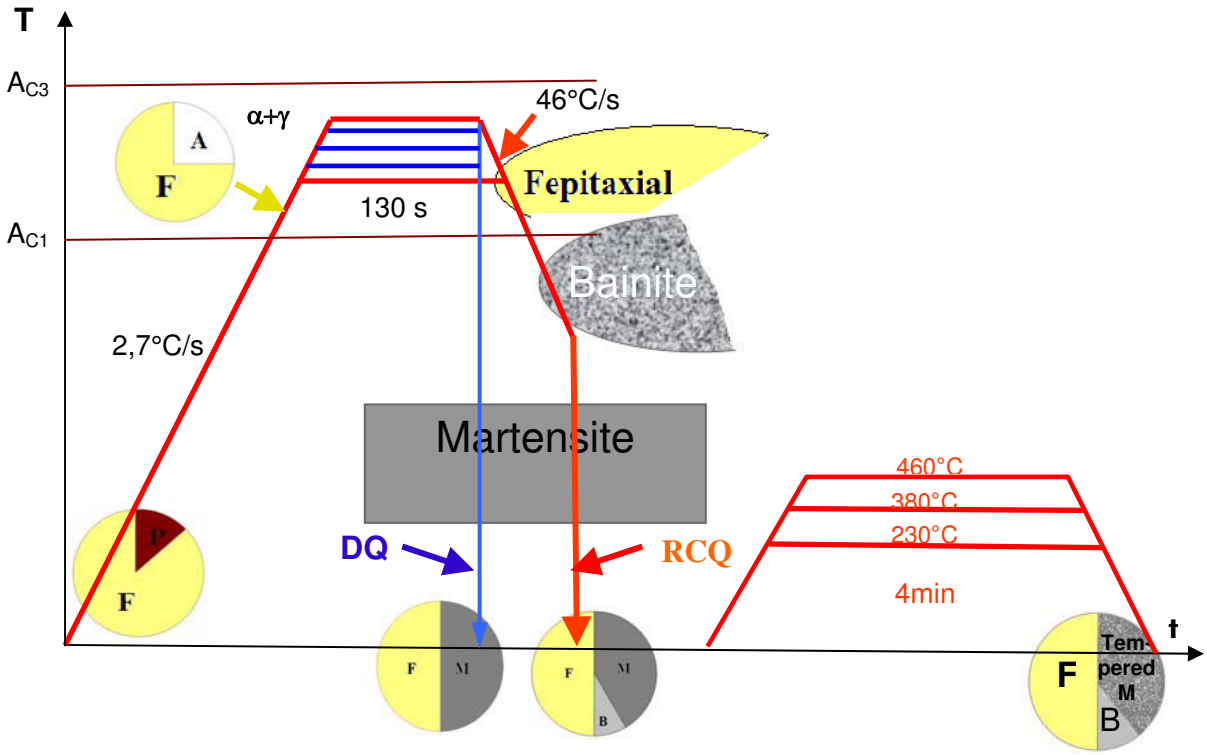

Figure II.4. Scheme of the thermal cycles used to obtain DP microstructures.

DQ and tempering: the samples are heated to different annealing temperatures (Table II.2), held for 130 sec at the given temperature and then water quenched to room temperature. For tempering studies samples are post-heated at different temperatures (230°C, 380°C and 460°C) for 4 minutes. The microstructure after the DQ cycle consists of martensite and ferrite with various ferrite and martensite contents, depending on the annealing temperature.

Tquenching, °C
755
763
785
790
810
840

Table II.2. Annealing temperatures for DQ cycle.

RCQ and tempering: the specimens are annealed at two different temperatures (810°C and 840°C) for 130 sec, rapidly cooled at 46 °C/s rate to quenching temperature and then water quenched (Table II.3). For the tempering studies samples are post-heated at different temperatures (230°C, 380°C and 460°C) for 4 minutes. Some cycles reproduce the industrial HOWAQ-TWICE heat treatments. The RCQ cycle allows the ferrite volume fraction to be controlled during the rapid cooling at 46°C/s.

All specimens are immediately transferred after quenching to a freezer chamber and stored there at -20°C until needed to prevent carbon redistribution before further characterization.

T holding, °C	*T quenching, °C*
810	480
	600
	700
	790
840	520
	600
	700
	820

Table II.3. Parameters of RCQ thermal cycles.

II.A.4.2 Direct quenching

The samples directly quenched (DQ) from intercritical annealing temperatures are used as *reference* microstructures to analyze and interpret more complex RCQ microstructures. The different annealing temperatures are used to vary the phase content of the sample which then influences the mechanical and formability properties of the steel.

The microstructure is observed in the transverse direction (Figure II.5).

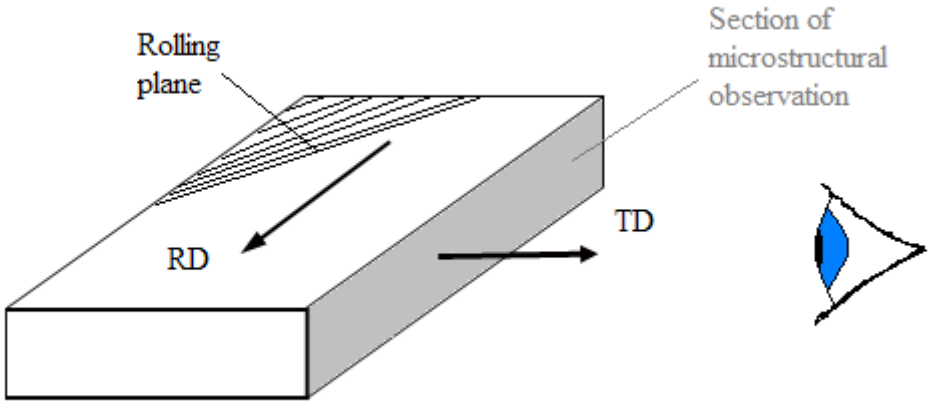

Figure II.5. Schematic sample showing the observation direction. RD is a rolling direction, TD is a transverse direction.

The microstructures of the steel directly quenched after intercritical annealing consist of a mixture of martensite and ferrite (Figure II.6) with different amounts of both phases. Figure II.6 shows that, as the annealing temperature increases, the volume fraction of martensite increases. The martensite phase is continuous around the ferrite phase. In the 810°C and 840°C-annealed samples the ferrite volume fraction is low and the microstructure is almost fully martensitic.

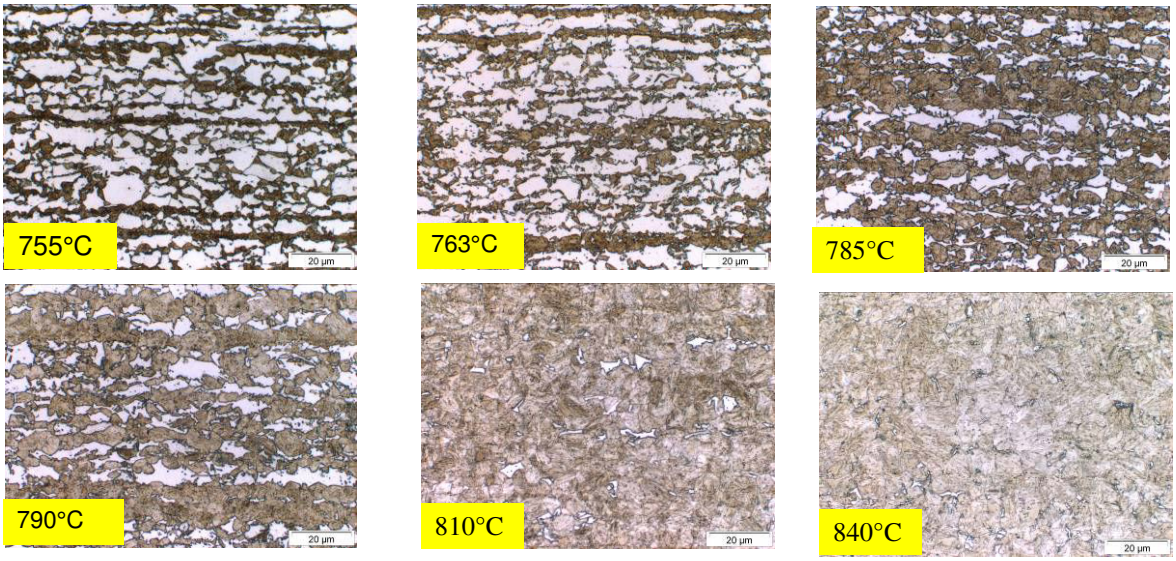

Figure II.6. Microstructures of DQ DP steel: the dark-etching phase is martensite, the white-etching phase is ferrite (light microscopy, picral and metabisulfite etching).

Figure II.7 shows the variation of the martensite volume fraction as a function of the annealing temperature. Calculated points are obtained by an equilibrium calculation using Ceqsci® model. Experimental points are obtained by an image analysis using Aphelion® analyzer. The experimental and calculated points are compared on this figure and it can be seen that there is a good agreement between these two data.

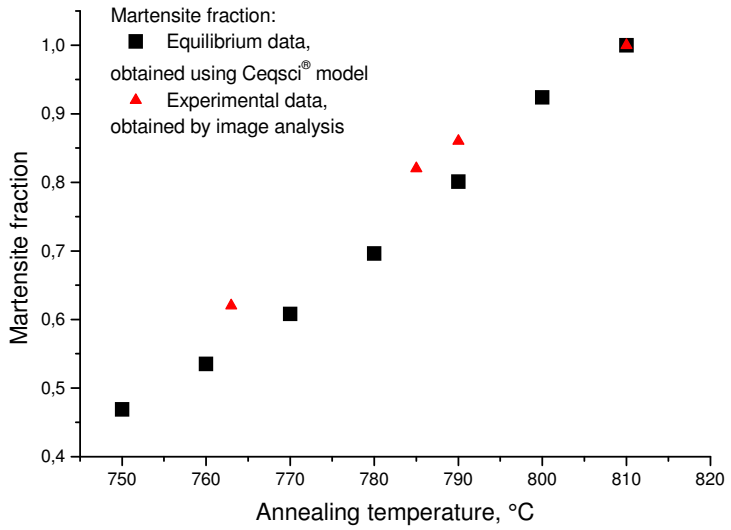

Figure II.7. Martensite volume fraction as a function of annealing temperature.

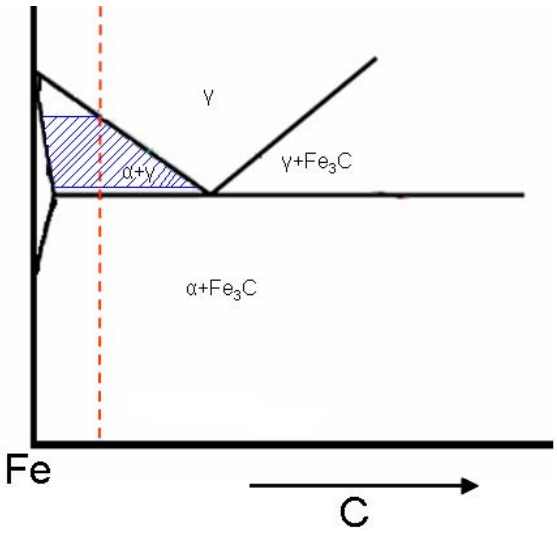

Figure II.8. Schematic Fe-C phase diagram: the annealing temperature field for a given chemical composition of the steel.

The fraction of martensite in the microstructure is varied by quenching from different intercritical annealing temperatures (Figure II.8). So the composition of martensite is varied too. After quenching, the total carbon content, C_{total} can be represented as follows:

$$C_{total} = C_m f_m + C_\alpha f_\alpha \qquad \text{II.1}$$

Where C_m, C_α are the carbon concentrations in martensite and ferrite respectively; f_m, f_α are martensite and ferrite volume fractions respectively.

The carbon content of ferrite is close to zero, so we can make the following assumption for the martensite carbon concentration:

$$C_m = C_{total} / f_m \qquad \text{II.2}$$

Experimental martensite carbon content values are obtained by Electron Energy Loss Spectroscopy (EELS) (Table II.4) and compared with the data obtained from the equilibrium calculation, using Ceqsci® model (Figure II.9). There is a good agreement between these two data.

Tannealing, °C	Ferrite fraction,%	C_m, wt. %
760	378	0.28±0.04
790	14	0.17±0.01
810	~1	0.15±0.01

Table II.4. Variation in martensite carbon content, C_M with annealing temperature. EELS measurements in the TEM.

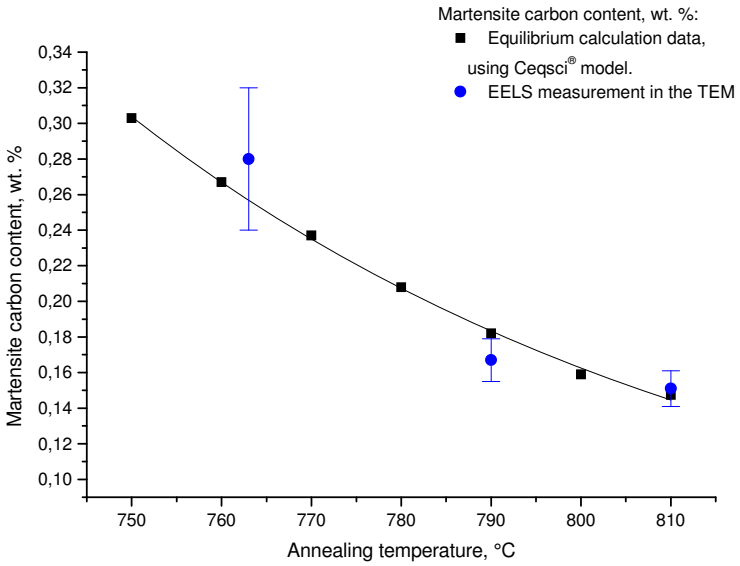

Figure II.9. Comparison of experimental and calculated martensite carbon contents.

II.A.4.3 Rapid cooling and quenching heat treatment

During the rapid cooling (at 46°C/s) in RCQ heat treatment, epitaxial ferrite [KORZ82] can be formed. After that, at lower temperatures, the bainite transformation is likely to occur. Then during the water quenching any residual austenite is transformed to martensite. The rapid cooling allows some control of the ferrite content: the required ferrite fraction is obtained (Figure II.10).

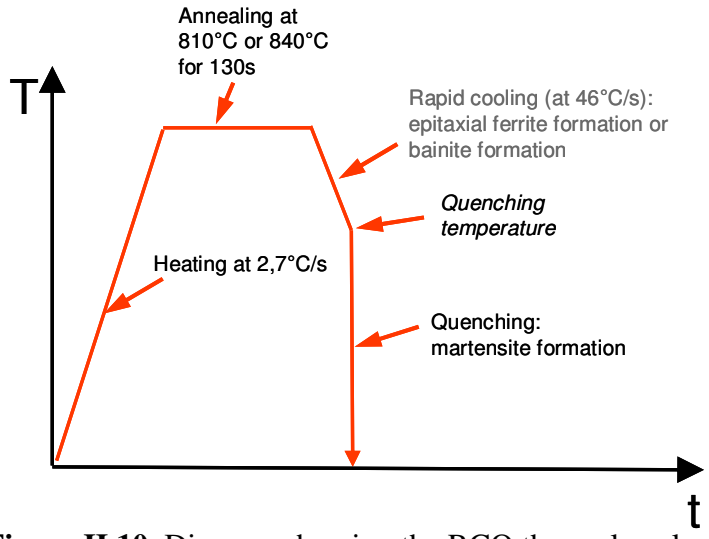

Figure II.10. Diagram showing the RCQ thermal cycle.

Figure II.11 shows the microstructures obtained after RCQ heat treatment. The total amount of martensite increases with increasing annealing and quenching temperatures. For the constant annealing temperature (810°C or 840°C) the amount of ferrite decreases with increasing quenching temperature. For the constant quenching temperature more ferrite is formed after annealing at 810°C than after annealing at 840°C. For the lowest quenching temperatures (480°C and 500°C) the martensite islands are surrounded by the ferrite. For higher quenching temperatures (more than 600°C) the martensite phase becomes connected. The original banded structure remains evident after annealing at 810°C. At 840°C annealing temperature, the structure becomes more uniform as the volume of martensite increases. For the highest quenching temperature (820°C) microstructure is almost fully martensitic.

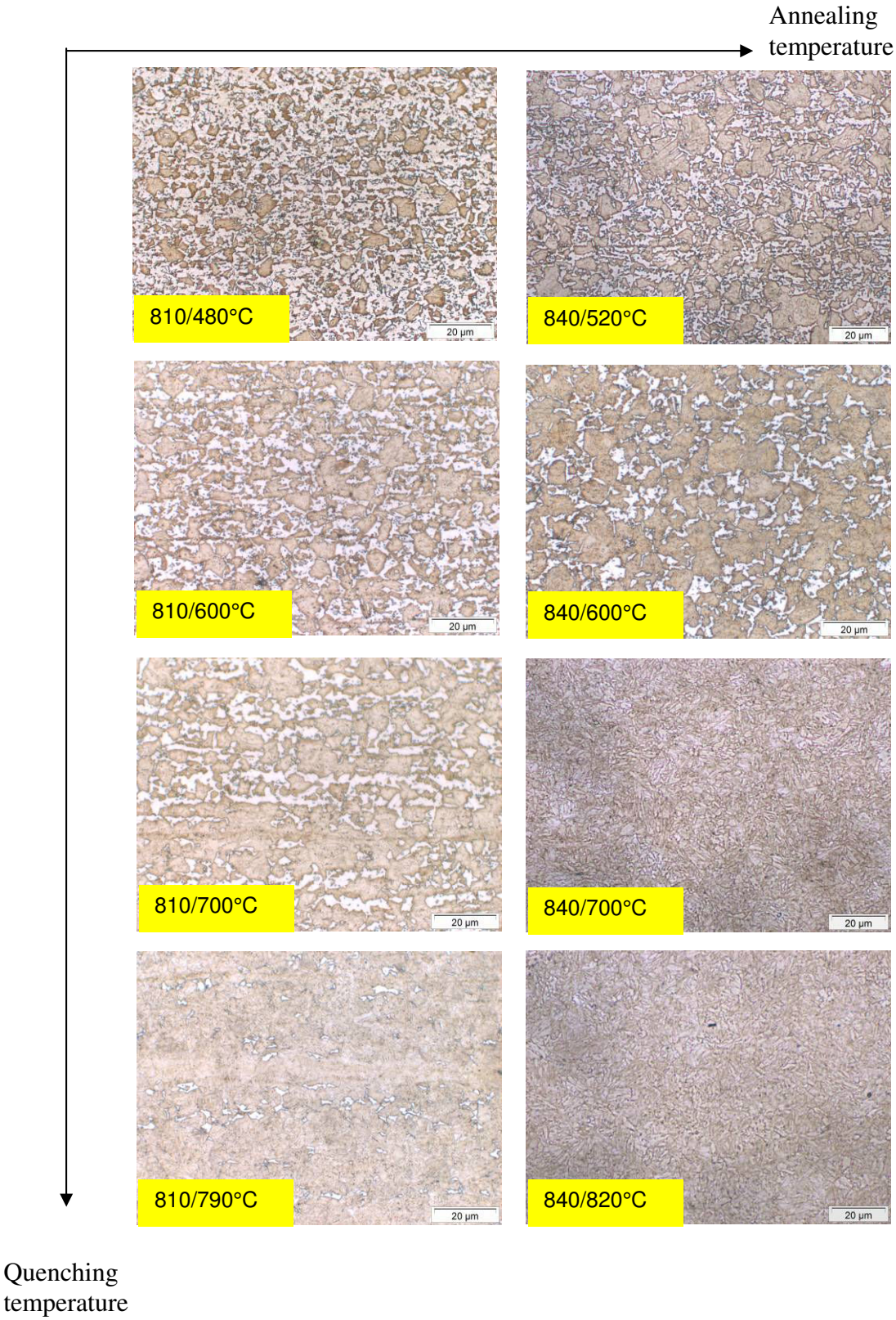

Figure II.11. Microstructure evolution with annealing/quenching temperature. Picral and metabisulfite etching. White-etching phase is ferrite, dark-etching phase is martensite.

Rapid cooling at 46°C/s just intersects the ferrite and bainite noses of the CCT diagram [DELB03]. Then the water-quenching transforms the remaining austenite into martensite. The lower the quenching temperature, the greater amount of ferrite/bainite will be formed in the structure before quenching.

Figure II.12 shows the variation in ferrite content with quenching temperature, measured by image analysis. Ferrite fraction decreases with increasing quenching temperature.

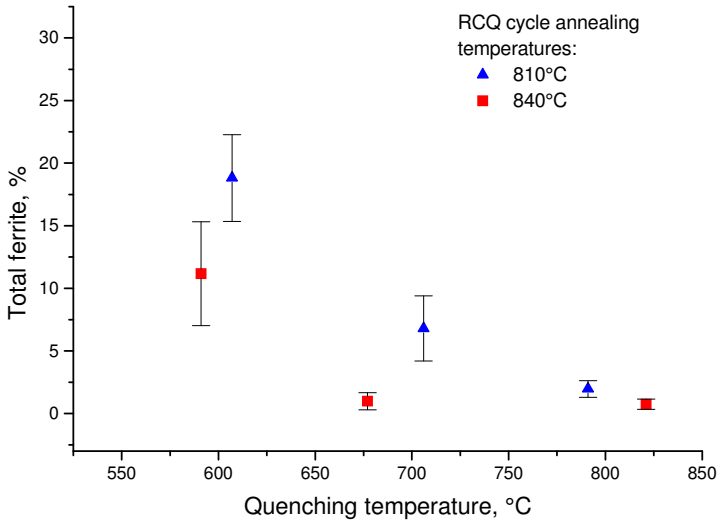

Figure II.12. Ferrite percent as a function of quenching temperature.

It is important to note that almost all ferrite present in the RCQ microstructure is ferrite, formed during the rapid cooling at 46°C/s from the annealing temperature. The amount of intercritical ferrite for the selected annealing temperatures (810°C and 840°C) is very low, about 1% and it acts mainly as already existing nucleation sites for subsequent ferrite growth upon rapid cooling [SPEI81A].

II.A.5 Summary

The DP steel microstructures are obtained from initial ferrite and pearlite microstructure using two annealing cycles: the direct quenching (DQ) from the annealing temperature and the rapid cooling and quenching (RCQ). The martensite volume fraction changes with annealing temperature for the DQ cycle and with annealing and quenching temperatures for the RCQ cycle. As a consequence, the martensite carbon content varies with annealing (DQ cycle) or annealing and quenching (RCQ) temperatures. In order to understand the martensite phase substructure evolution with the different heat treatment parameters, the detailed microstructure analysis using the FEG-SEM, will be carried out in the chapter III. The influence of the heat treatment on the carbon distribution in the martensite phase will be studied using the powerful NanoSIMS technique in the chapter IV.

The phases content in the microstructure, their carbon content will affect the mechanical behaviour of the steel. The mechanical properties of the different obtained microstructures will be measured in the next section. This chapter is a framework for investigation and comprehension of the DP steel mechanical and damage behaviour.

II.B Mechanical properties

A knowledge of the mechanical properties is essential for a practical application of any steel. The aim of this section is to study the relationship between the heat treatment parameters, the microstructure and the subsequent mechanical behaviour of the reference DP steel.

II.B.1 As-quenched material

Mechanical properties of the as-quenched Dual Phase steel are presented in this section.

II.B.1.1 Stress-strain curves

The stress strain curve is a graphical representation of the relationship between stress and strain during loading at a constant strain rate.

Samples of as-quenched DP steel exhibit continuous stress-strain behaviour with no yield point elongation (Figure II.13). Continuous yielding is typical of DP steels. The heterogeneous dislocation distribution is supposed to be the main reason for the specific mechanical properties of DP steels. The as-quenched material does not show a defined yield point because the combination of high residual stresses and a high mobile dislocation density causes plastic flow to occur easily at low plastic strains: the austenite which transformed to martensite produces heavily dislocated ferrite regions which lie in close proximity to the martensite particles [MAND85]. Plastic flow begins simultaneously at many sites throughout the specimen and discontinuous yielding is suppressed. A DP steel changes its specific mechanical behaviour if this heterogeneity is removed (for instance, after a tempering treatment) [SPEI81A].

Figure II.13 shows, that for high quenching temperatures (i.e. high martensite fraction) the high strength levels are obtained. Higher ductility can be obtained using lower quenching temperatures (i.e. decreasing martensite fraction).

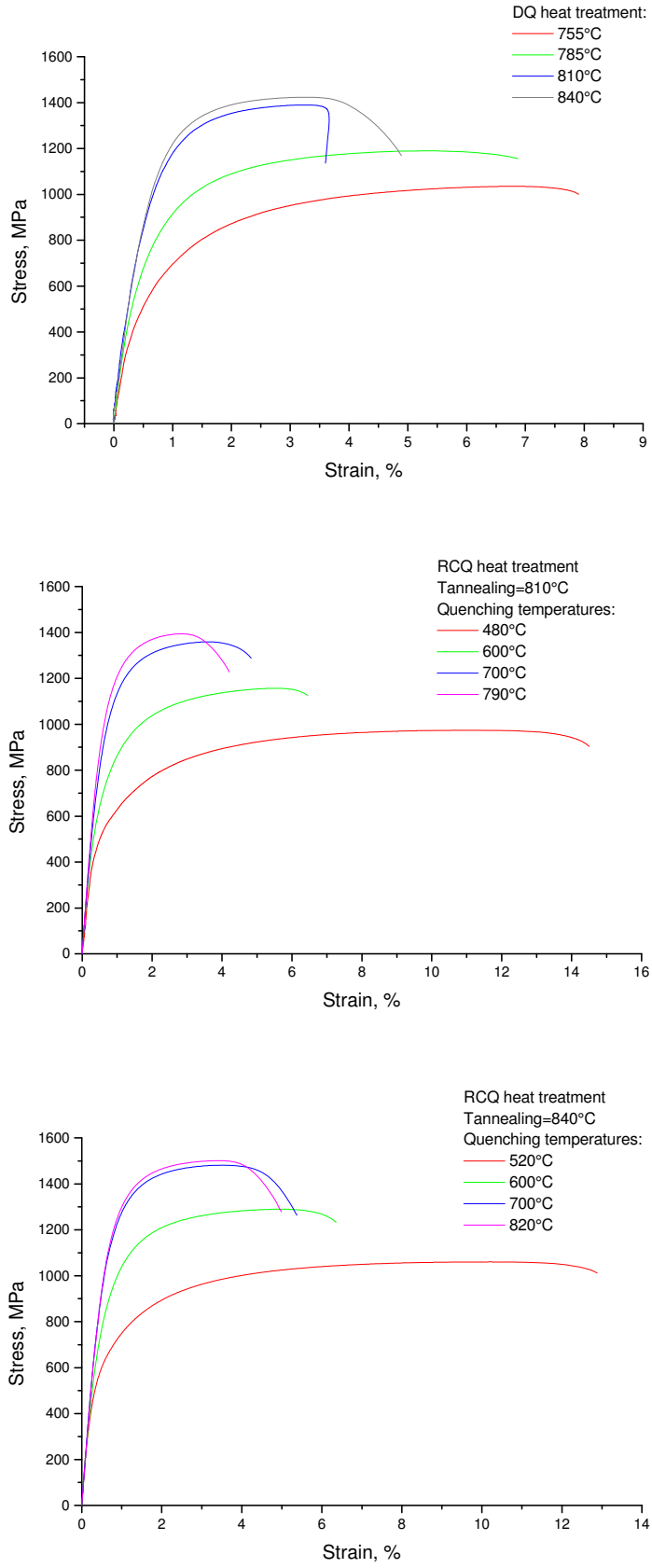

Figure II.13. Stress-strain curves for as-quenched material: DQ and RCQ quenching cycles.

II.B.1.2 Mechanical properties evolution

Yield strength

The yield strength (YS) is the stress at which the material begins to deform plastically. Knowledge of the yield strength is necessary for the control of many steel production techniques such as rolling and forging for instance. The plastic strain of 0.2% is used to define the offset yield strength.

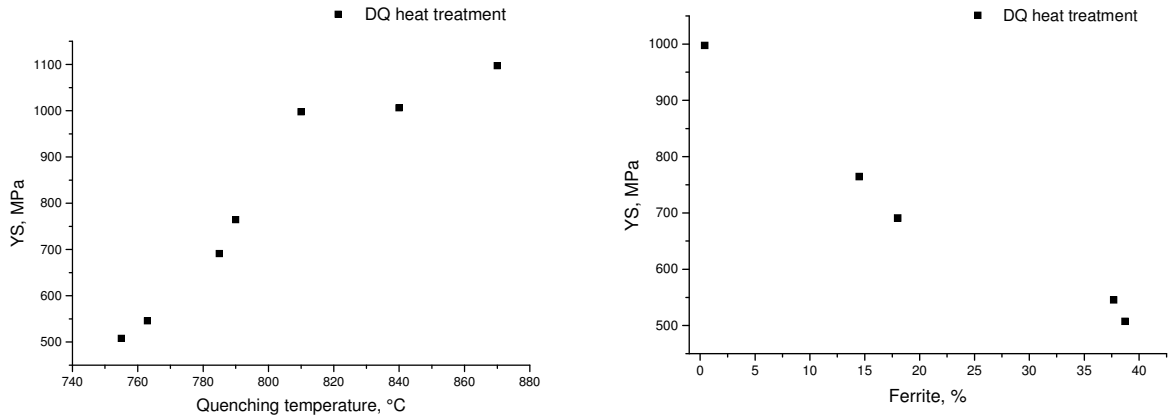

a b

Figure II.14. *YS* evolution with quenching temperature (a) and with ferrite fraction (b) for the DQ heat treatment.

Figure II.14a shows the *YS* evolution with quenching temperature for DQ steel. The *YS* increases with increasing quenching temperature. It increases with increasing content of martensite in the steel or decreases with increasing ferrite content in steel (Figure II.14b).

The dislocations generated at the ferrite-martensite interface during the martensite formation are believed to be very mobile and account for the continuous-yielding behaviour of DP steels. The presence of the residual stresses probably contributes to the lowering of the yield strength and the rapid work-hardening rate of martensite-containing steels [SPEI81A].

Tensile strength

Tensile strength is a key mechanical property for steels used for automotive applications. Ultimate tensile strength (*UTS*) corresponds to a maximum load per unit area.

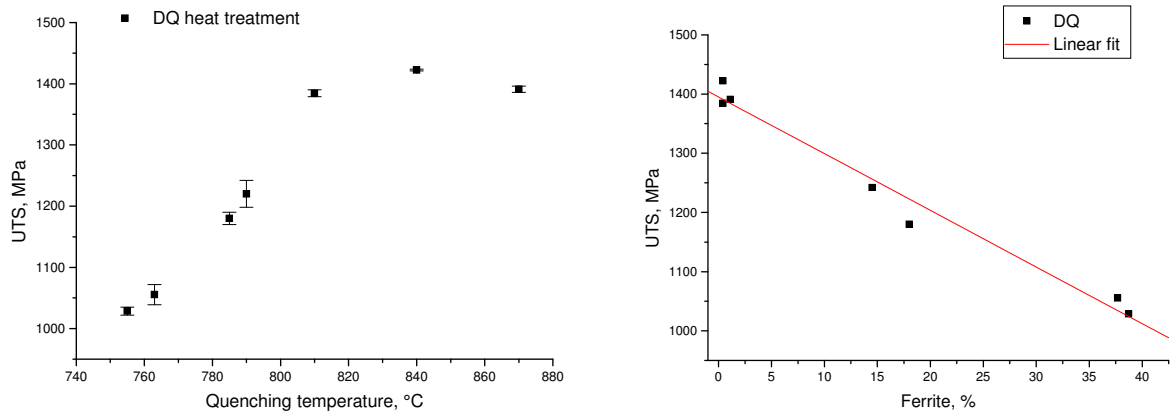

a b

Figure II.15. *UTS* versus quenching temperature (a) and ferrite fraction (b) for the DQ heat treatment.

Figure II.15 shows the variation of *UTS* with quenching temperature and ferrite content in the steel. *UTS* increases with increasing quenching temperature and with decreasing ferrite fraction. It can be seen that *UTS is almost a linear function of the ferrite volume fraction.*

Ductility

The uniform elongation (UE) value gives an extent to which the steel can be deformed plastically without fracture.

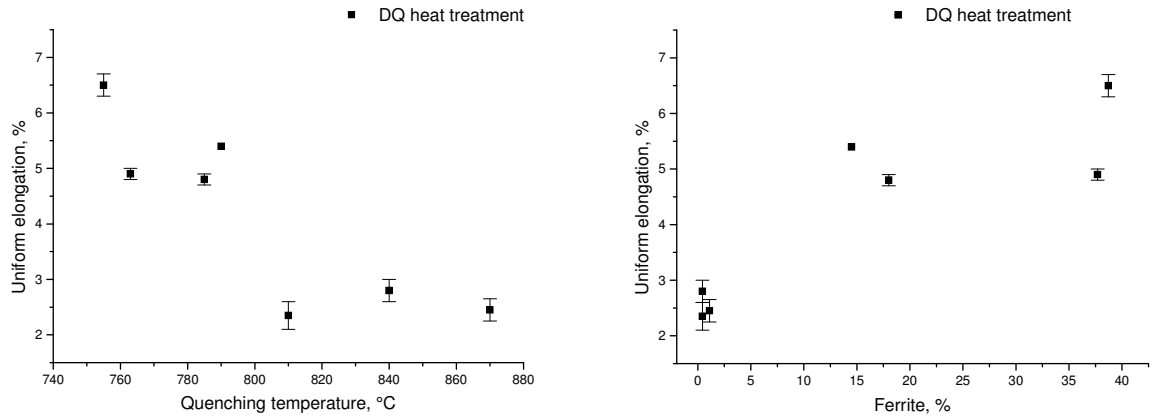

a b

Figure II.16. *UE* versus quenching temperature (a) and ferrite fraction (b) for the DQ heat treatment.

The effects of the quenching temperature and ferrite fraction on *UE* are illustrated in Figure II.16. The *UE* tends to decrease with increasing quenching temperature (Figure II.16a). The *UE* value increases with increasing ferrite volume fraction or decreases with increasing martensite volume fraction (Figure II.16b). Thus, the ductility is controlled by the ferrite fraction.

II.B.2 Tempered material

Mechanical properties of the tempered Dual Phase steel are presented in this section.

II.B.2.1 Stress-strain curves

The mechanical properties of DP steels can be altered by tempering. Different microstructural changes in the steel are observed during tempering which strongly impact the mechanical behaviour of the steel.

The tempering behavior can be influenced by the particular dislocations and residual stresses distribution, and by martensite tempering phenomena [WATE03].

For this reference DP steel, a yield point is observed after the tempering treatment (Figure II.17). The appearance of a well defined yield point is the clearest external evidence of dislocation pinning by interstitial carbon atoms. If carbon segregates to dislocations and pinning occurs then a higher stress is needed to initiate dislocation movement and initiate plastic flow [WATE03].

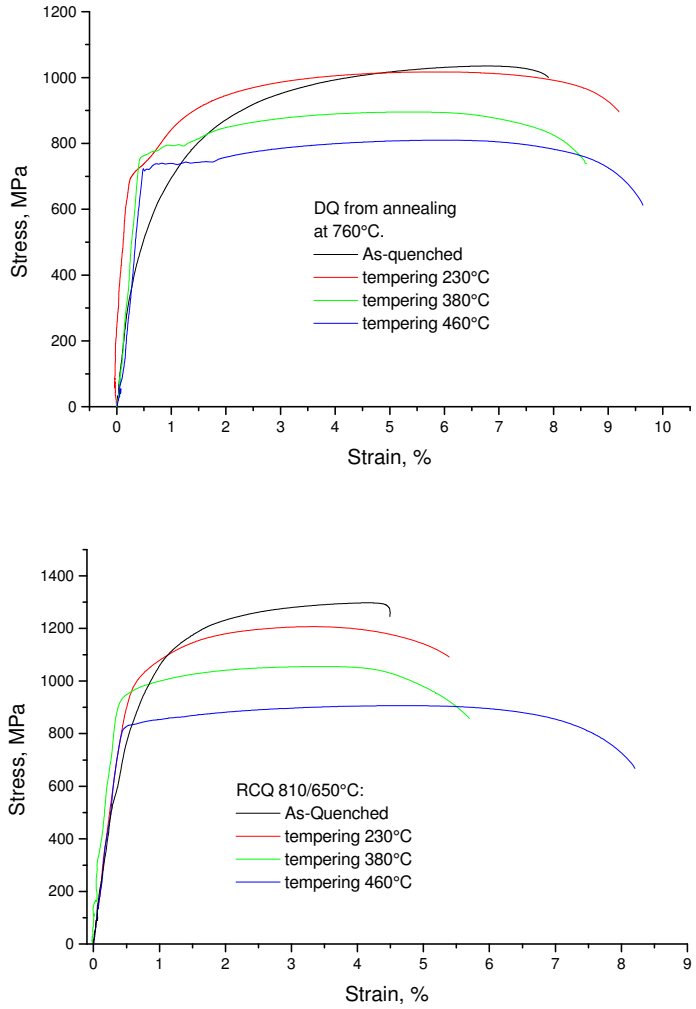

Figure II.17. Stress-strain curves for tempered material. DQ and RCQ cycles and tempering.

I.B.2.2 Mechanical properties evolution with tempering

Yield strength

Figure II.18 shows the evolution of yield strength (*YS*) with tempering temperature. The *YS* reaches first a maximum and then begins to decrease. The initial increase in *YS* with increasing tempering temperature can be due to two reasons:

- First, the pinning of dislocations by carbon atoms: carbon atoms diffuse to dislocations to anchor them. Therefore a higher stress is needed to initiate dislocation movement. The increase in the *YS* of DP steel is associated with a reduction of number of mobile dislocations, due to the formation of Cottrell atmospheres around the dislocations.

- Second, it is well-known that the austenite-martensite transformation results in a 3.6-3.8% increase of the martensite volume after transformation, dependent on its carbon content. The volume change causes large numbers of dislocations and residual stresses in the ferrite phase immediately surrounding the martensite, from which the DP steel obtains its low *YS*. This martensite tempering reactions cause an important volume contraction in the martensite of about 0.5 vol. %. The martensite volume decrease can significantly reduce the internal stresses in the ferrite phase. It is strongly believed that these reduced internal stresses in ferrite in combination with dislocations already pinned by interstitial carbon atoms and small precipitates result in the increase of the *YS* [WATE03].

Further reduction in *YS* is associated with the tempering effect that starts in the martensite phase. The following decrease of *YS* is a result of softening of the steel during tempering: the decrease of the martensite strength with increase in the tempering temperature.

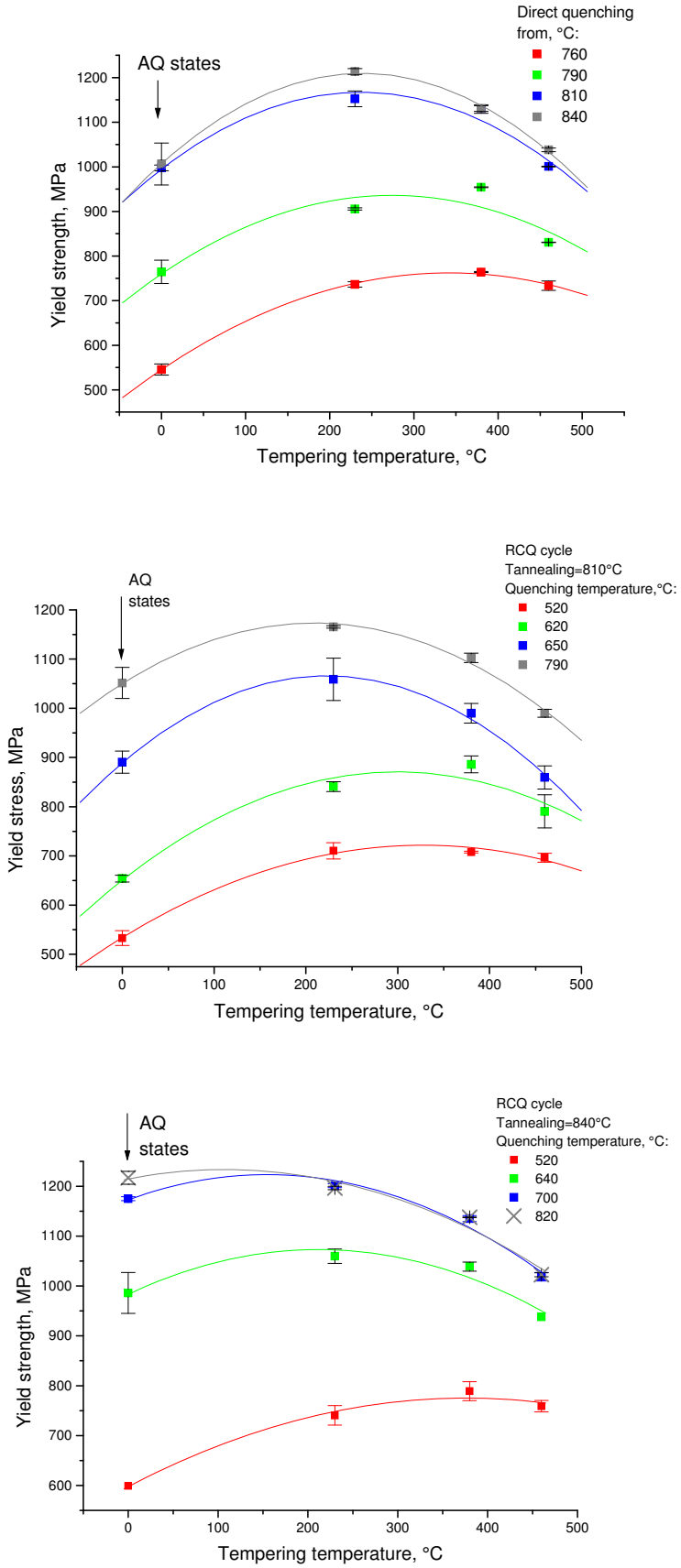

Figure II.18. Yield strength evolution with tempering temperature. DQ and RCQ cycles and tempering.

Tensile strength

The effect of the tempering temperature on the ultimate tensile strength (*UTS*) of DP steel is illustrated in Figure II.19. The strength level of this steel decreases as the tempering temperature increases.

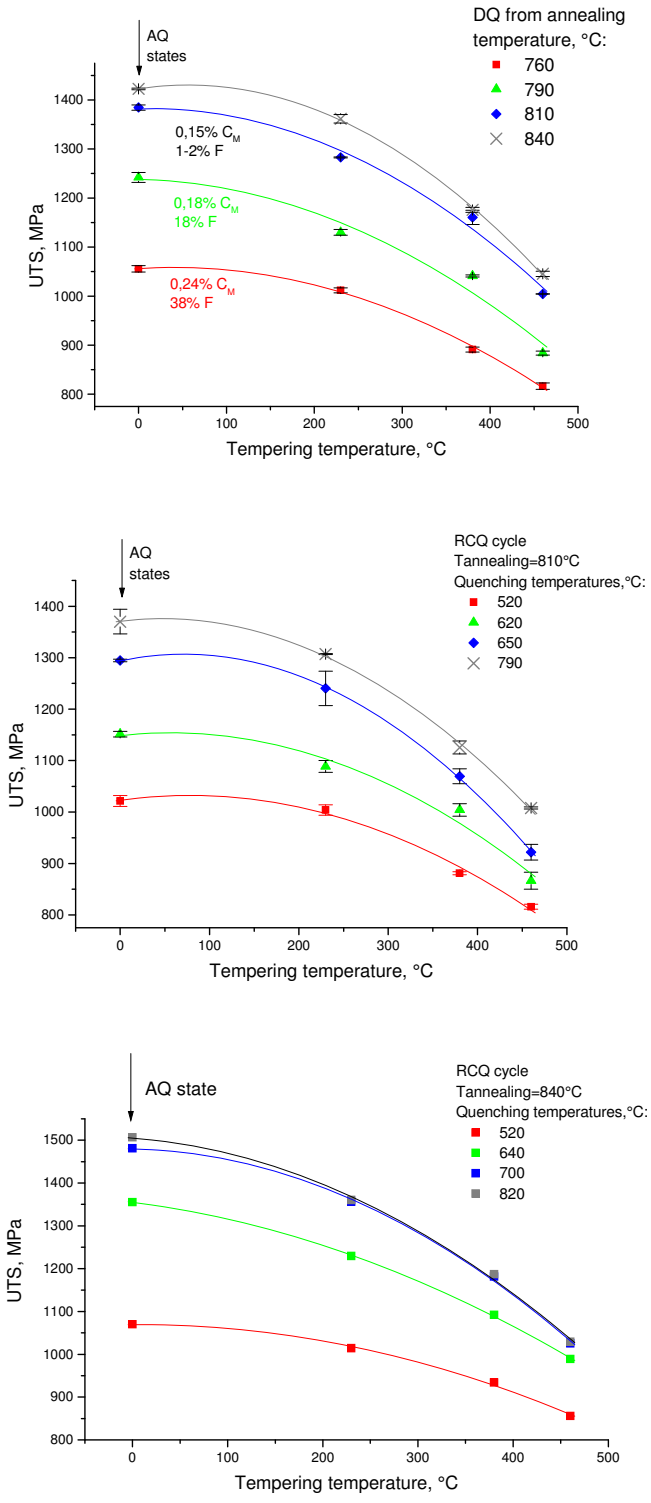

Figure II.19. Ultimate tensile strength evolution with tempering. DQ and RCQ cycles and tempering.

It is interesting to compare these results with those of Speich on the hardness of low temperature tempered fully martensitic structures [SPEI92]. The evolution of hardness with tempering temperature is presented in Figure II.20.

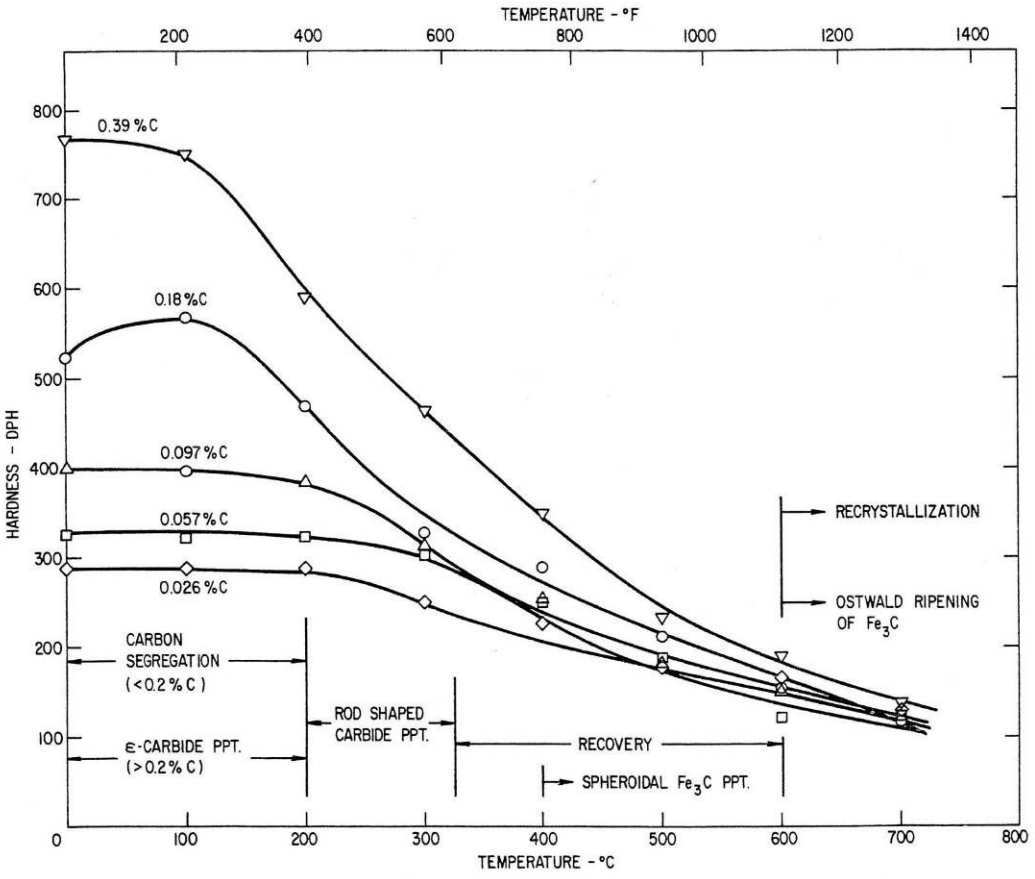

Figure II.20. Hardness evolution with tempering [SPEI92]. Fe-C alloys.

The hardness of the martensite reflects the strengthening effects of the substructure and of carbon. It is found that the hardness evolution with tempering depends on the martensite carbon content. In martensite with less than 0.2%C little change in hardness occurs at tempering temperatures below 200°C, since almost complete segregation of carbon has taken place on quenching. Also, no carbide precipitation or recovery occurs at this temperature. Tempering of martensite with carbon contents above 0.2% at temperatures below 200°C results in little hardness change, even though fine precipitate of ε-carbide are now formed. It is stated that the loss of solid solution hardening is nearly balanced by the hardening effects of the carbide precipitation [SPEI92].

In the reference DP steel the rate of softening is higher for the microstructures with high martensite content than for the microstructures with lower martensite content (the loss of the martensite strength is more intensive for the low carbon martensite). This effect is most likely due to the specific DP steel behaviour: the presence of the ferrite phase changes the driving force for the tempering reactions, which results in a different tempering behaviour.

Ductility

The effect of temperature on uniform elongation *(UE)* is less conclusive. However, for higher quenching temperatures the *UE* is less sensitive to tempering: the reduction of UE is weaker with an increase of tempering temperature (Figure II.21).

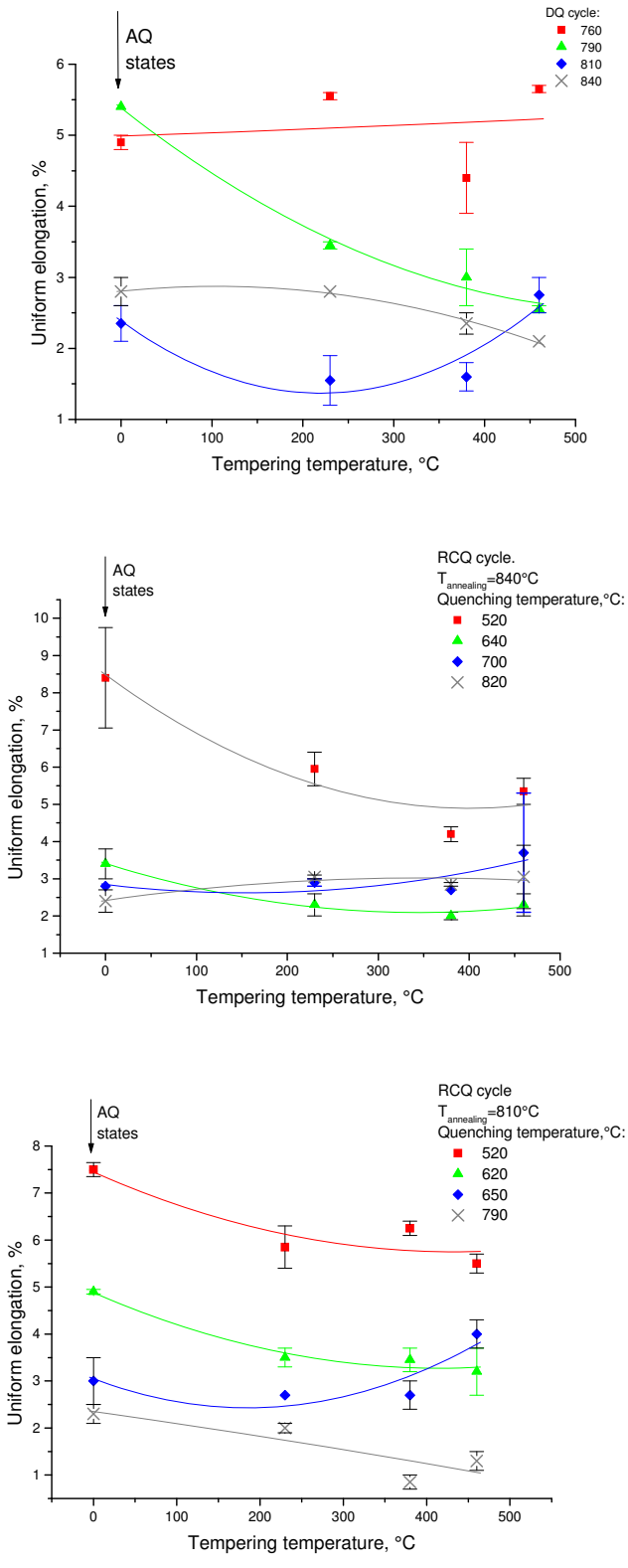

Figure II.21. *UE* evolution with tempering temperature.

II.B.3 Summary

The mechanical properties of the DP steel are described for the as-quenched state and after tempering. The evolutions of the yield strength (*YS*), ultimate tensile strength (*UTS*) and uniform elongation (*UE*) are obtained as a function of the heat treatment parameters and microstructural parameters. The as-quenched samples show a continuous stress-strain curve. An increase of the *YS* and *UTS* is observed with increase in quenching temperature for the as-quenched samples (i.e. a martensite fraction increase). After tempering at three different temperatures a yield point appears. *YS* first increases with tempering and then decreases because of the martensite softening. *UTS* decreases with tempering because of the martensite phase softening. The results of analysis of the uniform elongation values are not conclusive, probably because of poor accuracy of a measurement technique.

As shown in this chapter the mechanical properties of the DP steel are controlled by the volume fraction of the martensite phase. The martensite carbon content does not appear to influence the mechanical properties of the studied DP steel.

In order to develop an advanced understanding of the DP steel damage behaviour, the damage mechanisms will be characterized and modeled in the following chapters.

Chapter III

Fine characterisation of the microstructure

The microstructure characterisation at a fine scale is carried out in the present chapter. The as-quenched microstructure is studied by the SEM-FEG in order to detect auto-tempering reactions in the martensite phase. The SEM analysis is carried out for martensite phase morphology study as a function of the heat treatment parameters. The RX analysis permits to detect the percentage of the retained austenite in the as-quenched microstructure. The precipitation reactions during tempering are investigated using the SEM. The banded microstructure is studied trough the electron beam microprobe analysis (EBMA).

Scanning electron microscope permits a more detailed analysis of the DP steel microstructure. The martensite internal microstructure in the as-quenched and tempered conditions is analyzed using SEM. This approach permits to obtain a higher resolution images.

The understanding of the microstructure evolution with heat treatment parameters is the aim of this chapter.

III.1 Autotempering study

Most of commercial DP steels have M_s temperatures that are considerably above room temperature (200-400°C). Some products manufactured from these steels have appreciable dimensions and cooling through the M_s-M_f region is sufficiently slow that extensive redistribution of carbon atoms may occur after martensite transformation. As a result the as-quenched martensite in these steels is said to be "auto-tempered". Thus, before further study of the tempering behaviour of the reference DP steel, it is indispensable to analyze the as-quenched microstructure.

It was reported by Speich [SPEI69] that, even for the rapid quenching of thin specimens, there is ample time for carbon diffusion to defects in the martensite during quenching (but the quenching rate is sufficiently high so no carbide precipitation occurred).

In low-carbon, low-alloy steels, appreciable carbon segregation to dislocation sites occurs during quenching. Also, segregation of carbon from the martensite to interlath austenite films may occur during quenching. As a result the initial carbon distribution is very complex [SPEI69].

The as-quenched samples were studied by FEG-SEM microscopy to analyze the initial state of martensite before tempering.

Figure III.1 shows FEG-SEM images of the as-quenched microstructures with different martensite contents. For the lowest annealing temperatures (755°C, 785°C and 810°C), the martensite structure did not show the presence of carbon precipitation. The martensite phase appearance is smooth. For the 810°C-annealing temperature, the structure remained precipitation-free. For the 840°C-annealing temperature, some rippling (showed by arrows in Figure III.1) was observed in the martensite substructure. This could be due to carbon precipitation during quenching. This specimen has the highest M_S temperature. Conceivably, the carbon redistribution occurred during quenching.

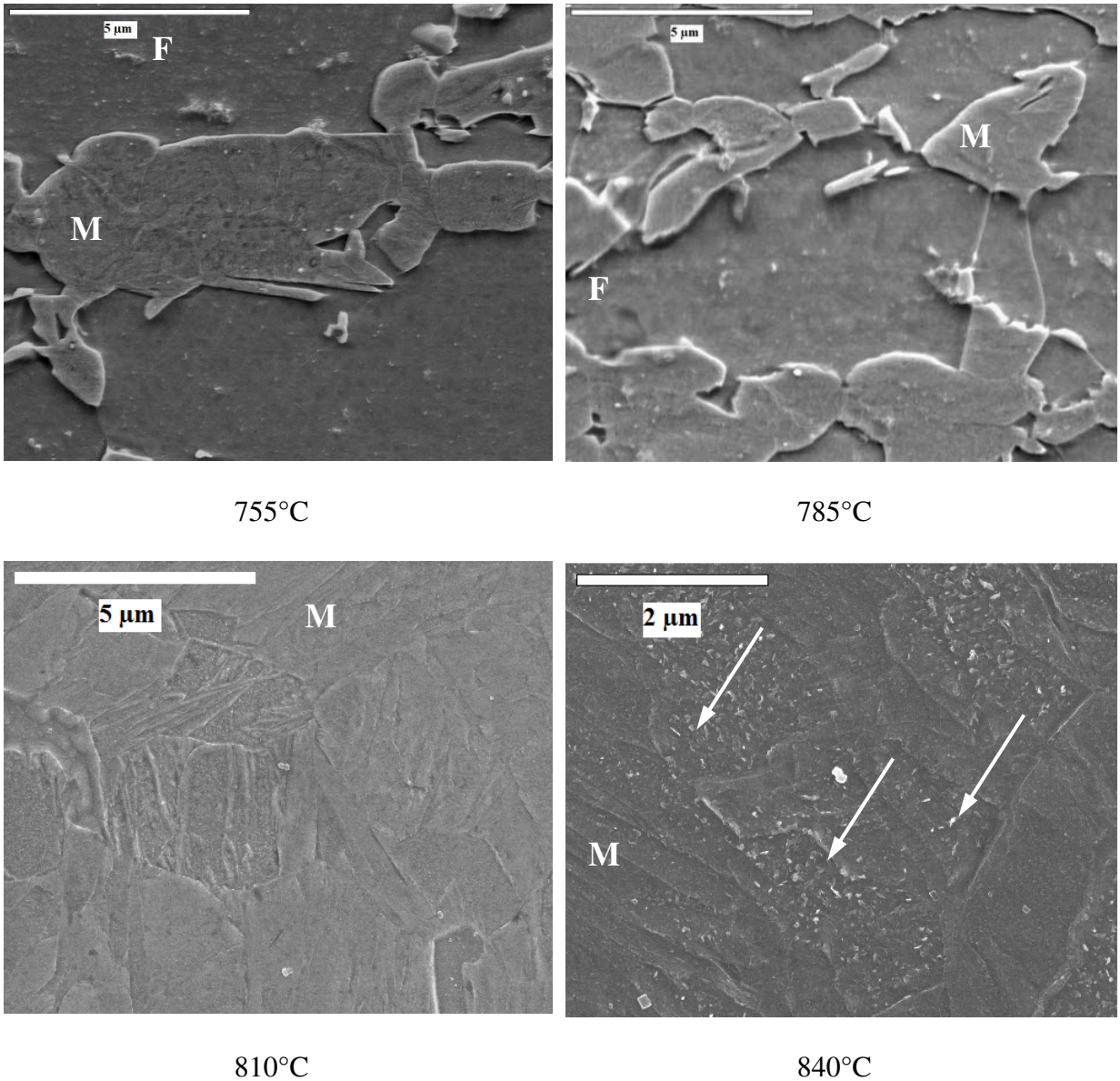

Figure III.1. Microstructures for samples directly quenched from different temperatures. Quenching temperatures are shown below each image. (SEM, picral etching).

Figure III.2 is a transmission electron micrograph for a sample after quenching from 840°C. It confirms the autotempering precipitates presence in the as-quenched martensite.

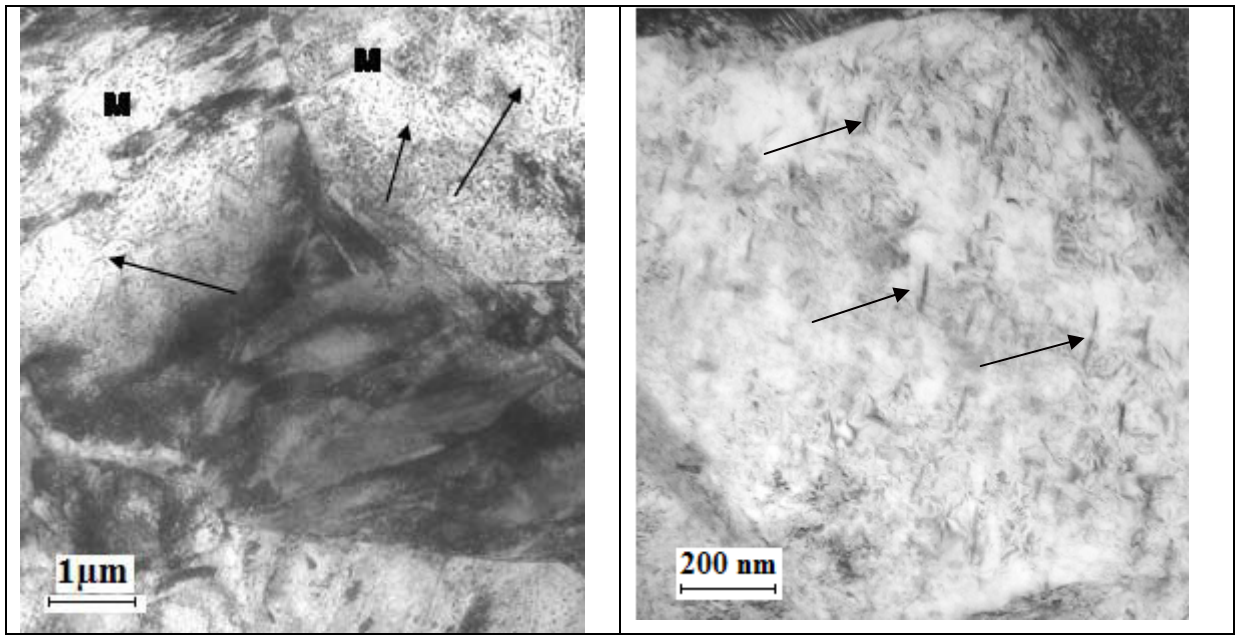

Figure III.2 Bright field TEM micrograph revealing carbides precipitation in the as-quenched specimen (precipitates are shown by arrows).

III.2 As-quenched microstructure study

Martensite substructure

The microstructure is observed in the transverse direction (Figure II.5). Figure III.3 shows FEG-SEM images of as-quenched samples. A lath-type martensite is found in all specimens: for the studied martensite carbon contents, the lath martensite morphology is predicted [KRAU01].

The martensite volume fraction increases with increasing annealing and quenching temperatures. For higher quenching temperature, martensite islands are connected. For the highest quenching temperatures (820°C and 790°C), the microstructure is almost fully martensitic.

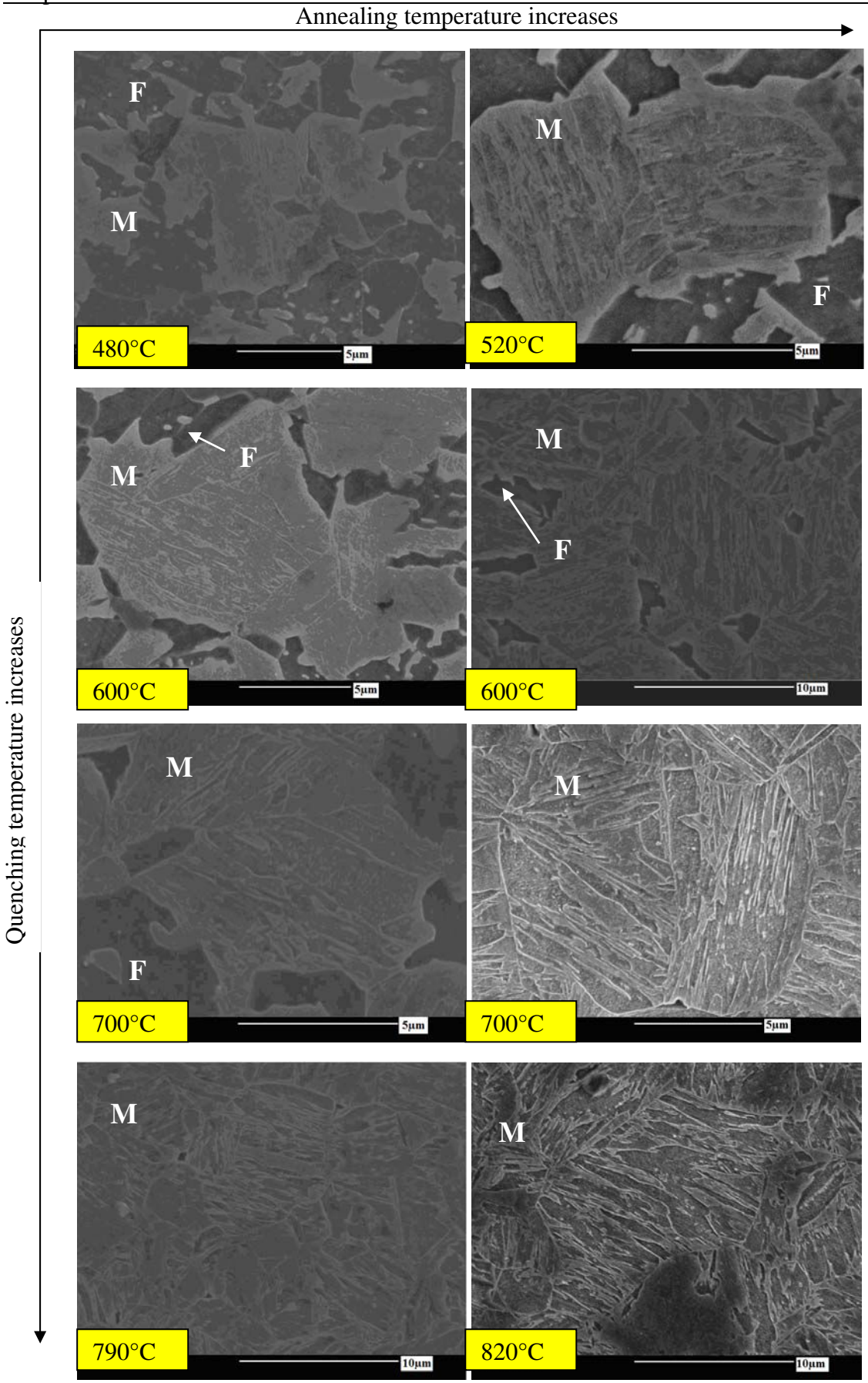

Figure III.3. Martensite substructure study, SEM images, Nital 2%. Annealing temperatures: left column - 810°C, right column - 840°C; quenching temperature is shown on each image. (F-ferrite, M-martensite).

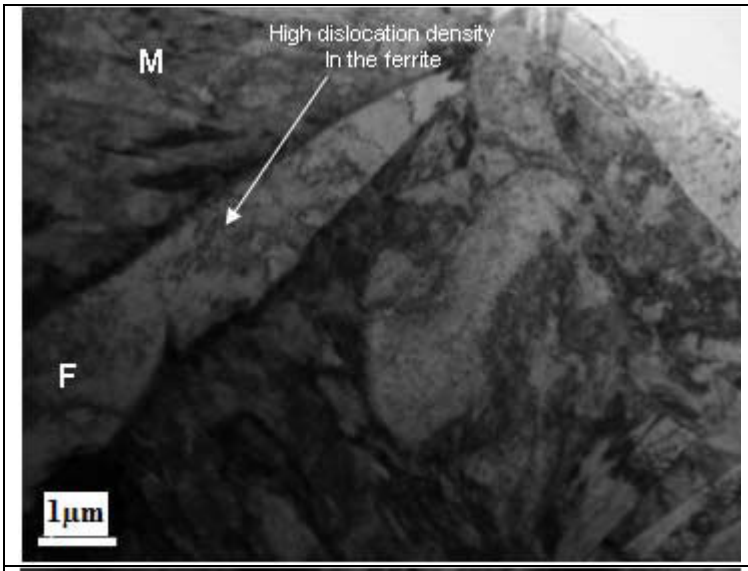	a: 810°C-annealed sample, Martensite -1% ferrite, As-quenched condition, High dislocation density in the ferrite, Lath ferrite.
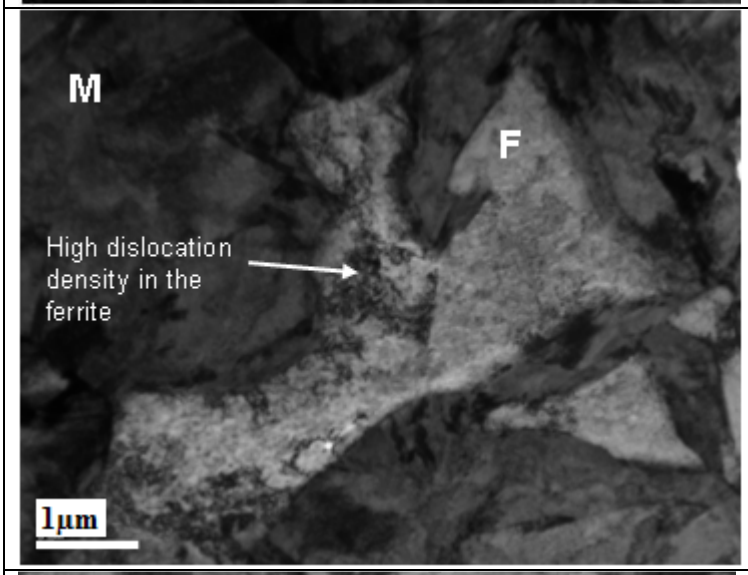	b: 790°C-annealed sample, Martensite-15% ferrite, As-quenched condition, High dislocation density in the ferrite.
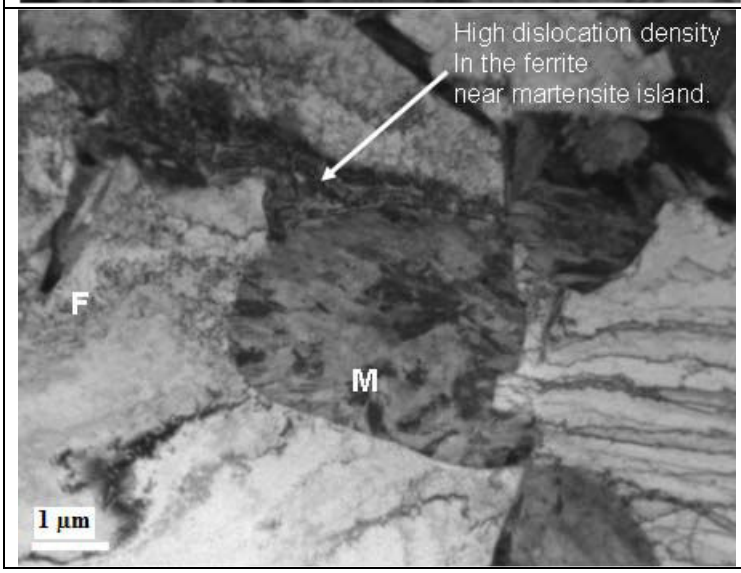	c: 760°C-annealed sample, Martensite-38% ferrite, As-quenched condition, High dislocation density in the ferrite.

Figure III.4 High dislocation density at the ferrite/martensite interface, transmission electron micrographs, bright field.

Specific Dual Phase microstructure

Austenite to martensite transformation results in volume expansion. Ferrite must plastically deform in order to accommodate this volume expansion. As a result, a high dislocation density and residual stresses are created at the ferrite/martensite interface [SPEI81A].

Transmission electron microscopy (TEM) is used to observe an area near ferrite/martensite interface. TEM images, for DQ samples after different annealing temperatures in the as-quenched condition, are shown in Figure III.4. A high dislocation density is revealed in the ferrite near martensite.

A high magnification TEM image of the ferrite/martensite interface in the 760°C annealed sample is shown on Figure III.5 (same area that Figure III.4c).

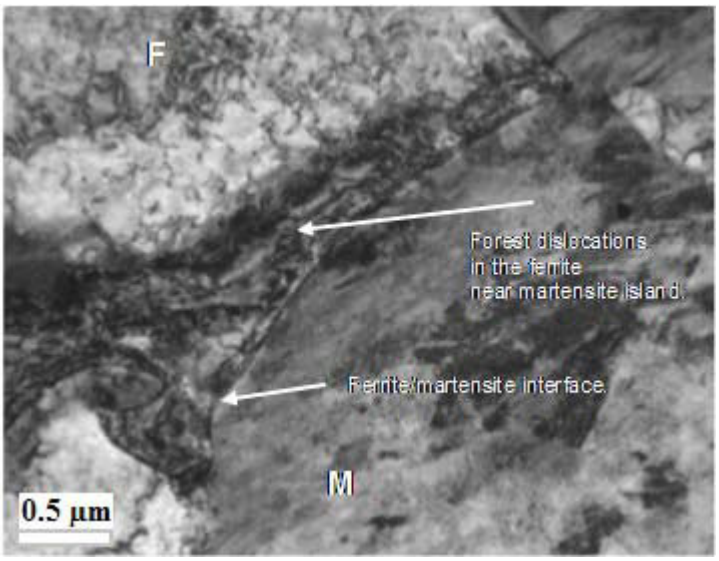

Figure III.5. High dislocation density in the ferrite near martensite island, DQ sample annealed at 760°C in the as-quenched condition, transmission electron micrograph, bright field.

This high dislocation density in the ferrite near martensite island forms a dislocation forest. It is reported that these forest dislocations are responsible for a DP steel mechanical behaviour [RIGS77].

Transmission electron micrograph shows a lath ferrite morphology in the 810°C annealed sample (Figure III.4a). Ferrite in this sample is surrounded by martensite. An increase in the ferrite fraction from 1 % to 38% leads to a ferrite morphology change. In this case, ferrite surrounds martensite (Figure III.6).

Retained austenite

Austenite can be present in final structure if sufficient local carbon concentration is reached during previous thermal treatments so that the M_S temperature is lower than room temperature.

For the studied water-quenched samples, the retained austenite is undetectable by X-ray diffraction analysis. We can conclude then that the retained austenite volume fraction is less than 3% (detection limit of the X-ray diffraction analysis). It will have a minimum influence on the mechanical behaviour of the DP steel.

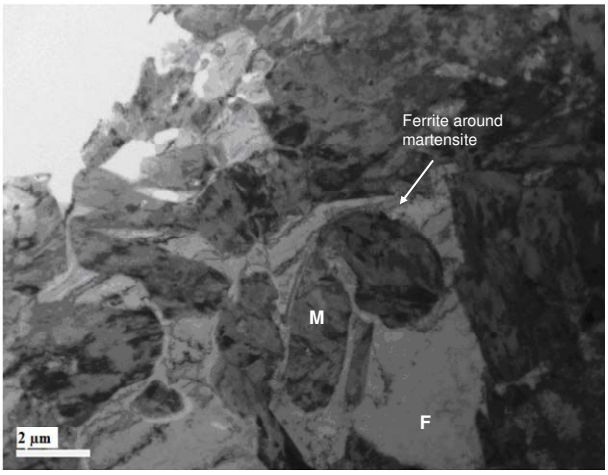

Figure III.6. Ferrite morphology in the 760°C annealed sample, TEM bright field.

III.3 Evolution of microstructure with tempering

As-quenched martensite is unstable and already starts to decompose at room temperature. During tempering the decomposition of martensite will tend to the equilibrium state, i.e. ferrite and cementite structure and thus the free energy of the steel is minimized. This decomposition proceeds in several stages [SPEI92], where transformations during tempering are usually overlapping. For relatively low tempering temperatures (100-200°C) ε carbide precipitation occurs, at higher tempering temperatures (200-500°C) the ε carbides dissolve and supply carbon atoms for the growing cementite. Alloy carbides replace cementite at tempering temperatures above 500°C [SPEI92].

The evolutions of microstructure during tempering at 230°C, 380°C and 460°C for 4 annealing temperatures in reference DP steel are presented in Figure III.7.

Tempering at 230°C.

According to the literature, the first stage of tempering occurs in the temperature range of 100°C-200°C. Tempering at low temperatures results in carbon redistribution in martensite and the formation of transition carbides.

After tempering at 230°C, some precipitates are observed in the martensite structure: the carbides precipitate inside the martensite laths.

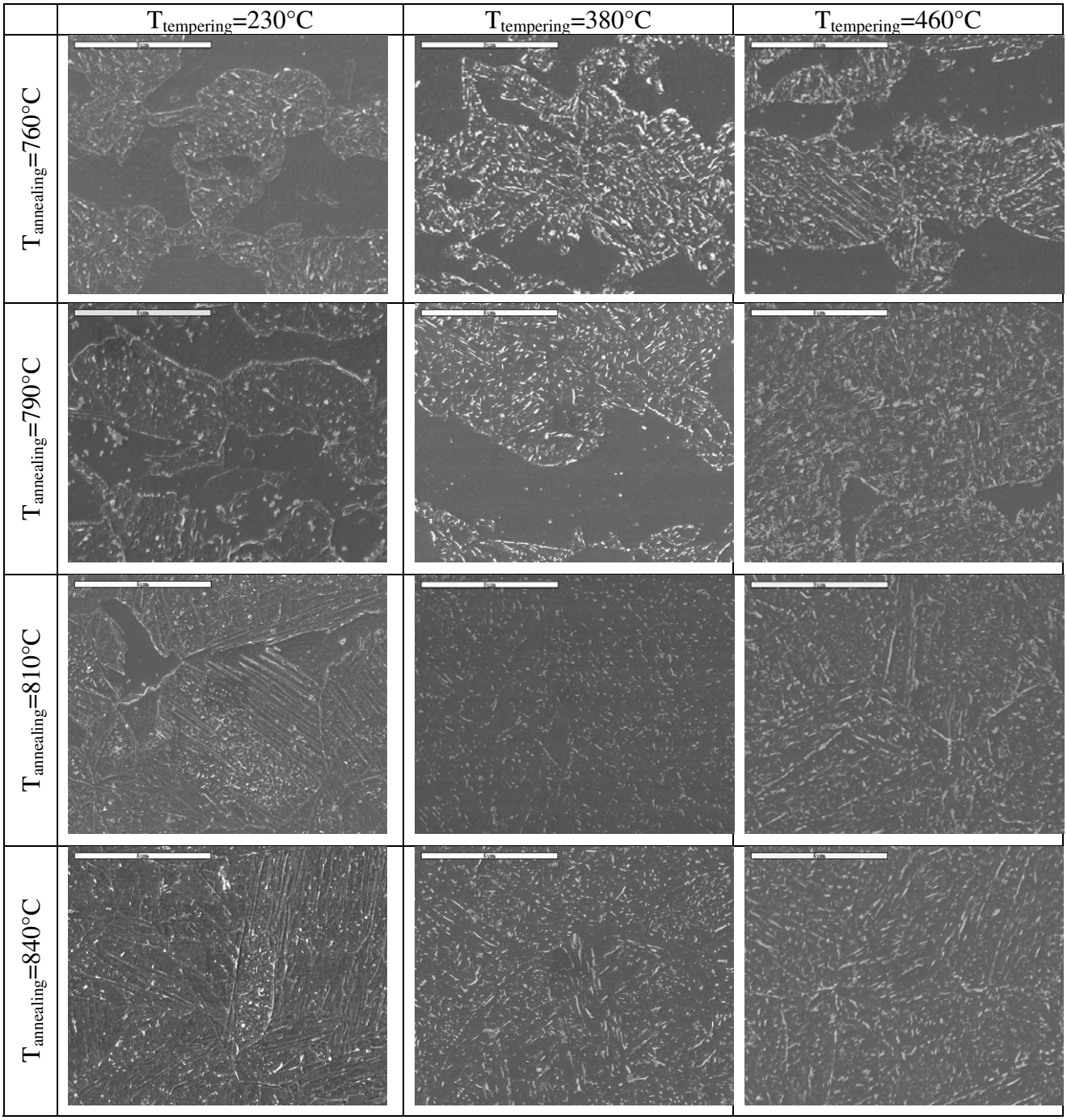

Figure III.7. The evolution of different DQ microstructures with tempering.SEM, picral etching. Scale is 5 µm.

Tempering at 380°C

The precipitation density is more pronounced at this temperature.

During tempering at 380°C, the precipitation of carbide occurs in the martensite. The carbide rods are observed in the martensite structure. At this stage, precipitates are homogeneously distributed (Figure III.8).

The carbon content of the martensite (which is controlled by the annealing temperature) begins to be more important factor for higher tempering temperature. The coarser carbides present for the 760°C-annealed microstructure, while for the higher annealing temperature the dispersion of fine carbides characterize the martensite microstructure (Figure III.8).

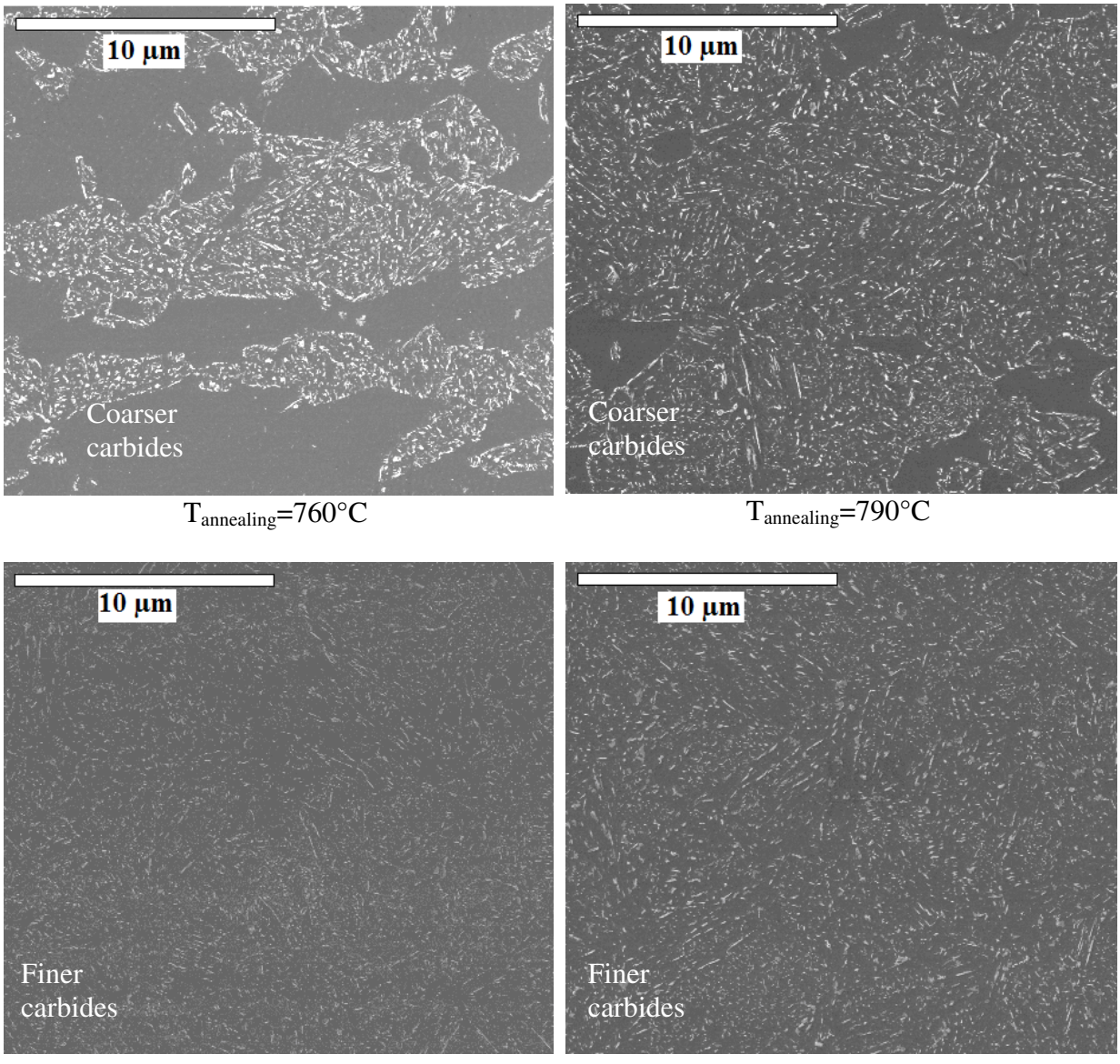

$T_{annealing}$=760°C $T_{annealing}$=790°C

$T_{annealing}$=810°C $T_{annealing}$=840°C

Figure III.8 SEM microstructures for 380°C tempering. Annealing temperatures are shown on the figure. Picral etching.

Tempering at 460°C.

The coarsening of carbide precipitates occurs at this tempering temperature. Carbide chains can be seen at martensite/ferrite boundary and at martensite/martensite (prior austenite) grain boundary in fully martensitic microstructure (Figure III.9).

Also, the carbide chains are observed inside the martensite, at the lath boundaries. This is in accordance with the literature [SPEI92], where *the larger particles lying on interlath boundaries grow at the expense of the intralath particles, resulting in a final dispersion of cementite particles only on interlath boundaries.*

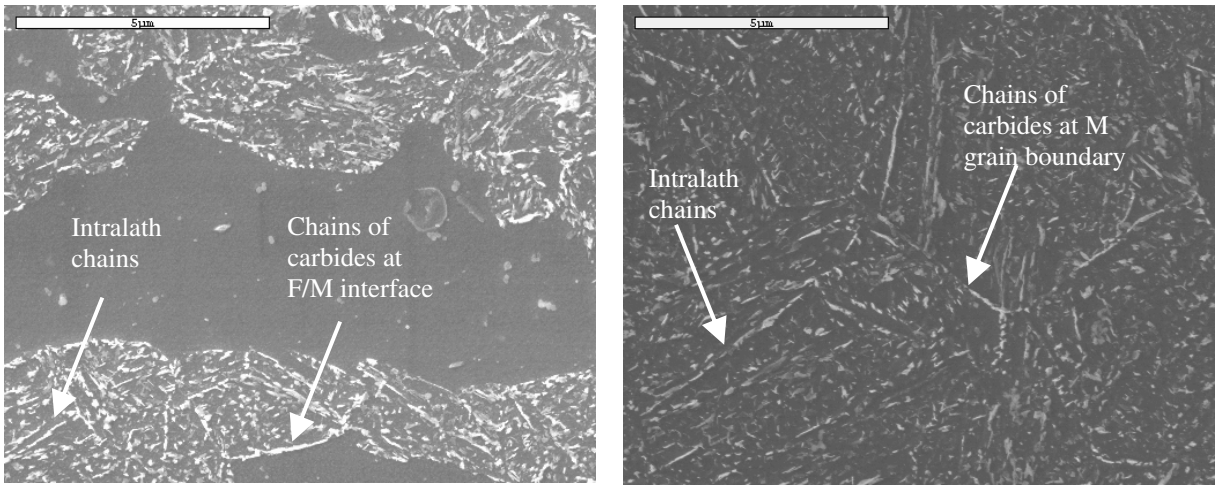

$T_{annealing}$=760°C $T_{annealing}$=810°C

Figure III.9. SEM microstructures after tempering at 460°C. Annealing temperatures are shown on the images. Picral etching.

III.4 Macrosegregation analysis

In general, macro- and micro-segregation are undesirable as they have marked deleterious effects on mechanical properties. A study is carried out to reveal and measure the intensity of the macro-segregation in DP steel. This data is necessary in assessing the possible change in the mechanical behaviour due to the segregation.

For the segregation study in the reference DP steel, a sample directly quenched after intercritical annealing at 760°C is investigated using the Electron beam microprobe analysis (*EBMA*).

The results of electron beam microprobe microanalysis are shown in Figure III.10. The images are the Mn-distribution maps at the ½ thickness of the specimen.

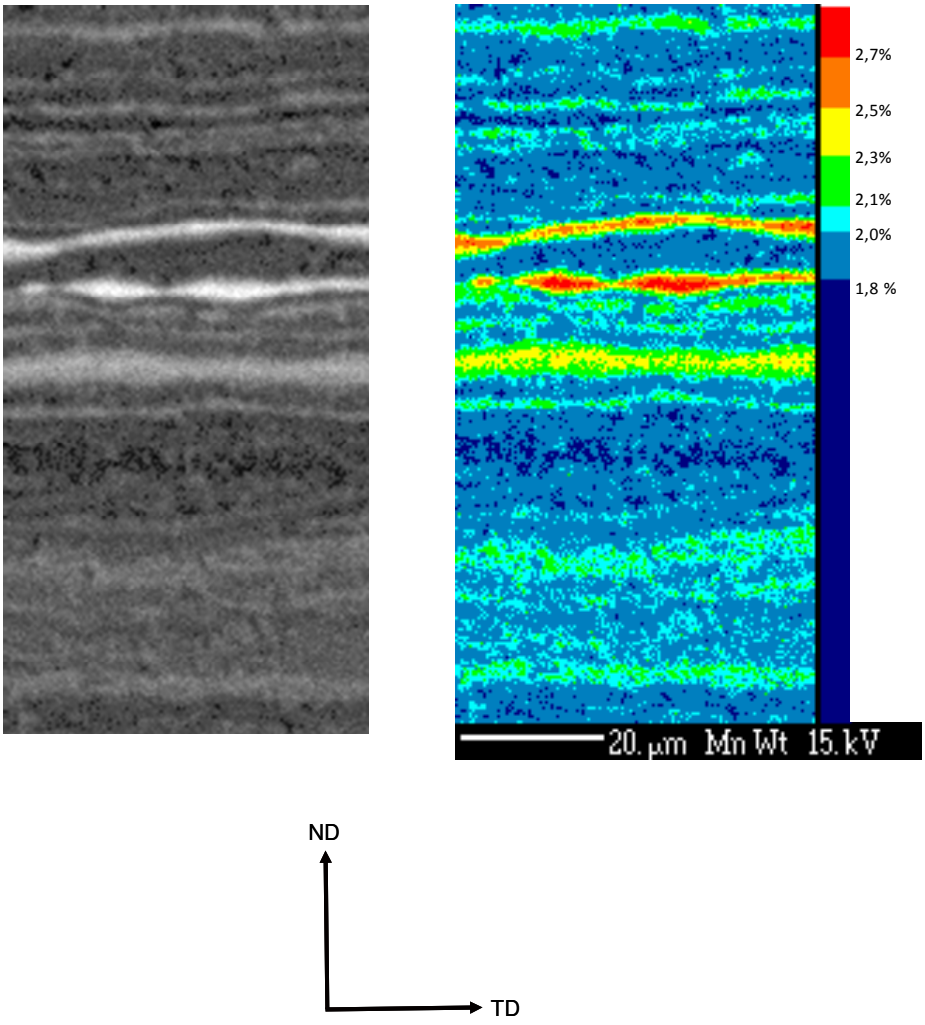

Figure III.10. Mn-distribution *EBMA* maps for the reference DP steel quenched from 760°C. ND is a rolling plane normal.

Three bands of higher Mn concentration correspond to the central segregation. A line profile of the Mn concentration in the segregated zone is shown in Figure III.11. The Mn concentration varies from 1.5 to 3.2 % wt. The nominal Mn concentration in the studied steel is 1.9 %wt.

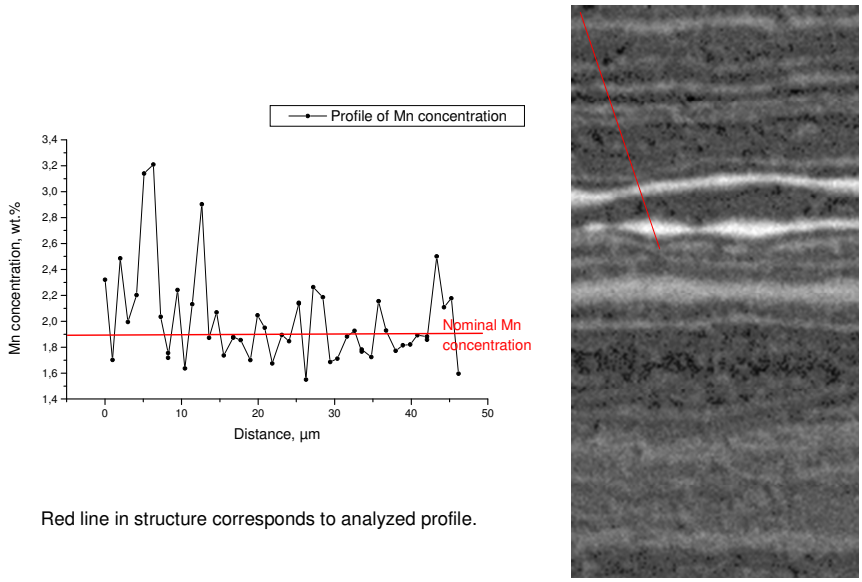

Figure III.11. Mn profile in central segregation zone.

Figure III.12. represents the superposition of Mn-distribution *EBMA* map on the sample microstructure.

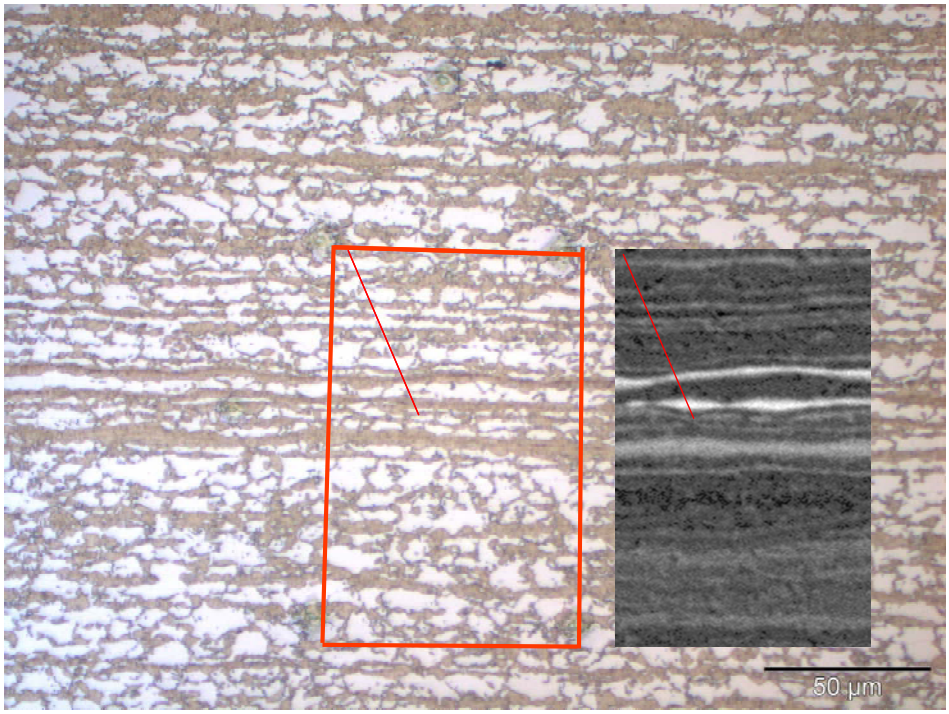

Figure III.12. Superposition of the *EBMA* Mn map on the microstructure.

Figure III.12 points out that the martensite bands are located in the regions of higher Mn content. That is, segregation defines the local microstructure. In steels with low carbon contents, much of the pearlite forms in the high-Mn regions. Since the austenite forms from this pearlite, much of the austenite must also lie in regions of higher Mn-content.

Now, Mn and carbon distribution maps are acquired simultaneously in order to estimate the possibility of influence of segregations of these elements on the mechanical behaviour of the DP steel. Figure III.13 shows the carbon and Mn distribution *EBMA* maps for the ½ thickness of the sample. The strong central segregation of Mn is observed in this sample.

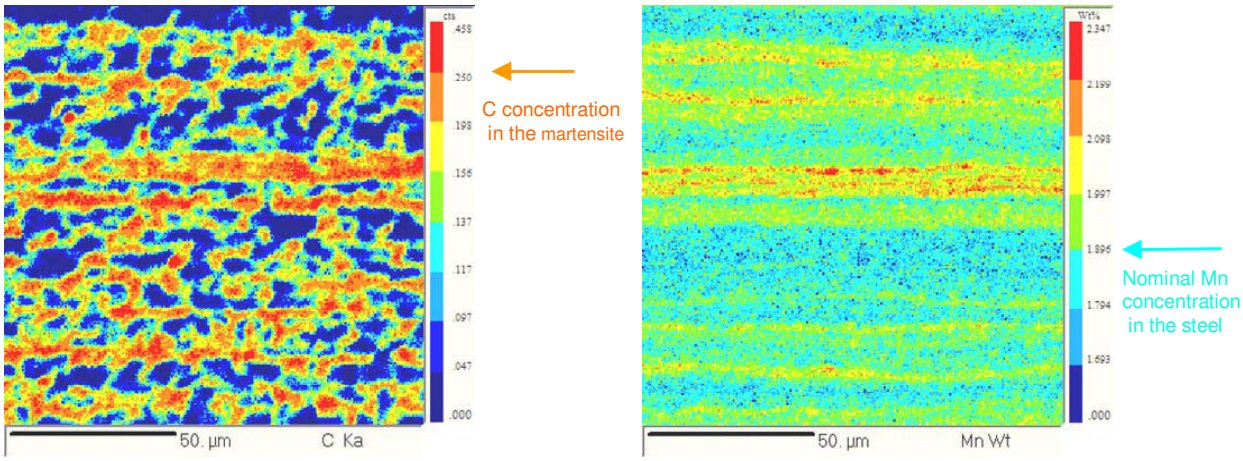

Figure III.13. Carbon (left) and Mn (right) distribution *EBMA* maps at the ½ thickness of the sample.

Before start any analysis of distribution *EBMA* maps, it should be noted that probe spreading in the sample during *EBMA* analysis gives an average elemental concentration for $1\mu m^3$ of material that is why the concentrations of carbon may be exaggerated. This should be kept in mind when analysing the carbon and Mn distribution *EBMA* maps.

In the ferrite-martensite structure almost all carbon is concentrated in the martensite, the ferrite carbon concentration is close to zero. Martensite carbon content, measured by EELS analysis, is 0.28±0.04 wt. %. In the central segregation region the maximum carbon concentration, measured by electron probe microanalysis, is 0.24 % which is in accordance with the EELS value**.**

The same measurements are made at ¼ thickness of the sample. Figure III.14 shows the Mn and carbon *EBMA* maps obtained at the ¼ thickness.

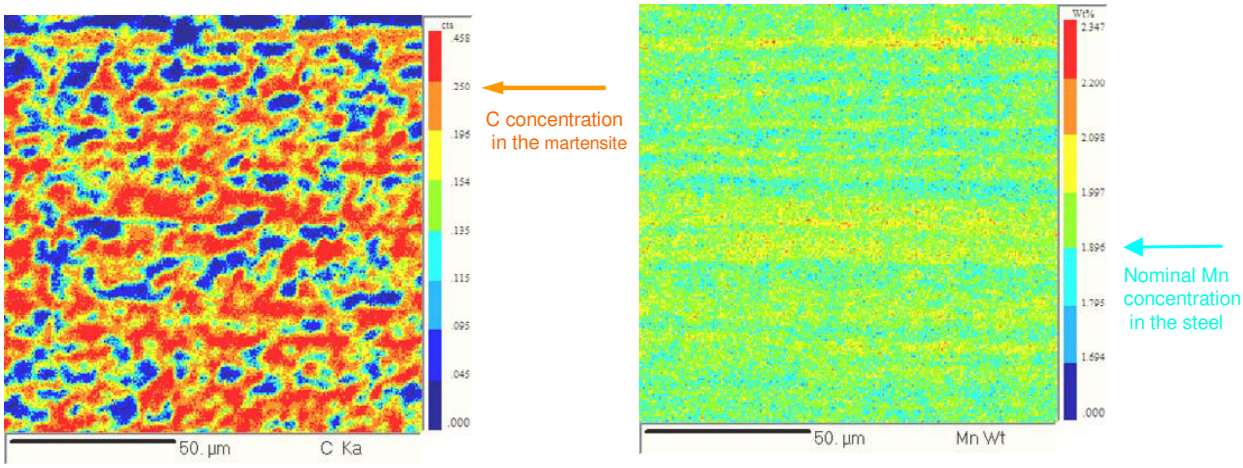

Figure III.14. Carbon (left) and Mn (right) *EBMA* maps at ¼ thickness.

The average carbon concentration measured at ¼ thickness is also in accordance with the EELS value. In the Mn-distribution *EBMA* map, it can be seen that the Mn concentration varies periodically in a banded structure which corresponds to the martensite phase morphology.

The main results of *EBMA* measurements can be summarized as follows:

- There is no difference in carbon concentration in the martensite islands at the ½ thickness and at the ¼ thickness of the sample,

- The segregation defines the local microstructure: in the high Mn region austenite is formed, in the low Mn region ferrite is formed.

It was reported [KRAU99] that the martensite strength is predominantly controlled by its carbon content and independent on the concentration of the substitutional elements in the steel; therefore, considering the above results, it can be concluded that the martensite strength is the same at ¼ thickness and at the ½ thickness.

However, the martensite fraction is higher at the ½ thickness of the material due to macrosegregation [LIVC90, BERA96]. The distribution of the martensite phase influences the mechanical behaviour. Connected martensite islands at the ½ thickness of the specimen provide an easy crack-propagation path [BECK79, HAYA77] which has a detrimental effect on the steel mechanical properties.

III.5 Summary

The reference DP steel microstructure was investigated at a fine scale. Autotempering carbides, formed during quenching, are detected in the 840°C-annealed sample, thus, carbon distribution is heterogeneous in the as-quenched condition. A lath martensite morphology is found in all specimens, which is consistent with the martensite carbon content. The high dislocation density is observed at the ferrite/martensite interface. Carbide precipitation is observed for all tempering temperatures.

The macro segregation was studied in order to estimate its influence on the mechanical properties. The martensite carbon content is found to be the same at the ¼ thickness and at the ½ thickness. Thus, the martensite strength is the same throughout the sample. However, a higher martensite fraction at the ½ thickness due to macro segregation can influence the mechanical behaviour of the steel.

Chapter IV

Carbon distribution analysis by NanoSIMS

IV.1 Introduction

Secondary ion mass spectrometry (SIMS) is a powerful technique used to analyze the chemical composition of solid surfaces by sputtering the surface of the specimen with a focused primary ion beam and collecting and analyzing ejected secondary ions. These secondary ions are measured with a mass spectrometer to determine the elemental composition of the surface. SIMS is the most sensitive surface analysis technique. For instance, the detection limit for carbon in iron is better than 0.0063 wt. % with the NanoSIMS technique while it is 0.025 wt. % with PEELS method [VALL06, SCOT99].

NanoSIMS carbon ion maps give an image of the carbon distribution in the microstructure. The intensity of the signal is proportional to the carbon content of the phase. Thus, any contrast between ferrite and martensite in the reference DP steel is formed due to different carbon concentrations in these phases.

The carbon distribution in DP steel is an extremely important parameter which influences the mechanical behaviour of the steel. The fine microstructure study using NanoSIMS analysis makes it possible to understand the role of carbon distribution in damage mechanisms of the DP steel.

Analyses were performed on the reference DP steel after direct quenching and tempering. The study of the carbon distribution in the as-quenched state facilitates interpretation of the more complex tempered microstructures. Samples with different martensite and ferrite volume fractions were investigated.

IV.2 Experimental results and discussion

The *NanoSIMS* analysis was carried out in the Gabriel Lippmann research centre, Luxemburg.

IV.2.1 Investigation of the as-quenched state

Secondary ion images are obtained for the as-quenched condition of the reference DP steel to determine the carbon distribution in the initial state (i.e. before tempering).

The study of the carbon distribution in the as-quenched state is a compulsory stage of analysis because this structure will be inherited in the tempered state.

The microstructure of the studied specimens consists of martensite and ferrite with different volume fractions which were varied by changing the annealing temperature (Table II.4).

The resulting carbon distribution *NanoSIMS* ion maps together with the corresponding SEM images are shown in Figure IV.1. The SEM images are presented to illustrate the analysed microstructure. The carbon concentration scale is represented on this figure too. The increase in the intensity from black to red indicates the increase in carbon concentration.

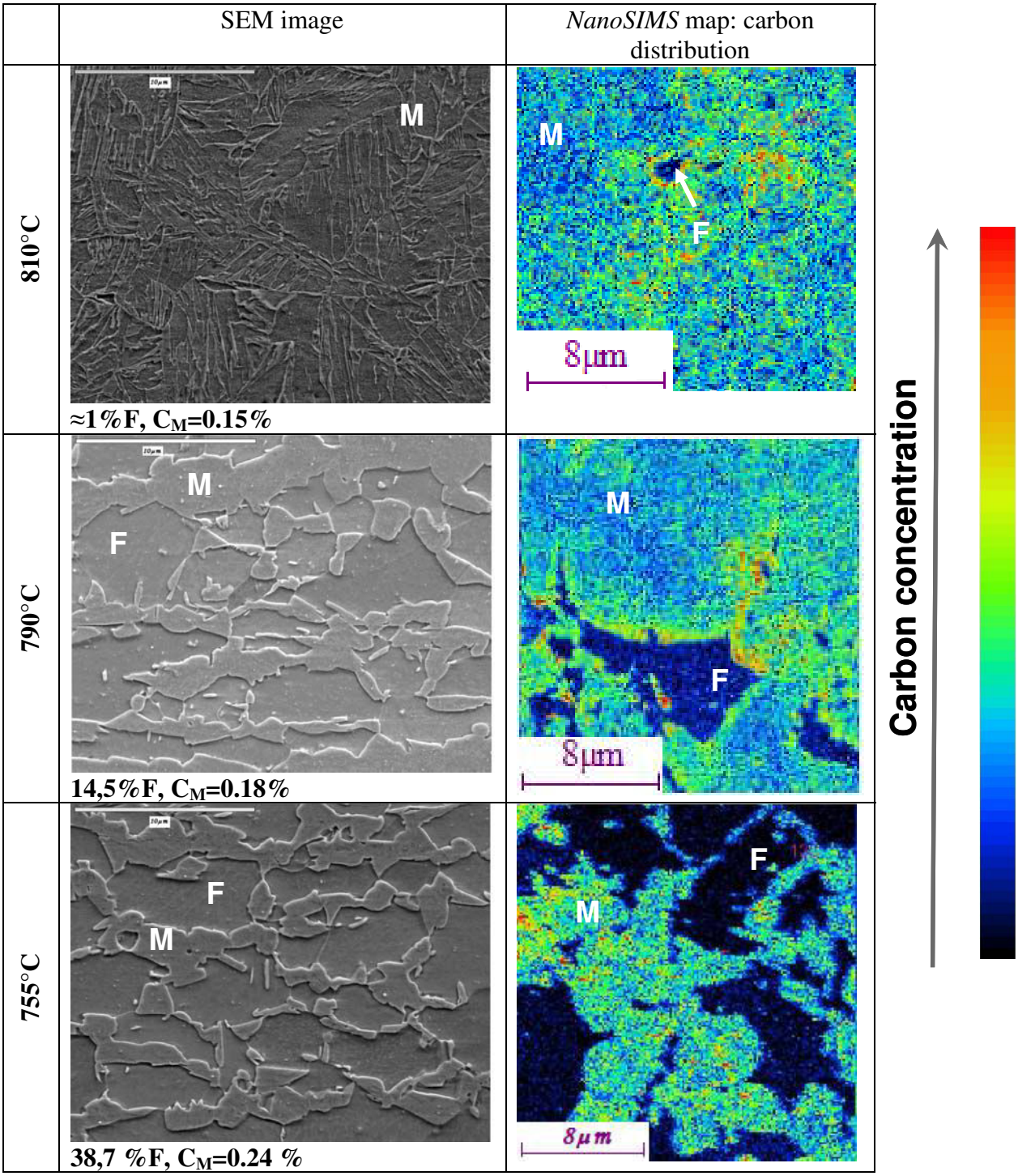

Figure IV.1. The SEM images and *NanoSIMS* carbon ion maps for as-quenched samples.

The *810°C*–annealed sample contains a very small percentage of ferrite, the microstructure is almost entirely martensitic. The carbon distribution in this sample is heterogeneous. In the vicinity of small ferrite islands an enrichment of the ferrite/martensite interface can be noticed: the intensity of the carbon signal is higher near the ferrite/martensite interface.

In the *790°C*-annealed sample the carbon distribution in the martensite phase is heterogeneous. A higher intensity of carbon atoms is detected at the ferrite/martensite interface (Figure IV.2).

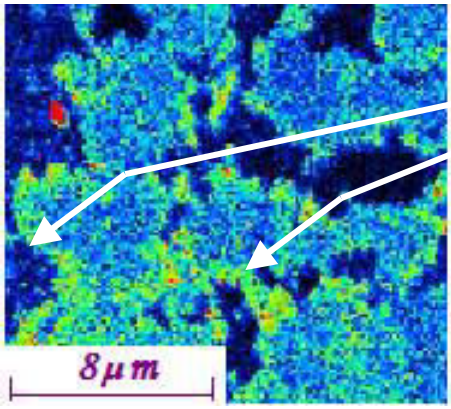

Figure IV.2. *NanoSIMS* carbon ion map for the 790°C-annealed sample.

The *755°C*-annealed sample shows the same heterogeneous martensite phase, but in this case no carbon enrichment is found at the ferrite/martensite interface (Figure IV.3). The interface presents even a small depleted layer.

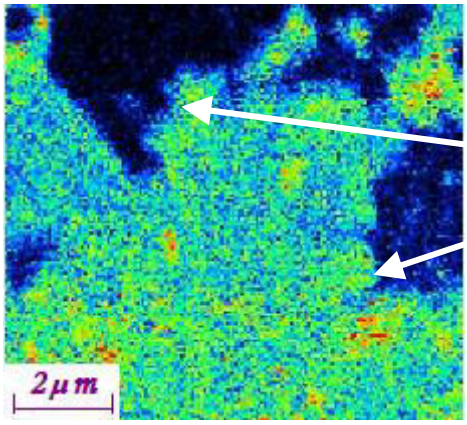

Figure IV.3. *NanoSIMS* carbon ion map for the 755°C-annealed sample.

The important point to note is that the different microstructures are obtained for different annealing temperatures: *the carbon distribution in martensite islands changes as a function of annealing temperature.* Local enrichment or depletion of the ferrite/martensite can be present. It can be supposed that these different carbon distributions will influence the steel damage behaviour and notably the ferrite/martensite interface behaviour during mechanical testing.

IV.2.2 Investigation of carbon distribution after tempering

Tempering treatments change the carbon distribution in DP steels. During tempering carbon diffusion occurs: carbon atoms diffuse to martensite crystal defects (dislocations, lath boundaries, grain boundaries) and form segregations or carbide particles at high tempering temperatures ($T_{tempering}$ > 200°C). It is reported that ε carbide does not form when $C_M \leq 0,2\%$ [PORT92]. The reason for the 0,2%C limit is thought to be due to the fact, that the M_S temperatures of very low-carbon martensites are high enough to allow considerable carbon diffusion to lath boundaries during direct cooling from M_S temperature to room temperature [PORT92].

Specimens with two different phase contents were studied after tempering at different temperatures using the *NanoSIMS* technique. The sample description is presented in Table IV.1.

$T_{holding}$, °C	Ferrite, %	C_M, %	$T_{tempering}$, °C	$t_{tempering}$, min
810	0,4	0,15	230, 380, 460	4
760	37,7	0,24		

Table IV.1. Samples in the tempered condition studied by *NanoSIMS*.

The obtained *NanoSIMS* carbon ion maps together with the SEM images are shown in Figures IV.4, II.5 and IV.6.

Carbide precipitation is found out in all tempered samples. The intensity of the carbide precipitation depends on the tempering temperature: it obviously increases with increasing tempering temperature.

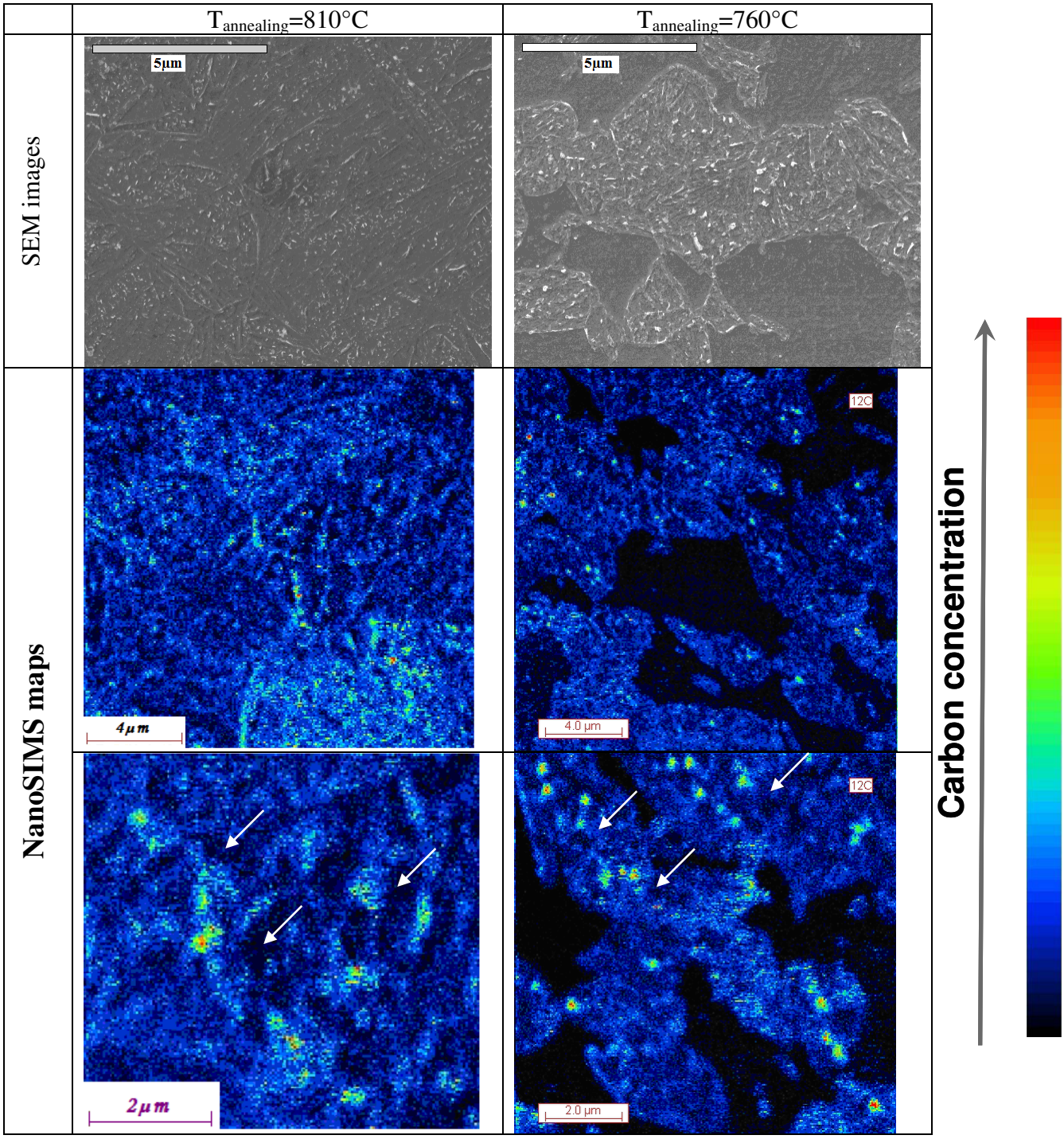

Figure IV.4. The SEM images and *NanoSIMS* ion maps for 230°C-tempered specimens. Depleted zones are shown by arrows.

The first precipitates appear at 230°C tempering temperature. For the 760°C-annealed sample, the carbides are localised inside the martensite phase, no preferable carbon segregations at martensite/ferrite interfaces are detected. At this tempering temperature the 760°C-annealed structure has coarser carbides than the 810°C-annealed structure. This could be related to the different carbon content of the martensite phase in these two microstructures (Table II.4).
The dark carbon-depleted zones emerge after tempering at this temperature inside the martensite phase.

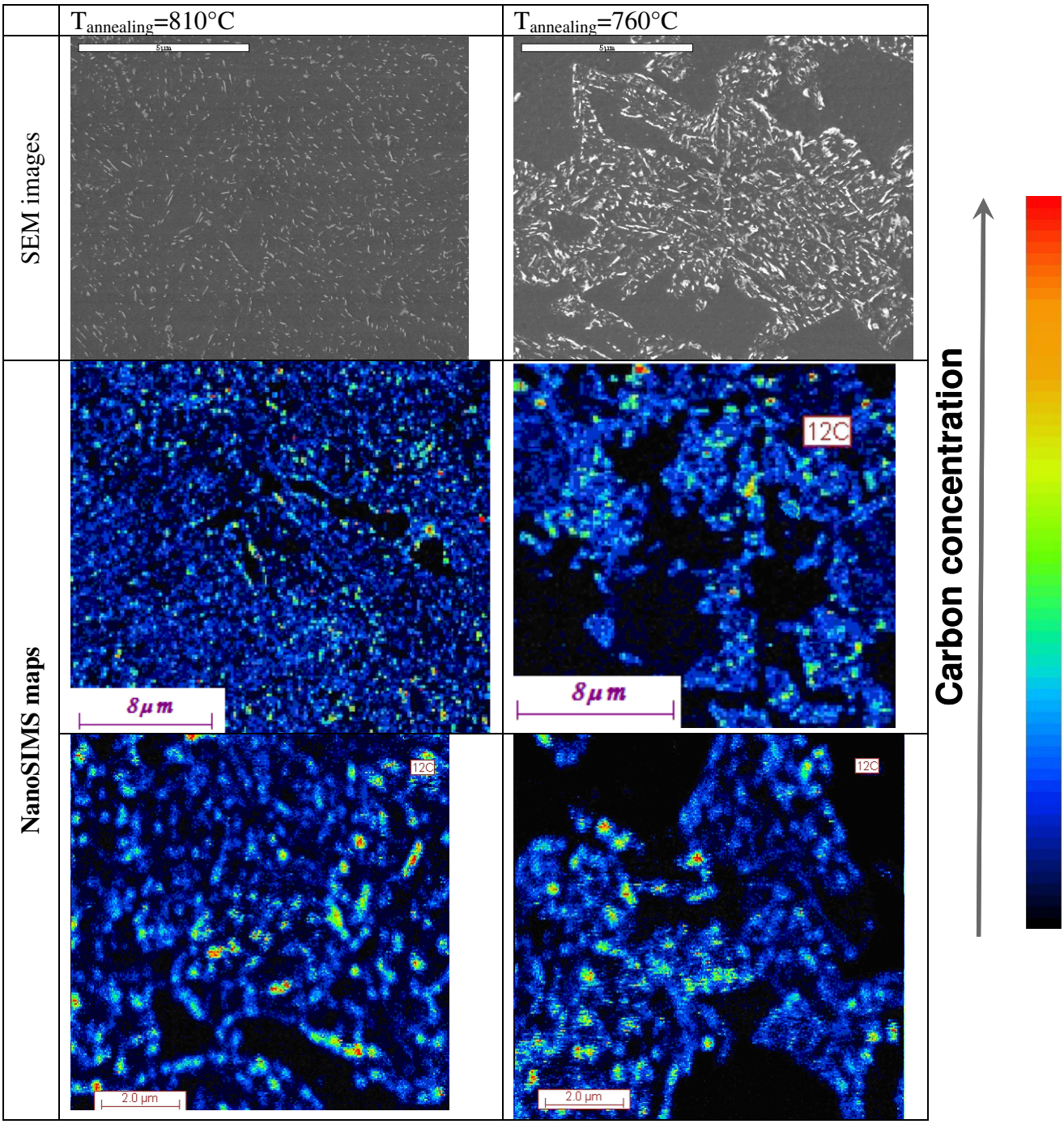

Figure IV.5. SEM images and *NanoSIMS* carbon distribution maps for 380°C-tempered samples.

A marked phase separation is observed in the martensite phase at 380°C tempering temperature. Extensive carbide precipitation occurs in the martensite phase at this tempering temperature and this leads to the appearance of carbon-depleted and carbon-enriched zones in the *NanoSIMS* carbon ion maps. The carbide precipitation, in the 810°C-annealed specimen through the martensite island, is observed to be heterogeneous. The ferrite/martensite interface in this sample contains more carbide precipitates, which is detected as a stronger carbon ions signal in the *NanoSIMS* maps. In the 760°C-annealed sample, no preferential carbon precipitation at the interface is detected.

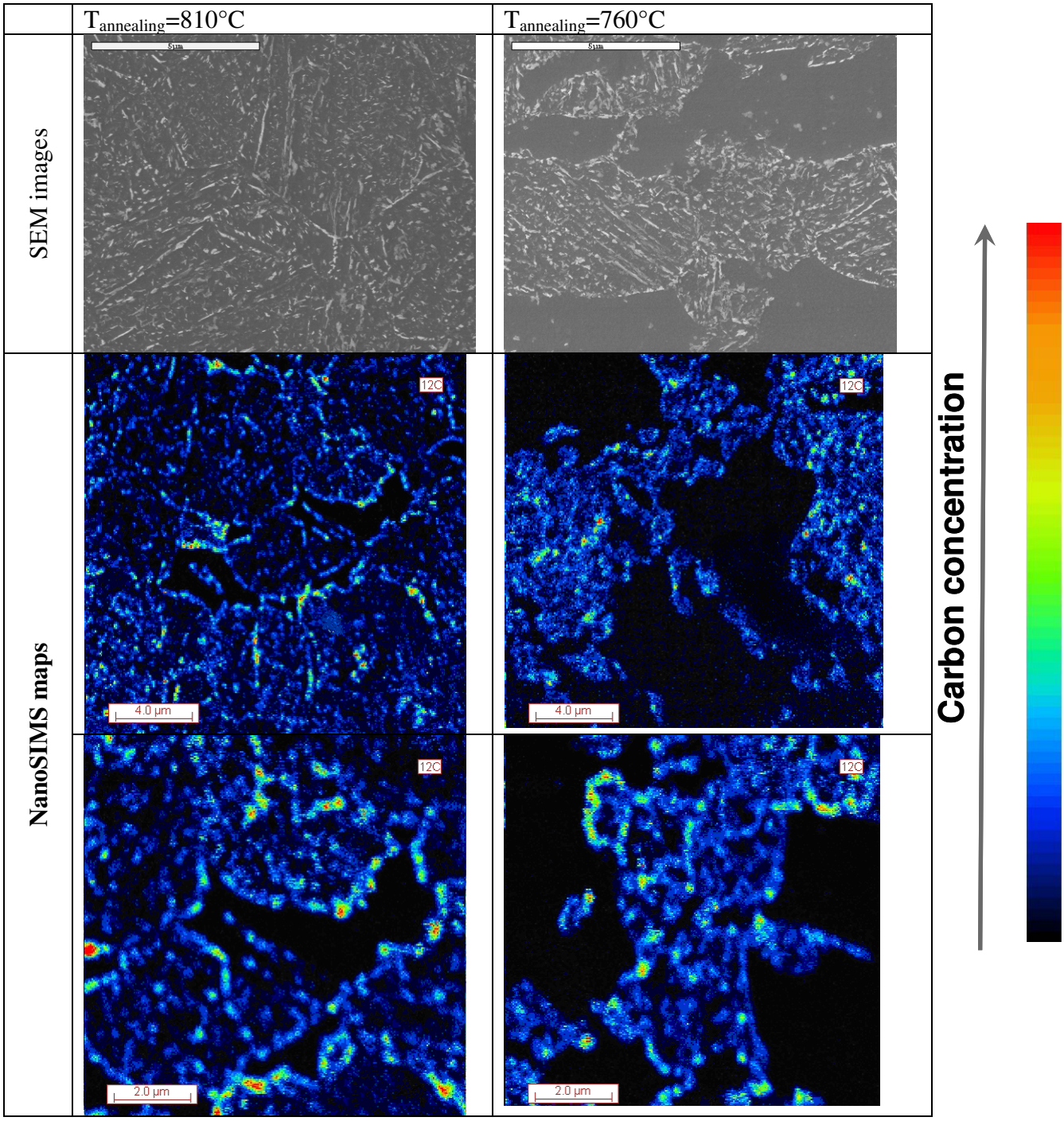

Figure IV.6. SEM images and *NanoSIMS* carbon ion maps for 460°C-tempered samples.

A distinct martensite phase separation is found at the 460°C tempering temperature. The large depleted zones are situated near the fine high carbon intensity zones. The ferrite/martensite interface contains chains of precipitates (probably cementite) in the 810°C-annealed specimen. In the 760°C-annealed sample no preferential carbon precipitation at the interface is detected.

Note: we do not compare the intensities of the as-quenched and tempered images because they were obtained at different acquisition conditions.

IV.3 Understanding the carbon distribution

In order to explain the observed carbon distribution in the as-quenched and then in the tempered condition we will consider the austenite formation during heating and annealing of initial cold-rolled microstructure. The austenite transformation can be separated into several stages which have different time-scales.
It is reported that the nucleation of austenite in the pearlite structure occurs at carbides. Once austenite has nucleated in pearlite, its subsequent growth is presumably controlled by the rate of carbon diffusion in the austenite [SPEI69A].
First, austenite nucleates on cementite of the initial microstructure. This cementite has a Mn concentration higher than the ferrite matrix for several reasons [GOUN05]:

1. carbides form in Mn segregated zones,
2. they are enriched in Mn during the formation process .

The carbon profile in the austenite depends on kinetics of austenite formation during heating and annealing. The austenite formation stages are as follows:

- cementite dissolution stage,
- austenite growth.

Figure IV.7 shows an austenite formation diagram [SPEI81], which permits to define the controlling kinetic processes. Using this diagram, the steps in austenite formation can be identified for given annealing temperature and time.

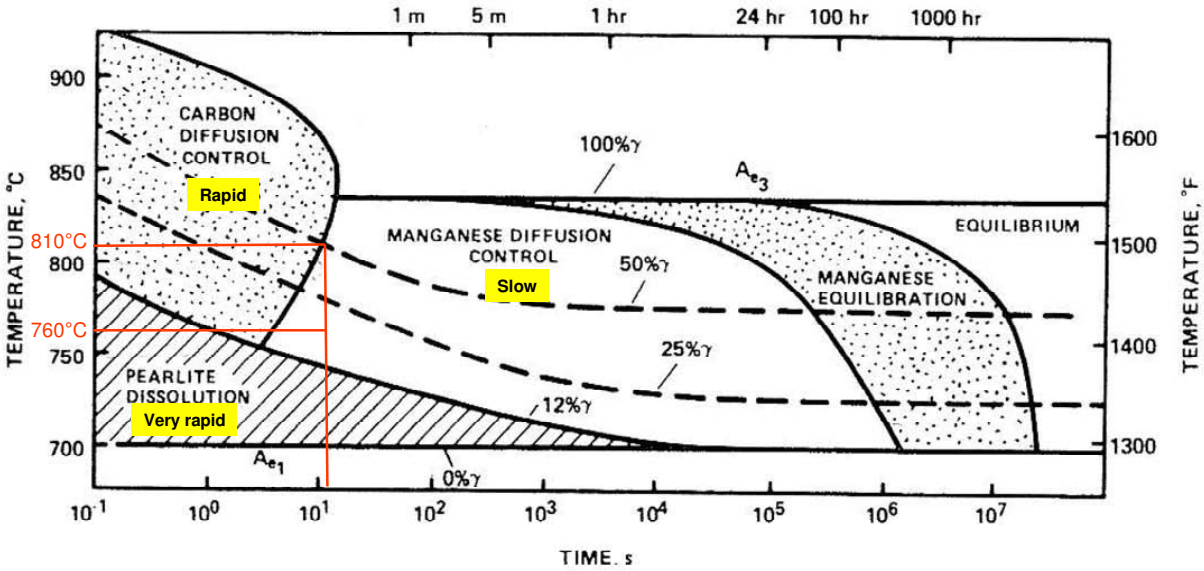

Figure IV.7. Austenite growth diagram for Fe-0.12C-1.5Mn-0.24Si steel [SPEI81].

According to this diagram, for used annealing temperatures, the austenite growth is successively controlled by the carbon diffusion in the austenite and Mn diffusion in the ferrite and in the austenite (Figure IV.7).

For applied annealing cycles, only the first two processes should be taken into account. The carbon profile in the austenite at the end of the annealing is a function of kinetics conditions

(transformation tie-lines) and the Mn redistribution depends strongly on both the cementite dissolution and the growth of austenite.

There are two possibilities:

*First possibility**:***

The cementite dissolution is completed (or/and quasi completed) but the Mn profile in the austenite is not homogeneous: austenite, growing from the cementite, inherits its Mn concentration. Figure IV.8 shows the carbon and Mn profiles in the austenite phase after complete dissolution of cementite at 750°C [GOUN05].

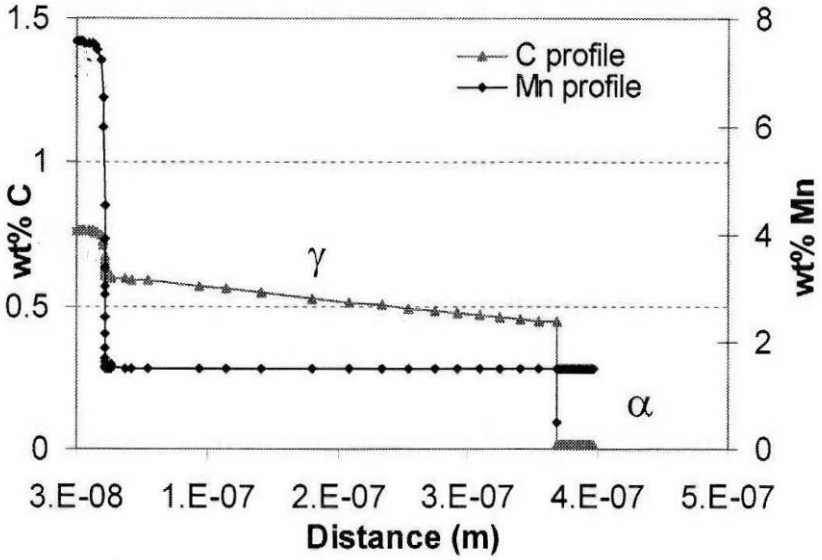

Figure IV.8. Carbon and Mn profiles in the γ calculated by DICTRA® package after complete dissolution of cementite. Fe-0.15C-1,58Mn steel [GOUN05].

The electron beam microprobe analysis (EBMA) shows this type of microstructure (Figure IV.9) [PETI99]. Mn distribution in the martensite islands is heterogeneous: Mn concentration is higher in the centre of a martensite island than in the periphery.

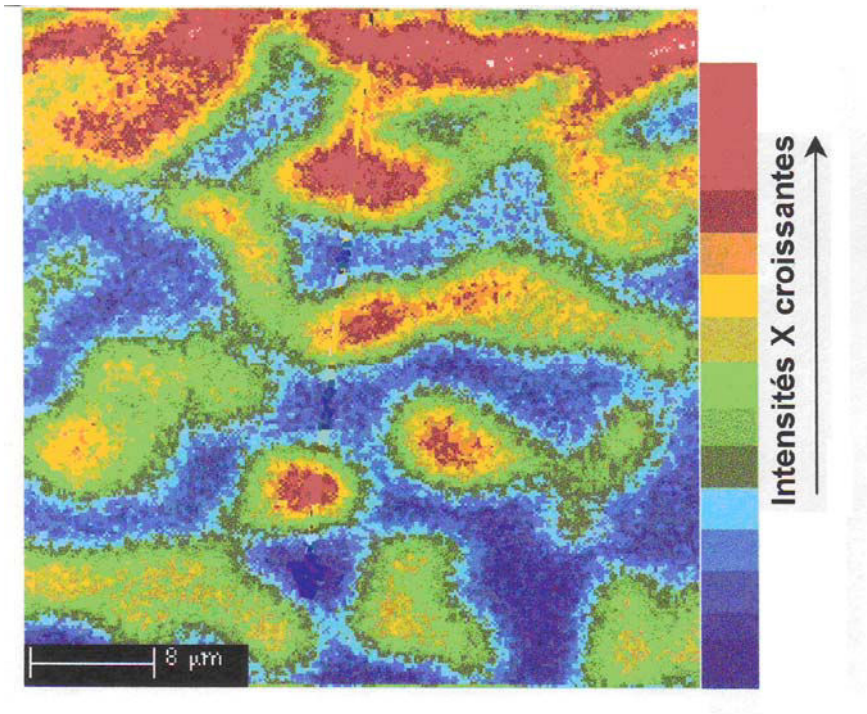

Figure IV.9. Mn distribution *EBMA* map for Fe-0.07C-1.5Mn-0.32Si-0.59Cr steel annealed at 775°C for 33 min and then quenched [PETI99].

It is known that manganese lowers the chemical potential (activity) of carbon in solution: carbon will diffuse to regions rich in Mn [PORT92].

Therefore, the carbon profile can be produced due to the Mn heterogeneous distribution. Carbon atoms will move to the Mn-enriched areas until the carbon chemical potential, μ_{Ci} is equalized:

$$\mu_{C1}(X_{Mn1}, X_{C1}) = \mu_{C2}(X_{Mn2}, X_{C2})$$

Where X_i is the concentration.

The centre of austenite islands is richer in Mn than the periphery. At a given heat treatment time, the transformation tie-line gives the carbon iso-activity in the austenite island. This gives a carbon concentration higher in the center than in the periphery (the carbon concentration difference can be estimated from the phase diagram, at a given austenite volume fraction and equilibrium tie-line).

This case is intensified at low temperatures because of the slower Mn diffusion and the higher slope of the (α+γ) zone in the phase equilibrium diagram.

Second possibility:

The cementite dissolution is completed and Mn profile in the austenite island is homogeneous. Two cases are possible:

1. The transformation has reached the quasi-equilibrium state (the austenite transformation is controlled by the Mn diffusion in the ferrite). In this case, the carbon activity is constant (Mn concentration is constant) and thus the carbon concentration is constant. So, there is no difference in carbon concentration between the center and the periphery of the austenite island.

2. The case when the austenite transformation is controlled by the carbon diffusion in austenite. There is a gradient of carbon concentration between the center and the periphery of the austenite island. (In this case the delta carbon can be estimated from the equilibrium tie-lines). This behaviour is typical for high annealing temperatures.

Thus, carbon enriched or depleted layer could be observed at the ferrite/martensite interface depending on Mn profile in the austenite (i.e. cementite dissolution and growth of austenite). The microstructure is composed by a distribution of austenite grain size. And, it is important to note, that carbon distribution is influenced by the austenite grain size since it defines the characteristic diffusion length. It means that the carbon distribution is size-dependent.

IV.4 Summary

The heat treatment parameters influence the carbon distribution in the martensite islands. It has been established by *NanoSIMS* analysis that the carbon distribution in the austenite island is a function of the heat treatment parameters. The austenite formation process during heating and annealing apparently governs the carbon distribution in the austenite island. Carbon enriched or carbon depleted layer is observed at the ferrite/martensite interface.

Evidently, this particular carbon distribution is inherited in the tempered microstructure. During the tempering the martensite phase separates to ferrite and carbides. As a result carbon rich areas are observed at the carbides locations and carbon depleted areas are observed near carbides. This distribution intensifies with increasing tempering temperature.

Chapter V

Damage resistance through hole expansion

The forming process influences the mechanical properties of the finished part. Various test methods are available to establish the suitability of sheet metal for the forming processes involved during industrial operations. The Hole Expansion (HE) test, described in the experimental part, is one of the various tests employed to asses steel formability: higher the value of HE, better will be steel formability. It is one of the best methods for evaluating the suitability of sheet steel for forming 'flanges' because it closely resembles the process used under production conditions to form such flanges (plunged rims) starting with punched holes [ISO06, THUR98].

Complex modes of deformation pertain to the damage resistance. In the case of hole flanging, the deformation mode at the edge of the hole is a combination of bending with stretching. Therefore, the hole flangeability cannot be estimated accurately by the simple uniaxial tensile test due to the different deformation mode [HYUN02]. It was reported that the HE is influenced significantly by the microstructure parameters and that the difference in mechanical behaviour (hardness) of phases is a dominant factor in controlling the damage resistance of the steel [HASE04].

V.1 Damage resistance of the as-quenched material

Figure V.1 shows the evolution of *HE* value with quenching temperature for DQ and RCQ heat treatments.

The *HE* value increases in a non-linear manner with increasing quenching temperature (for DQ and RCQ cycles). The *HE* evolution with quenching temperature exhibits the S-shape curve. For low quenching temperatures low values of *HE* are obtained, for high quenching temperatures high values of *HE* are obtained.

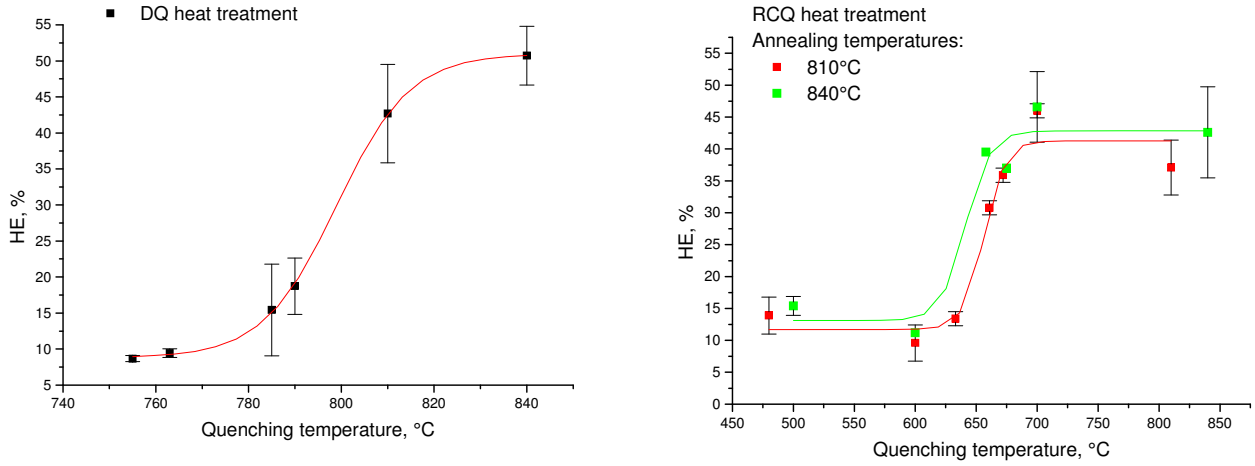

a b

Figure V.1. The evolution of *HE* value: a) – for DQ heat treatment versus quenching temperature, b) – for RCQ heat treatment versus quenching temperature.

It is well established [HASE04] that the *HE* property of steel is controlled by its microstructure. Now the *HE* values will be plotted versus a microstructural parameter. Figures V.2 and V.3 illustrate the variation in the *HE* ratio with the ferrite fraction for DQ and RCQ microstructures.

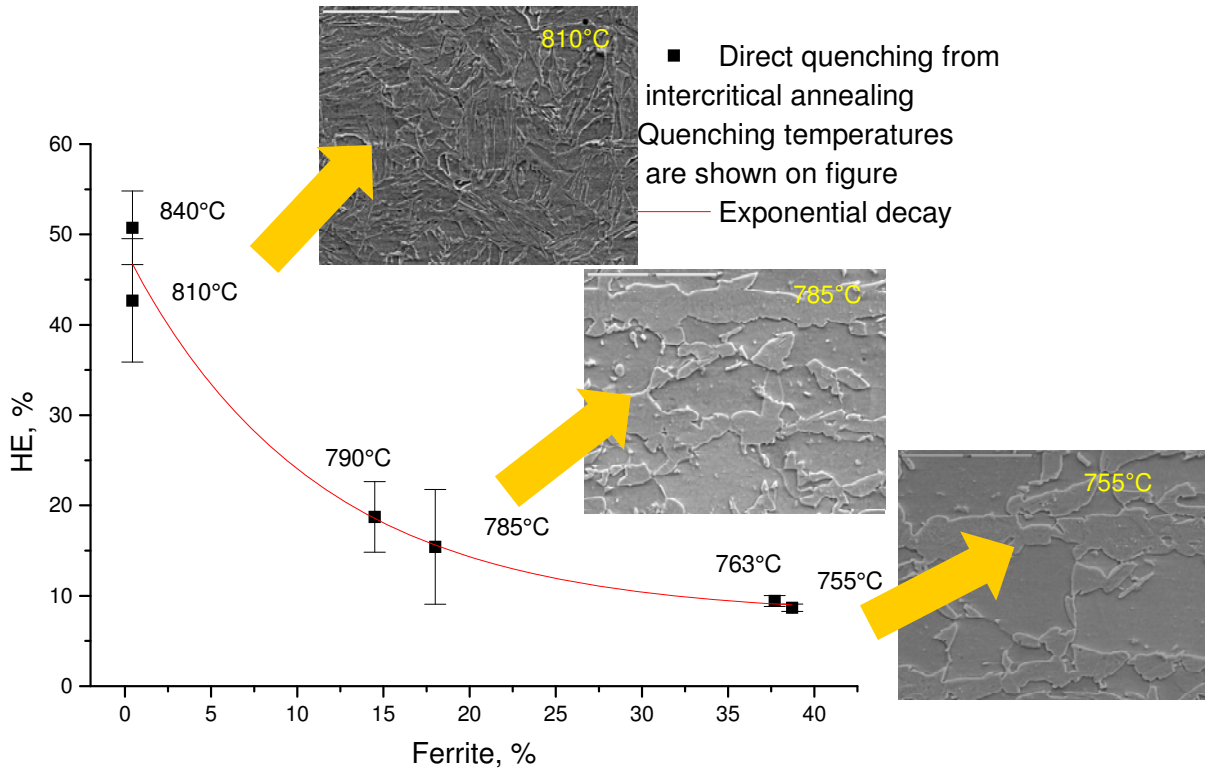

Figure V.2. *HE* ratio versus ferrite fraction for DQ heat treatment. Quenching temperatures are shown on the figure. Experimental points are fitted by exponential function.

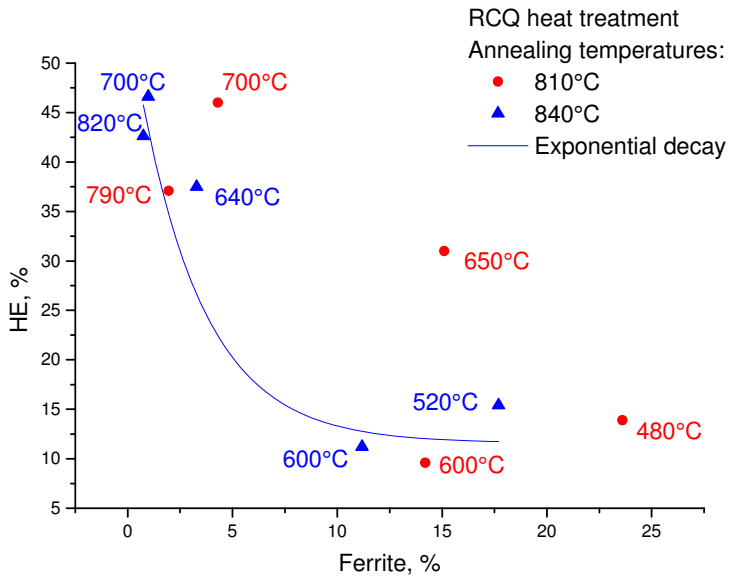

Figure V.3. *HE* ratio versus ferrite fraction for RCQ heat treatment. Quenching temperatures are shown on the figure. Experimental points are fitted by exponential function.

A unexpected evolution of the hole expansion ratio with ferrite fraction is observed for studied DP steel. Generally, it is reported that the *HE* increases with increasing fraction of ductile phases (like ferrite) in the microstructure [HYUN02].

However, in this study, the highest *HE* values are observed for steels with low ferrite percent in the microstructure. The increase in the ferrite fraction leads to a dramatic decrease of the *HE* ratio. Thus, not only the ductile phase fraction controls the *HE* value of the steel, but the mechanical properties of both phases (ferrite and martensite) and their evolution with different heat treatment and tempering parameters should be analysed in order to understand these experimental results.

Let's consider now the *HE* evolution with tempering.

V.2 Hole Expansion evolution with tempering temperature

The as-quenched material usually shows low *HE* values. The tempering treatment is employed to improve the formability of the DP steel. Figures V.4 and V.5 show the evolution of *HE* ratio with tempering temperature.

It can be seen that the *HE* ratio is considerably improved by the tempering treatment. For instance, *HE* ratio for the DQ steel changes from 10% (the as-quenched state) to 77% (tempered at 460°C). The observed increase of the *HE* values could be due to several effects:

- Decrease of the residual stresses at the ferrite/martensite interface during tempering,
- Decrease of the difference in the mechanical behaviour between ferrite and martensite during tempering (i.e. martensite softening).

Tempered DP steel microstructure provides a better damage resistance in the *HE* test.

The *HE* evolution both with tempering and microstructure is studied in the next section in order to clarify their influence on the damage resistance of the steel.

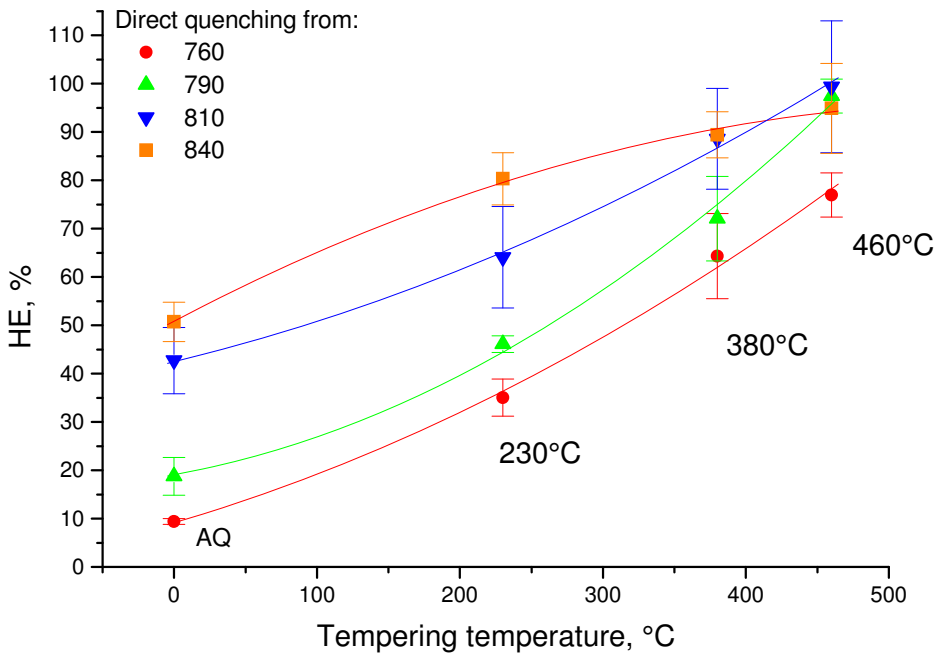

Figure V.4. Influence of tempering on *HE* ratio for DQ heat treatment.

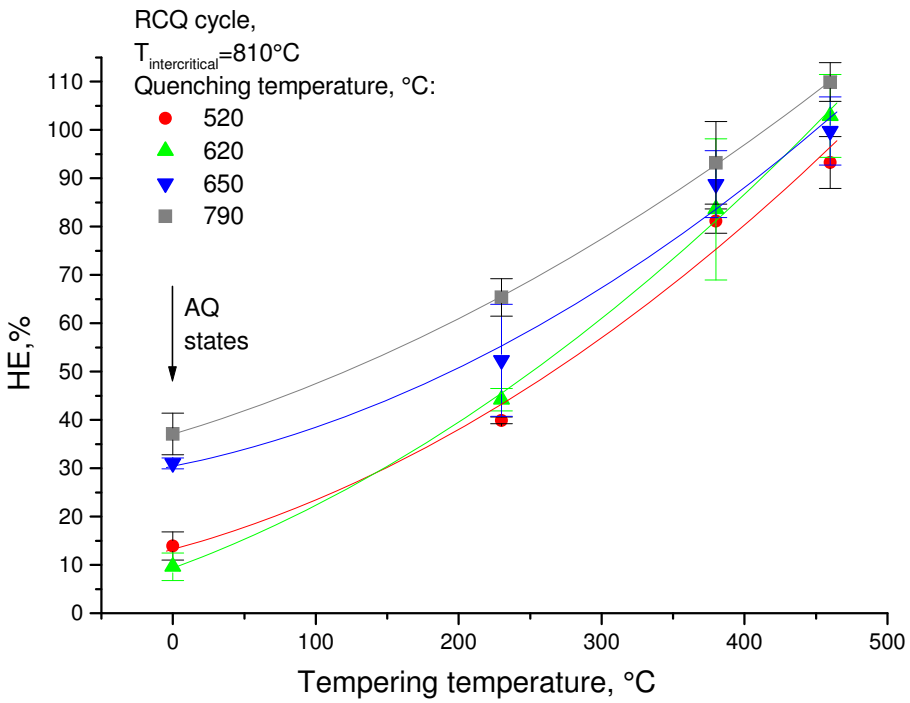

a

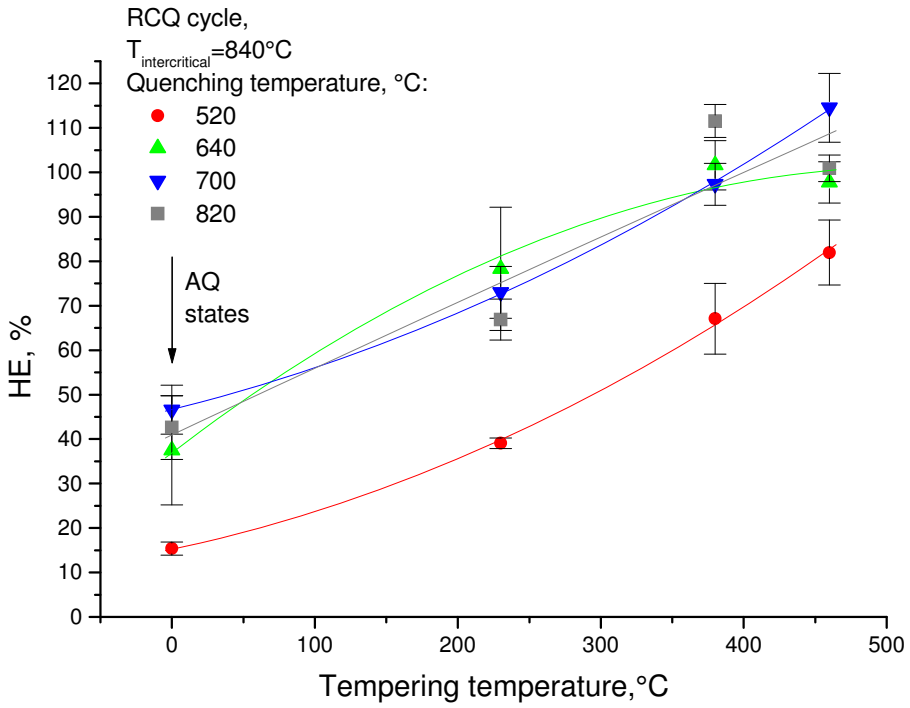

b

Figure V.5. Influence of tempering on *HE* ratio for RCQ heat treatments: a) – annealing at 810°C, b) – annealing at 840°C.

V.3 HE-ferrite fraction correlations evolution with tempering temperature

As has been observed, the steel microstructure has a significant influence on the *HE* ratio of the as-quenched material. During the tempering treatment, different microstructure changes occur, which could influence the damage resistance of the steel. The evolution of the *HE* ratio with tempering versus ferrite volume fraction for DQ and RCQ heat treatments is presented in Figures V.6 and V.7 respectively.

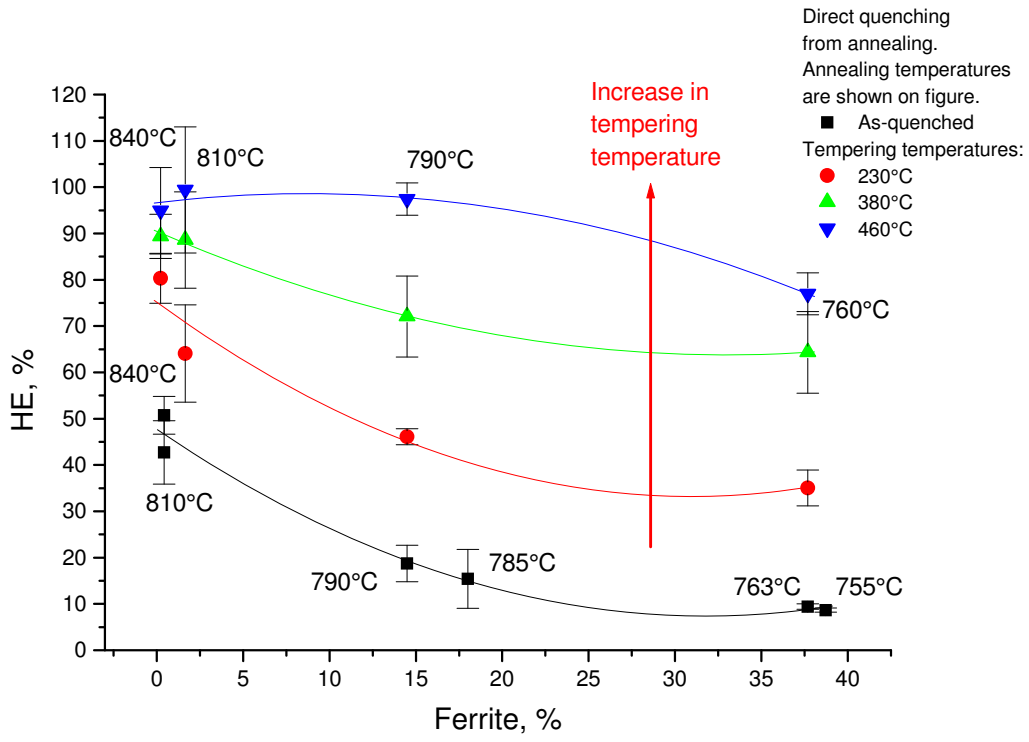

Figure V.6. Evolution of the *HE* ratio with ferrite content for DQ heat treatment in the as-quenched state and after tempering treatment

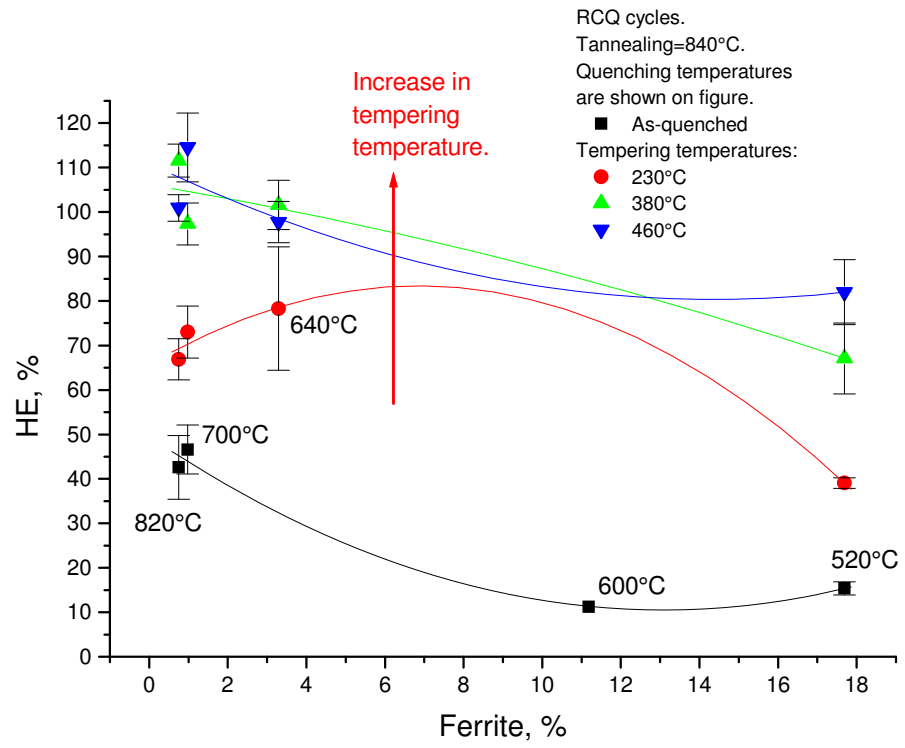

a

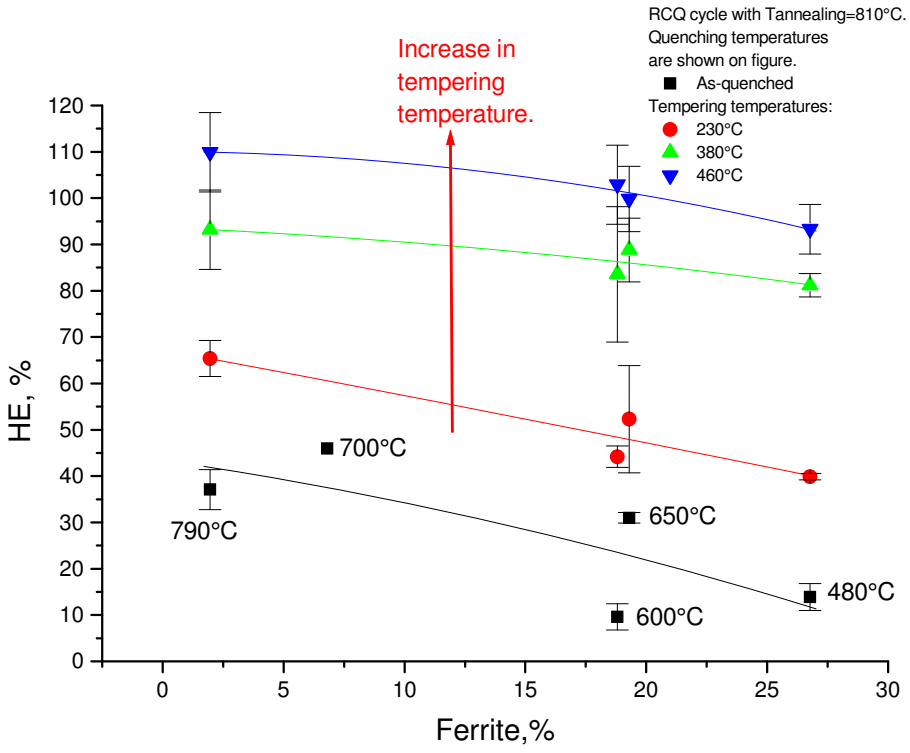

b

Figure V.7. Evolution of the *HE* ratio with ferrite content for RCQ heat treatment in the as-quenched state and after tempering treatment: a – annealing at 810°C, b – annealing at 840°C.

Damage resistance is strongly influenced by the steel microstructure. As previously indicated an increase in the ferrite volume fraction leads to a dramatic decrease of the *HE* ratio. The tempering treatment improves the formability of the DP steel. The samples with higher ferrite fraction show almost the same level of *HE* ratio as the samples with small ferrite fraction: the slope of the fitted curves decreases and becomes independent of the ferrite content. This behaviour is observed to be the same for the DQ and RCQ material.

Several observations can be made from the experimental *HE* value evolutions with heat treatment and microstructural parameters:

- The *HE* value evolution with quenching temperature exhibits S-shape curve,
- An increase in the ductile phase fraction (ferrite) leads to a dramatic decrease of the *HE* value for the studied DP steel,
- Tempering treatment improves the *HE* value.

V.4 Mechanical properties: correlation between HE and UTS

It is of interest to look now at the relationships between damage resistance and mechanical properties. The ductility (Uniform Elongation at the tensile testing) does not vary significantly with tempering temperature, so we will focus on *HE* and *UTS* correlations for DQ heat treatment. The *HE-UTS* relationship for the DQ microstructure in the as-quenched and tempered condition is presented in Figure V.8.

An increase in annealing temperature (in the range 760°C-810°C) results in an increase of the *HE* values and the *UTS* levels. *HE* ratio increases with increasing tempering temperature, while *UTS* level decreases.

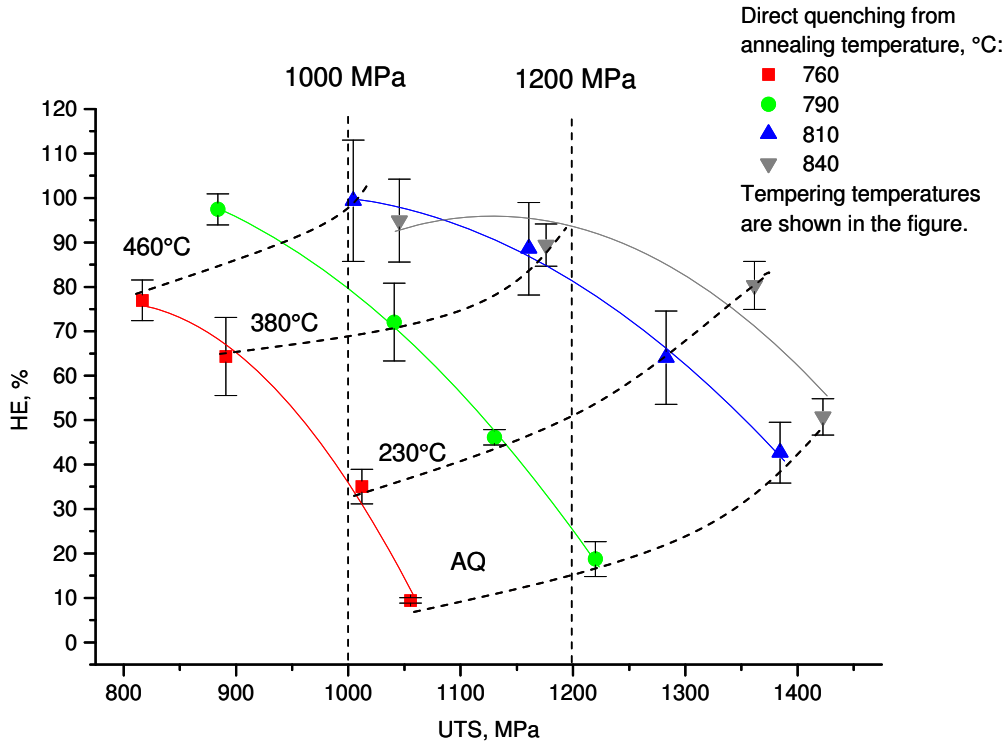

Figure V.8. The relationship between *HE* ratio and *UTS* for the DQ microstructure in the as-quenched and tempered conditions.

A *direct microstructure design* is possible using the experimental data presented in Figure V.8. Let us consider two *UTS* levels: 1000 MPa and 1200 MPa, which are required for applications of the studied DP steel.

UTS=1000 MPa

As can be seen from Figure V.8, for a *UTS*=1000MPa, the *HE* ratio varies from 36.5% to 100% as a function of the annealing and tempering treatment. The lowest *HE* level corresponds to the martensite with 37.7 % of ferrite microstructure tempered at 230°C (Figure V.9).

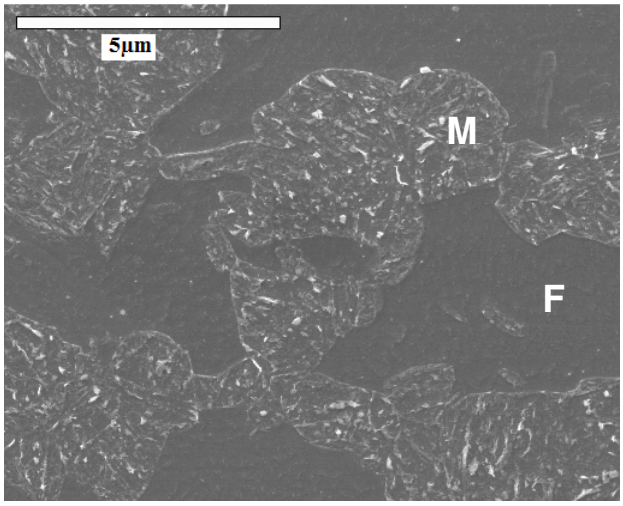

Figure V.9. DQ microstructure. $T_{annealing}$=760°C, $T_{tempering}$=230°C.

Now if a high *HE* levels are required the higher annealing and tempering temperatures should be used: a higher martensite volume fraction is then obtained. The microstructure consists of tempered martensite with 14.5% of ferrite (Figure V.10).

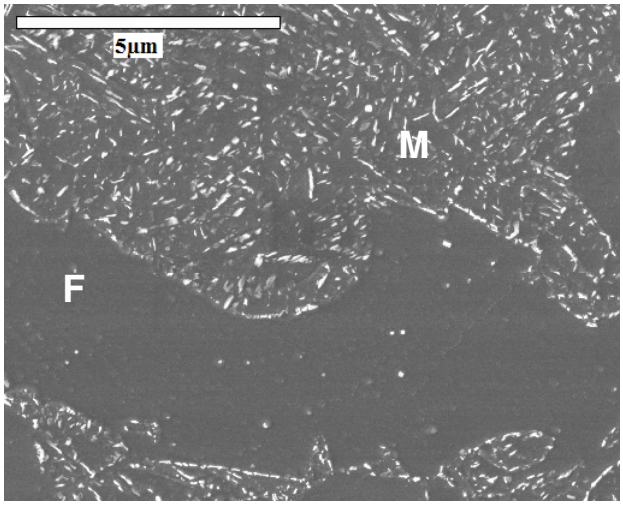

Figure V.10. DQ microstructure. $T_{annealing}$=790°C, $T_{tempering}$=380°C.

Finally, for the considered *UTS* level a 100% *HE* ratio can be reached if the 810°C-annealing temperature and 460°C-tempering temperature are utilized. In this case the microstructure is almost 100% martensitic (the ferrite fraction is about 1%) (Figure V.11).

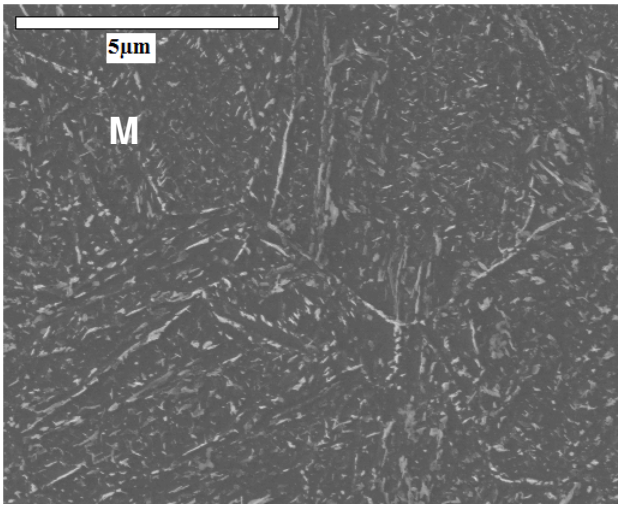

Figure V.11. DQ microstructure. $T_{annealing}$=810°C, $T_{tempering}$=460°C.

UTS=1200 MPa

Now the *UTS*=1200 MPa level is considered. Figure V.8 indicates that the *HE* ratio varies from 25% to 93,5 % depending on the annealing and tempering temperatures.

The 790°C-annealed microstructure in the as-quenched state provides a lowest level of the *HE* ratio (1200 MPa is not attainable when quenching from 760°C is used). This microstructure is composed of fresh martensite with 14.5% of ferrite phase (Figure V.12).

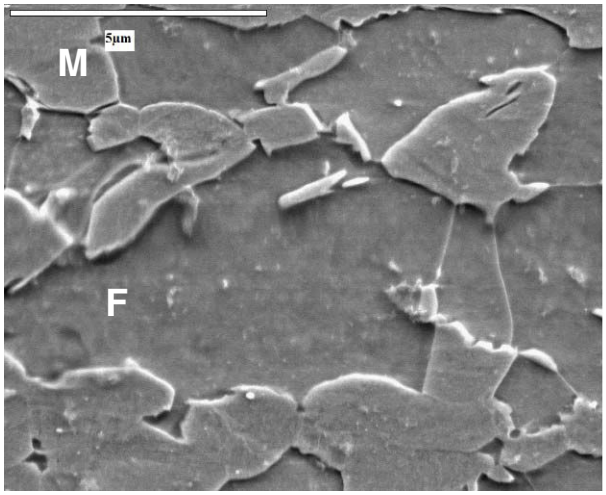

Figure V.12. DQ microstructure in the as-quenched condition. $T_{annealing}$=790°C

In order to improve the *HE* ratio a higher annealing temperatures should be used. Annealing at 810°C and 840 °C temperatures with tempering at about 380°C increases of *HE* ratio to 90%. The corresponding microstructure consists of tempered martensite (the ferrite content is about 1%) (Figure V.13).

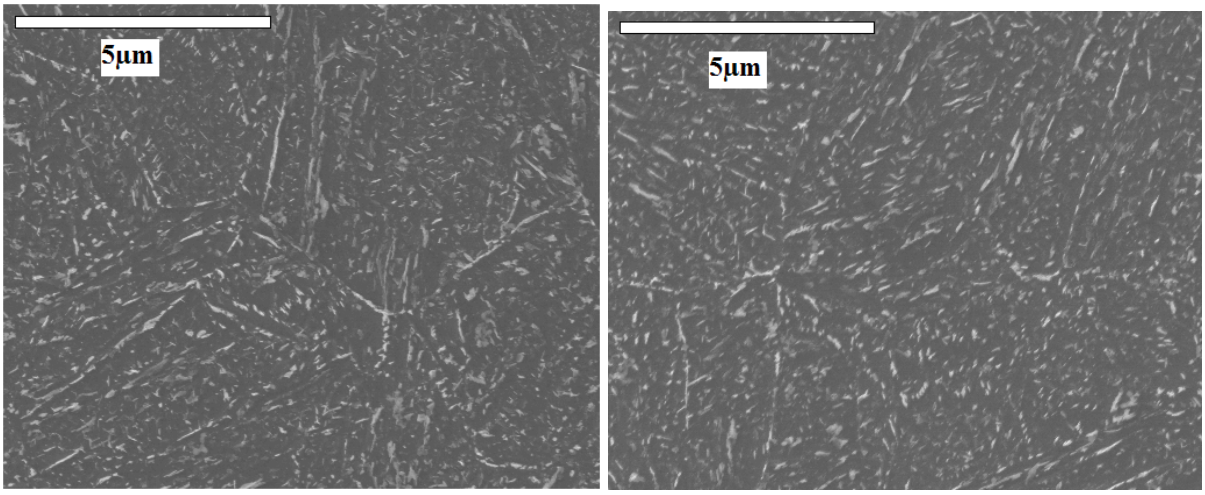

Figure V.13. DQ microstructure. $T_{annealing}$=810°C (left) and 840°C (right), tempering at 380°C.

Thus, in order to obtain a better steel damage resistance (a higher HE value) it is necessary to use high annealing and tempering temperatures. These heat treatment parameters permit to obtain the tempered martensite - ferrite microstructure with low ferrite fraction.

V.5 Summary

Steel formability is of great importance in obtaining the required final properties of different automotive parts. The damage resistance of the steel is defined through the *Hole Expansion (HE)* testing. The DP steel *HE* value evolution with quenching temperature exhibits an S-shape curve. The DP steel formability changes drastically and in an unexpected way with increasing ferrite fraction. Thus, for the studied DP steel an increase in the volume fraction of ductile phase (i.e. ferrite) does not improve the *HE* value. The tempering treatment improves the damage resistance of the studied DP steel: an increase in the *HE* value is observed with increasing tempering temperature.

The experimentally obtained mechanical properties data permits to carry out a direct microstructure design. The *HE* value could be improved using high annealing and tempering heat treatment parameters.

Although a great deal of experimental work has been carried out to characterise the DP steel mechanical behaviour, this is still not fully understood. There is therefore a need for the investigation and comprehension of damage mechanisms. The void distribution in the studied DP steel as a function of the heat treatment parameters and microstructure is investigated in the next chapter in order to detect the operating damage mechanisms. This is the primary aim of the present thesis work and will be addressed in the following chapters.

The simplest model of the crack nuclei formation involves the pile-up of a series of edge dislocations at a grain boundary or another strong obstacle. Crack nucleus is formed, when several of the dislocations at the head of the pile-up coalesce [HONE84]. Martensite island in DP steels could act as an obstacle for dislocation and a void would be formed at the ferrite/martensite interface.

Chapter VI

Damage mechanisms

Ductile fracture involves a high degree of plastic deformation. The basic mechanisms are: void nucleation, void coalescence (also known as micro crack formation), crack propagation, and failure, often resulting in a cup-and-cone shaped failure surface [TEIR88].

VI.1 Fractography analysis of tensile test specimens

Fractographic analysis is used to understand the type and the causes of fracture. The fracture surfaces are examined at a fine scale, using the SEM. This detailed investigation provides a grasp of the failure mode as a function of the microstructural parameters.

The fracture surfaces of the broken tensile test samples were analyzed in the SEM. The samples were studied in the as-quenched state after annealing at 760°C, 790°C and 810°C and after tempering at 230°C, 380°C and 460°C. The full description of these samples is given in Table V.I.

Annealing temperature	760°C	810°C	790°C
Martensite volume fraction, %	62±2	99	86±3
Martensite carbon content measured by PEELS technique, wt %	0.28	0.15	0.17
Analyzed conditions	As-quenched, tempered at 230°C, 380°C and 460°C		As-quenched

Table VI.1. The description of samples for fractographic analysis.

The SEM micrographs of fracture surfaces are represented below for the 760°C and 810°C annealed samples (Figures VI.1 and VI.2, respectively).

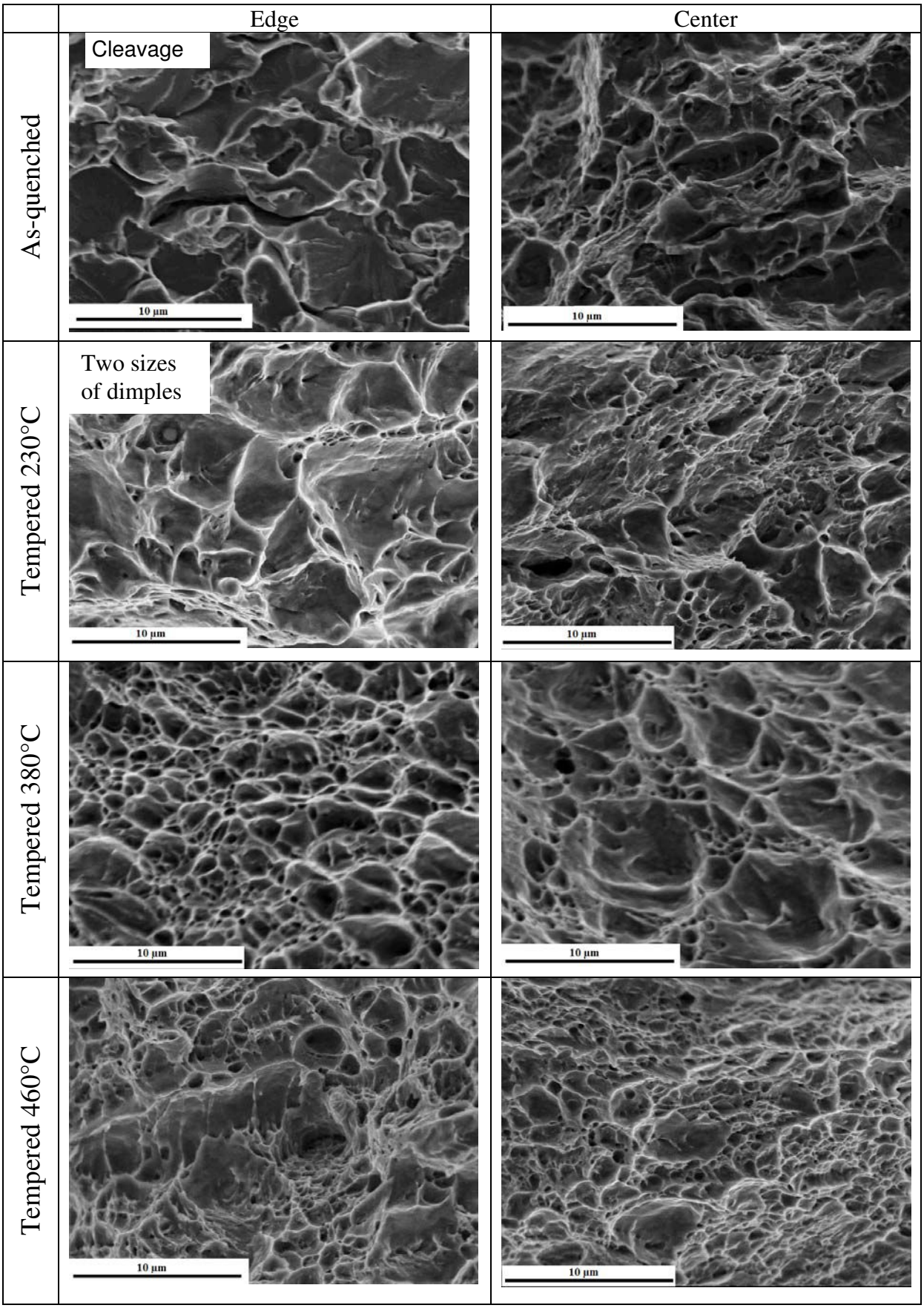

FigureVI.1. Fractography of the 760°C- annealed sample: as-quenched and tempered conditions.

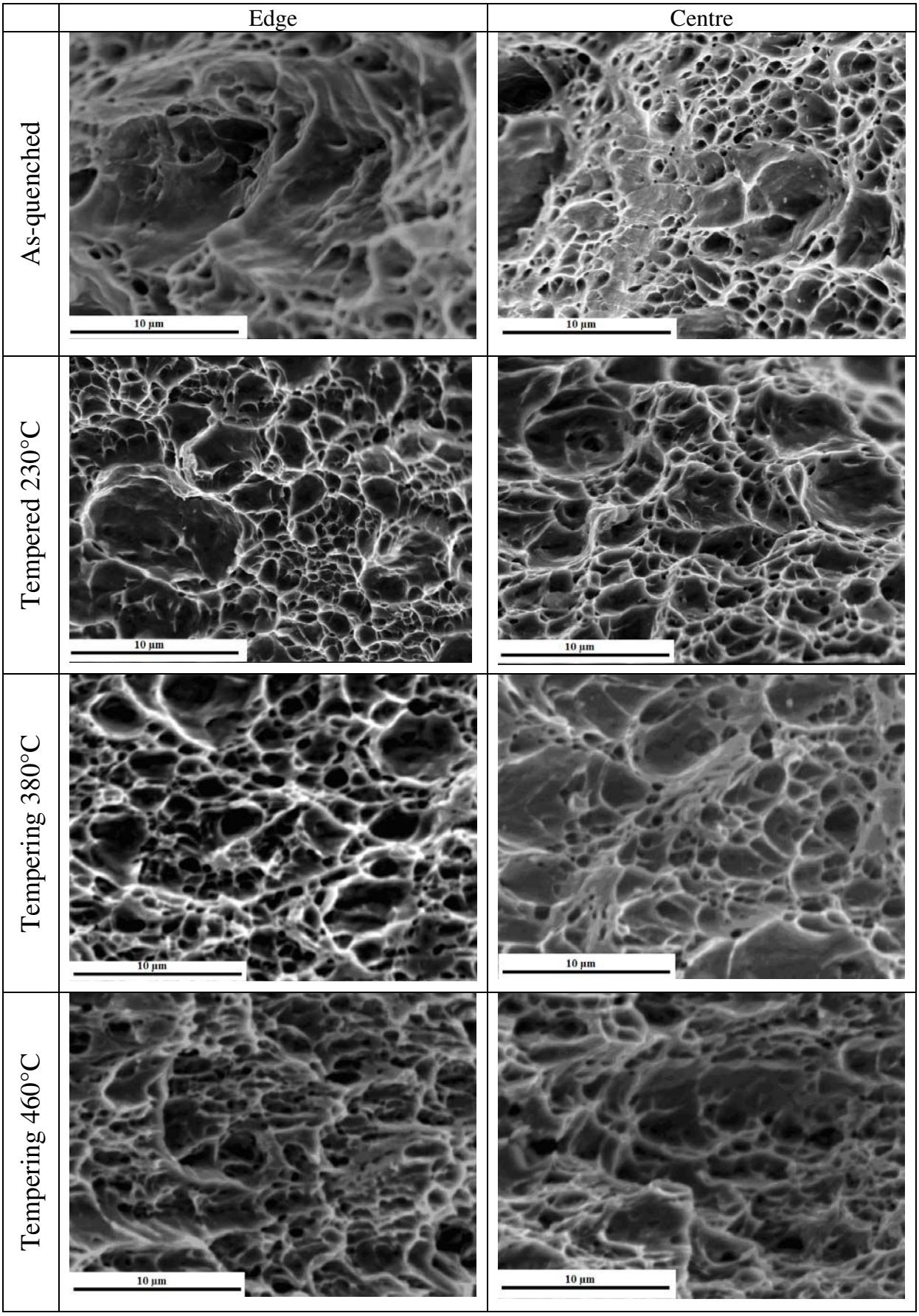

Figure VI.2. Fractography of the 810°C-annealed sample: as-quenched and tempered conditions.

The 760°C-annealed sample in the as-quenched condition shows a brittle mode of fracture (FigureVI.1). A *cleavage* surface is observed for this sample: the fracture surface is made up of planar facets, corresponding to the cleavage planes of different grains. The material splits along definite crystallographic structural planes (These are [100] planes in the case of BCC iron). Smooth repeating surfaces are seen in the SEM. Also the facets show steps, arranged in so-called "river patterns". *The nucleation of fracture occurs by the brittle cleavage of martensite. The low intrinsic fracture toughness of the martensite leads to the cleavage fracture* [TEIR88].

Tempering of this microstructure eliminates cleavage fracture (FigureVI.1). This effect is probably due to martensite softening during tempering. The fracture surfaces of tempered samples show ductile failure. The fracture surface is composed of dimples.

The fracture surfaces of the 230°C - tempered sample show two sizes of dimples (FigureVI.1): the large dimples are surrounded by the small ones. The small dimples probably nucleate at carbides, formed during the tempering.

The 810°C-annealed sample shows ductile fracture behaviour (FigureVI.2): a dimpled fracture surface is detected in all specimens. Two sizes of dimples are identified in the tempered condition. The small dimples probably form at tempered carbides.

Summarizing the above observations, it can be concluded that the fracture process in DP steel is strongly influenced by the phase volume fraction and as a consequence by the carbon content of the martensite phase: martensite with a higher carbon content shows a brittle behavior. Increasing the martensite volume fraction, at a constant carbon level in the steel, leads to the decrease of carbon concentration in the martensite and thus more ductile martensite is formed. Also, these results illustrate that the fracture mechanism changes as a result of the tempering treatment.

The following study on void formation in these samples will provide a further understanding of the phenomena involved in damage behaviour.

VI.2 Formation of microstructural damage during tensile testing

The aim of this study is to establish the relationship between the steel microstructure and damage mechanisms.

Metallographic analysis of tensile test samples after fracture was carried out in the TD×RD plane according to Figure VI.3 using the FEG-SEM. The analysis was carried out for the as-quenched and tempered conditions. The samples were examined after nital or picral etching depending on the microstructure.

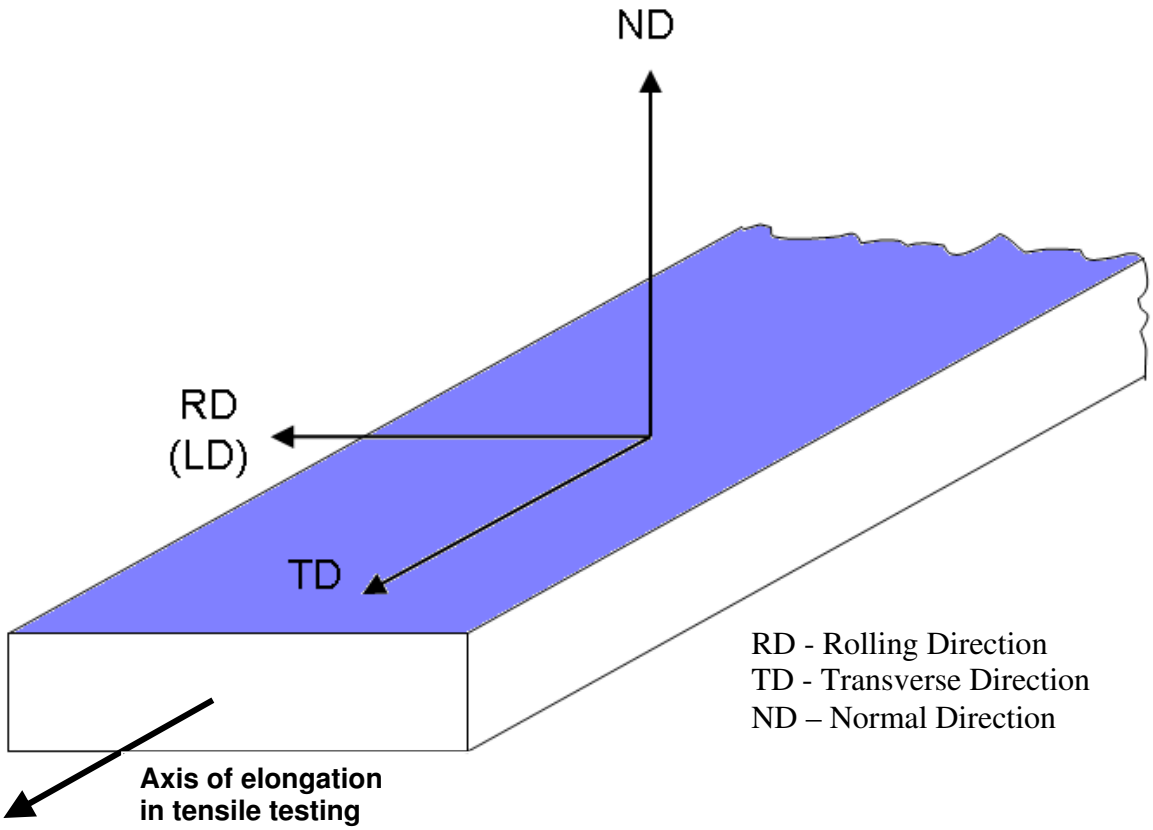

FigureVI.3. Diagram showing the plane of observation for the study of void formation in tensile test specimens.

VI.2.1 Study of the as-quenched samples

Figure VI.4 shows the damage in the microstructure for samples, annealed at different temperatures.

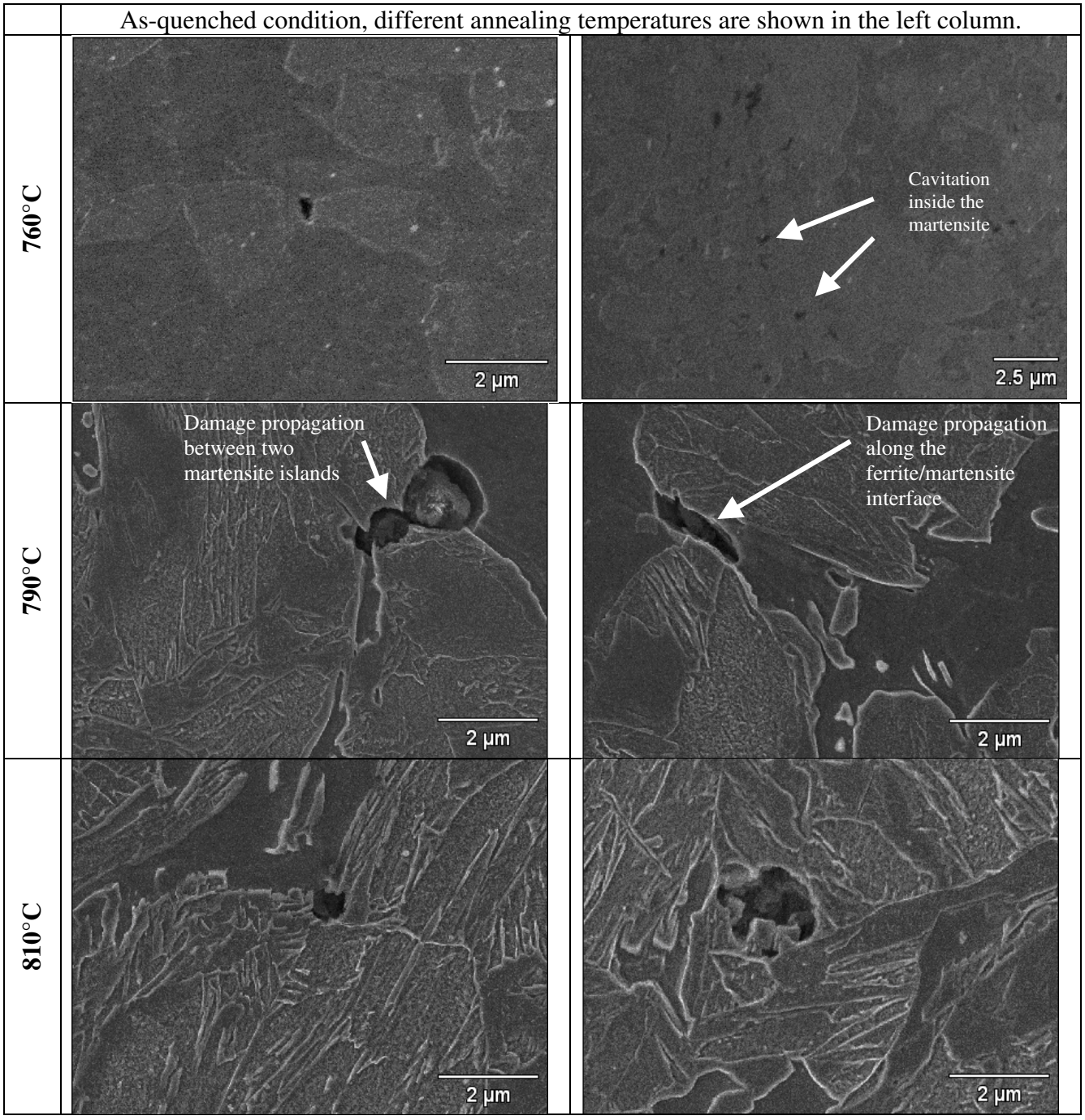

Figure VI.4. The void distribution in the as-quenched material.

Void nucleation in DP steels has been associated with the martensite phase: it is either a consequence of decohesion at the ferrite/martensite interface or brittle fracture of the martensite [STEI88].

In the 810°C-annealed sample with small ferrite fraction voids are found at the ferrite/martensite interface (Figure VI.4).

Cracks are also found in this sample between closely spaced martensite islands, i.e. at the martensite/martensite interface (prior austenite) (Figure VI.5).

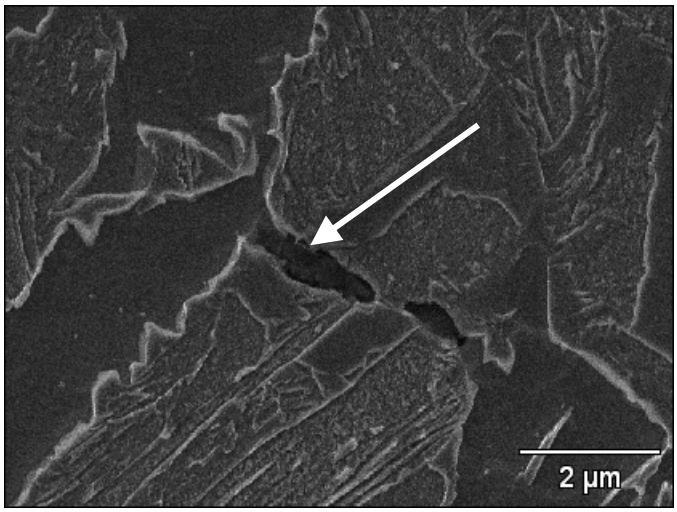

Figure VI.5. Crack in the 810°C-annealed sample in the as-quenched condition.

In the 790°C-annealed sample, voids nucleate at the ferrite/martensite interface or between closely situated martensite islands (Figure VI.4).

In the 760°C-annealed sample, voids are found at the ferrite/martensite interface, between the very closely localized martensite islands (Figure VI.6) and also the internal structure of the martensite is damaged (Figure VI.4).

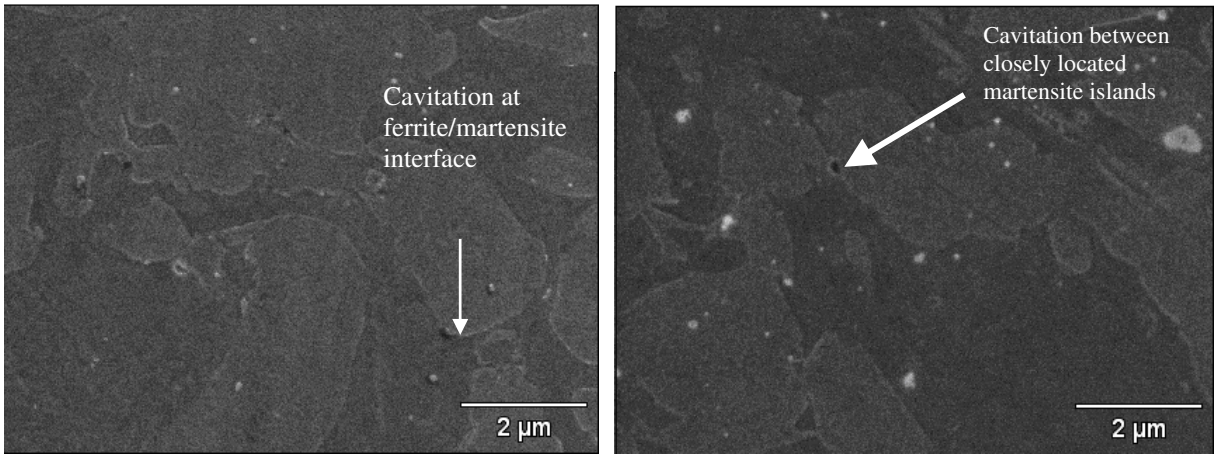

Figure VI.6. Void location in the 760°C-annealed sample in the as-quenched state.

VI.2.2 Study of the tempered samples

Tempering introduces changes in the DP steel microstructure which could influence the damage behaviour of the steel. Figure VI.7 shows the voids distribution in tempered steel specimens for 760°C and 810°C annealing temperatures.

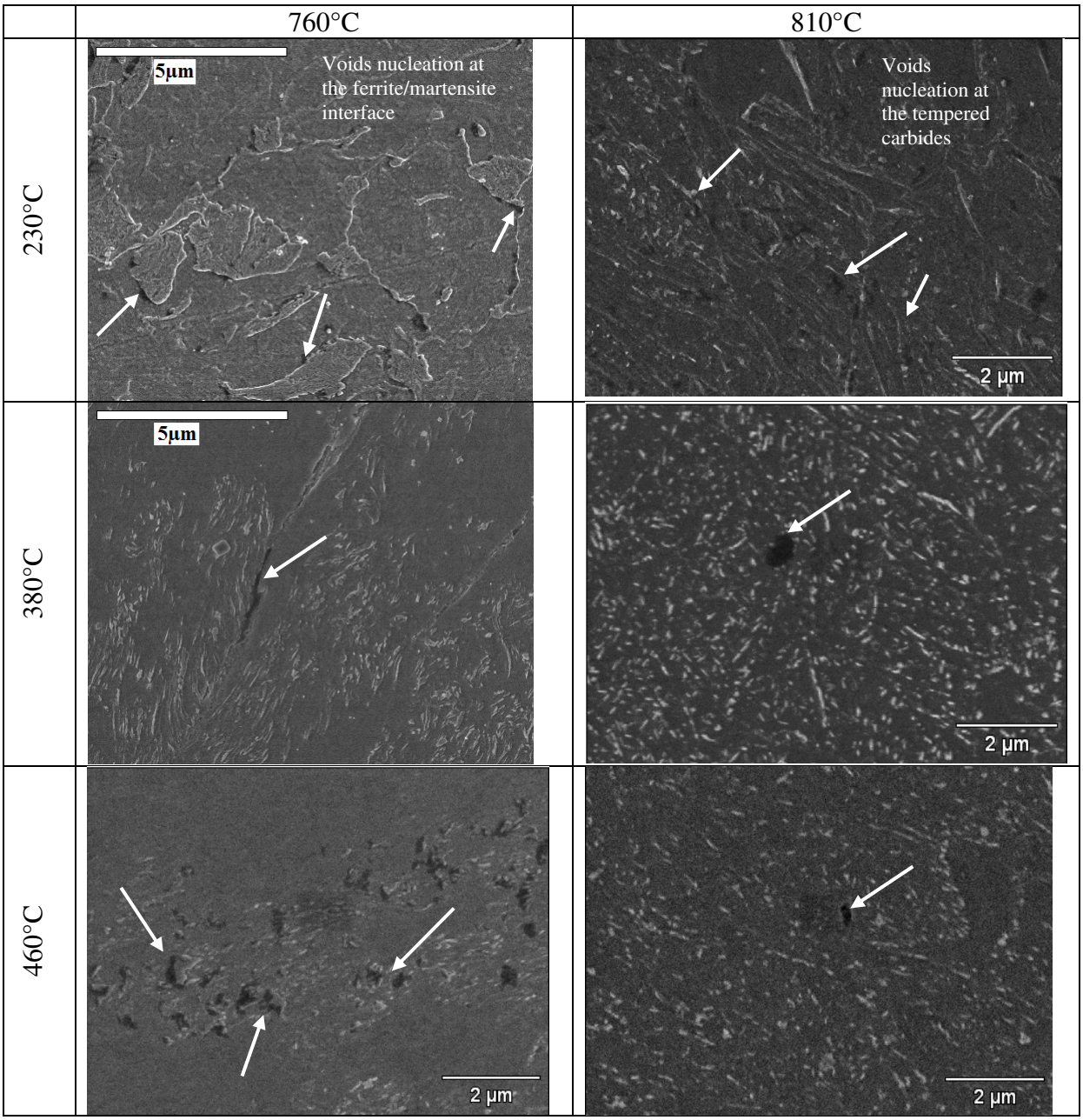

Figure VI.7. The voids distribution in tempered steel specimens (760°C and 810°C – annealing temperatures).

Tempering at 230°C.

The low temperature-annealed sample (760°C) shows cavities at the ferrite/martensite interface (Figure VI.7)..

In the high temperature annealed sample (at 810°C) voids develop at the *tempered carbides* in the martensite (Figure VI.7). Multiple damage sites are present in the martensite phase of this sample.

Tempering at 380°C.

After tempering at 380°C the sample with a higher ferrite percent (annealed at 760°C) shows void formation at the ferrite/martensite interface (Figure VI.7). Some damage inside the martensite is also seen: voids nucleate at the tempered carbides inside the martensite (Figure VI.8).

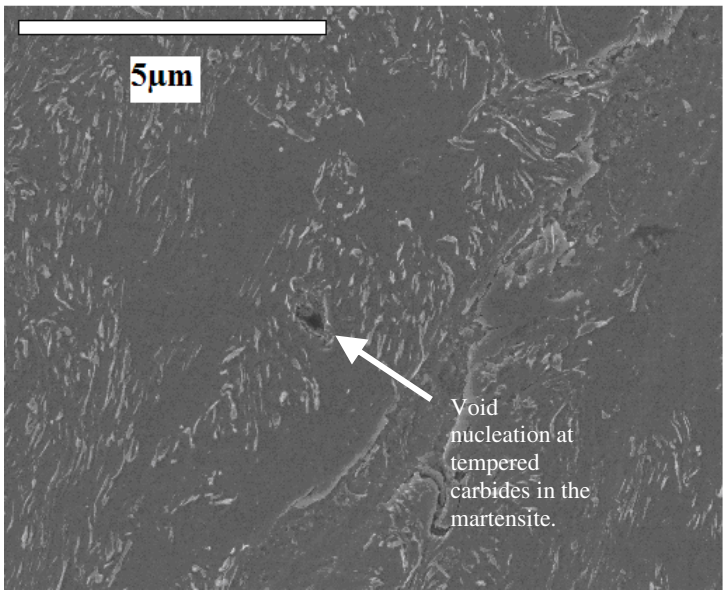

Figure VI.8. Void nucleation in 760°C-sample tempered at 380°C.

For low ferrite fraction sample (annealing at 810°C) voids nucleate at tempered carbides inside the martensite phase (Figure VI.7).

Tempering at 460°C.

After tempering at 460°C voids in the 760°C-annealed sample nucleate at tempered carbides. Multiple nucleation sites are present in the martensite phase (Figure VI.7).

In the 810°C - annealed sample void formation occurs at the tempered carbides inside the martensite and in some cases at tempered carbides precipitated on ferrite/martensite interface (Figure VI.9).

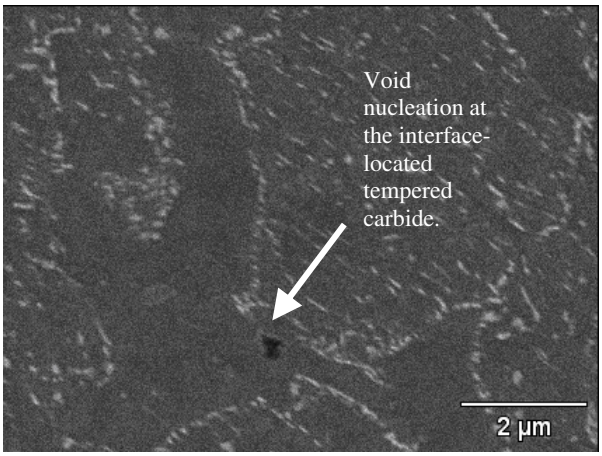

Figure VI.9. Void distribution in the 810°C-annealed sample tempered at 460°C.

The experimental observations of the void distribution can be summarized as-follows:

- The void nucleation in the studied DP steel is associated with the martensite phase or with carbides in the tempered martensite. The voids at the ferrite/martensite interface and at carbides in the tempered martensite are observed.

- Obviously, a change in the void nucleation mechanism occurs during tempering: the ferrite/martensite interface decohesion is replaced by void formation at the carbides.

VI.3 Damage behaviour evolution with tempering

As can be seen, damage behaviour of the DP steel changes with tempering. The difference in the kinetics of void nucleation in the as-quenched and tempered conditions has been confirmed by in situ tensile testing. The number of cavities per cubic millimeter, N has been measured as a function of the plastic strain using an in situ tensile test during X-ray tomography experiments by the methodology presented in details in [MAIR08] for a dual-phase steel containing 86% of martensite in the as-quenched conditions and after a tempering at 380°C for 4 minutes, as shown in Figure VI.10. These trends can be described by an empirical expression of the form [MAIR08]:

$$N = A\frac{\varepsilon_{eq}}{\varepsilon_N}.\exp\left(\frac{\varepsilon_{eq}}{\varepsilon_N}\right)$$

where A is a constant and ε_N is a critical value of the strain for which nucleation starts to occur in the material. It is possible to capture the experimental evolution with:

- A=3700 $mm^{-3,}$

- ε_N =0.08 for the as-quenched condition,

- ε_N = 0.17 for the tempered condition.

This analysis shows that the tempering is very efficient to slow down the nucleation of damage in the steel and it increases the number of cavities at fracture.

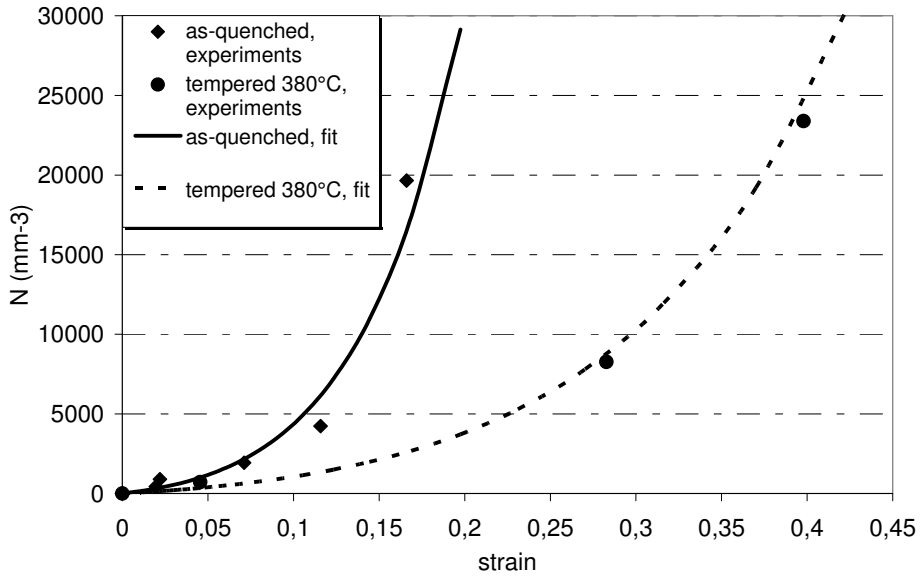

Figure VI.10. Number of cavities per cubic millimeter, measured by X-ray tomography, as a function of the plastic strain by the methodology presented in details in [MAIR08] for a dual-phase steel containing 86% of martensite in the as-quenched conditions and after a tempering at 380°C for 4 minutes.

VI.4 Summary

The DP steel damage mechanisms are determined in this chapter. Fractographic analysis shows a strong dependence of the damage mode on the steel microstructure: the brittle cleavage surface is replaced by the ductile dimple surface when tempered treatment is applied. Also, an increase in the martensite volume fraction leads to the change in the fracture mechanism: the ductile dimple surface is observed for the high annealed sample while the low annealed sample has a brittle fracture surfaces.

Cavities form at the local strain incompatibilities such as ferrite/martensite interfaces and tempered carbide/martensite matrix interfaces.

The tempering treatment reduces plastic incompatibilities between the ferrite and martensite phases, which leads to a more uniform stress partitioning and less solicitation of the ferrite/martensite interface. As a result, a probability of void nucleation at the ferrite/martensite interface is decreased. However, in tempered microstructures a new tempered carbide/martensite matrix interface is formed which will act as a site for void nucleation. These two damage mechanisms are taken into account in the damage modeling which is carried out in the next chapter.

Chapter VII

Modeling of DP steel damage behaviour

The change in DP steel damage mechanism with tempering temperature has been described in chapter VI. A simple model for DP steel damage behaviour based on a mean field approach has been proposed recently by [LAND]. This model is explained in section VII.1. The physical aspects of the ferrite/martensite interface decohesion phenomena are reasonably well described. However, the experimentally observed void formation at the carbide particles in tempered martensite (see chapter VI) is not taken into account.

A quantitative description of interfacial decohesion between small (< 1 μm) cementite particles in a martensite matrix requires Finite Element Modeling (FEM) to correctly calculate the local triaxiality and the local stress at the particle/matrix interface. This is beyond the scope of this project. Instead, a simple mean field analysis is proposed which reproduces the correct experimentally observed trends. This extension to the existing model makes it possible to consider the physical aspects of tempered martensite damage behaviour, i.e. void formation at tempered carbides.

VII.1 Application of the existing model

A model for predicting the DP steel ductility based on the ferrite/martensite interface decohesion has been developed [LAND].

In untempered DP steels the dominant damage mechanism is interface decohesion at ferrite/martensite boundaries. This occurs when the local stress σ_c (at the interface) exceeds some critical decohesion stress σ_d. The local stresses at the interface can be related to the macroscopic applied stress by the equation [ARGO75, LAND]:

$$\sigma_C = \sigma_{eq}(1 + T_{loc}) \tag{VII.1}$$

Where σ_{eq} is the Von Mises equivalent stress and T_{loc} is the local triaxiality at the interface [LAND]. The latter can be approximately related to the macroscopic triaxiality T (§I.7.1) by the relation:

$$T_{loc} = T\frac{\sigma_{eq}}{\sigma_{eq} - \sigma_i} \tag{VII.2}$$

Where σ_i represents the internal stresses formed due to the strong deformation incompatibilities between the two phases [ALLA08] i.e. the kinematic hardening component. It can be seen that the local triaxiality T_{loc} increases with increasing σ_i and so the probability of interface decohesion also rises.

In fact equation VII.2 very likely underestimates the value of T_{loc} close to the interface. This has been confirmed in some recent work [ALLAIN], using an FEM approach. In this work three different geometrical configurations of elastic particles (simulating martensite) in an elastic-perfectly plastic matrix (simulating ferrite) strained in uniaxial tension to 22% elongation were simulated (Table VII.1).

Configuration	Volume fraction of martensite	Martensite island shape	Shape factor	T_{loc} from mean field (eq VII.2)
1	0.8 %	Spherical	1	0.34
2	5 %	Spherical	1	0.40
3	5 %	Ellipsoid	1.5	0.41

Table VII.1. Geometrical configuration for FEM simulations.

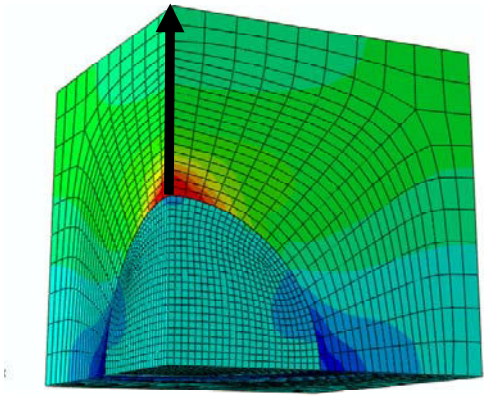

Figure VII.1a. FEM simulation of T_{loc} variation around a spherical martensite island in ferrite (courtesy of S. Allain).

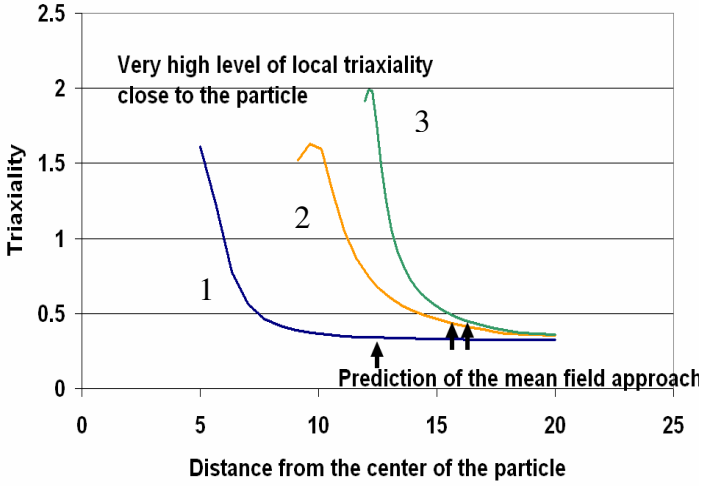

Figure VII.1b. Variation of T_{loc} along the indicated directrix for three different martensite distributions. The values given by mean field calculations are shown arrowed (courtesy of S. Allain).

Evidently the local triaxiality is much higher near the particle interface than the mean field approach suggests (Figure VII.1), nevertheless the trends are well respected so it seems reasonable to apply eq. VII.2 in this simplified approach.

The next problem is to calculate the back stress σ_i at the ferrite/martensite interface. Again there is no simple method to do this correctly. One phenomenological approach which has been used successfully involves a "law of mixtures" type description [ALLA08]:

$$\sigma_i = f_m(1-f_m)\left|\sigma_m - \sigma_\alpha\right| \qquad \text{(VII.3)}$$

Where σ_m and σ_a are the flow stresses of martensite and ferrite respectively and f_m is the martensite volume fraction. Note that equation VII.3 has not yet proved, however, from a pragmatic point of view, it reproduces well the observed experimental behaviour in ferrite/martensite steels. Now the problem is to measure the ferrite and martensite flow stresses. Again we will make a simplifying assumption.

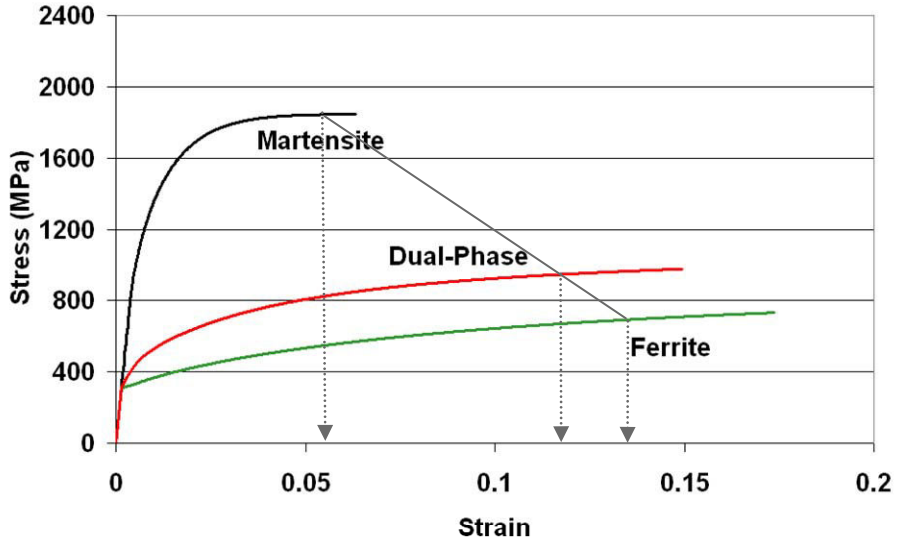

Figure VII.2. FEM calculation of the stress and strain partition in a DP steel with 22% martensite volume fraction and Cm = 0.27% wt (courtesy of S. Allain).

Figure VII.2 shows the result of a FEM simulation to calculate the stress and strain partitioning during uniaxial tension in a DP steel [ZHON92, JACQ07, CHOI09] with 22% martensite and C_m = 0.27% wt. Now damage effects are not expected to become significant until near the end of uniform elongation. At this point the flow stress in martensite is nearly constant and that of ferrite is only slowly increasing. It is therefore possible, under these particular conditions, to substitute the Vickers hardness values for the flow stress.

Assuming that $\sigma=3H_V$, equation VII.3 can thus be rewritten as:

$$\sigma_i = 3 \cdot f_m (1 - f_m) \left| Hvm - Hv\alpha \right| \tag{VII.4}$$

Where Hvm and $Hv\alpha$ are the martensite and ferrite hardnesses respectively.

In a similar manner, the value of σ_{eq} is determined through the martensite and ferrite hardnesses as follows [LAND]:

$$\sigma_{eq} = 3 \cdot \left[(1 - f_m) Hv\alpha + f_m Hvm \right] \tag{VII.5}$$

The as-quenched martensite hardness is a function of the martensite carbon content (Figure VII.3) and is determined as follows [LAND]:

$$Hvm_{AQ} = 150 + (940 - 150)(1 - \exp(-2.7 C_m)) \tag{VII.6}$$

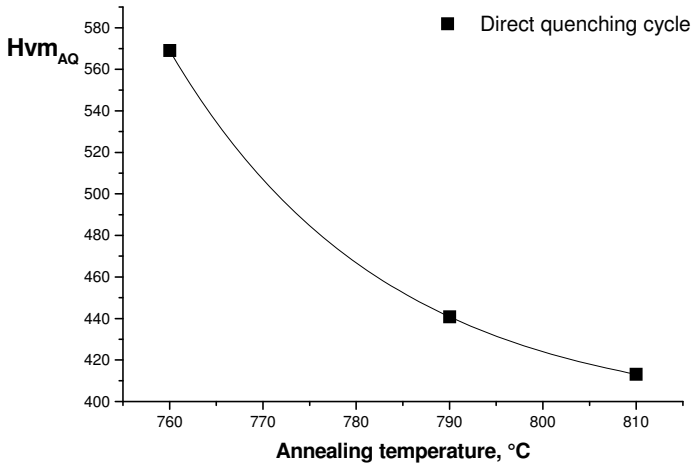

Figure VII.3. Calculated as-quenched martensite hardness as a function of annealing temperature.

During tempering the martensite hardness changes depending on the tempering temperature, T and tempering time, t [SPEI69]. This can be described by the following fitted equation [LAND]:

$$Hvm_T = \frac{Hvm_{AQ} + (100 + 75C_m)}{1 + \left(A \exp\left(-\frac{Q}{RT} \right) \cdot t^n \right)} \qquad \text{(VII.7)}$$

Where A=300s^{-1}, n=1/3, Q is the activation energy for precipitation of cementite, Q=44000J/mol, R is the gas constant, T is the absolute temperature and C_m is the martensite carbon content. The calculated variation of Hvm_T with tempering temperature for the studied DP steel is shown in Figure VII.4. Here C_m was taken from the experimental PEELS data.

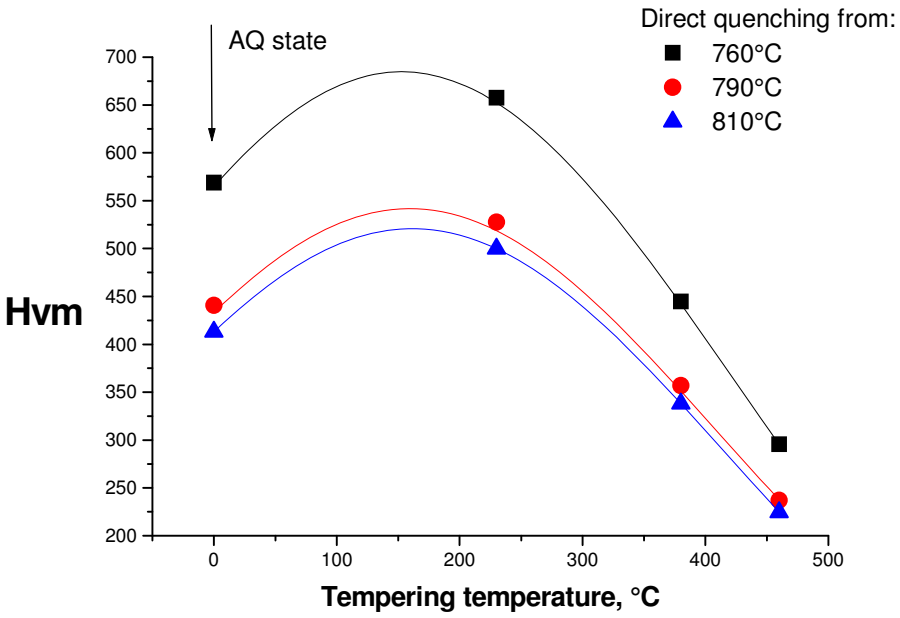

Figure VII.4. Calculated variation of martensite hardness Hvm_T as a function of tempering temperature (240 sec).

Tempering of martensite at temperatures below 150°C results in a hardness increase. It is assumed that the hardening effects of carbide precipitation exceed the loss in solid solution strengthening in this region. At higher tempering temperatures the martensite hardness begins to decrease as the solid solution component is reduced and softening from recovery increases.

Now taking the hardness value of ferrite to be constant (150 H_V) and substituting the values for Hvm_T in equations (VII.4) and (VII.5) we calculate σ_i and σ_{eq} for the three different experimental martensite fractions f_m (62%, 85.5% and 99%). Substituting these data in equation VII.2 and taking T = 0.33 for a uniaxial tension test gives T_{loc} and hence, using equation VII.1, the local interface stress σ_c. This value is plotted in Figure VII.5 as a function of tempering temperature for the three different martensite fractions.

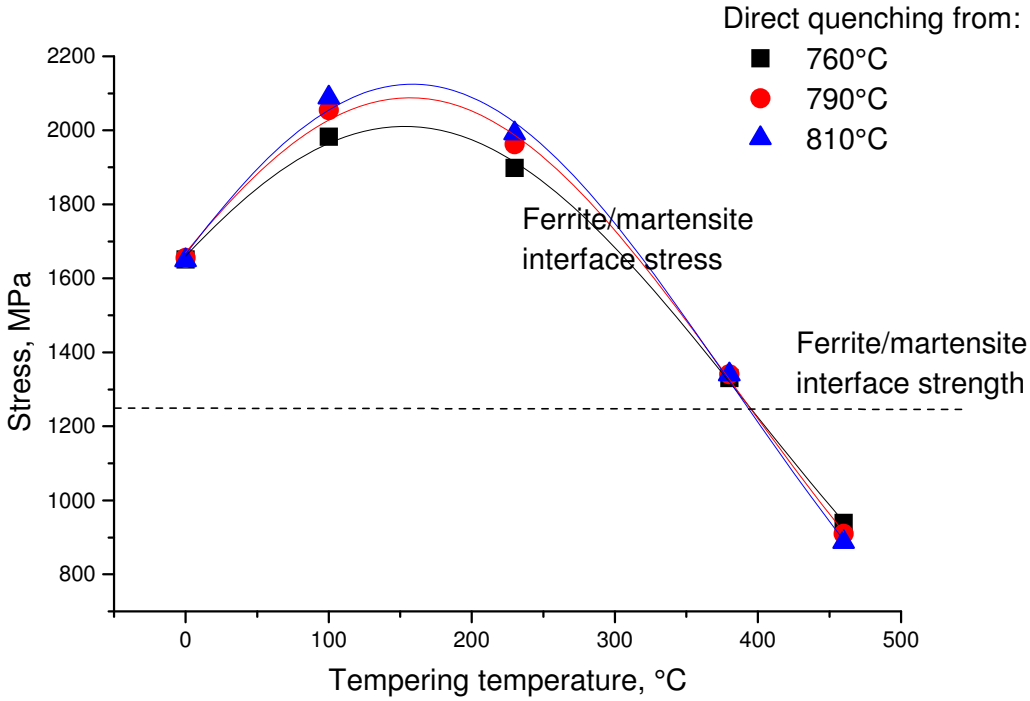

Figure VII.5. Calculated variation in the interface stress σ_c as a function of tempering temperature (tempering time = 240 sec).

Superimposed on Figure VII.5 is the ferrite/martensite interface strength σ_d which is approximately equal to 1230 MPa [TOMO81]. The model thus predicts that higher intercritical annealing temperatures result in higher interface stresses, in spite of the fact the difference in the hardness of the two phases decreases as the martensite fraction increases. At low tempering temperatures (<300°C) the interface stress actually *increases*, compared to the as-quenched state. Thus the material becomes more susceptible to damage at the ferrite/martensite interface. It is only at tempering temperatures above ~300°C that significant reductions in the interface stress (again compared to the as-quenched state) are achieved. The model predicts that damage by ferrite/martensite interface decohesion should be suppressed at tempering temperatures above 400°C.

VII.2 Extension to include internal martensite damage

According to the experimental observations, voids form at the tempered carbides in the martensite (Figure VI.7). For the 760°C-annealed sample decohesion at the ferrite/martensite interface is observed at 230°C tempering temperature. For 380°C tempering temperature and higher this damage mechanism is suppressed and instead we observe interior martensite damage at carbide particles. For the 810°C annealed sample the interior damage of martensite (i.e. void formation at tempered carbides) is observed at lower tempering temperatures (230°C) and ferrite/martensite decohesion is suppressed, even though the ferrite/martensite interface stress σ_c is higher.

It is difficult to model damage behaviour in tempered martensite as we do not have access to most of the important parameters such as the volume fraction of carbides, their size and shape distribution, the evolution of the matrix carbon concentration and the local stress triaxiality. Accordingly it is of interest to study first the simpler case of fresh martensite and to consider the critical nucleation strain required for the development of interface decohesion at an arbitrary defect as a function of the martensite carbon content.

We start by following the approach by Riedel [RIED93] who considered the stresses exerted by a plastically deforming matrix on a brittle inclusion:

$$1.4\sigma_{eq} + 0.5\sigma_h = \sigma_C \qquad \text{VII.8}$$

here σ_c is the critical stress for decohesion at the inclusion, σ_{eq} is the applied equivalent stress and σ_h is the hydrostatic stress. Now σ_{eq} can be replaced by an empirical Voce equation whose coefficients, *a, b,* and *c* depend only on the martensite chemical composition [ALLAIN]:

$$\sigma(\varepsilon) = a + b(1 - \exp(-c\varepsilon)) \qquad \text{VII.9}$$

The fitting parameters used were obtained using data from a wide variety of compositions including the steel studied in this work:

$$a = 682 + 33Mn + 81Si + 58(Cr + Mo)$$
$$b = 2722 \times C^{0.78}$$
$$c = 179 + \frac{7.52 \times 10^{-4}}{C^{4.61}}$$

The precision of the Voce model for fresh martensite is illustrated by Figure VII.6. Here the solid lines represent the model output and the dotted lines are the experimental flow curves.

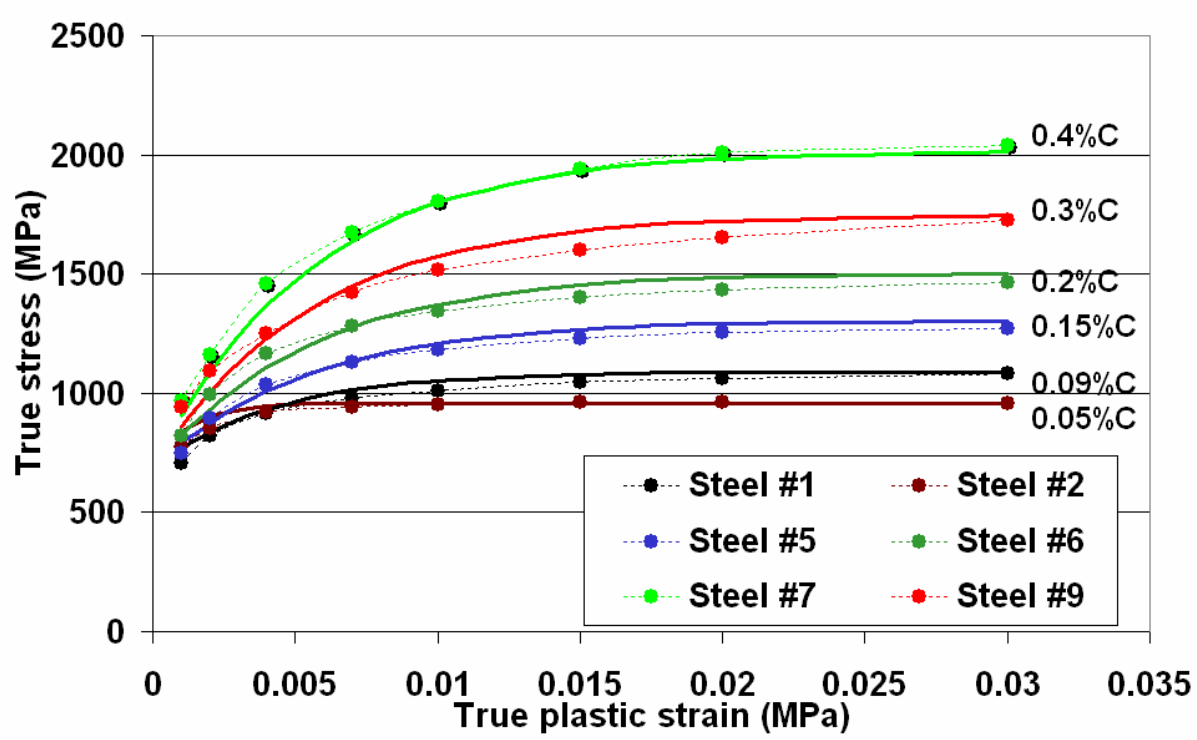

Figure VII.6. Precision of the Voce model for fresh martensite for different initial carbon concentrations (courtesy of S. Allain).

Now equation VII.8 can be rewritten as:

$$c1.4(a+b(1-\exp(-c\varepsilon))+0.5T\sigma_{eq}\left(\frac{\sigma_{eq}}{\sigma_{eq}-C(\sigma_{eq}-\sigma_y)}\right)=\sigma_C \qquad \text{VII.10}$$

Here we have used the relations:

$$\sigma_h = T_{loc}\cdot\sigma_{eq}$$

$$T_{loc} = T\frac{\sigma_{eq}}{\sigma_{eq}-\sigma_i}$$

and the simplifying assumption of [IBRA75] which presumes saturation of the internal stress:

$$\frac{\sigma_i}{\sigma_{eq}-\sigma_y} = C \qquad \text{VII.11}$$

Where σ_y is the martensite yield stress, C is a constant usually taken to be of the order of 0.5. Now, if we define a value for the decohesion stress σ_c, it is possible to solve equation VII.10 to find the critical strain ε_{nuc} required to nucleate decohesion. We do not know the precise value for σ_c in fresh martensite, so we have considered three values, 1000 MPa, 1500MPa and 1700 MPa (note that higher values do not give any solution). In Figure VII.7 we plot the critical nucleation strain ε_{nuc} as a function of the fresh martensite carbon content for two different values of constant *C*, 0.5 and 1.0.

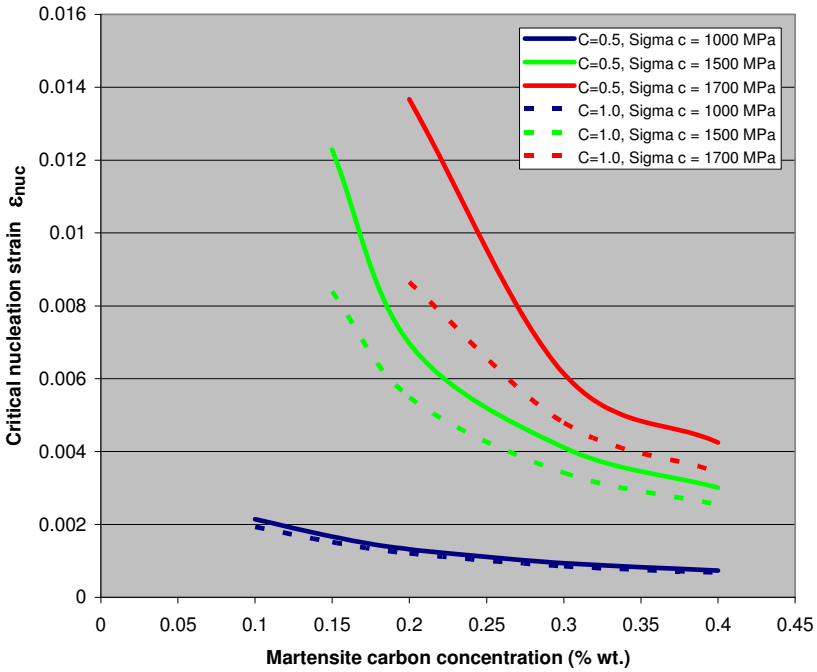

Figure VII.7. The variation in the critical nucleation strain ε_{nuc} as a function of the fresh martensite carbon content.

The first observation is that the critical strain is always small, less than 2% in the case above. This is not an unreasonable value for fresh martensite. The model predicts that ε_{nuc} decreases as the martensite carbon concentration increases, so higher carbon martensites are more prone to show decohesion at inclusions. Increasing the kinematic component by increasing the constant C tends to increase the sensitivity to damage. It is interesting to compare this behaviour with the experimentally observed damage occurring in tempered martensite. Figure VII.8 shows void nucleation in samples annealed at 760°C and 810°C (initial fresh martensite carbon concentrations 0.28% wt. and 0.15% wt. respectively). After tempering at 230°C the damage mechanism in the 760°C annealed sample is ferrite/martensite interface decohesion, while the damage mechanism in the 810°C annealed sample is void formation at tempered carbides. This is exactly the opposite of the behaviour expected for fresh martensite.

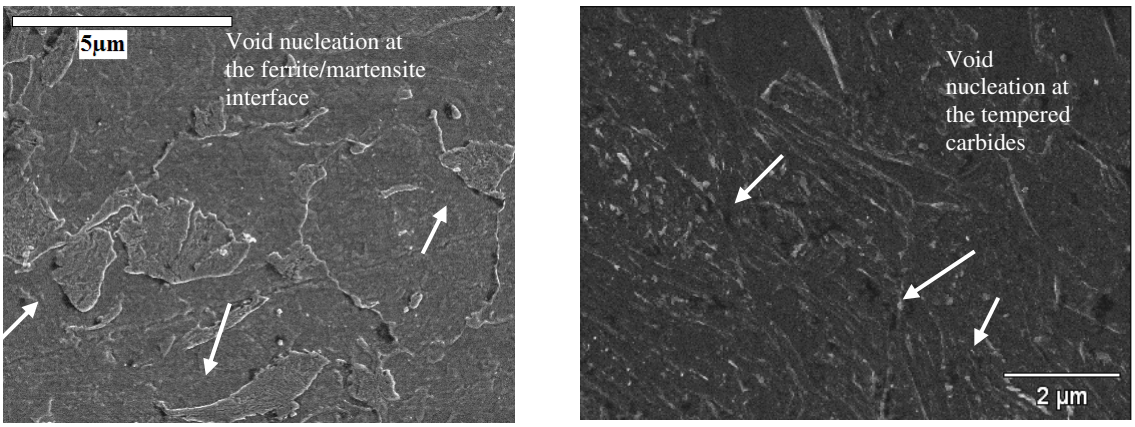

Annealing at 760°C Annealing at 810°C

Figure VII.8. The void distribution in 230°C tempered samples.

Void formation at tempered carbides in the 760°C annealed sample is observed experimentally after tempering at 380°C (Figure VII.9). Again this runs contrary to the model for fresh martensite as tempering at higher temperatures reduces the martensite carbon content and thus should increase the critical nucleation strain.

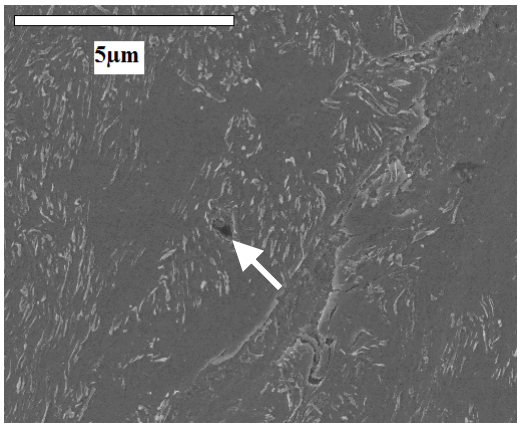

Figure VII.9. Void nucleation at carbide in tempered martensite (760°C annealed sample after tempering at 380°C).

Of course the problem is that we are dealing with a complex three phase system, where there are multiple competing hardening/damage processes and it is probably not possible to understand the ensemble behaviour by studying one or two components in isolation.

Though, this model can be successfully applied to explain experimental evolution of *HE* value. For the as-quenched state, a monotonic decrease of the *HE* ratio with ferrite fraction was observed (§5.1). Now considering figure VII.5 we note that for the as-quenched state the local stress at the ferrite/martensite interface is independent of the annealing temperature. That is the ferrite/martensite interface susceptibility for decohesion does not depend on the annealing temperature. We can deduce that during *HE* testing of the as-quenched DP steels the acting damage mechanism is the martensite fracture. Considering Figure VII.7, the critical nucleation strain ε_{nuc} required for the interface decohesion at an arbitrary defect decreases as the carbon concentration of the fresh martensite increases. So high carbon martensite (i.e. in DP steel annealed at a lower temperature) are more susceptible for fracture, which explains its lower *HE* values. Tempering treatment improves *HE* values of DP steel. During tempering treatment, the martensite carbon content decreases due to carbide precipitations. So critical nucleation strain ε_{nuc} will increases with increasing tempering temperature. That is internal martensite damage decreases with increasing tempering temperature, which has a beneficial effect on the *HE* values.

An attempt to describe the void nucleation at the tempered carbides in the martensite phase has been made using the same principles as the ferrite/martensite decohesion model. However, equation VII.4 for the stress developed at the carbide/martensite interface cannot be used, because of very low carbide fraction (maximum equilibrium fraction for cementite is 0.04). So we use the same approximation as equation VII.11 in order to express σ_i in terms of of σ_{eq}, σ_y and a constant of proportionality, C. The expression VII.5 for σ_{eq} is simplified as the carbide fraction is negligible compared to the martensite fraction. Thus we write:

$$\sigma_{eq} = 3 \cdot Hvm_T \qquad \text{(VII.9)}$$

There remains the problem that we do not know the variation of the martensite yield stress σ_y with tempering conditions. We thus use interpolated values from experimentally determined data for 100% martensitic steels with compositions and tempering treatments close to our experimental conditions [COBO09]. Now, assuming that C=0.5 and substituting in eq. VII.8 and eq. VII.2 , the local stress at the carbide/martensite interface can be calculated using eq. VII.1 The results of this calculation are shown in Figure VII.10.

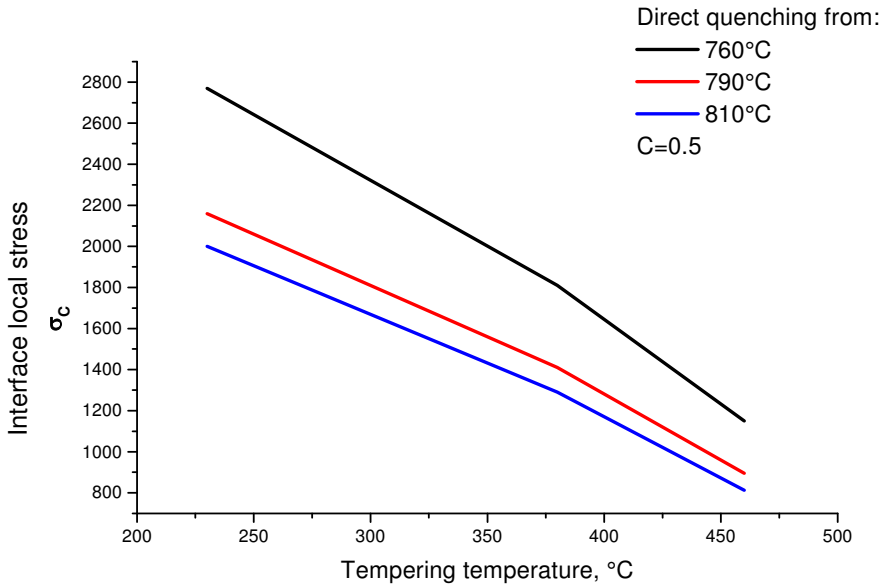

Figure VII.10. Calculated variation in the carbide/martensite interface stress as a function of tempering temperature for three different samples.

Figure VII.6 shows that the carbide/martensite interface stress decreases with increasing tempering temperature for three samples. That is, the probability to form voids at tempered carbides decreases with increasing tempering temperature. This trend contradicts the experimental observations in Chapter VI.

A systematic variation of the martensite yield strength and the value of C did not have any significant effect on this result. It seems that the problem lies with the over-simplified expression for σ_{eq}. Ideally this should be replaced with a Voce type empirical equation fitted to tempered martensite. Further experimental data on fully martensitic steels with the same initial carbon content as the martensite in the studied DP steel samples is therefore required.

We know that the strain incompatibility between carbides and the martensite matrix generates an internal stress, σ_i in a similar way to that occurring at the ferrite/martensite interfaces. Considering eq. VII.1, if we fix a critical decohesion stress[†] and σ_{eq} is known then we can determine the required value of local triaxiality T_{loc}. Thus σ_i can be determined using equation VII.2. Now, we calculate the ratio σ_i / σ_{eq}, It can be seen that, if the σ_i / σ_{eq} ratio increases, then the local triaxiality, T_{loc} at the carbide/martensite interface must increase. Figure VII.11 shows the evolution of this ratio with tempering temperature for three DP samples.

[†] A value of σ_c = 2700 MPa was chosen

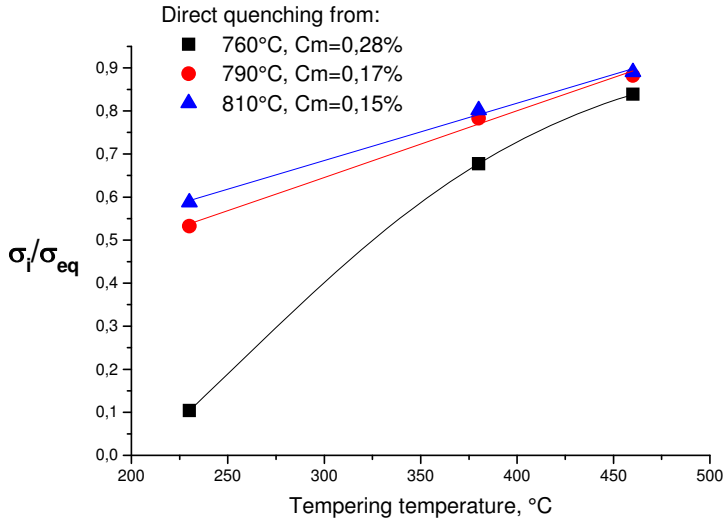

Figure VII.11. $\frac{\sigma_i}{\sigma_{eq}}$ ratio evolution with tempering temperature.

As can be seen, the σ_i / σ_{eq} ratio varies with the martensite carbon content and tempering temperature such that:

- the σ_i / σ_{eq} ratio increases with decreasing martensite carbon content. That is, the local triaxiality will be higher in a low carbon martensite and there is thus a higher probability of damage at the carbide/martensite interface. This trend is in agreement with the experimental observations, where in lower carbon martensite voids at carbides were found earlier (at lower tempering temperatures) than in higher carbon martensite,

- the σ_i / σ_{eq} ratio increases with increasing tempering temperature. That is, the local triaxiality increases with increasing tempering temperature. The probability of void nucleation at carbides therefore increases. This trend is also in agreement with experimental observations.

Now it is possible to combine the results of Figures VII.5 and VII.11 to obtain a qualitative understanding of the damage behaviour in this DP steels. The two graphs are shown together in Figure VII.12 for convenience. Here we have plotted directly T_{loc} instead of σ_i / σ_{eq}.

At low tempering temperatures T_{loc} at the martensite/carbide interface is small, whereas σ_c at ferrite/martensite boundaries is high, so the predominant damage mechanism is decohesion at ferrite-martensite boundaries. As the tempering temperature increases above 300°C σ_c drops whereas T_{loc} increases – a transition region between the two damage mechanisms must occur around this temperature. Further increases in tempering temperature will favour martensite/cementite decohesion. The initial martensite carbon content has only a small effect on σ_c, however, there appears to be a larger influence on T_{loc}. The triaxiality of stress at the martensite/cementite interface is significantly higher for lower initial martensite carbon levels. Thus the samples annealed at 810°C show martensite/cementite decohesion at lower tempering temperatures.

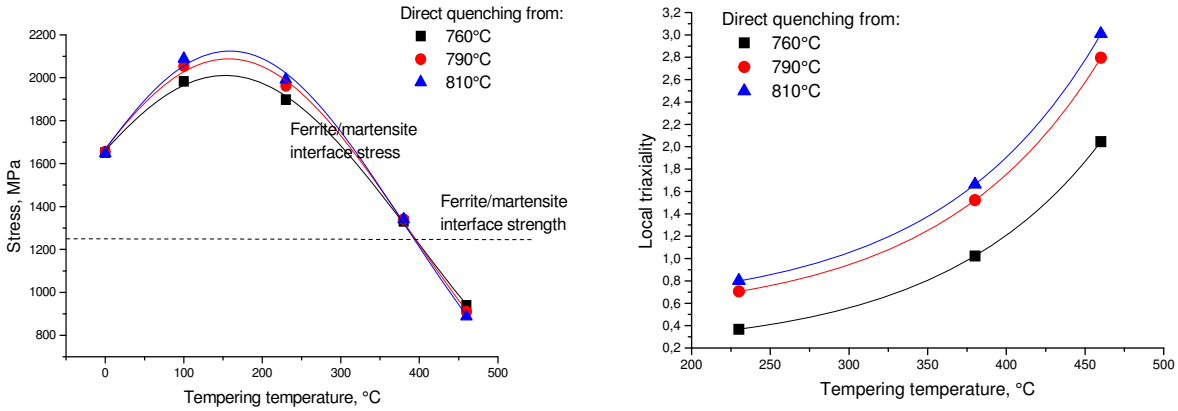

Figure VII.12. Variation of the interface stress σ_c at ferrite/martensite boundaries and the local triaxiality T_{loc} at martensite/cementites interfaces with tempering temperature.

VII.3 Summary

Two damage mechanisms (ferrite/martensite interface decohesion and void nucleation at carbide interfaces in tempered martensite) were identified. Ferrite/martensite decohesion is essentially independent of the as-quenched martensite carbon content and decreases rapidly with tempering temperatures above 300°C. On the other hand void nucleation at carbide interfaces in tempered martensite is strongly influenced by the as-quenched martensite carbon content. Lower carbon content martensites (i.e. higher intercritical annealing temperatures) promote this type of damage. Increasing the tempering temperature further decreases the martensite carbon content (through carbide precipitation) and favours void nucleation at carbide interfaces. Concerning the first damage mechanism, a recently developed model for ferrite/martensite decohesion using a mean field approach was applied and provided results which were qualitatively in agreement with the experimental observations. Several approximations utilized in this model were justified with the aid of recent FEM calculations.

Modeling is much more difficult in the case of tempered martensite internal damage, as many of the required experimental data are not accessible. In order to break the problem down, the simpler case of damage at an arbitrary inclusion in fresh martensite was studied. The critical nucleation strain ε_{nuc} required for the development of interface decohesion at an arbitrary defect as a function of the martensite carbon content was derived. It was found, not surprisingly, that ε_{nuc} decreases as the fresh martensite carbon concentration increases, so higher carbon martensites are more prone to show decohesion at inclusions. This behaviour is exactly the opposite to that observed for tempered martensite and it was not possible to apply the model. However, it was to possible to explain experimental evolution of *HE* value.

An attempt to compute the interface stress developed at carbide interfaces in tempered martensite using a mean field approach similar to that used for ferrite/martensite also failed. It was found that the calculated interface stress always decreased with tempering temperature for any sensible range of input parameters. The problem is most likely associated with the lack of suitable flow curve data for tempered martensite.

A simple approach which does reproduce well the experimental trends involves fixing the interface decohesion strength and calculating the triaxiality required to attain this value as a

function of the tempered martensite mechanical properties. From this, the ratio of internal to equivalent stress can be deduced. This ratio is directly proportional to the local stress triaxiality at the interface so it is a reasonable indicator of the probability of damage occurring. Although the calculated trends are correct, this model is not quantitative. An expression for the flow curves of tempered martensite is required in order to extend the analysis. This will require extensive experimental work.

The models developed in this chapter are simple approximations which, while they cannot provide a quantitative description of the complex damage formation mechanism occurring in tempered DP steels, do provide a basic understanding of the experimentally observed trends and could be used as the starting point for a more detailed analysis in future.

General conclusions and suggestions for further work

Conclusions

The main aim of this thesis has been to study and to understand the evolution of Dual Phase steel microstructures during annealing and tempering and to investigate the relations between the microstructure and damage mechanisms. An improved knowledge of these often complex phenomena is necessary in order to widen the application of existing grades and to aid in the development of newer damage resistant alloys.

Dual Phase steels were developed on the basis of the full ferritic and martensitic steels data. However, DP steel damage behaviour is more complex than either of these because of its specific microstructure. In consequence, DP steel damage resistance cannot be predicted using existing models based on standard mechanical properties.

In this work we concentrated on a reference DP steel composition: Fe-1.9Mn-0.15C-0.215Si-0.195Cr used in industrial grades. Starting from the full hard cold rolled condition, twelve different continuous annealing cycles were simulated. At the end of isothermal intercritical holding specimens were either water quenched or rapid air cooled to different intermediate temperatures and then water quenched. A detailed study of the resulting microstructures provided an understanding of how the basic microstructural parameters such as the martensite volume fraction and the ferrite/martensite constituent morphologies varied with the applied thermal cycle. A very important microstructural characteristic, which is controlled by the annealing parameters, is the martensite carbon content. Advanced characterization techniques such as Electron Energy Loss Spectroscopy (EELS) in the TEM and high spatial resolution Secondary Ion Mass Spectroscopy (NanoSIMS) were used in order to provide qualitative and quantitative measurements of the local carbon distribution in martensite.

TEM observations confirmed the presence of a high dislocation density in ferrite at the ferrite/martensite interface. These forest dislocations are responsible for the characteristic DP mechanical behaviour: i.e. low yield point to ultimate tensile strength ratio and continuous yielding behaviour.

The damage resistance of the different as-quenched microstructures was assessed using the standard hole expansion test (HE). Here we found a surprising and counter-intuitive result; the HE ratio in this alloy shows a monotonic decrease with increasing volume fraction of the ductile phase (ferrite). Unfortunately it was not possible to directly observe the microstructure after HE testing so we do not know if damage was initiated at ferrite/martensite interfaces or inside the martensite. We found, by applying a recently developed model for ferrite/martensite decohesion using a mean field approach, that the interface stress generated at ferrite/martensite boundaries in as-quenched DP structures is independent of the intercritical annealing temperature. This implies that the dominant damage mechanism during HE testing of as-quenched DP steels must be internal martensite damage. By considering the stresses exerted by a plastically deforming as-quenched martensite matrix on a brittle inclusion, we showed that the critical nucleation strain ε_{nuc} required for the development of interface decohesion at an arbitrary defect decreases as the carbon concentration of the fresh

martensite increases. So higher carbon martensites are more prone to show decohesion at defects and could therefore be the dominant damage initiation sites in HE testing.

It is common practice to apply a tempering treatment to improve the damage properties of DP steels. HE tests showed a clear positive relation between the tempering temperature and resistance to damage. SEM analysis of the fracture surface of tensile test specimens taken from as-quenched and from quenched and tempered sheets confirmed the presence of a transition from brittle to ductile behaviour as the tempering temperature increased.

The difference in the damage behaviour between as-quenched and tempered conditions has been confirmed by X-ray tomographic data from the ESRF synchrotron at Grenoble. It was found, by in-situ tensile testing of quenched and quenched and tempered alloys, that tempering slows down remarkably the nucleation rate of void formation and the total number of cavities just before fracture is increased.

A detailed study of the void distributions in as-quenched and tempered specimens revealed that there are two competing damage mechanisms: ferrite/martensite interface decohesion and void nucleation at carbide interfaces in tempered martensite. Ferrite/martensite decohesion is essentially independent of the as-quenched martensite carbon content and decreases rapidly with tempering temperatures above 300°C. On the other hand, void nucleation at carbide interfaces in tempered martensite is strongly influenced by the as-quenched martensite carbon content. Lower carbon content martensites (i.e. higher intercritical annealing temperatures) promote this type of damage. Increasing the tempering temperature further decreases the martensite carbon content (through carbide precipitation) and favours void nucleation at carbide interfaces. Concerning the first damage mechanism, the previously cited model for ferrite/martensite decohesion provided results which were qualitatively in good agreement with the experimental observations. Several approximations utilized in this model were justified with the aid of recent FEM calculations.

Modeling is much more difficult in the case of tempered martensite internal damage, as many of the required experimental data are not accessible. As stated previously, the critical nucleation strain ε_{nuc} required for interface decohesion at an arbitrary defect in fresh martensite decreases as the fresh martensite carbon concentration increases, so higher carbon martensites are more prone to show decohesion at inclusions. This behaviour is opposite to that observed for tempered martensite. Other attempts to apply mean field models for fresh martensite also failed.

A simple approach which does reproduce well the experimental trends involves fixing the decohesion strength at the carbide/martensite interface and calculating the triaxiality required to attain this value as a function of the tempered martensite mechanical properties. From this, the ratio of internal to equivalent stress can be deduced. This ratio is directly proportional to the local stress triaxiality at the interface so it is a reasonable indicator of the probability of damage occurring. Although the calculated trends are correct, this model is not quantitative. An expression for the flow curves of tempered martensite is required in order to extend the analysis. This will require further extensive experimental work.

The models developed in this thesis are simple approximations which, while they cannot provide a quantitative description of the complex damage formation mechanism occurring in tempered DP steels, do provide a basic understanding of the experimentally observed trends and could be used as the starting point for a more detailed analysis in future.

Suggestions for the further work

One clear motivation behind this work is the general need to improve damage resistance as steel mechanical properties increase. Indeed, one of the biggest challenges which will face the proposed 3rd Generation of advanced high strength steels is how to cope with the increased susceptibility to damage which is likely to be a consequence the higher carbon contents necessary to obtain the required increase in tensile strength and ductility. Understanding and mastering damage in medium carbon DP steels is a first step along this path.

- It is clear that damage in tempered martensite is a complex phenomenon that requires more sophisticated modeling in order to be fully understood. Probably a finite element approach is required in order to properly take into account the influence of carbide morphology and volume fraction,

- This will require experimental data on the flow curves of tempered martensite as well as a means to measure the carbon distribution in tempered martensite islands. The volume fraction of precipitated carbides is another required parameter which could be deduced if the mean carbon concentration in martensite and the martensite phase fraction is known. These are experimentally difficult but not impossible tasks,

- This approach could then be extended to other grades of DP steels taking into account the influence of the addition of different alloying and microalloying elements,

- The damage behaviour of more complex microstructures such as Transformation Induced Plasticity (TRIP), ferrite-bainite and CP (Complex Phase) steels could then be investigated.

Appendix 1: Experimental procedure

The equipment and techniques used in this work are described in the present appendix. The procedures employed for the characterization of microstructure and mechanical properties are also presented.

A1.1 Dilatometry

Dilatometry is used to obtain information on phase transformations in steel and to carry out some heat treatments. The dilatometer registers length changes that occur during heat treatments of the sample (Figure A1.1).

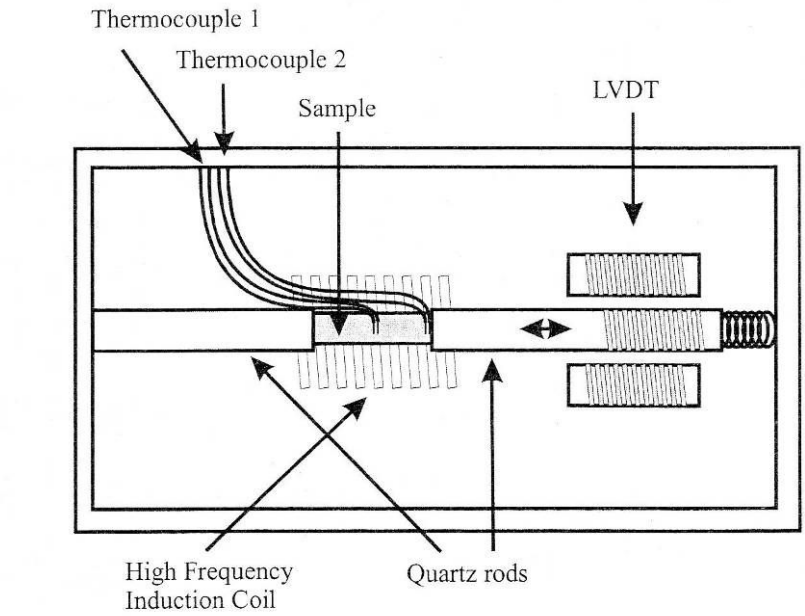

Figure A1.1. Schematic representation of the dilatometer.

A Bähr DIL 805 dilatometer was used for the experiments in this work (Figure A1.2). The cooling is carried out by helium gas injection. Before each experiment a vacuum is made in the cell. The samples are parallelepipeds with dimensions 1,2x4x10 mm.

Figure A1.2. Bähr DIL 805 dilatometer (www.bahr.de).

The type 805 dilatometer consists of the following main components (Figures A1.3 and A1.4):

-Quenching and deformation measuring head,
-High-frequency generator,
-Hydraulic system,
-Vacuum system,
-Cooling water supply,
-Gas supply (He),
-Measuring electronics,
-Data recording and control unit.

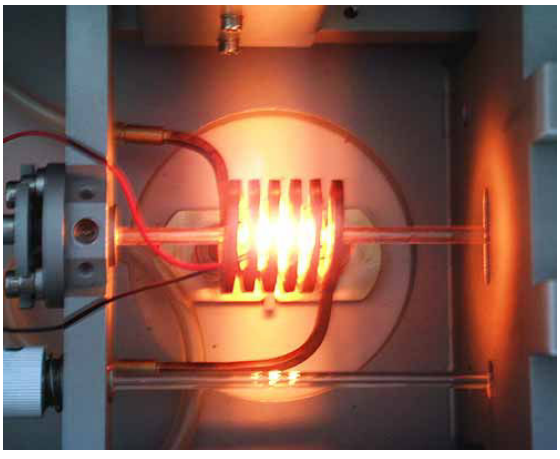

Figure A1.3. Heating in dilatometer (www.bahr.de).

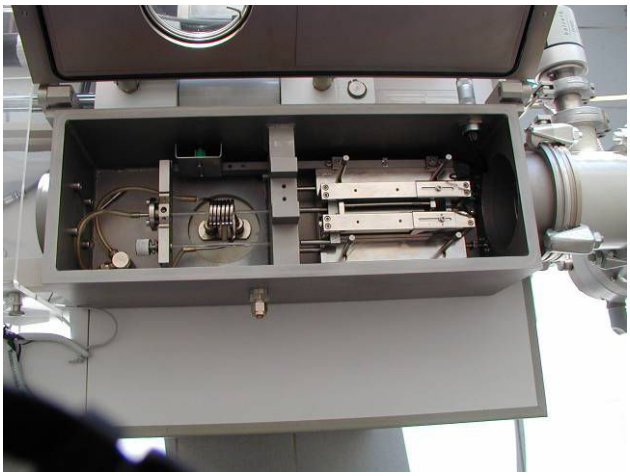

Figure A1.4. Experimental cell.

Pt-Rt/Rh 10% (type S) thermocouples are used for temperature control. Heating is by induction from room temperature to 1500°C, with a resolution 0,1°C. Cooling is by gas injection. Maximum cooling rate: 700-300°C: ~100-110°C/s; 400-200°C: ~80°C/s for Ø4mm. Maximum heating rates are presented in Table A1.1.

Curie point=760°C	Before	after
Ø4mm	~700°C/s	~60°C/s

Table A1.1. Dilatometer heating rates.

A1.2 Heat treatments

The thermal treatments were carried out in an AET continuous annealing simulator. Heating is performed by infrared lamps. Air cooling and water quenching thermal cycles can be carried out on this AET simulator. The temperature homogeneity is verified via multiple thermocouple measurements.

Figure A1.5. AET continuous annealing simulator.

Table A1.2 lists the main simulator characteristics for 1mm thickness samples.

Maximal working temperature	900°C
Heating rate	30°C/s
Cooling rate (in 900-450°C range)	50°C/s
Homogeneity of the useful zone	±5°C

Table A1.2. Heat treatment simulator characteristics.

Figure A1.6 shows a diagram of samples for the continuous annealing simulator. The locations for tensile test sampling are also shown.

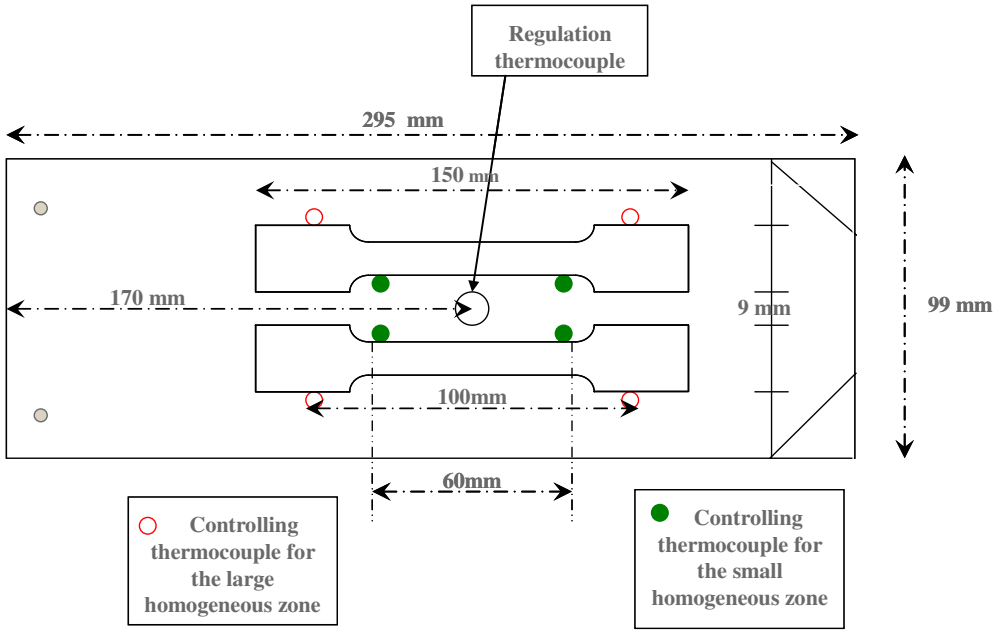

Figure A1.6. Heat treatment sample for AET simulator: 99 mm x 295 mm, hole diameter 3.8 mm.

The regulation thermocouple serves for thermal cycle piloting; the temperature homogeneity is verified via controlling thermocouples. The position of the controlling thermocouples (large or small homogeneous zone) is chosen as a function of sample dimensions.

The tempering treatments at all studied temperatures were performed in salt baths. The temperature was controlled by thermocouple.

A1.3 Microstructure characterization

A1.3.1 Light microscopy

Light optical microscopy (LOM) examination was performed prior to any electron metallographic technique to provide initial information about the microstructure and to conduct the qualitative analysis of phase components.

The microstructure samples are taken in transverse direction (Figure II.5). The specimens for LOM observation were mounted under heat and high pressure. Temperature sensitive samples were cold mounted. Then, samples were mechanically polished.

The microstructural constituents of the specimen were revealed by using a suitable chemical etchant. Metabisulfite (Table A1.3) is ideal to reveal DP structures; picral (Table A1.3) is used to distinguish carbon phases; Picral and metabisulfite together give better contrast [LAWS80]. Then, the microstructures were analyzed by light microscopy [COLI07, DRIL02].

Picral	Metabisulfite
4g picric acid	7g sodium disulfite
10ml ethanol	100 ml distilled water

Table A1.3. Metallographic etchants.

A1.3.2 Quantitative analysis

Microstructural quantification is performed on the LOM specimens.The phase fractions were determined by an Aphelion® semi-automatic image analyzer (Figure A1.7). Images of etched microstructures were acquired by light microscopy at a magnification of 100 [DRIL02, LEPE80].

Figure A1.7. Aphelion® image analyzer.

A1.3.3 Scanning electron microscopy

Detailed microstructure observations were carried out in FEG-SEM.
The SEM specimens must be electrically conductive, at least at the surface, and electrically grounded to prevent the accumulation of electrostatic charge. Two important reasons for coating, even when there is more than enough specimen conductivity to prevent charging, are to maximize signal and improve spatial resolution.

Samples for electron microscopic examination were cut from the centre of test specimens (place of thermocouple weld). SEM samples were then polished and etched in 2% nital or picral and metabisulfite.

The samples for carbide analysis in the FEG-SEM (Table A1.4) were OPS polished and slightly etched with picral reagent. Low accelerating voltages and work distances were used to improve the resolution. The In Lens method permits to reduce the relief brilliance in secondary electron mode.

Microscope	LEO 982
Acceleration tension	3-5kV
Work distance	4-6mm
Mode	In Lens

Table A1.4. Conditions of FEG-SEM analysis.

A1.3.4 Electron probe microanalysis

The study of carbon and manganese segregations was carried out on CAMECA SX100 electron probe microanalyser (Figure A1.8).

Figure A1.8. Electron probe micro analyser [www.cameca.com].

An electron beam of ≈1µm diameter was used for the analysis. Approximately 1 μm^3 of material is analyzed at each measuring point. The test conditions for carbon and manganese maps are listed in table A1.5.

Parameter	C	Mn
Accelerating voltage, keV	10	15
Current, µA	2	2
Step, µm	0.5	0.5
Time, s/pixel	0.1	0.1

Table A1.5. Acquisition parameters for C and Mn maps.

The interaction of the electron beam with the sample causes the emission of characteristic X-rays. The emitted X-rays are then analyzed in a Wavelength-Dispersive Spectrometer (WDS) by single-crystal monochromators which diffract a precise wavelength onto a detector where the photons are counted. The elemental concentrations can be determined using a reference sample. The quantification of the distribution of chemical elements (a map of the distribution) can be made by scanning a small area of the sample [BENO87].

The manganese concentration was determined correlating the intensity in the distribution map and the intensity given by the quantitative analysis. The detection limit for manganese concentration is 0.018 wt. %. The carbon concentration is determined using standard samples.

A1.3.5 *NanoSIMS* analysis

The Cameca NanoSIMS50, which associates high spatial resolution and high sensivity, is a powerful tool to analyze carbon distribution in steels. The Cameca NanoSIMS50 provides high-resolution elemental images (Table A1.6). The NanoSIMS50 allows analysis of bulk materials and does not require complex specimen preparation.

Lateral resolution	50 nm
Detection limit for carbon	0.0063wt.%

Table A1.6. Characteristics of Cameca NanoSIMS 50 [VALL06].

SIMS intensity measurements are carried out using a focused Cs^+ primary ion beam (<1pA) scanned across an area of 1µm×1µm. A pre-sputtering of the surface is performed before measurement in order to eliminate any carbon surface contamination. The pressure in the analysis chamber reaches 3-4×10^{-10} Torr.
The samples are embedded in an aluminium ring using Wood's alloy (Figure A1.9).


a

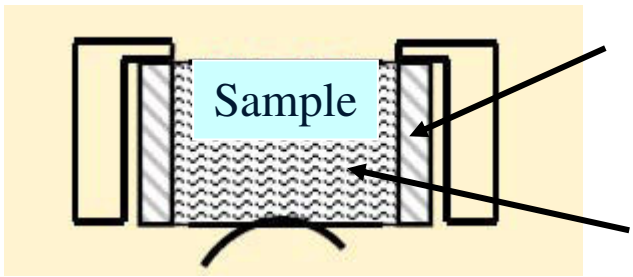

b

Figure A1.9. NanoSIMS sample holder.

After pre-sputtering the surface, short acquisition times (few minutes) are required for the carbon images using the NanoSIMS 50. It has been shown that the sputtering of only 200 carbon atoms are required to obtain a carbon analytical signal [VALL06].

Secondary ion mass spectroscopy is based on the sputtering of a few atomic layers from the sample surface, induced by a "primary" ion bombardment. A primary ion impact triggers a cascade of atomic collisions, which induce the emission of atoms and atomic clusters. During the ejection process, some of them are spontaneously ionized. These "secondary ions" are a characteristic of the analyzed area chemical composition. They are separated according to their mass, and an image containing quantitative information is formed for a selected mass (Figure A1.10).

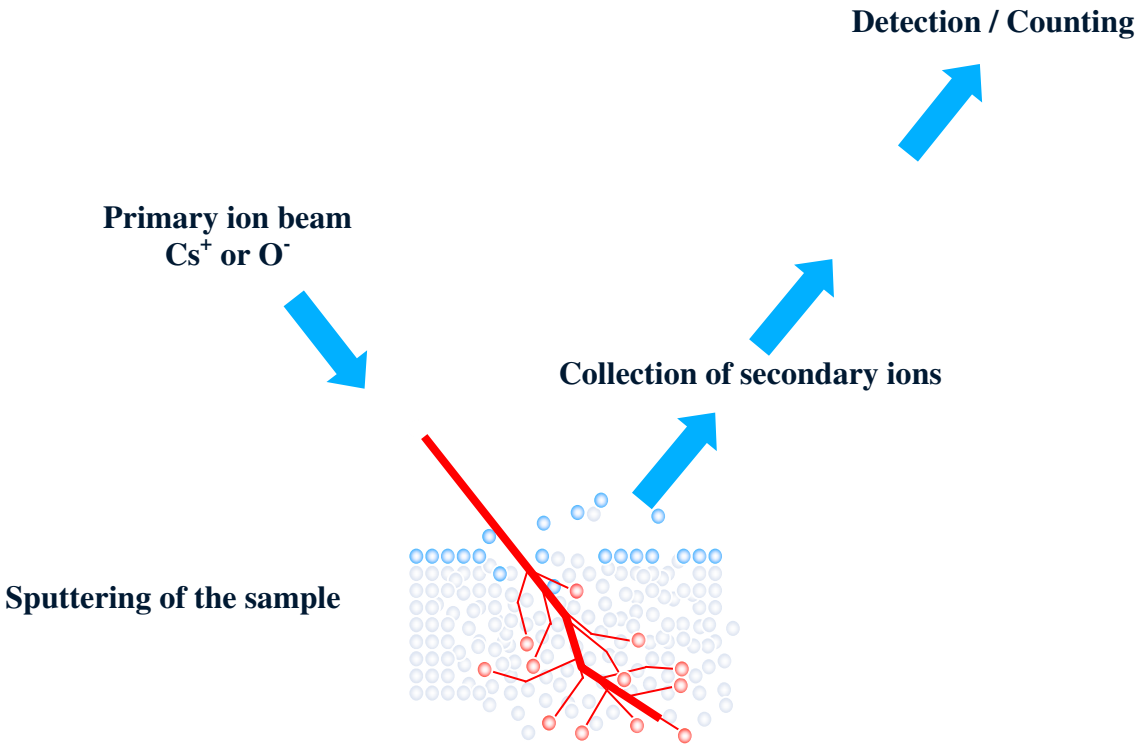

Figure A1.10. Scheme of signal formation in NanoSIMS (courtesy of N.Valle).

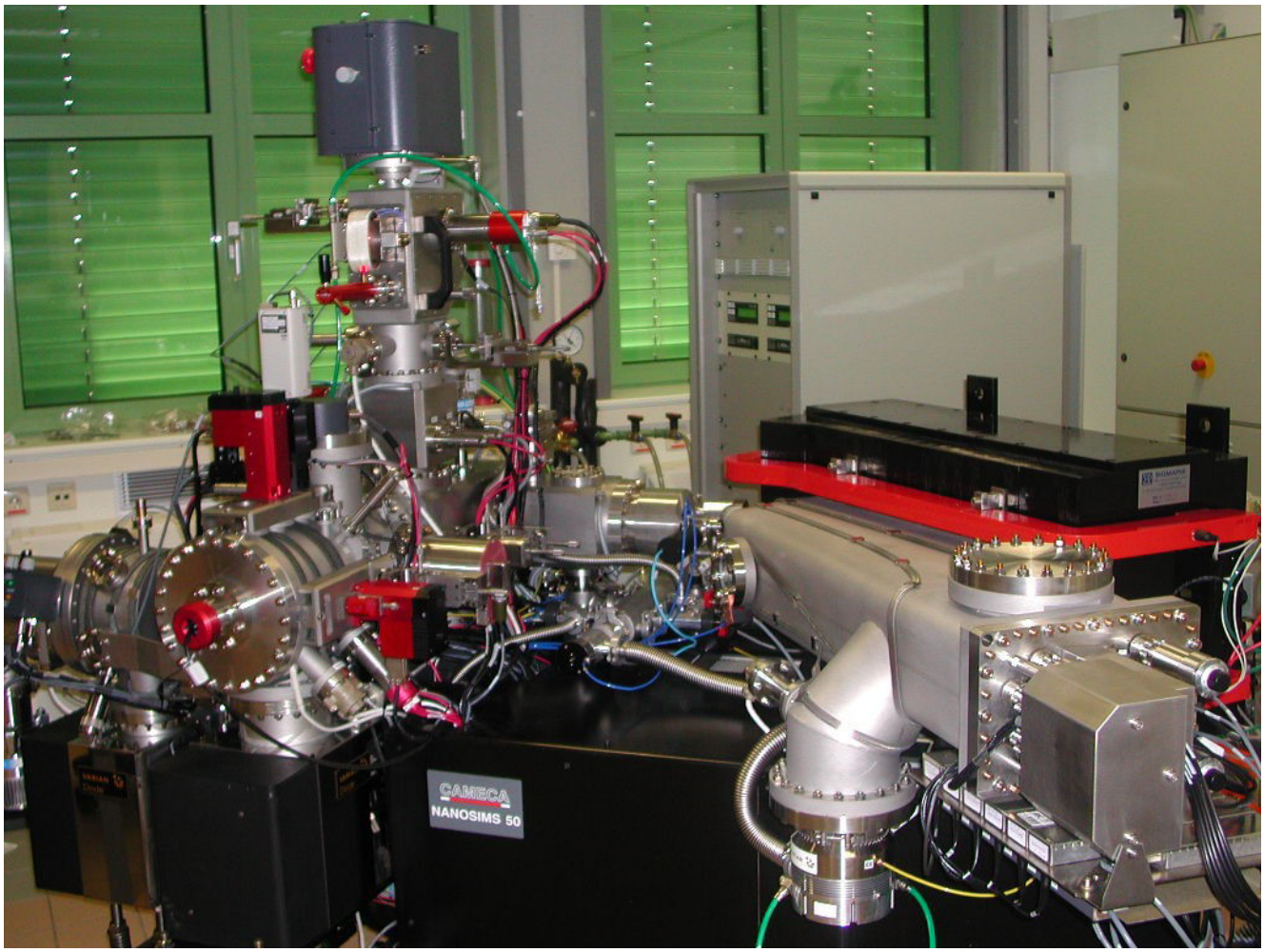

Figure A1.11. A dynamical SIMS instrument.

Typically, a secondary ion mass spectrometer consists of (Figure A1.11):

- primary ion gun generating the primary ion beam,
- primary ion column, where the primary ion beam is accelerated and focused on the sample,
- high vacuum sample chamber holding the sample and the secondary ion extraction lens,
- mass analyzer separating the ions according to their mass to charge ratio,
- ion detection unit.

To ensure that secondary ions do not collide with background gases on their way to the detector SIMS requires a high vacuum. It also diminishes surface contamination by adsorption of background gas particles during measurement.

A1.3.6 Transmission electron microscopy (TEM)

A Phillips CM200 TEM fitted with a Gatan EELS spectrometer was used for microstructure observations and carbon concentration measurements.

TEM samples were mechanically polished to a thickness of 50 μm. Disk shaped foils were prethinned in the centre by dimpling and electropolished in a jet polishing apparatus using a solution consisting of 5% perchloric acid in acetic acid at a temperature of 15°C. The foils were then examined in TEM operated at 200 kV.

Quantitative analysis of martensite carbon content is carried out by Electron Energy Loss Spectroscopy (EELS) in the TEM. TEM experiments were carried out at a temperature of -169°C in a liquid nitrogen cooling holder in order to eliminate the carbon contamination on the specimen surface during analysis. The detection limit for carbon is of the order of 0.025 wt. % [SCOT99].

When the electrons in an electron microscope traverse a thin foil a certain number will undergo inelastic collisions with the atomic electrons in the specimen. These collisions cause the incident electron to lose a discrete amount of energy. The energy lost is characteristic of the atomic number *Z* of the participating atom and the type of transition involved (*K,L,M*). The number of such inelastic collisions depends principally upon the mass-thickness of the specimen and the energy of the incident electrons. An energy loss spectrometer after the specimen collects the scattered electrons and separates them according to their momentum into an electron energy loss spectrum. Individual elements in the specimen give rise to well defined peaks or edges in the EELS spectrum. The intensity in these edges can be measured and used to calculate the absolute concentration of a given element A (in atoms / cm^2) using the theoretical or experimental cross sections [SCOT99].

Figure A1.12 shows second difference EELS Carbon-K edge and Iron-$L_{2,3}$ edges spectra from martensite island in the martensite-38% ferrite sample. From the ratio of the intensity of the C-K to Fe-$L_{2,3}$ edges the carbon concentration is measured 0.274% wt.

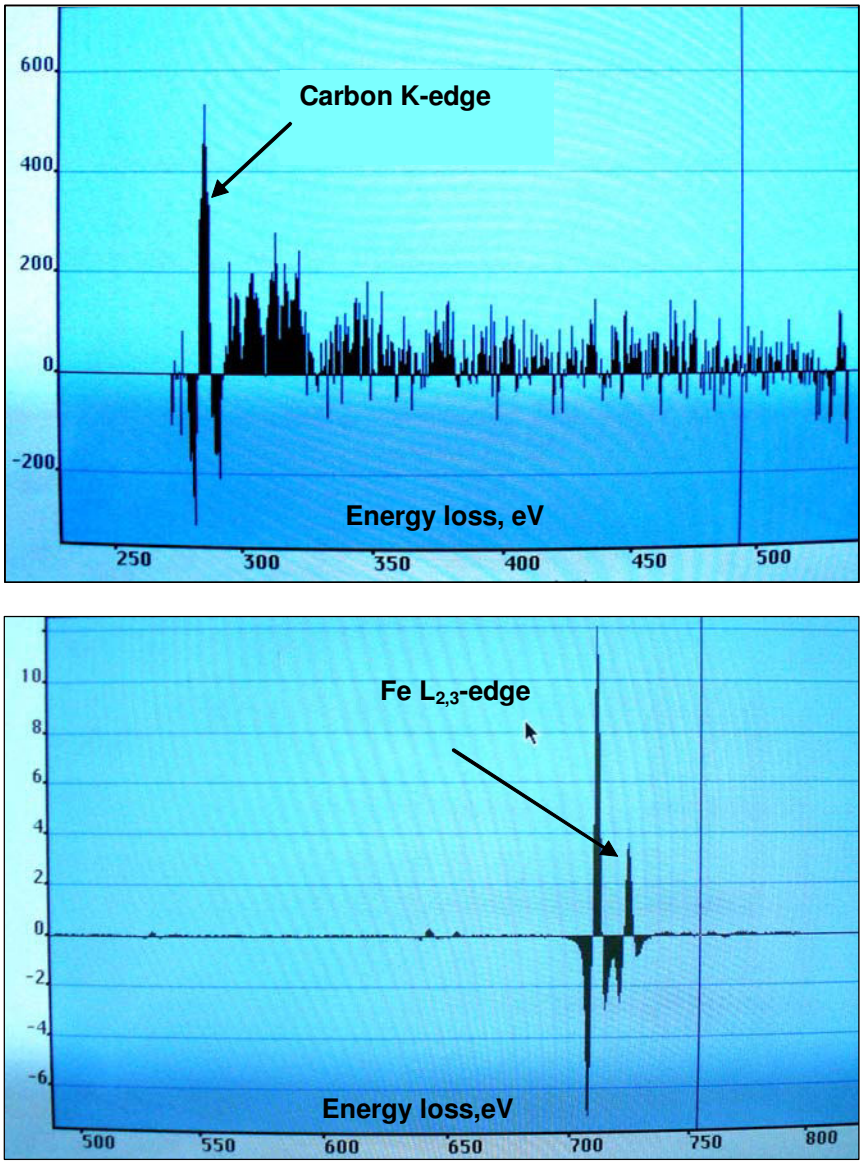

Figure A1.12. Second difference EELS Carbon-K edge and Iron-$L_{2,3}$ edges spectra.

A1.4 Mechanical characterization

A1.4.1 Tensile properties

Flat tensile samples of 50 mm gauge length and 12.5 mm width were tested according to the European standard EN 10002-1 (Figure A1.13). The testing speed was 0.008 s^{-1}. The stress-strain curves for samples were determined. The mechanical properties are characterized by means of the yield stress (YS), the ultimate tensile strength (UTS) and the uniform elongation (UE).

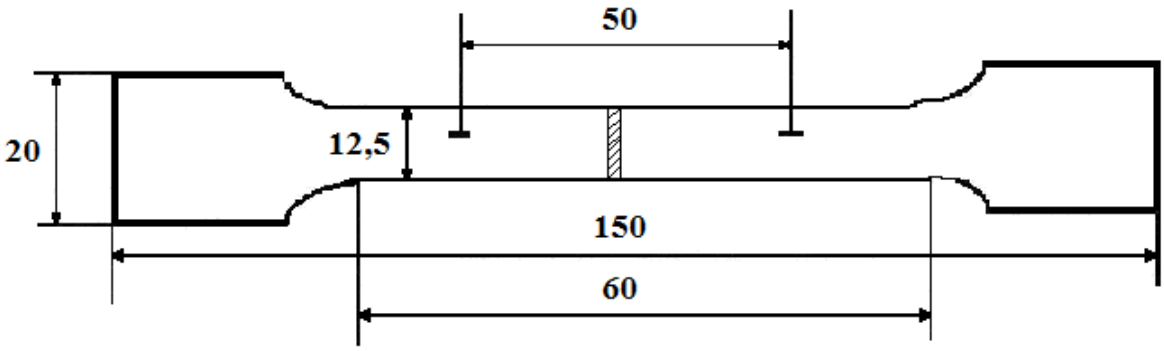

Figure A1.13. Scheme of tensile specimen.

The tensile loading axis corresponds to the transverse direction of the sheet.

A1.4.2 Charpy pendulum impact test

Samples of 55x10x1.2 mm are V-notched with a 45° angle and 2 mm depth. The specimen is held horizontally against two supports with the notch vertical and is struck on the face opposite the notch by the knife-edged hammer of a pendulum (Figure A1.14).

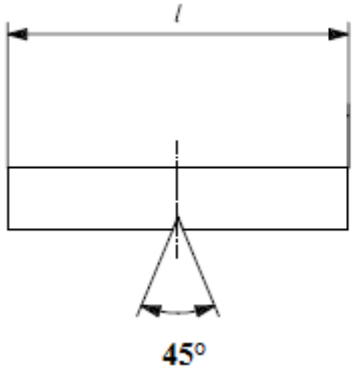

Figure A1.14. Charpy test specimen [ISO148].

Figure A1.15. Charpy test equipment.

Zwick impact testing machine of 50J is used (Figure A1.15). The samples are tested in transverse direction.

A1.4.3 Limiting Hole Expansion ratio, HE

Hole Expansion is a standardized test carried out according to the ISO TC 164 specifications.

For the hole expansion test, a hole in the central part of the test piece (100x100mm) is punched using a 10 mm diameter punch. A clamping force is applied to the test piece to prevent any material draw-in from the clamped area during the test. The hole is then expanded by a conical punch with a top angle of 60°. *HE* tests are carried out at ambient temperature.
The conical expansion tool presses into the punched hole of the test piece at a rate which enables the operator to stop the test when the first relevant crack appears through the full thickness of the test piece (Figures A1.16, A1.17, A1.18).

The inside diameter is then measured in two directions perpendicular to each other, avoiding the crack.

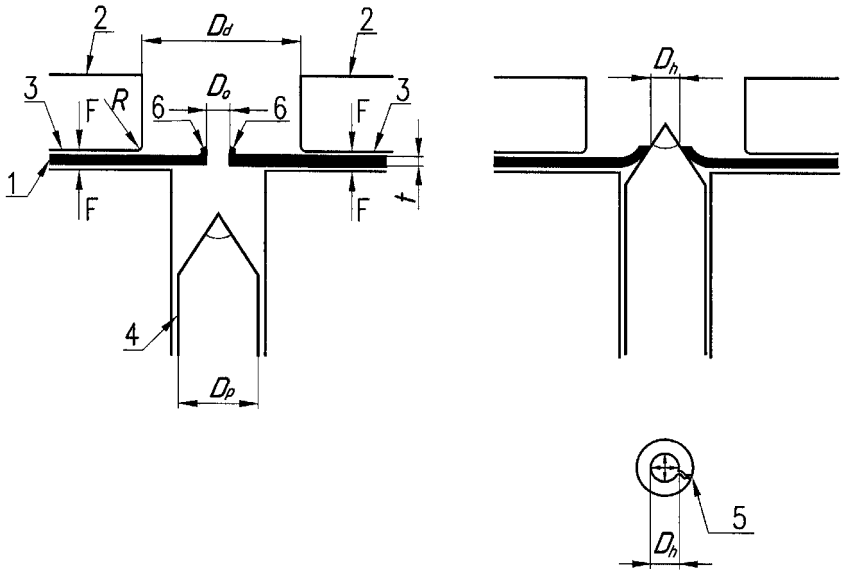

Figure A1.16. Illustration of hole expanding test [ISO479]: 1 - Test piece, 2 – Die, 3 - Die shoulder, 4 – Punch, 5 – Crack, 6 - Burr;D_d -Inside diameter of the die of expansion tool, D_h - Hole diameter after rupture, D_o - Initial hole diameter, D_P - Diameter of the punch of expansion tool, *F*- Clamping force, *R* -Corner radius of the die of expansion tool, *t* - Thickness of the test piece.

The hole expansion ratio *HE* is determined by the following formula:

$$HE = \frac{D_h - D_0}{D_0} \cdot 100\%$$

Where D_o is the initial hole diameter (Figure A1.16), and D_h is the hole diameter after rupture.

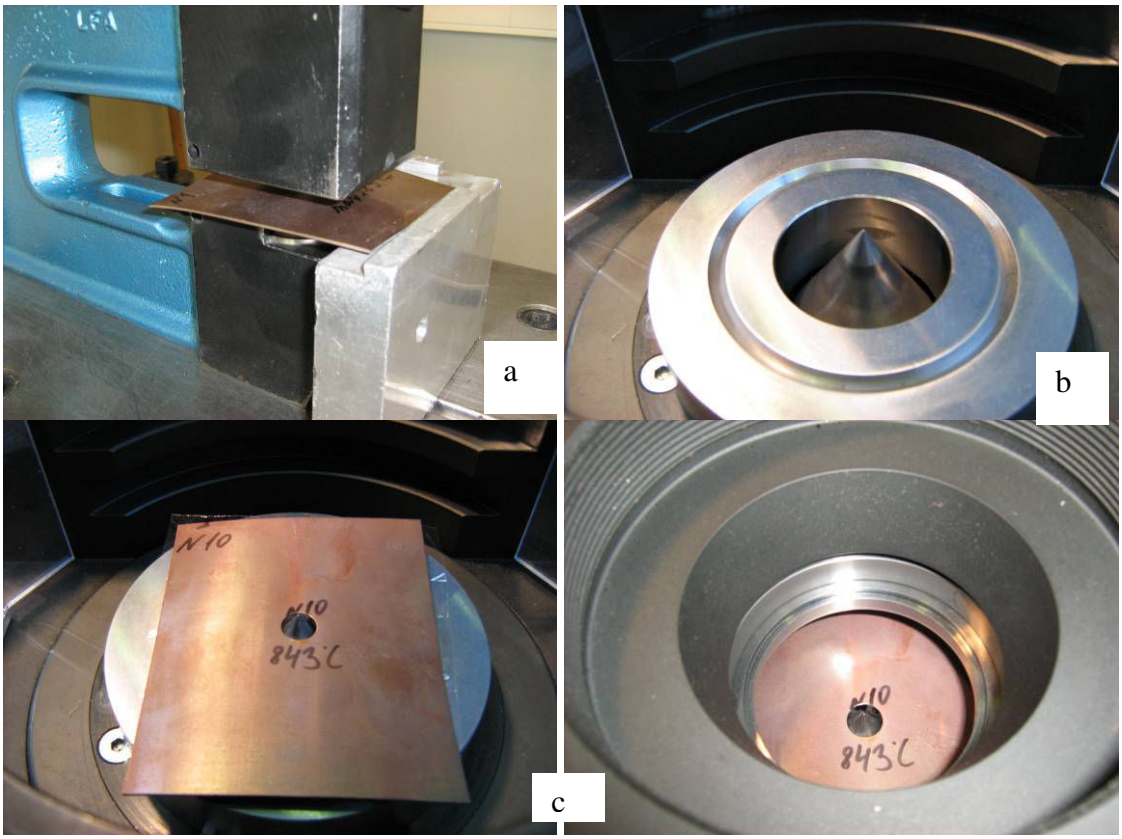

Figure A1.17. a – punching a hole in sample, b – *HE* conical punch, c – *HE* conical punch and sample, c – the starting position for *HE* test.

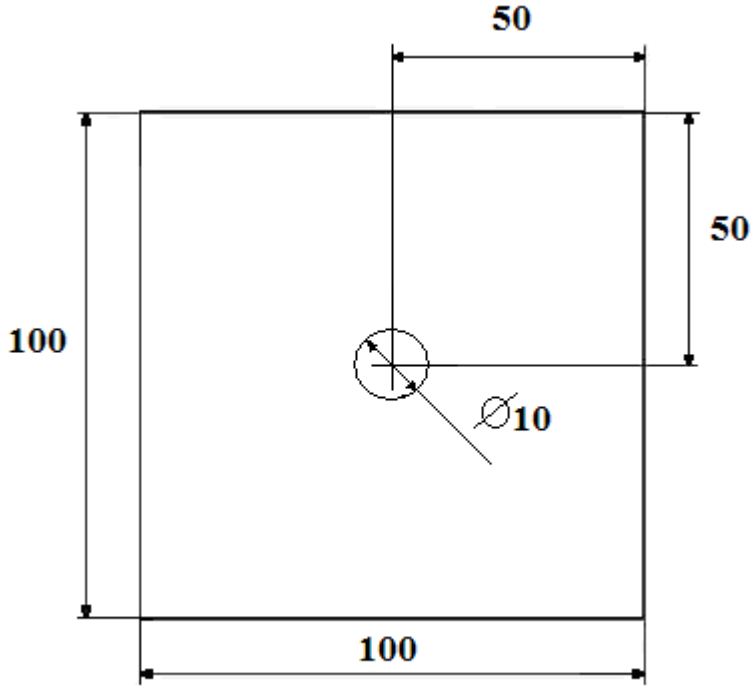

Figure A1.18. Scheme of *HE* sample.

A1.5 Fractography

After tensile testing the fracture surfaces of the broken specimens were analyzed in the SEM as illustrated in Figure A1.19. Ultrasonic cleaning in ethanol was used before SEM analysis.

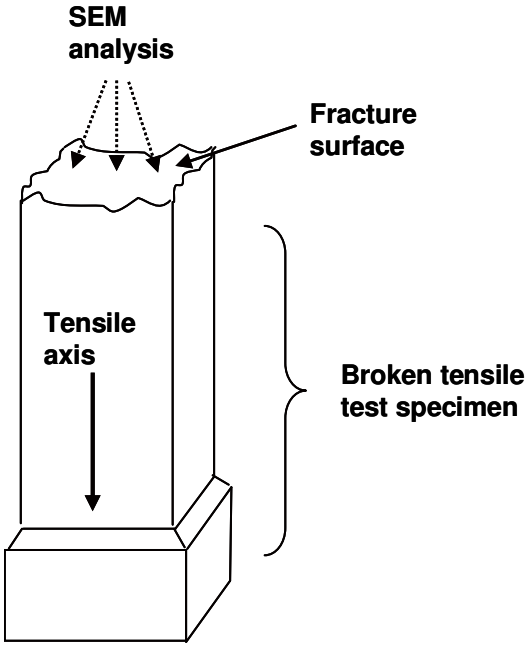

Figure A1.19. Schematic showing the fractographic analysis of tensile test specimens.

A1. 6 Void analysis

For the void nucleation study the longitudinal section of broken tensile specimens near the fracture surface was analyzed in SEM (Figure A1.20). The samples were polished and etched before analysis. Ultrasonic cleaning was used after each cycle of polishing to remove disturbed metal from the voids.

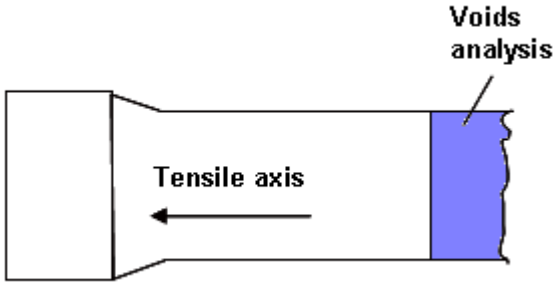

Figure A1.20. Schematic of void analysis of tensile test samples.

Appendix 2: Charpy impact test

A measurement of steel brittleness is obtained by detecting the amount of energy absorbed when a notched specimen is broken under conditions of impact loading. A sample's notch is a place of stress concentration and could act as a fracture nucleus.

The Charpy impact test is a standardized test which determines the amount of energy required to break a material under impact loading [ISO06C]. It is widely applied in industry, but a major disadvantage is that the results are only comparative, since the absorbed energy depends critically on the sample geometry and the shape of the notch.

The material is considered to be brittle, when it breaks with a small amount of absorbed energy in impact test. For a given steel the fracture mode varies with testing temperature.

To evaluate the possible fracture morphology variation with testing temperature the Charpy test is conducted for different as-quenched RCQ samples. Figure A2.1 illustrates the absorbed energy as a function of test temperature for different heat treatment parameters.

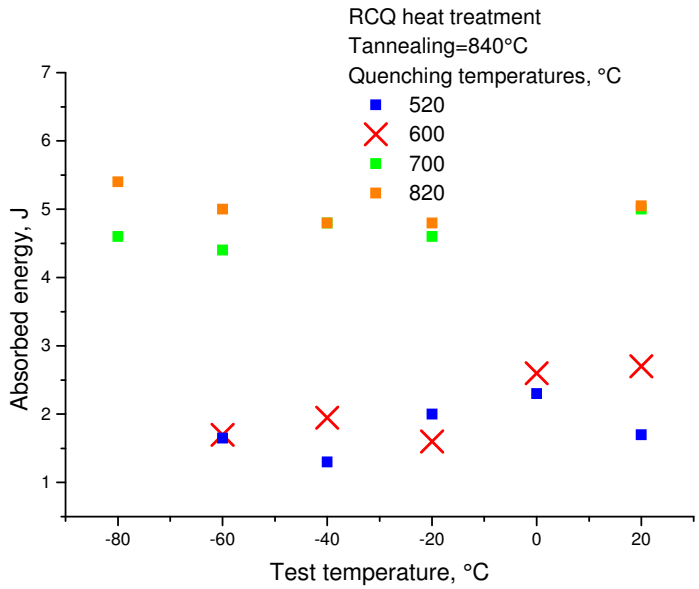

Figure A2.1. The part of transition curve for RCQ samples.

Two regions of fracture energy can be distinguished with a lower and a higher absorbed energy. The samples after quenching from 520°C and 600°C show lower fracture energy, than the 700°C and 820°C quenched samples.

The ductile surface fraction was measured for the broken samples. Figure A2.2 shows the ductile surface fraction as a function of test temperature for different RCQ samples.

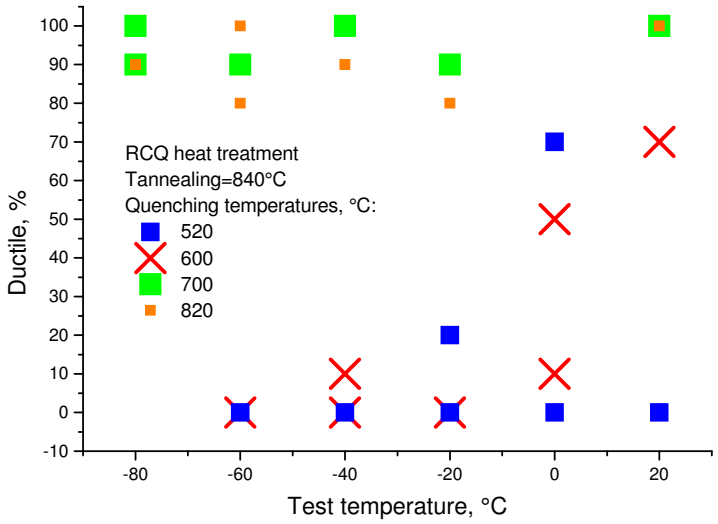

Figure A2.2. Ductile surface fraction for different test temperatures.

The ductile surface fraction for samples after quenching from 820°C and 700°C is 90-100% for all test temperatures. For samples, quenched from lower temperatures (500°C and 600°C) the ductile surface fraction is much lower and is equal to zero for most testing temperatures.

Figure A2.3 is SEM micrographs of fracture surfaces for specimens tested at room temperature. It illustrates a damage mode change with quenching temperature. Sample after quenching from 520°C has a large brittle zone. Increase in quenching temperature to 600°C leads to decrease of the brittle zone fraction. After quenching from 820°C the fracture surface is fully ductile.

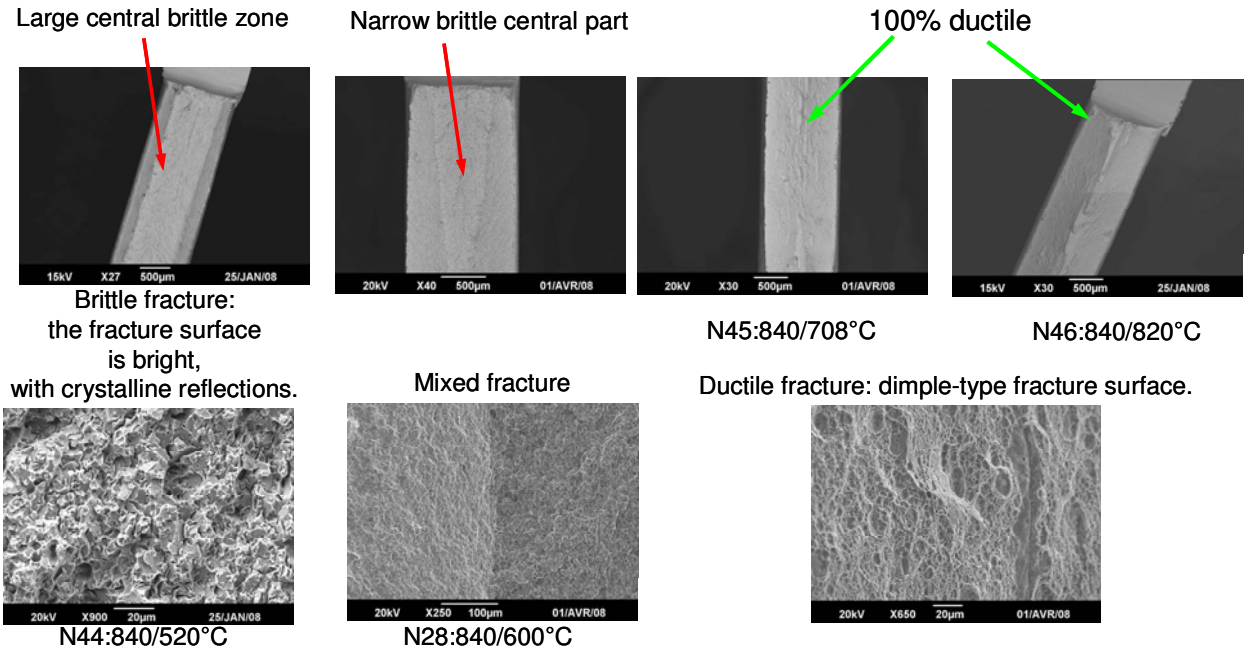

Figure A2.3. Fracture surface observations in the SEM.

As has been shown in § II.A.4.3, an increase in quenching temperature leads to a decrease of ferrite fraction (Figure II.12). Thus, an absorbed energy decreases with increasing ferrite fraction. Also, damage mode changes from ductile to brittle with an increase in the ferrite fraction.

Considering all Charpy test results, it can be concluded that the change in microstructure leads to a change in the fracture mode. The heterogeneous ferrite – martensite microstructure leads to a brittle failure of the steel. And more homogeneous, almost full martensitic microstructure shows a ductile failure in the impact test.

Appendix 3 : Résumé élargi de la thèse en français

Introduction

Les aciers Dual-Phases (DP), constitués majoritairement d'une phase ductile, la ferrite et d'une phase dure, la martensite, occupent une place importante en tant que matériaux destinés à l'industrie automobile. Ces aciers présentent un bon compromis entre la résistance mécanique et la ductilité. Une bonne résistance à l'endommagement est exigée pour leur utilisation en tant que des pièces de structures et de renfort pour l'automobile.

Il a été établi que la résistance à l'endommagement des aciers Dual-Phases est tributaire de la fraction de la ferrite, d'une part, et du gradient de dureté entre la ferrite et la martensite, d'autre part. L'accroissement de la fraction de la ferrite conduit à une amélioration de la résistance à l'endommagement. Cependant, pour une composition chimique donnée de l'acier, l'augmentation de la fraction de la ferrite entraîne un enrichissement en carbone de la phase martensitique et par conséquent accentue le gradient de dureté entre la ferrite et la martensite.

Ce travail de thèse est consacré, entre autres, à l'étude des mécanismes d'endommagement des aciers Dual-Phases. Pour cerner ces mécanismes et identifier les paramètres microstructuraux ayant un impact sur l'endommagement, nous avons choisi un acier Dual-Phases de grade DP 780 dont la composition chimique (% massique) : 0.15C–0.215Si–1.9Mn–0.195Cr.

Cet acier a été soumis à des traitements thermiques variés (trempe rapide, refroidissements contrôlés, revenu, …) permettant la genèse de différentes microstructures.

Pour répondre aux objectifs ainsi édictés et mener ce travail à terme, nous avons organisé de façon didactique, le manuscrit de cette thèse en sept chapitres :

Le premier chapitre est dédié à l'état de l'art concernant les aciers Dual-Phases. Le second chapitre est consacré, quant à lui, à la présentation des traitements thermiques (trempe rapide, refroidissement contrôlés, revenu, …) auxquels l'acier DP 780, sélectionné pour cette étude, a été soumis. Nous nous sommes, bien évidemment, focalisés sur les évolutions de la microstructure et des propriétés mécaniques de cet acier DP, en fonction des paramètres (température et temps de maintien, vitesse de refroidissement, …) des différents traitements thermiques.

Une caractérisation fine de la microstructure de l'acier Dual-Phases sélectionné est détaillée dans le troisième chapitre.

Le quatrième chapitre a permis de mettre en exergue le rôle de la concentration locale de carbone, dans la martensite. Une analyse approfondie de la distribution du carbone, dans la martensite (brute de trempe et revenue) et au niveau des interfaces ferrite/martensite y est présentée.

La résistance à l'endommagement de l'acier a été analysée en faisant appel à un essai mécanique pertinent, l'essai d'expansion de trou. Les résultats ainsi obtenus sont analysés et discutés dans le cinquième chapitre.

Les mécanismes d'endommagement ont été identifiés et regroupés dans le sixième chapitre. Un modèle simple de prédiction qualitative de l'endommagement a été développé dans le septième et dernier chapitre.

A3.I Etude bibliographique

Les différents aspects de la microstructure et du comportement mécanique des aciers Dual-Phases sont présentés dans ce chapitre.

A3.I.1 La microstructure des aciers Dual-Phase (DP)

La microstructure de l'acier DP est constituée d'une phase molle, la ferrite et d'une phase dure, la martensite. Cette microstructure peut être obtenue en effectuant un recuit intercritique dans le domaine ($\alpha+\gamma$) (Figure A3.I.1) : une montée et un maintien en température dans le domaine biphasé ($\alpha+\gamma$) suivi d'une trempe.

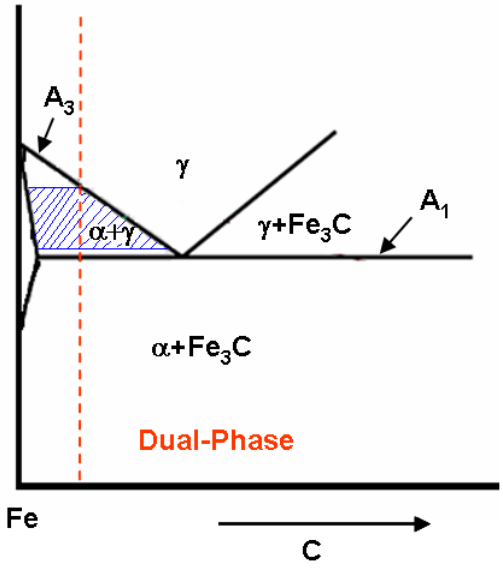

Figure A3.I.1. Schéma du diagramme Fe-C montrant l'intervalle intercritique ($\alpha+\gamma$).

La transformation de l'austénite en martensite a lieu à basse température et la ferrite se déforme pour accommoder l'augmentation de volume qui est due à cette transformation : des dislocations d'accommodation et des contraintes résiduelles sont générées à l'interface ferrite/martensite (Figure A3.I.2) [SPEI81A].

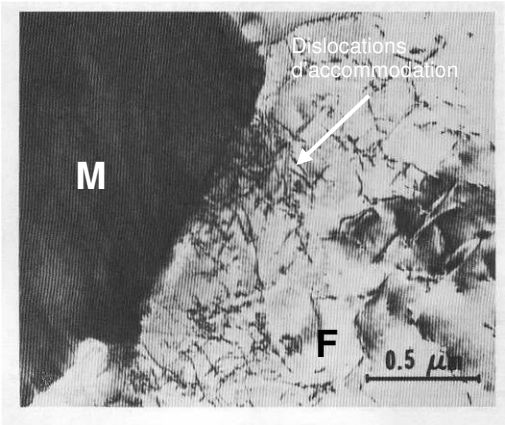

Figure A3.I.2. Micrographie, obtenue en microscopie électronique en transmission, montrant les dislocations d'accommodation à l'interface ferrite/martensite [SPEI81A].

Deux types de ferrite peuvent être identifiés dans l'acier DP : la ferrite intercritique proeutectoïde, présente au cours du maintien dans le domaine ($\alpha+\gamma$) et la ferrite se formant pendant le refroidissement. Cette dernière, se développant à partir de la ferrite proeutectoïde pendant le refroidissement, est appelée la ferrite epitaxiale ou d'épitaxie (Figure A3.I.3) [KORZ82].

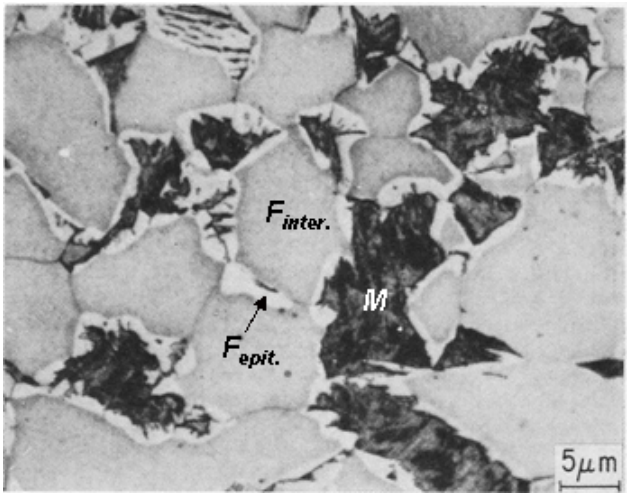

Figure A3.I.3. Micrographie optique montrant les deux types de ferrite dans un acier DP : Gris = ferrite intercritique, Blanc = ferrite epitaxiale, Noir = martensite [SPEI81A].

A3.I.2 La martensite

La martensite est un constituant important des aciers DP. La martensite est une solution solide sursaturée en carbone [BHAD99]. Elle est obtenue par une transformation sans diffusion : le cisaillement à l'état solide. Les atomes de carbone, piégés au cours du refroidissement, occupent les sites octaédriques des mailles cubiques centrées de fer α.

En fonction de la concentration en carbone de l'austénite différent types de martensite peuvent se former : martensite en lattes ou la martensite en plaquettes [KRAU01].

Les éléments d'alliages sont ajoutés dans les aciers DP pour augmenter la trempabilité. L'addition des éléments d'alliages supprime les transformations diffusives et favorisent l'apparition des structures hors-équilibre, bainitiques ou martensitiques.

A3.I.3 Revenu de la martensite

Un revenu permet d'améliorer les propriétés d'une structure martensitique conduisant ainsi à un meilleur compromis entre la ductilité et la résistance mécanique.

Au cours du revenu, la martensite se décompose en suivant les étapes suivantes [SPEI92] :

- La précipitation de carbure ε,
- La décomposition de l'austénite résiduelle,
- La formation de la cémentite,
- La précipitation des carbures alliés.

La distribution du carbone ou la précipitation des carbures peuvent se produire pendant la trempe. Ce processus est appelé l'auto-revenu.

A3.I.4 Revenu dans les aciers DP

Les phénomènes de revenu dans les aciers DP sont plus complexes du fait de leur microstructure composite ferrite/martensite. Le processus de revenu est aussi influencé par la distribution spécifique des dislocations et des contraintes résiduelles.

Les phénomènes suivants sont mis en évidence pendant le revenu des aciers DP [WATE03]:

- Le piégeage des dislocations par les atomes de carbone dans la ferrite,
- La formation des clusters (ou amas) de carbone ou de carbures ε,
- Le revenu de la phase martensitique.

A3.I.5 Comportement mécanique des aciers Dual Phase

Plusieurs facteurs influencent la répartition des déformations entre la ferrite et la martensite, on peut citer : le taux de la martensite, concentration de carbone dans la martensite et le revenu.

La répartition des déformations entre la ferrite et la martensite ainsi qu'entre les grains de la même phase est hétérogène, pendant le chargement mécanique [SHEN86].

Il a été confirmé que la déformation de la phase martensitique doit être prise en compte [KRAU01, RACH77].

La courbe de traction typique des aciers DP, ainsi que les courbes de traction de ces composants, la ferrite et la martensite, sont présentées sur la Figure A3.I.4.

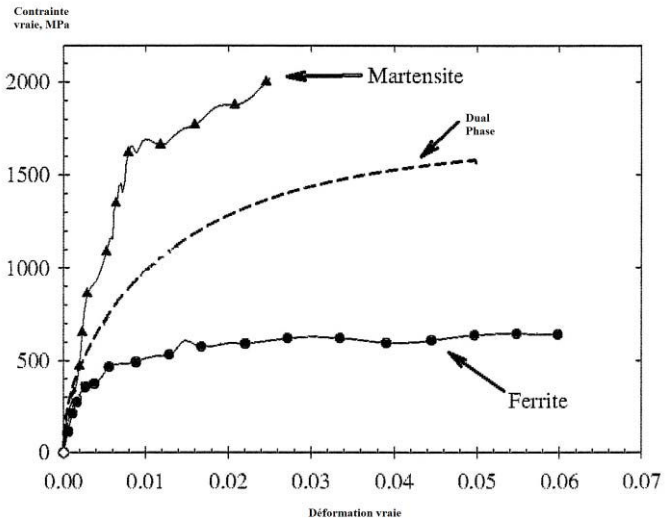

Figure A3.I.4. Diagramme : contrainte vraie versus déformation vraie pour l'acier DP et ces composants – la ferrite et la martensite [JACQ07].

La déformation d'un acier DP suit les étapes les suivantes [ABBA03] :

- Les deux phases sont élastiques,
- La ferrite est déformée plastiquement, tandis que la martensite est élastique,
- Les deux phases se déforment plastiquement.

A3.I.6 Absence de palier élastique dans les aciers Dual-Phases

Les aciers DP ont, en général, un comportement mécanique continu (c'est-à-dire le palier élastique est absent) (Figure A3.I.4). Ce comportement est attribué à la présence des dislocations d'accommodation et des contraintes résiduelles à l'interface ferrite/martensite. L'écoulement plastique commence simultanément sur plusieurs sites et le comportement mécanique discontinu est supprimé [SPEI81A].

Deux conditions doivent être remplies pour que l'acier DP ait un comportement mécanique continu [HANS81]:

1. La densité des dislocations mobiles doit être suffisante (10^6-$10^8 cm^{-2}$),
2. Ces dislocations doivent rester mobiles à la température ambiante.

Les contraintes résiduelles dans la ferrite contribuent aussi au comportement continu des aciers DP. Elles participent à l'initiation de l'écoulement plastique [RIGS77].

A3.I.7 L'endommagement lors de la rupture ductile

La rupture ductile de l'acier DP se déroule en trois étapes: la nucléation, la croissance et la coalescence des cavités. On distingue deux types de nucléations des cavités :

1) la nucléation homogène qui intervient sans être associée à une inclusion,
2) la nucléation hétérogène qui est associée à l'hétérogénéité dans la structure (présence de précipités ou d'inclusions).

Dans le processus d'endommagement ductile des aciers DP, le rôle de la martensite est très important. Il a été montré que les cavités apparaissent soit suite à la décohésion de l'interface ferrite/martensite, soit suite à la rupture de la martensite [STEI88, STEV77, BALL82].

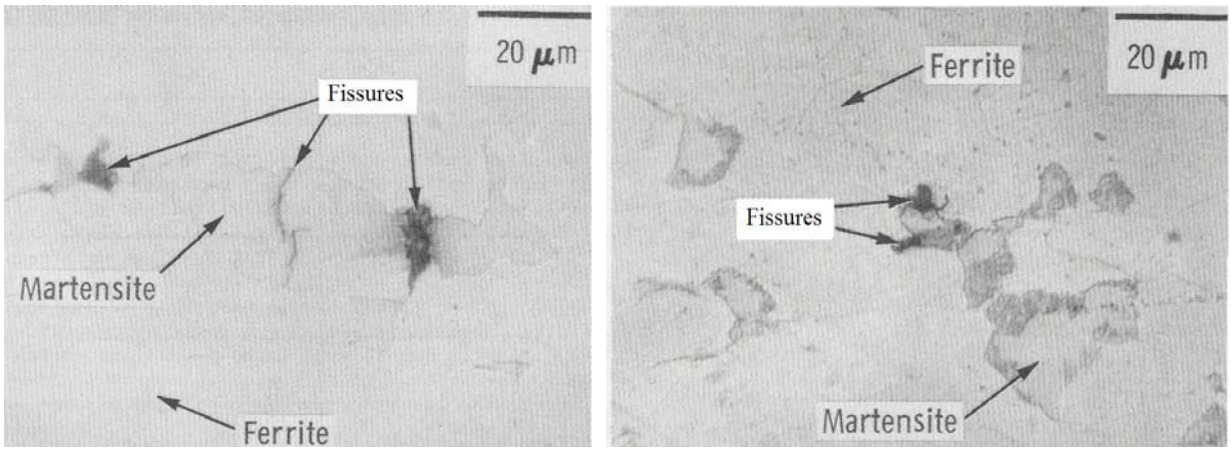

Brut de trempe : fissure pointue Etat revenu : fissure arrondie

Figure A3.I.5. Observation d'endommagement dans l'acier DP [STEV77].

Le revenu modifie le mécanisme de nucléation et de croissance des cavités dans les aciers DP. Le revenu adoucit la martensite et améliore ainsi la capacité de matériau à distribuer la déformation (Figure A3.I.5) [STEV77].

Etude expérimentale

A3.II La microstructure et les propriétés mécaniques

La microstructure contrôle les propriétés mécaniques et par la suite les possibilités d'applications de matériau pour l'industrie de l'automobile. Le but de ce chapitre est de comprendre l'influence des paramètres des traitements thermiques sur la formation de la microstructure DP. L'optimisation des propriétés mécaniques est nécessaire pour une application pratique de l'acier. Ainsi, l'évolution des propriétés mécaniques avec les différents traitements thermiques est étudiée dans le présent chapitre.

A3.II.1 Composition chimique et microstructure initiale

Un acier industriel de grade DP 780 est utilisé comme matériau modèle pour nos observations. L'acier est reçu à l'état brut de laminage à froid (LAF) sans revêtement. L'épaisseur de la tôle est de 1,2 mm et la composition chimique est présentée dans le Tableau A3.II.1 ci-dessous :

C	Si	Mn	Cr
0.15	0.215	1.9	0.195

Tableau A3.II.1. Composition chimique de l'acier DP 780 (% massique).

La tôle laminée à froid est issue de la tôle laminée à chaud (LAC) ayant une épaisseur de 2,73 mm. La température de fin de laminage est estimée à 889°C et la température de bobinage à 562°C.
Les microstructures de l'acier après laminage à chaud et laminage à froid sont présentées sur la Figure A3.II.1. La microstructure issue du LAF est constituée de ferrite et de perlite. Le taux de perlite déterminé par analyse d'image est estimé à 24.5±4.2 %. Le calcul à l'aide de logiciel Ceqcsi® donne 29 % de perlite ce qui est en accord avec les résultats expérimentaux. Après le LAF la microstructure est fortement déforme est présente une structure en bandes.

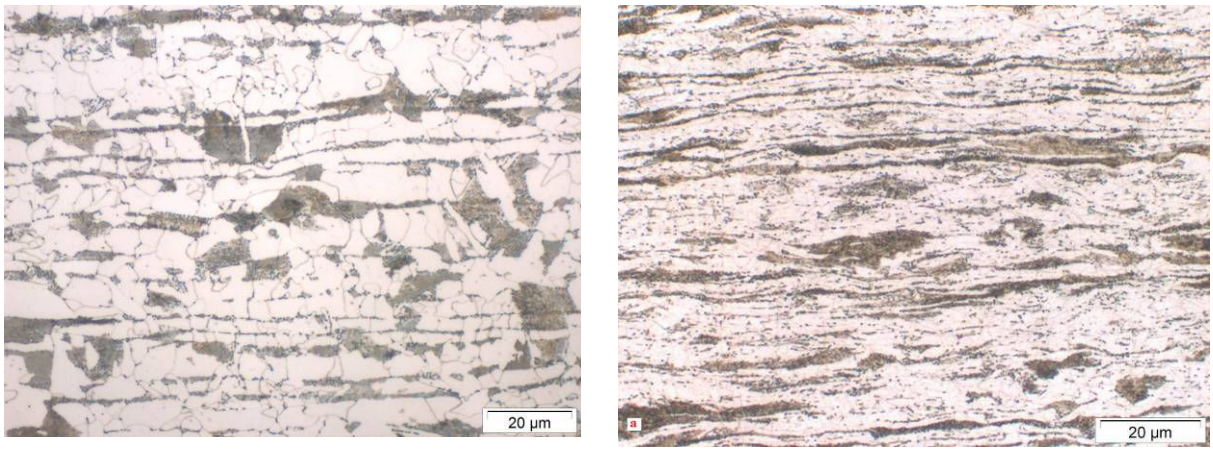

a b

Figure A3.II.1. Micrographies optiques montrant la microstructure de l'acier laminée à chaud (a) et à froid (b), (attaque au Nital).

A3.II.2 Traitements thermiques

Les microstructures sont directement dictées par le traitement thermique imposé. Deux cycles thermiques sont utilisés (Figure A3.II.2) :

- une trempe directe depuis la température de maintien isotherme, DQ (DQ pour Direct Quenching)
- un refroidissement rapide suivi d'une trempe, RCQ (RCQ pour Rapid Cooling and Quenching).

Un traitement de revenu est appliqué après chaque type de cycle thermique.

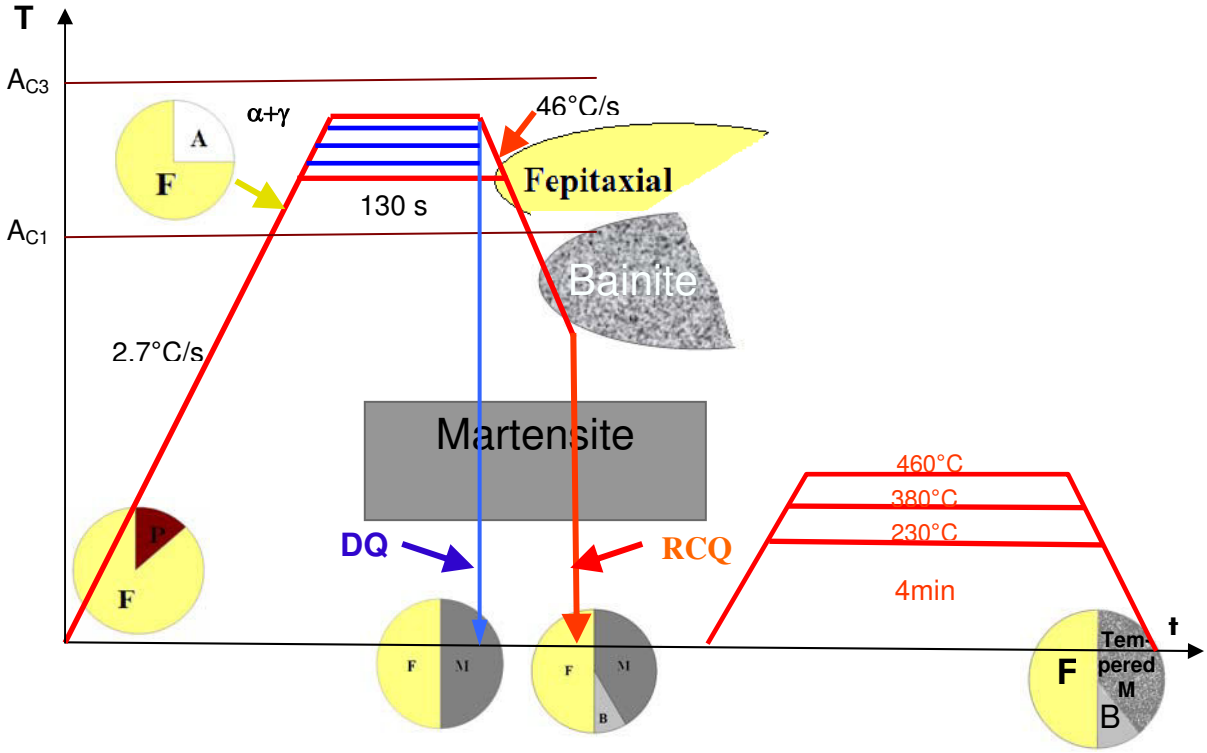

Figure A3.II.2. Schéma des cycles thermiques appliqués à l'acier DP780.

La transformation austénitique a lieu au chauffage, entre 746°C et 845°C (A_{C1} et A_{C3}).

DQ et revenu :

les échantillons sont chauffés à différentes températures de maintien (Tableau A3.II.2). Un palier de maintien de 130 sec est appliqué avant trempe directe à l'eau. Le revenu est effectué aux différentes températures (230°C, 380°C et 460°C) pendant 4 min.

T_{trempe}, °C
755
763
785
790
810
840

Tableau A3.II.2. Températures de maintien pour le cycle DQ.

RCQ et revenu :

Deux températures de maintien sont utilisées 810°C et 840°C. Après le maintien de 130 sec, les échantillons sont refroidis à la vitesse de 46°C/sec jusqu'à la température de trempe et ensuite trempés à l'eau (Tableau A3.II.3). Les conditions de revenu sont identiques à celles utilisées pour les échantillons DQ.

Les échantillons brut de trempe sont systématiquement mis au congélateur afin d'éviter la redistribution de carbone.

$T_{maintien}$, °C	T_{trempe}, °C
810	480 600 700 790
840	520 600 700 820

Tableau A3.II.3. Températures de maintien et de trempe pour le cycle RCQ.

A3.II.3 Trempe directe (DQ)

Les microstructures des échantillons DQ sont utilisés comme microstructures de référence afin de faciliter l'interprétation des microstructures, plus complexes, obtenues au cours du traitement RCQ.

La microstructure DQ est constituée de ferrite et de martensite. La Figure A3.II.3a montre que le taux de martensite augmente avec l'accroissement de la température de maintien. Par conséquent, le taux de carbone dans la martensite diminue avec l'accroissement de température de maintien comme le montre la Figure A3.II.3b. Le taux de carbone, dans la martensite, mesuré par analyse en perte d'énergie (EELS) est comparé avec les concentrations d'équilibre données par le logiciel Ceqcsi®.

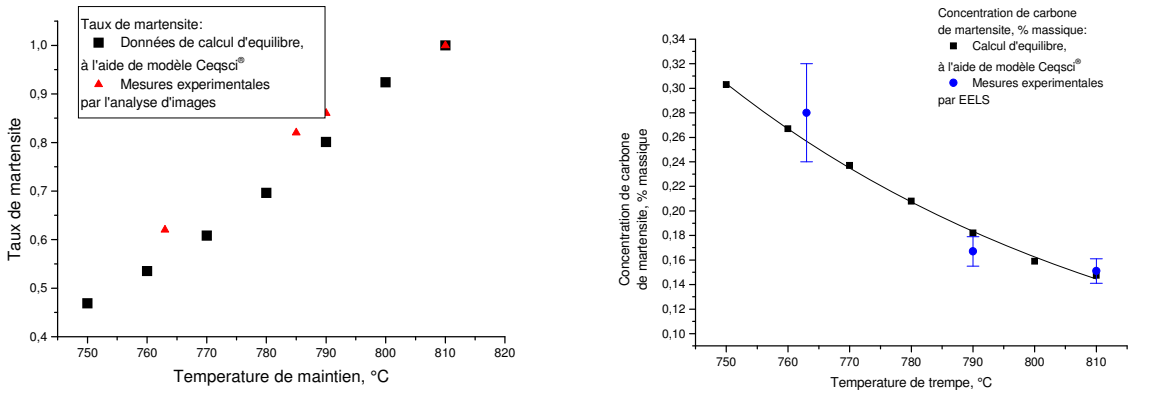

a b

Figure A3.II.3. Evolution du taux de martensite (a) et de la concentration de carbone dans la martensite (b) pour les échantillons DQ.

A3.II.4 Cycle RCQ

Pendant le refroidissement rapide à 46°C/sec, la ferrite se forme. La bainite peut également apparaître aux plus basses températures. Puis, pendant la trempe à l'eau, l'austénite se transforme en martensite. Le refroidissement rapide permet de contrôler le taux de ferrite dans la microstructure.

Le taux de ferrite diminue avec l'accroissement les températures de maintien et de trempe (Figure A3.II.4).

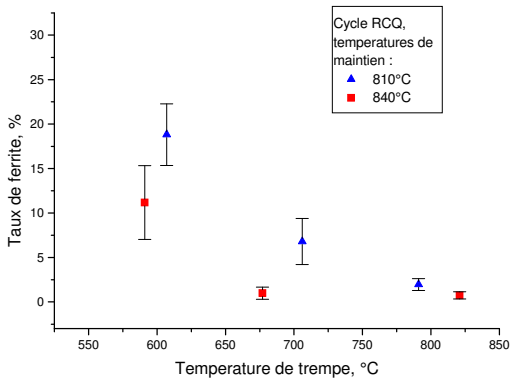

Figure A3.II.4. Evolution du taux de la ferrite en fonction de la température de trempe.

Il est important de noter que dans les microstructures RCQ, quasiment toute la ferrite est formée au cours du refroidissement à 46°C/sec. Le taux de la ferrite intercritique est de l'ordre 1-2%.

Différentes microstructures de l'acier DP ont été obtenues à travers la variation des cycles thermiques. L'évolution des propriétés mécaniques avec la microstructure est étudiée dans le chapitre suivant. La microstructure sera aussi caractérisée de manière détaillée. Ce travail facilitera la compréhension des phénomènes d'endommagement de l'acier DP.

A3.II.5 Comportement en traction

Les courbes de traction des échantillons bruts de trempe présentent un écoulement continu. Elles ne présentent aucun palier élastique (Figure A3.II.5). Ce comportement est caractéristique des aciers DP et il est attribué à leur microstructure (§I.6).

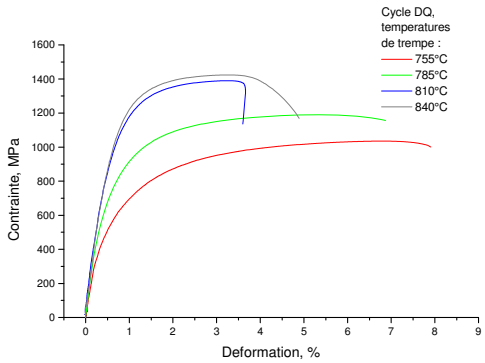

Figure A3.II.5. Courbes de traction pour les cycles DQ.

A3.II.6 Evolutions des propriétés mécaniques à l'état brut de trempe

La Figure A3.II.6a présente l'évolution de la limite d'élasticité avec la température de trempe pour les échantillons DQ. L'analyse de ces courbes montre l'augmentation de la limite d'élasticité avec l'accroissement de la température de trempe, c'est-à-dire avec la diminution du taux de ferrite dans la microstructure (Figure A3.II.6b).

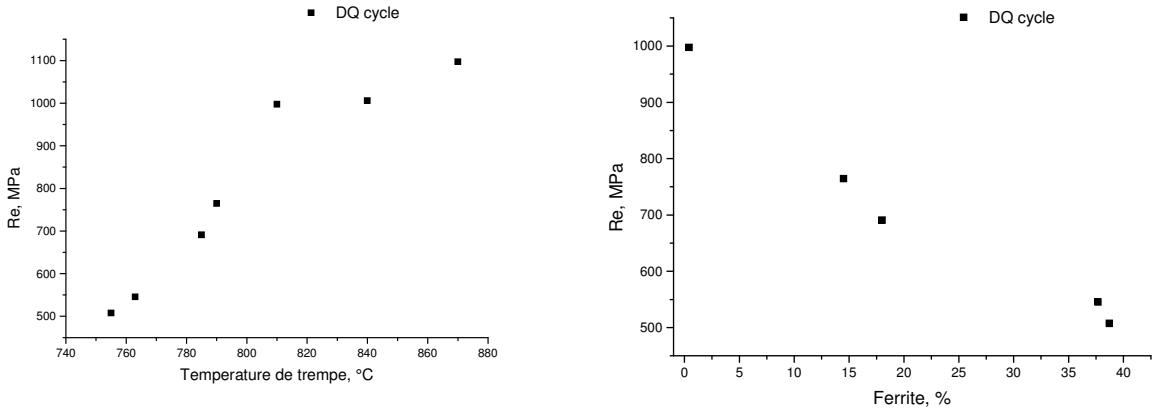

a b

Figure A3.II.6. Evolution de la limite élastique (Re) en fonction de la température de trempe (a) et du taux de ferrite (b).

L'évolution du niveau de résistance mécanique avec la température de trempe et le taux de ferrite dans la microstructure est présentée sur la Figure A3.II.7 (a et b). La Figure A3.II.6b montre que la résistance mécanique (Rm) est pratiquement une fonction linéaire du taux de ferrite.

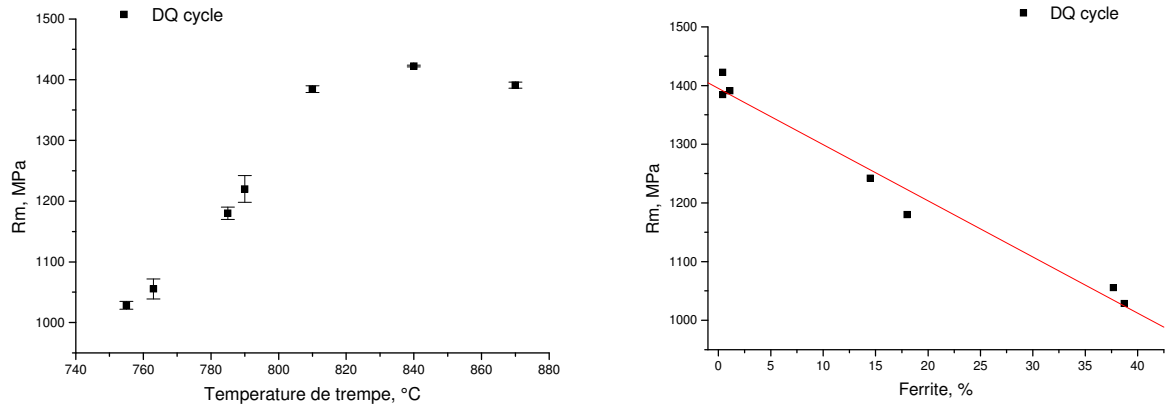

a b

Figure A3.II.7. Evolution de Re avec la température de trempe (a) et le taux de ferrite (b).

La Figure A3.II.8 présente l'effet de la température de trempe et du taux de ferrite sur l'allongement de l'acier. L'allongement diminue avec l'accroissement de la température de trempe et augmente avec l'extension du taux de la ferrite.

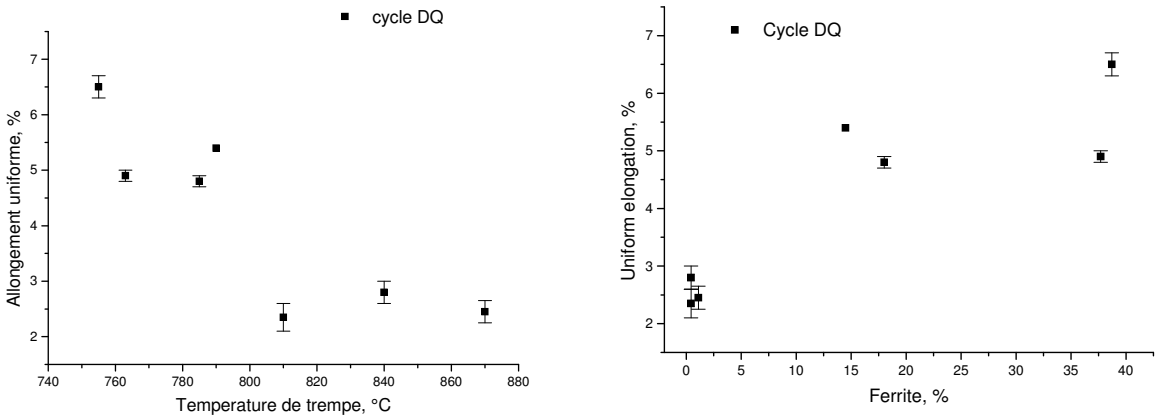

a b

Figure A3.II.8. Evolution de l'allongement uniforme avec la température de trempe (a) et du taux de ferrite (b).

A3.II.7 L'évolution des propriétés mécaniques avec le revenu

Un comportement discontinu en traction est observé après le revenu (Figure A3.II.9). L'apparition du palier élastique est probablement due à un ancrage des dislocations par le carbone [WATE03].

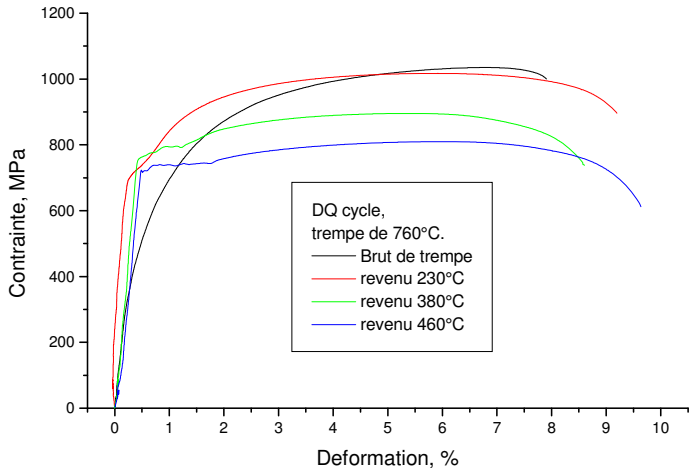

Figure A3.II.9. Courbes de traction après des traitements de revenu.

Avec l'augmentation de la température de revenu, la limite d'élasticité (Re) d'abord augmente et ensuite diminue (Figure A3.II.10). Ce comportement peut être expliqué de la manière suivante :

- l'ancrage des dislocations par le carbone pendant le revenu : une contrainte plus élevée doit être appliquée pour initier leur mouvement,
- la réduction de contraintes résiduelles dans la ferrite pendant le revenu peut expliquer l'augmentation de limite d'élasticité.

La réduction de la limite d'élasticité est associée à l'adoucissement de la martensite.

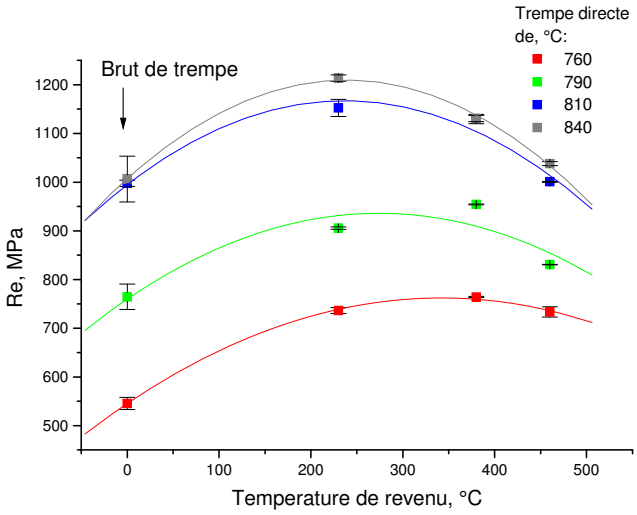

Figure A3.II.10. Evolution de la limite élastique (Re) en fonction de la température de revenu.

On observe une diminution de la résistance mécanique avec l'accroissement de la température de revenu (Figure A3.II.11), ce comportement est lié à l'adoucissement de la martensite.

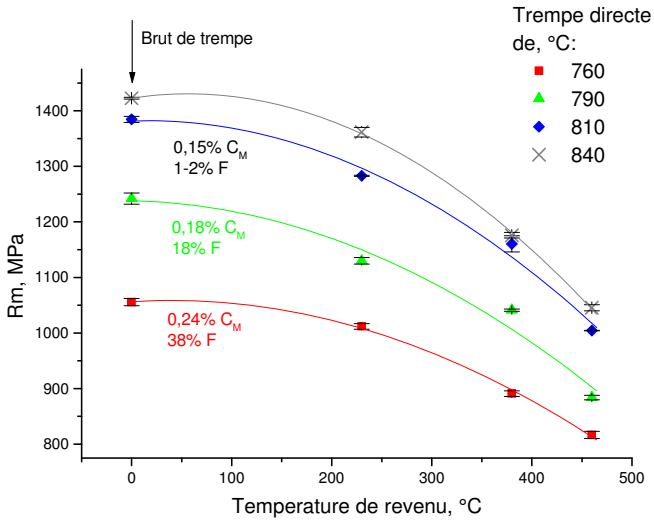

Figure A3.II.11. Evolution de la résistance mécanique (Rm) avec le revenu.

L'adoucissement de l'acier est plus marqué pour des structures à taux de martensite élevée (martensite avec moins de carbone). Cet effet est probablement dû au comportement spécifique de l'acier DP : la présence de ferrite change le force motrice pour le revenu.

Les propriétés mécaniques sont mesurées à l'état brut de trempe et après le revenu. Les mécanismes d'endommagement seront étudiés afin de comprendre les facteurs contrôlant la résistance à l'endommagement de l'acier.

A3.III Caractérisation détaillée de la microstructure

Dans ce chapitre, nous abordons l'évolution de la microstructure avec les paramètres des traitements thermiques. Les phénomènes d'auto-revenu, la sous-structure de la martensite, l'évolution de la microstructure avec le revenu et la structure en bandes seront passés en revue dans le présent chapitre.

A3.III.1 Etude de l'auto-revenu

Les aciers DP ont une température M_s beaucoup plus élevée que la température ambiante (200-400°C). Si le refroidissement dans l'intervalle M_s-M_f est suffisamment lent, une redistribution du carbone peut se produire [SPEI69]. Ainsi, l'étude de la microstructure à l'état brut de trempe est indispensable avant d'analyser les états après le revenu.

Les échantillons DQ sont analysés par MEB-FEG (microscope électronique à balayage équipé d'un canon à émission de champ) à l'état brut de trempe, avant le revenu. Pour les basses températures de maintien (755°C, 785°C et 810°C), la structure de la martensite ne présente pas de carbures d'auto-revenu. L'apparition de la structure "granulée" dans les îlots de la martensite, après le maintien à 840°C, est détectée. Elle peut être due à la précipitation des carbures pendant la trempe (Figure A3.III.1a).

La micrographie électronique à transmission (Figure A3.III.1b) confirme la présence des précipités dans la martensite brute de trempe après le maintien à 840°C

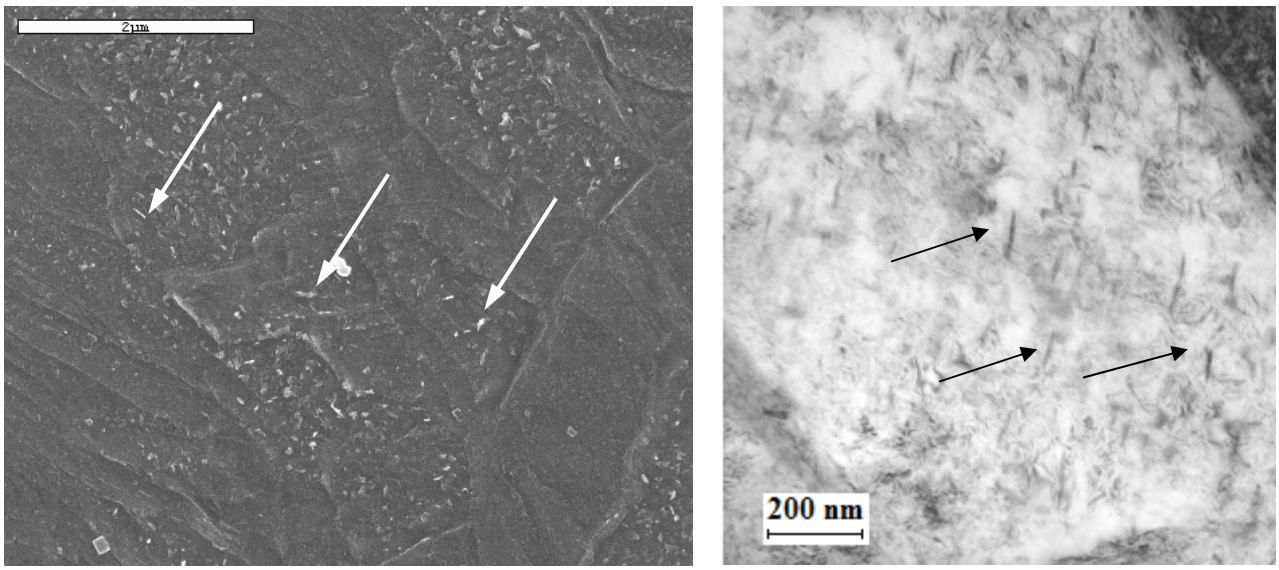

a b

Figure A3.III.1. Micrographie obtenue au MEB (a) et MET (b), montrant la précipitation de carbures dans les îlots martensitiques de l'échantillon maintenu à 840°C.

A3.III.2 L'étude de la morphologie de la martensite au MEB-FEG

Le MEB-FEG permet de révéler la structure fine de la martensite. La martensite en lattes (Figure A3.III.2) est présente pour toutes les températures de maintien Ces observations sont est en accord avec les données de la littérature [KRAU01].
Pour l'acier DP 780 étudié, un taux de l'austénite résiduelle de moins de 3% peut être apprécié. Son influence est donc marginale sur le comportement mécanique de l'acier.

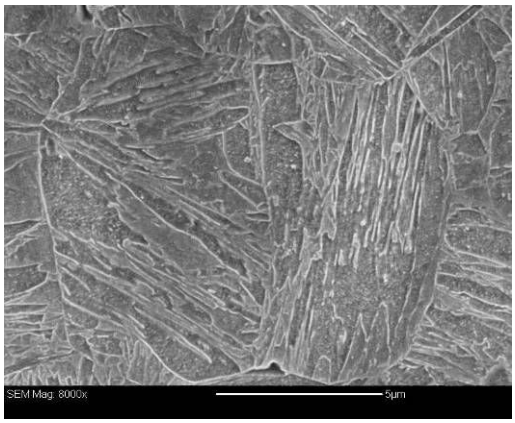

Figure A3.III.2. Micrographie MEB révélant la martensite en lattes dans l'échantillon RCQ après le maintien à 840°C suivi d'une trempe à 700°C.

A3.III.3 L'évolution de la microstructure avec le revenu

La martensite à l'état brut de trempe étant instable, elle peut se décompose à la température ambiante. La structure s'approche alors de celle de l'équilibre, c'est-à-dire une structure ferritique plus des carbures (cémentite). Il y a plusieurs étapes pour la décomposition de la martensite [SPEI92], et les réactions sont souvent superposées [SPEI92] :

- Les carbures ε précipitent aux basses températures de revenu (100-200°C),
- Les carbures ε se dissolvent par la suite et la cémentite se forme aux températures les plus élevées du revenu (200-500°C),
- Les carbures alliés remplacent la cémentite aux températures de revenu supérieurs à 500°C.

L'évolution de la microstructure avec le revenu est présentée sur la Figure A3.III.3 pour un échantillon après un maintien à 760°C. Le revenu à 230°C provoque la redistribution du carbone et la formation de carbures. La précipitation des carbures est plus prononcée pour une température de revenu de 380°C puis elle devient plus grossière à 460°C.

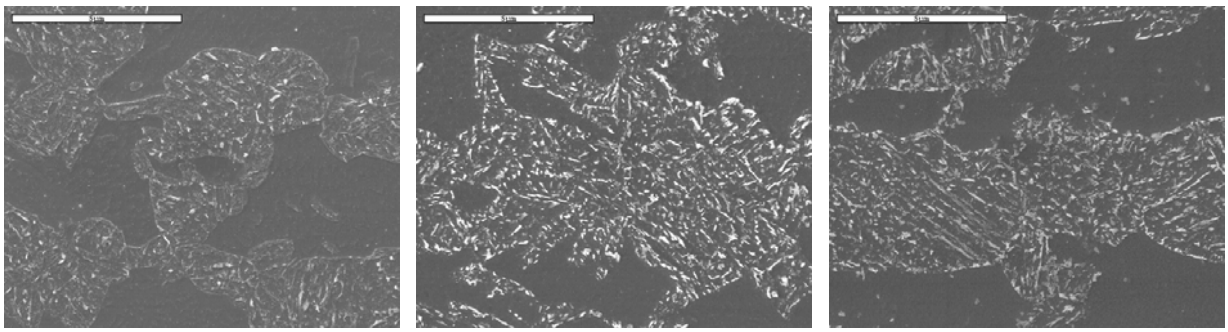

Revenu à 230°C Revenu à 380°C Revenu à 460°C

Figure A3.III.3. Micrographies, obtenues au MEB-FEG, montrant l'évolution de la microstructure avec le revenu pour le cycle DQ après un maintien à 760°C, (Attaque au Picral).

A3.III.4 L'analyse des structures en bandes à la sonde électronique de Castaing

En général, les ségrégations (macro et micro) sont indésirables car elles entraînent une détérioration des propriétés mécaniques.

L'intensité de la macro-ségrégation est mesurée pour un échantillon DQ, après un maintien à 760°C, à l'aide de la sonde électronique de Castaing. Les cartographies du manganèse et du carbone sont acquises simultanément pour estimer l'influence sur le comportement mécanique.

La figure A3.III.4 montre les cartographies à ½ d'épaisseur (dans la zone de ségrégation centrale). Le taux de carbone mesuré dans la martensite est égal à 0.24% ce qui correspond au taux de carbone donné par l'analyse en perte d'énergie (*EELS*).

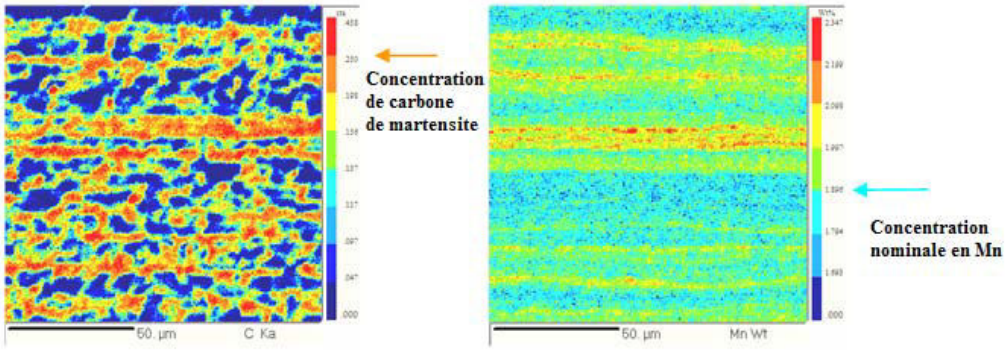

a b

Figure A3.III.4. Cartographies obtenues avec la sonde de Castaing pour le carbone (a) et le Manganèse (b) à ½ d'épaisseur.

La Figure A3.III.5 montre les cartographies de carbone et de Manganèse au ¼ d'épaisseur. Le taux de carbone mesuré est aussi en accord avec le niveau de carbone donné par perte d'énergie (*EELS*).

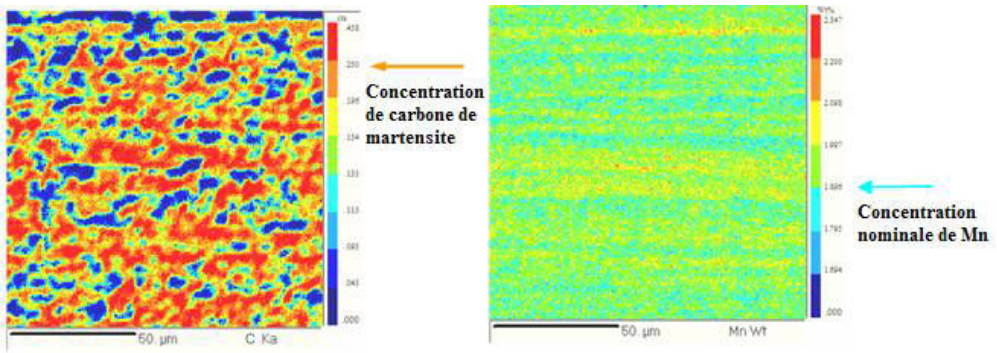

a b

Figure A3.III.5. Cartographies obtenues avec la sonde de Castaing pour le carbone (a) et le manganèse (b) au ¼ d'épaisseur.

Les résultants obtenus à la sonde électronique de Castaing peuvent être résumés comme suit :

- Il n'y a pas de différence de taux de carbone dans la martensite au ¼ et à ½ et épaisseur,
- La ségrégation définie la microstructure locale : la martensite se trouve dans les zones riche en Mn et la ferrite se trouve dans les zones pauvres en Mn.

Les données de la littérature [KRAU99] montrent que la résistance mécanique de martensite est fonction de sa concentration en carbone. Ainsi, on peut conclure que la résistance mécanique de la martensite est la même au ¼ et à ½ 'épaisseur.
Cependant, le taux de martensite est plus élevé au centre, suite à la macro-ségrégation. Cela facilite la propagation de la fissure dans la microstructure, ce qui peut détériorer les propriétés mécaniques.

A3.IV Analyse de distribution de carbone par NanoSIMS

A3.IV.1 Introduction

La spectrométrie de masse d'ions secondaires (SIMS) est une technique d'analyse puissante qui permet d'analyser la composition chimique de la surface par pulvérisation de la zone analysée en surface avec un faisceau d'ions primaires. Cela amorce une cascade de collisions d'atomes ce qui provoque l'émission d'atomes et des clusters d'atomes. Pendant le processus d'éjection certains atomes sont spontanément ionisés. Ces ions secondaires sont caractéristiques de la composition élémentaire de la surface.

La spectrométrie de masse d'ions secondaires (SIMS) est donc une technique d'analyse très sensible : la limite de détection du carbone dans le fer avec la NanoSIMS est de l'ordre de 0.0063 % massique tandis que la limite de détection est d'environ 0.025 % massique avec la technique de perte d'énergie (PEELS) [VAL06, SCOT99].

La cartographie *NanoSIMS* donne une image de distribution du carbone dans la microstructure. L'intensité du signal est proportionnelle à la concentration du carbone dans la phase analysée. Ainsi, la différence de contraste entre la ferrite et la martensite dans l'acier DP est due à la différence du taux de carbone entre les deux phases.

Les échantillons bruts de trempe sont analysés afin de faciliter l'interprétation des microstructures, plus complexes après le revenu. Les échantillons avec les différents taux de phases sont analysés.

A3.IV.2 Résultats expérimentaux et discussion

Des cartographies du taux de carbone ont été réalisées grâce au NanoSIMS du Laboratoire Gabriel Lippmann, Luxembourg.

A3.IV.2.1 Cartographies du taux de carbone à l'état brut de trempe

Après le maintien à 810°C, l'échantillon contient très peu de ferrite, la structure est alors pratiquement 100% martensitique. La distribution du carbone, dans cet échantillon, est hétérogène. La figure A3.IV.1 montre un signal de carbone très intense au niveau de l'interface ferrite/martensite, nous enregistrons donc un enrichissement en carbone de l'interface ferrite/martensite.

Après recuit à 790°C, l'échantillon montre une distribution hétérogène en carbone dans la martensite. Le signal de carbone est aussi plus intense à l'interface ferrite/martensite (Figure A3.IV.2).

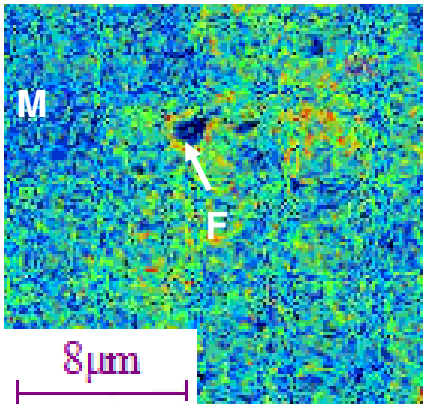

Figure A3.IV.1. Cartographie *NanoSIMS* du carbone pour un maintien à 810°C.

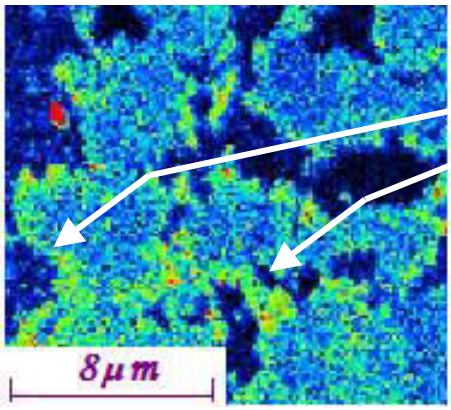

L'enrichissement de l'interface ferrite/martensite

Figure A3.IV.2. Cartographie *NanoSIMS* du carbone pour un maintien à 790°C.

L'échantillon, après maintien à 755°C, possède une distribution de carbone hétérogène dans la martensite : une couche appauvrie en carbone est observé à l'interface ferrite/martensite (Figure A3.IV.3).

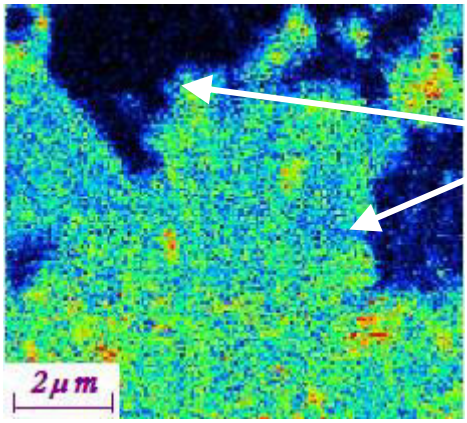

Couche appauvrie à l'ınterface ferrite/martensite

Figure A3.IV.3. Cartographie *NanoSIMS* du carbone pour un maintien à 755°C.

Il est important de noter qu'on obtient différentes microstructures pour les différentes températures de maintien et que la distribution en carbone dans la martensite change en fonction de la température de maintien : on enregistre ainsi soit un enrichissement soit un appauvrissement de l'interface ferrite/martensite. Ces phénomènes de différence de distribution du carbone à l'intérieur des îlots de martensite et au niveau de l'interface ferrite/martensite doivent avoir une incidence sur le comportement mécanique de l'acier DP.

A3.IV.2.2 Résultats des analyses du taux de carbone à l'état revenu

Le traitement de revenu influence la distribution du carbone dans la martensite. Pendant le revenu, le carbone diffuse vers les défauts cristallins de la microstructure (dislocations, joints de lattes, joints de grain) et forme ainsi soit une ségrégation soit une précipitation de carbures au niveau des défauts [PORT92] et par conséquent un appauvrissement des îlots martensitiques.

Après le traitement de revenu à 230°C (Figure A3.IV.4), l'intérieur des îlots de martensite montre un début d'appauvrissement en carbone au profit des précipités.

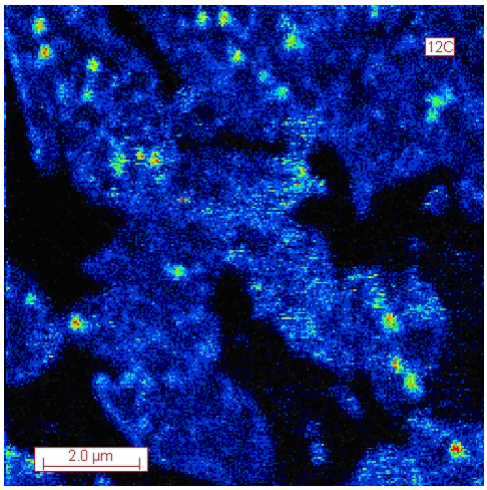

Figure A3.IV.4. Cartographie *NanoSIMS* de l'état DQ 760°C revenu à 230°C.

L'appauvrissement est plus prononcé après le revenu à 380°C. Pour l'échantillon traité à 810°C, le signal de carbone est plus intense à l'interface ferrite/martensite. Pour le maintien à 760°C, l'interface ferrite/martensite ne présente pas de précipitation préférentielle de carbures (Figure A3.IV.5).

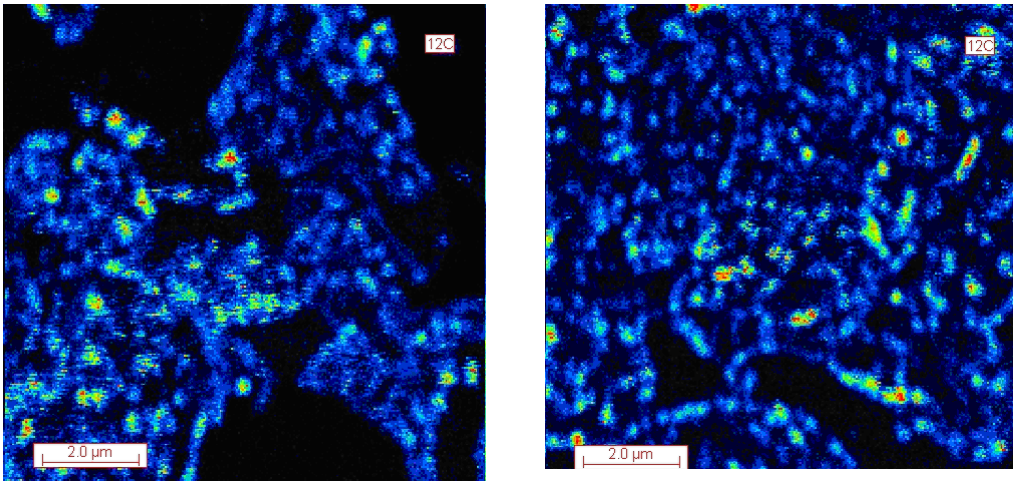

Maintien 760°C Maintien 810°C

Figure A3.IV.5. Cartographies *NanoSIMS* après le revenu à 380°C.

Le phénomène de ségrégation/précipitation aux interfaces est encore plus prononcé après le revenu à 460°C. Les zones appauvries à l'intérieur des îlots martensitiques sont plus étendues. Pour le maintien à 810°C, la précipitation préférentielle des carbures, au niveau des interfaces ferrite/martensite, est nettement bien mise en évidence. Les carbures dans la structure, après le maintien à 760°C, précipitent de manière plus homogène (Figure A3.IV.6).

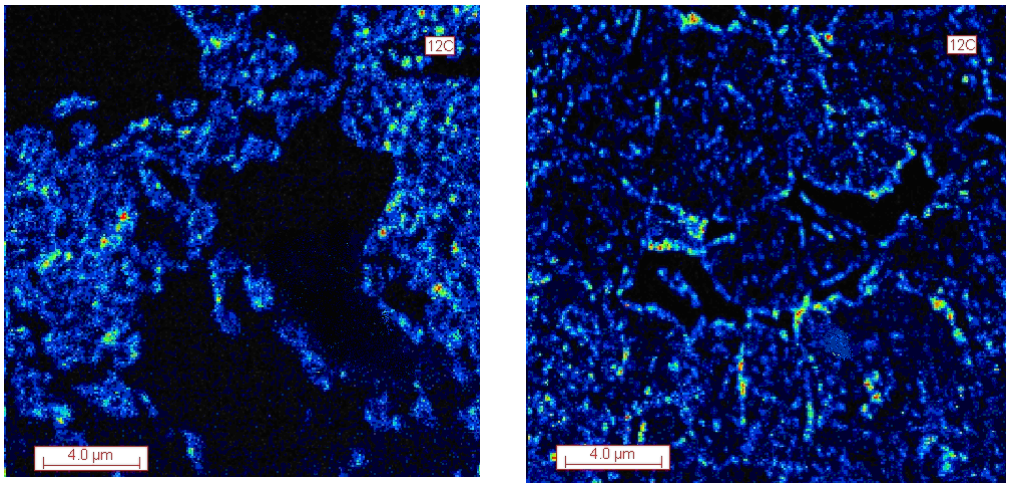

Maintien à 760°C Maintien à 810°C

Figure A3.IV.6. Cartographies *NanoSIMS* après le revenu à 460°C.

A3.IV.2.3 Compréhension des phénomènes de distribution du carbone dans la martensite

La transformation de l'austénite au cours du chauffage-maintien se fait en plusieurs étapes qui ont des échelles de temps différentes.
Dans un premier temps, l'austénite germe à partir des carbures de la microstructure initiale. Ces derniers ont une composition en manganèse différentes et supérieures à celle de la matrice ferritique et ce pour les deux raisons principales suivantes [GOUN05]:

- La première est due au fait que les carbures se forment préférentiellement dans les zones sièges de ségrégation de manganèse,
- La seconde est liée au processus de formation des carbures qui s'accompagnent d'un enrichissement en manganèse qui dépend des conditions de température et de composition.

Le profil de carbone dans les îlots d'austénite va dépendre de la cinétique de formation de l'austénite au cours du chauffage-maintien. La formation de l'austénite peut se décomposer de la manière suivante :

- dissolution de la cémentite,
- croissance de l'austénite.

Cette croissance va être successivement contrôlée par la diffusion du carbone dans l'austénite, la diffusion du manganèse dans la ferrite et enfin par la diffusion du manganèse dans l'austénite (Figure A3.IV.7). Compte tenu du temps de traitement effectué dans notre étude, seuls les processus où la transformation est contrôlée par la diffusion du carbone dans l'austénite et la diffusion du manganèse dans la ferrite doivent être pris en compte.

Le profil de carbone dans les îlots d'austénite, à la fin du maintien, va dépendre des conditions thermocinétiques (conodes de transformation) et du comportement du manganèse qui résulte de la dissolution de la cémentite (et certainement du fait que les îlots peuvent se trouver dans des zones ségrégées ou non).

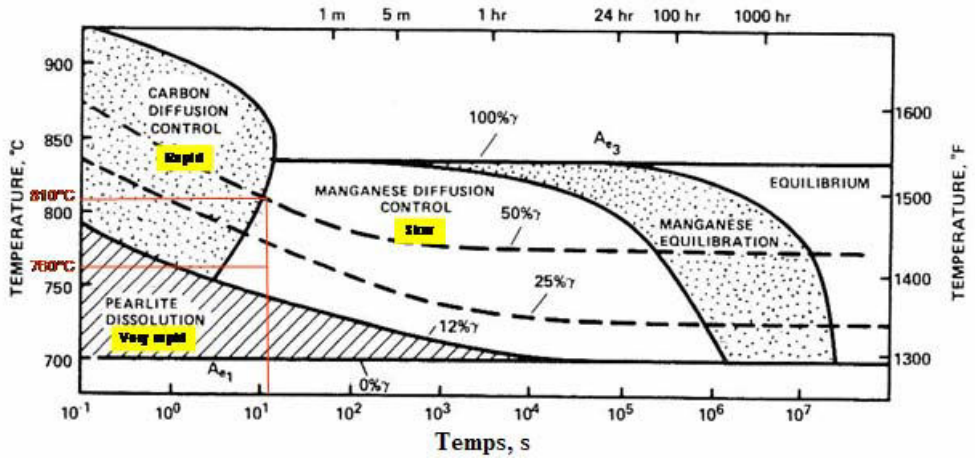

Figure A3.IV.7. Diagramme de croissance d'austénite pour l'acier Fe-0.12C-1.5Mn-0.24Si [SPEI81].

On peut isoler deux cas de figure :

Premier cas:

La dissolution de la cémentite est complète (et/ou quasi complète) mais le profil en manganèse dans les îlots d'austénite n'est pas réparti de manière homogène dû au processus de dissolution.

Des mesures effectuées à la sonde de Castaing montre, sans ambiguïté, ce type de comportement (Figure A3.IV.8). En effet, le cœur des îlots est plus riche en manganèse que la périphérie. Compte tenu du temps de traitement, la conode de transformation impose une isoactivité en carbone dans l'îlot. Ce qui a pour conséquence, compte tenu du profil en manganèse, d'imposer une concentration plus riche en carbone au cœur qu'à la périphérie. (La variation de carbone, ΔC peut être estimée à partir du diagramme des phase et en considérant la fraction d'austénite d'une part, et la conode d'équilibre, d'autre part).

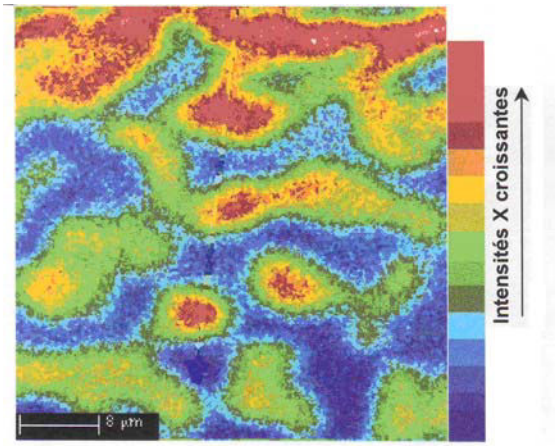

Figure A3.IV.8. Cartographie de distribution de Mn pour l'acier Fe-0.07C-1.5Mn-0.32Si-0.59Cr, maintien à 775°C pendant 33 min et la trempe [PETI99].

Cet état serait exacerbé lorsque les températures de traitement sont basses (parce que le processus de diffusion du manganèse est plus lent à basse température et le biphasé dans le diagramme de phase est plus pentu).

Deuxième cas:

La dissolution de la cémentite est complète et le profil en manganèse dans les îlots d'austénite est réparti de manière homogène. Dans ce cas, il existe deux cas de figure :

- La transformation a atteint un état de quasi-équilibre (on a atteint le moment où l'austénite est contrôlée par la diffusion du manganèse dans la ferrite), dans ce cas l'activité en carbone dans les îlots est constante (manganèse est constant) et donc la composition en carbone est constante. Il n'y a pas de différence de composition en carbone entre le cœur et la périphérie.

- Le deuxième cas : on est dans un processus où la transformation est contrôlée par la diffusion du carbone dans l'austénite, dans ce cas il existe un gradient de composition entre le cœur et la périphérie (on peut estimer le différentiel de composition en carbone à partir des conodes d'équilibre). Ce cas de figure est souvent rencontré lorsque les températures sont plus élevées.

Ainsi, l'enrichissement ou l'appauvrissement à l'interface ferrite/martensite peut être observé en fonction de profil de manganèse dans l'austénite (c'est-à-dire la dissolution de cémentite et la croissance d'austénite). La taille de grain d'austénite varie dans la microstructure. La distribution de carbone est influencée par la taille de grains d'austénite, car elle détermine la longueur caractéristique de diffusion.

A3.V Résistance à l'endommagement par l'expansion de trou

L'essai d'expansion de trou (HE) permet d'évaluer la formabilité de l'acier [ISO06, THUR98]. Les modes de déformation sont complexes pour l'expansion de trou. Les données de la littérature disponible montre que HE est influencé par la microstructure de l'acier et que la différence de dureté entre la ferrite et la martensite est un facteur important qui contrôle la résistance à l'endommagement des aciers DP.

A3.V.1 Résistance à l'endommagement de l'état brut de trempe

L'évolution de *HE* avec la température de maintien pour le cycle DQ et avec la température de trempe pour le cycle RCQ est illustrée sur la Figure A3.V.1.

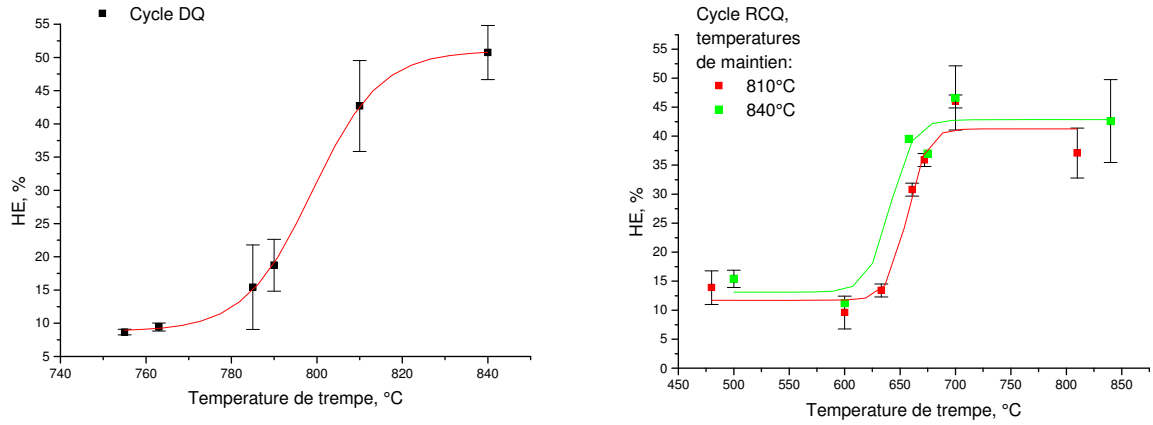

a b

Figure A3.V.1. Evolution de *HE* avec la température de trempe pour l'état trempé DQ (a) et l'état obtenu avec refroidissement rapide contrôlé RCQ (b).

La valeur de *HE* augmente de façon non-lineaire avec l'accroissement de la température de trempe, pour les deux cycles thermiques, DQ et RCQ.

Cependant, on observe une évolution inattendue avec l'augmentation du taux de ferrite : les valeurs de *HE* sont plus élevées pour les bas taux de ferrite et l'augmentation du taux de ferrite conduit à une chute du niveau de *HE* (Figure A3.V.2).

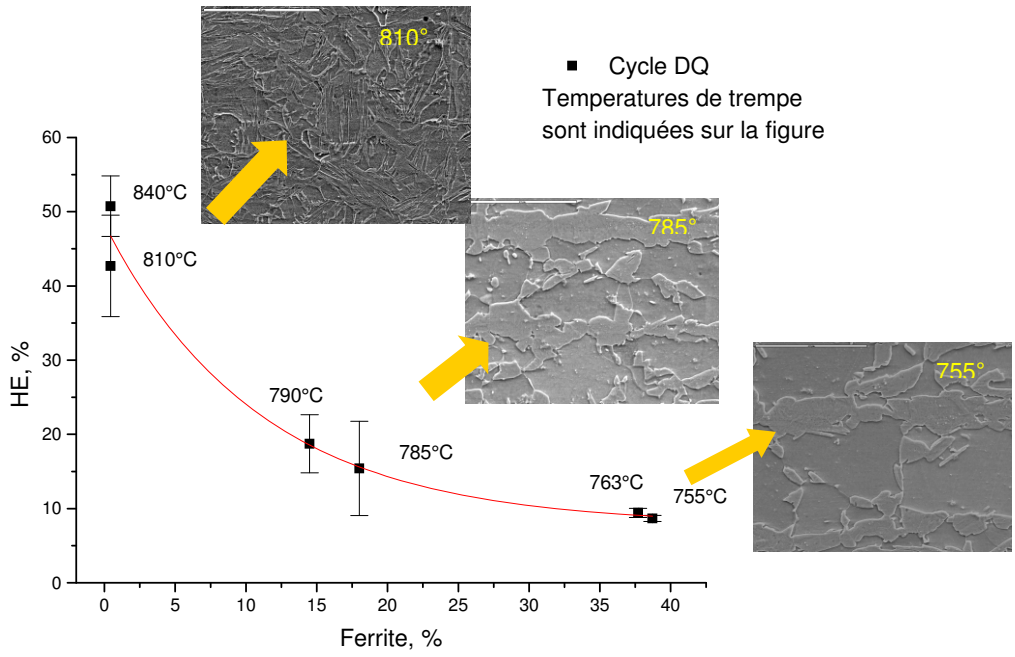

Figure A3.V.2. Evolution de *HE* avec l'accroissement du taux de ferrite.

A3.V.2 Résistance à l'endommagement de l'état revenu

Le revenu est utilisé pour améliorer la résistance à l'endommagement des aciers DP. La figure A3.V.3 montre l'évolution de *HE* avec la température de revenu.

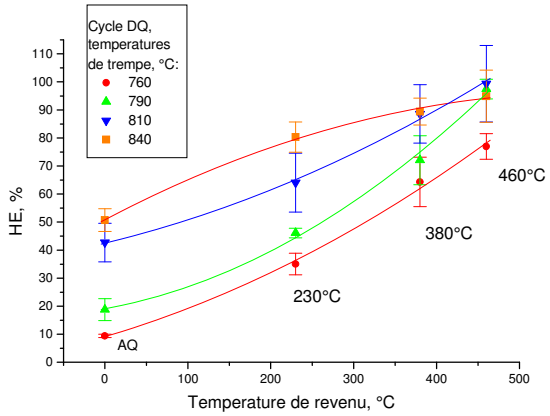

Figure A3.V.3. Evolution de *HE* avec le revenu.

La Figure A3.V.3 montre l'augmentation de *HE* avec l'accroissement de la température de revenu. A titre d'exemples, pour le revenu à 460°C, *HE* change de 10% à 77%. Cette amélioration est probablement due aux effets suivants :

- Diminution des contraintes résiduelles à l'interface ferrite/martensite,
- La différence de comportements mécaniques entre la ferrite et la martensite diminue avec le revenu (adoucissement de la martensite).

La microstructure est plus homogène après le revenu, ce qui améliore la résistance à l'endommagement.

A3.V.3 Corrélation entre l'expansion de trou, *HE* et la résistance mécanique, *Rm*

Il est important d'exploiter maintenant les corrélations entre l'expansion de trou, *HE* et la résistance mécanique, *Rm*. Les corrélations entre *HE* et *Rm* sont illustrées par la Figure A3.V.4.

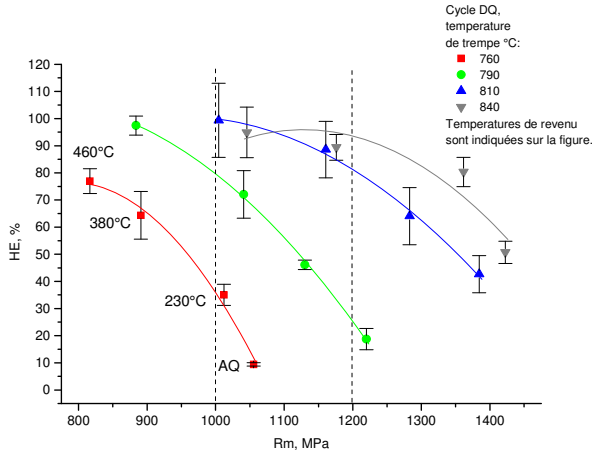

Figure A3.V.4. Corrélation HE-Rm.

Ces corrélations permettent d'optimiser les microstructures, donnant le meilleur compromis résistance mécanique - résistance à l'endommagement. A titre d'exemples, on peut considérer deux niveaux de résistance mécanique : 1000 MPa et 1200 MPa. Ces deux niveaux de résistance sont considérés comme des repères, standardisés par les constructeurs automobiles.

Niveau : Rm=1000MPa

Pour ce grade de résistance mécanique, le niveau de *HE* varie entre 36,5% et 100% en fonction des températures de maintien et de revenu. La microstructure (martensite-37,7 % de ferrite), obtenue après le revenu à 230°C donne le plus bas niveau de *HE* (Figure A3.V.4).
Afin d'améliorer l'expansion de trou, on doit augmenter les températures de maintien et de revenu. Le plus haut niveau de *HE* est atteint pour le maintien à 810°C et le revenu à 460°C. La microstructure, obtenue dans ce cas, est constituée pratiquement de 100% de martensite revenue.

Niveau : Rm=1200 MPa

Pour ce grade de résistance mécanique, le niveau de *HE* varie entre 25% et 93,5 %. Le niveau le plus bas de *HE* donne la microstructure brute de trempe : martensite et 14,5% de ferrite. Encore une fois, pour améliorer l'expansion de trou, il faut utiliser des températures élevées de maintien et de revenu. Le maintien à 810°C ou 840 °C, suivi d'un revenu à 360°C donne une microstructure pratiquement de 100% martensitique revenue et un niveau d'expansion de trou égal à 90%.

La résistance à l'endommagement de l'acier DP 780 est fonction de sa microstructure. L'augmentation du taux de ferrite conduit à une chute de l'expansion de trou. Le revenu améliore donc la résistance à l'endommagement de l'acier.

Dans le chapitre suivant, nous allons nous intéresser aux mécanismes d'endommagement de l'acier DP 780.

A3.VI Mécanismes d'endommagement

La rupture ductile est associée à la déformation plastique. Les étapes sont les suivantes : la germination, la croissance et la coalescence des cavités conduisant ainsi à la rupture du matériau [TEIR88].

A3.VI.1 Analyse fractographique des surfaces de rupture après l'essai de traction

L'analyse fractographique est utilisée pour comprendre le type et les raisons de la rupture. Les surfaces de rupture sont examinées en utilisant le MEB (microscope électronique à balayage).

Les échantillons sont observés à l'état brut de trempe et après revenu. L'échantillon après le maintien à 760°C est caractérisé par une rupture fragile à l'état brut de trempe. Les faciès de clivages sont ainsi mis en évidence par la micrographie de la Figure A3.VI.1.

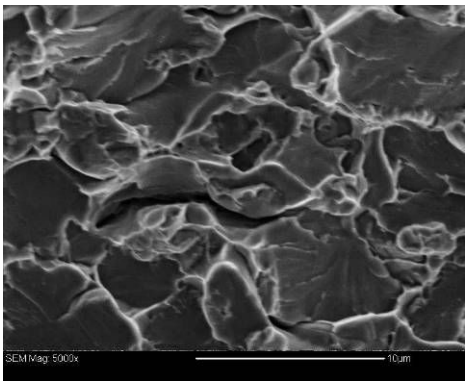

Figure A3.VI.1. Micrographie électronique, obtenue au MEB, montrant des faciès de rupture fragile d'un échantillon brut de trempe 760°C.

Le traitement de revenu élimine la rupture fragile (Figure A3.VI.2). Les surfaces de rupture sont ductiles, elles sont caractérisées par des cupules. Cet effet est probablement dû à l'adoucissement de la phase martensitique et à l'homogénéisation de la structure

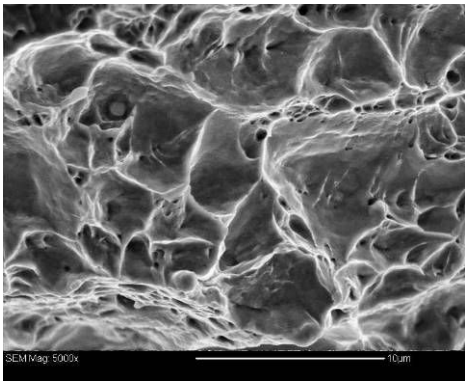

Figure A3.VI.2. Micrographie électronique, obtenue au MEB, montrant des faciès de rupture ductile d'un échantillon après la trempe 760°C et le revenu à 230°C.

Avec l'accroissement de la température de maintien, on observe un changement de mécanisme de rupture : les surfaces ductiles en cupules sont ainsi observées après le maintien à 810°C (Figure A3.VI.3).

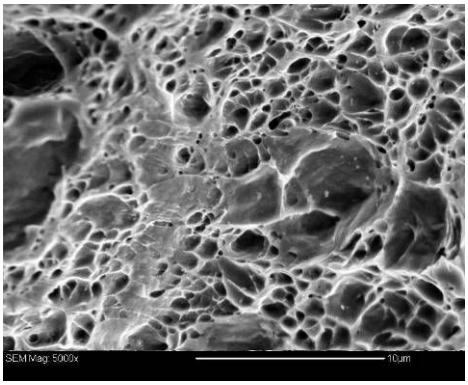

Figure A3.VI.3. Micrographie électronique, obtenue au MEB, montrant des faciès de rupture ductile d'un échantillon brut de trempe à 810°C.

On peut conclure que le mécanisme de rupture, dans les aciers DP de façon générale et pour l'acier DP 780 en particulier, est influencé par le taux des phases présentes ainsi que par le traitement de revenu.

A3.VI.2 L'endommagement pendant l'essai de traction

L'analyse métallographique des échantillons de traction est effectuée après la rupture. Les échantillons sont analysés au MEB-FEG après une attaque de révélation au Nital ou au Picral.

A3.VI.2.1 Etude de l'état brut de trempe

La germination des cavités dans les aciers DP est généralement associée à la phase martensitique : soit via la décohésion de l'interface ferrite/martensite, soit via la rupture fragile de la martensite [STEI88].

Après le maintien à 810°C, la nucléation des cavités a lieu sur les interfaces ferrite/martensite (Figure A3.VI.4).

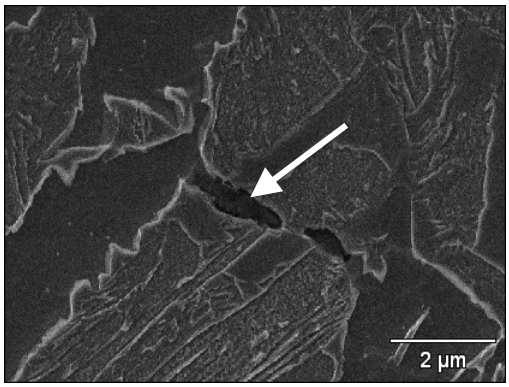

Figure A3.VI.4. Micrographie électronique, obtenue au MEB, montrant l'endommagement dans l'échantillon 810°C brut de trempe.

Pour l'échantillon ayant subi un maintien à plus basse température (790°C), les cavités germent sur les interfaces ferrite/martensite et entre les îlots proches de la martensite (Figure A3.VI.5).

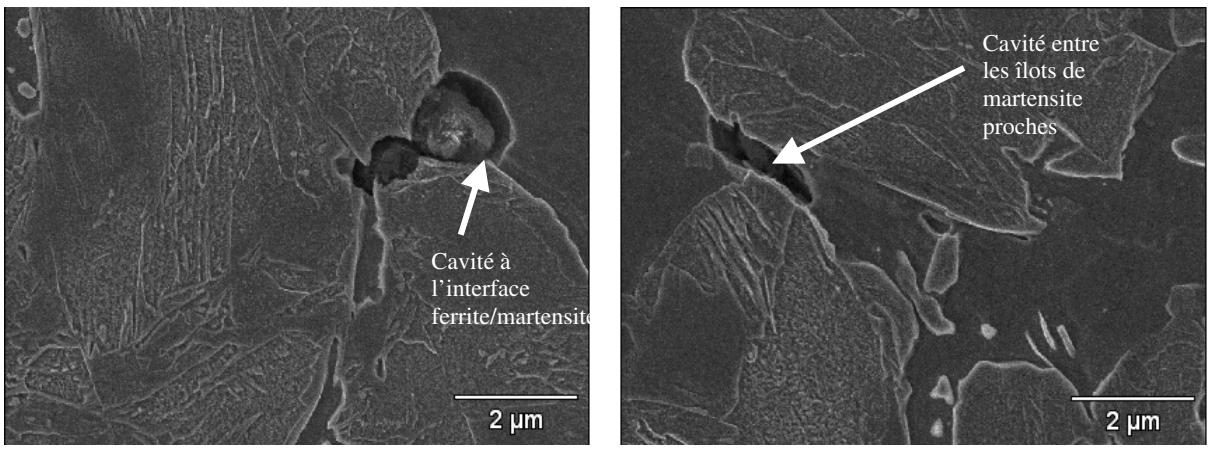

Figure A3.VI.5. Micrographie électronique, obtenue au MEB, montrant des cavités dans l'échantillon 790°C.

Pour l'échantillon ayant subi un maintien à 760°C, des porosités sont détectées sur les interfaces ferrite/martensite, entre les îlots proches de la martensite. Des cavités ont aussi été observées à l'intérieur de la martensite (Figure A3.VI.6).

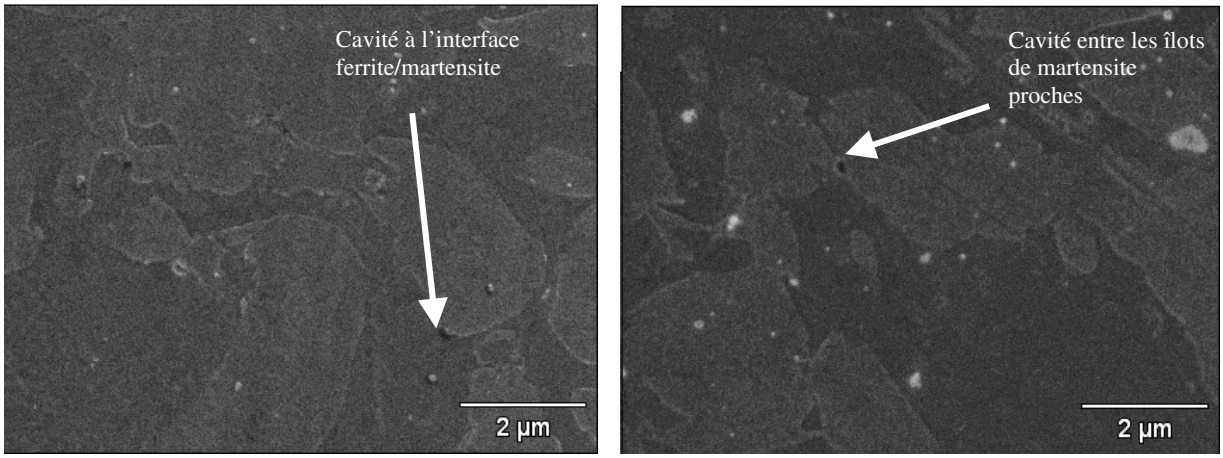

Figure A3.VI.6. Micrographie électronique, obtenue au MEB, montrant des cavités dans l'échantillon 760°C.

A3.VI.2.2 Etude de l'état revenu

Après le revenu, les cavités apparaissent sur les carbures de revenu : cela devient le mode d'endommagement dominant pour les échantillons ayant subi un traitement thermique : maintien/revenu, respectivement à 760°C / 380°C et à 810°C / 230°C (Figure A3.VI.7).

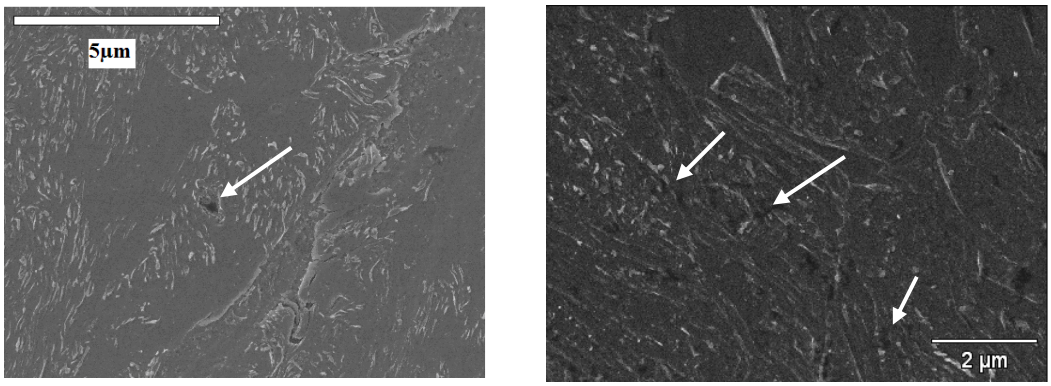

Maintien 760°C, revenu 460°C. Maintien 810°C, revenu 230°C.

Figure A3.VI.7. Micrographie électronique, obtenue au MEB, montrant des cavités sur les carbures de revenu.

Le mode d'endommagement dépend fortement de la microstructure de l'acier. La décohésion de l'interface ferrite/martensite est observée à l'état brut de trempe. Le revenu introduit un nouveau mécanisme d'endommagement : les carbures de revenu présentent les nouveaux sites de germination des cavités. Le modèle, permettant de prédire qualitativement le mécanisme d'endommagement en fonction des paramètres microstructuraux et de traitements thermiques, est développé dans le chapitre suivant.

A3.VII Modélisation de l'endommagement de l'acier Dual Phase

Le changement de mécanisme d'endommagement a été décrit dans le §A3.VI.2.Le phénomène de décohésion de l'interface ferrite/martensite a été décrit dans le model de l'endommagement de l'acier DP [LAND]. L'extension de ce modèle est proposée afin de prendre en compte la nucléation des cavités sur les carbures de revenu.

A3.VII.1 Modélisation de la décohésion de l'interface ferrite/martensite

La décohésion de l'interface a lieu lorsque la contrainte appliquée atteint la contrainte critique de cohésion σ_c, de cette interface. La contrainte critique est estimée à σ_c = 1230 MPa, pour l'interface ferrite/martensite [TOMO81]. L'évolution de la contrainte de l'interface ferrite/martensite avec le revenu est illustrée par la Figure A3.VII.1.

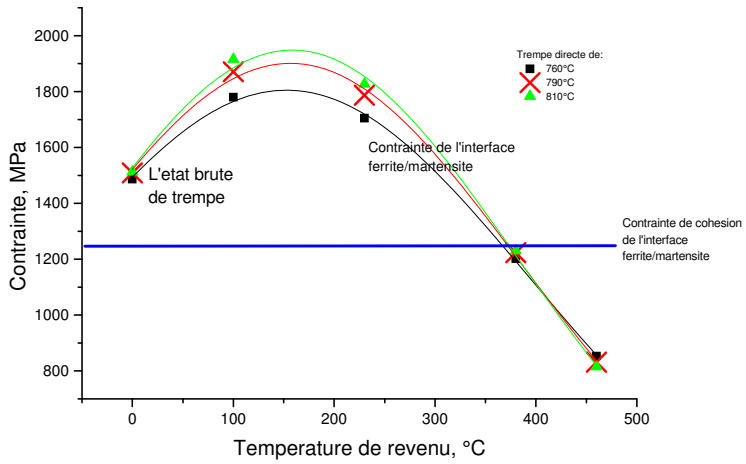

Figure A3.VII.1. Evolution de la contrainte de l'interface ferrite/martensite avec le revenu. La contrainte critique, σ_C, de cohésion de l'interface ferrite/martensite est indiquée sur le graphe (ligne horizontale à 1230 MPa).

Le modèle prédit que l'accroissement de la température de revenu conduit à une augmentation de la contrainte de l'interface ferrite/martensite, malgré une chute de la différence entre les niveaux de dureté des deux phases.
A basses températures de revenu (<300°C), la contrainte de l'interface augmente par rapport à l'état brut de trempe. Ainsi, le matériau devient plus susceptible à l'endommagement au niveau de l'interface ferrite/martensite. C'est seulement pour les plus hautes températures de revenu, que la réduction de contrainte à l'interface est observée (comparé à l'état brut de trempe). La suppression de l'endommagement à l'interface ferrite/martensite est prédite par le modèle à partir des températures de revenu de 400°C.

A3.VII.2 Formation des cavités sur les carbures de revenu

La modélisation de l'endommagement de martensite revenue est difficile, car nous ne possédons pas de paramètres pertinents suivants : fraction de carbures, leur morphologie, évolution du taux de carbone de la martensite avec le revenu. Par ailleurs, un système où trois phases coexistent, plusieurs mécanismes de durcissement et d'endommagement seront en compétition et cela mérite d'être étudié de façon concomitante, malgré la complexité qui se profile.

D'après les observations expérimentales, les cavités se forment sur les carbures dans la martensite revenue.

La décohésion de l'interface ferrite/martensite est observée à la température de revenu de 230°C pour le maintien à 760°C. Après le revenu à 380°C, la décohésion de l'interface ferrite/martensite est remplacée par celle occasionnée par les carbures apparaissant à l'intérieur de la martensite. Les cavités sur les carbures sont observées à plus basses température de revenu (230°C) pour le maintien à 810°C et l'endommagement à l'interface ferrite/martensite est supprimé malgré le fait que la contrainte critique, σ_c, est élevée.

Il est bien établi que l'incompatibilité de déformation entre les carbures et la martensite génère une contrainte interne, σ_i [ALLA08]. On peut calculer le rapport σ_i / σ_{eq}, où σ_{eq} est la contrainte équivalente appliquée. Le rapport σ_i / σ_{eq} est lié à la triaxialité locale, T_{loc}, à l'interface carbure/martensite [ARGO75, LAND] : la triaxialité augmente avec l'accroissement du rapport σ_i / σ_{eq} [ARGO75, LAND]. La Figure A3.VII.2 montre les résultats de calcul de triaxialité locale pour les différentes températures de revenu.

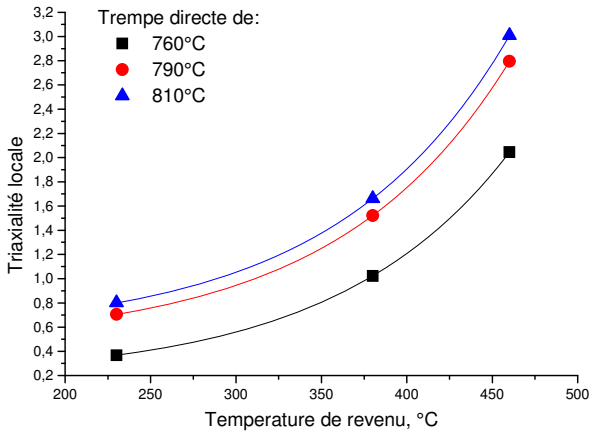

Figure A3.VII.2. Evolution de la triaxialité à l'interface carbure/martensite avec la température de revenu.

L'évolution de la triaxialité à l'interface carbure/martensite avec le taux de carbone de martensite et le revenu appelle les commentaires suivants:

- T_{loc} augmente avec la réduction du taux de carbone de la martensite : la probabilité de l'endommagement à l'interface carbure/martensite augmente ; ce qui est en accord avec les observations expérimentales,

- T_{loc} augmente avec l'accroissement de la temperature de revenu : la probabilité de l'endommagement à l'interface carbure/martensite augmente ; ce qui est aussi en accord avec les observations expérimentales.

Maintenant, il est possible de combiner les résultats des Figures A3.VII.1 et A3.VII.2 pour obtenir la caractéristique qualitative globale de l'endommagement de l'acier DP 780. A basses températures de revenu, T_{loc} est petit, tandis que la contrainte critique, σ_c, est élevée : le

mécanisme d'endommagement dominant est la décohésion au niveau l'interface ferrite/martensite.

Avec l'accroissement de la température de revenu (300°C) la contrainte critique, σ_c, chute, tandis que T_{loc} augmente ; ce qui permet de mettre en relief l'existence d'une région de transition entre deux mécanismes.

Aux plus hautes températures, le revenu favorise l'endommagement à l'interface carbure/martensite. L'impact du taux de carbone de martensite à l'état initial sur la contrainte critique, σ_c, est insignifiant.

Cependant, le taux de carbone de martensite a plus d'effet sur $T_{loc.}$. La triaxialité de contrainte à l'interface carbure/martensite est plus élevée pour les bas taux de carbone de martensite. Ainsi, l'apparition des cavités sur les carbures est observée à plus basses températures de revenu, pour l'échantillon ayant subi un maintien à 810°C.

Le modèle, développé dans le présent chapitre, permet ainsi de prédire qualitativement le mécanisme d'endommagement de l'acier Dual-Phases, en fonction des paramètres microstructuraux et du traitement thermique.

Conclusion générale

Dans ce travail, l'évolution de la microstructure et la relation entre la microstructure et les mécanismes d'endommagement de l'acier Dual-Phases 780 ont été abordés et reliés aux différents paramètres de traitements thermiques (trempe, revenu).

Les techniques d'analyse locale, comme la perte d'énergie (*EELS*) et la spectrométrie de masse d'ions secondaires *(SIMS)* ont été d'un grand apport à la détection du carbone dans la martensite et au niveau des interfaces, principalement ferrite/martensite. L'appréciation de la distribution du carbone au niveau des interfaces et dans les îlots de la martensite a permis de mieux comprendre l'évolution de la microstructure au cours des traitements thermiques.

L'étude approfondie de la microstructure nous a permis d'évaluer les principaux paramètres qui varient avec le traitement thermique. La concentration de carbone dans la martensite est apparue comme un paramètre central permettant la compréhension de l'évolution de la microstructure et le lien avec les propriétés de résistance mécanique et de résistance à l'endommagement.

La distribution spécifique des dislocations dans l'acier DP a été relevée par la microscopie électronique en transmission (MET). Ces dislocations sont responsables du comportement mécanique continu de l'acier DP.

L'expansion de trou s'est révélée comme un essai mécanique très pertinent pour la caractérisation de l'endommagement de l'acier DP 780. En effet, à l'aide de cet essai, nous avons pu montrer que la résistance à l'endommagement évolue de manière inattendue avec la variation du taux de la phase ductile (ferrite) : le niveau de formabilité chute avec l'augmentation de fraction de la ferrite. En considérant la déformation critique de décohésion pour la martensite brute de trempe il a été possible d'expliquer les évolution expérimentale de *HE* de l'état brut de trempe et revenu.

Le traitement de revenu s'est avéré efficace pour l'amélioration des propriétés d'endommagement de l'acier DP 780. L'impact du revenu sur la microstructure de l'acier DP 780 est attribué, entre autres, à la précipitation des carbures dans la martensite.

L'analyse fractographique a montré que le mécanisme de rupture est fortement influencé par la microstructure. L'augmentation du taux de martensite et le revenu suppriment la rupture fragile.

Deux sites de germination de cavités ont été identifiés : l'interface ferrite/martensite et l'interface carbure/martensite. La différence d'endommagement entre l'état brut de trempe et l'état revenu a été confirmée par l'essai de traction in situ : le revenu ralentit l'endommagement en diminuant le nombre de cavité, responsable de la rupture.

Un modèle qualitatif de mécanisme d'endommagement a été développé afin de pouvoir interpréter les résultats expérimentaux et de prédire l'endommagement de l'acier DP 780. Un changement de mécanisme d'endommagement a été relevé.

Le modèle qualitatif ainsi développé pour l'acier DP 780 servira de base d'approfondissement de modèles plus élaborés et quantitatifs permettant la compréhension et la prédiction de l'endommagement des aciers Dual-Phases, de façon générale.

Perspectives

L'amélioration des propriétés d'endommagement de l'acier à très haute résistance mécanique est le but principal de ce travail. En effet, l'augmentation de niveau de résistance mécanique (par l'augmentation de taux de carbone) amène à l'accroissement de la susceptibilité à l'endommagement. La compréhension et maîtrise des mécanismes d'endommagement sont donc indispensables.

- Les mécanismes d'endommagement de l'état revenu sont complexes et demandent la modélisation plus sophistiquée. Des calcules en éléments finis sont nécessaires afin de prendre en compte l'influence de la morphologie et de la fraction des carbures,

- Le travail expérimental supplémentaire est nécessaire afin de mesurer le taux de carbone dans la martensite revenu,

- Cette approche peut être appliquer à d'autre grades des aciers Dual-Phases prenant en compte l'influence des éléments de (micro) alliage,

- L'endommagement des microstructures plus complexes peut être aussi étudié.

Abbreviations and Symbols

List of abbreviations

AQ	As Quenched
A_{C1}	Austenite transformation start temperture during heating
A_{C3}	Austenite transformation end temperature during heating
at. %	atomic percent
bct	body centered tetragonal
CCR	Critical Cooling Rate
CCT	Continuous Cooling Transformation diagram
C_m	martensite carbon content
CP	Complex Phase
DDQ	Deep Drawing Quality
DP	Dual Phase steel
DQ	Direct Quenching
F	Ferrite
FC	Fast Cooled
FEG	field-emission gun
HA	High Alloyed
HE	Hole Expansion
HSLA	High strength Low Alloy steel
HT	HOWAQ-TWICE
LA	Low Alloyed
OIS	octahedral interstitial site
RA	Reduction of Area
RCQ	Rapid Cooling and Quenching
SEM	Scanning Electron Microscopy
SIMS	Secondary Ion Mass Spectroscopy
TEM	transmission electron microscopy
TME	Tempered Martensite Embrittlement
TRIP	Transformation Induced Plasticity
TS	tensile stress
TTT diagram	Fraction **t**ransformation as a function of **t**ime and **t**emperature
UE	Uniform Elonagation
UTS	ultimate tensile strength
WQ	water quenching
WQHM	Water Quenched with a High amount of Martensite
WQLM	Water Quenched with a Low amount of Martensite
wt.%	weight percent
YS	yield stress

List of symbols

α	ferrite
$a_{\alpha M}$	Martensite lattice parameter
$c_{\alpha M}$	Martensite lattice parameter
M_f	Martensitic finish temperature
M_S	Martensitic start temperature
γ	austenite

References

[ABBA03] Al-Abbasi F.M., Nemes J.A., Micromechanical modeling of dual-phase steels, Int. J. Mech. Sci., v. 45, 2003, pp. 1449-1465

[ALLA08] S.Allain, O. Bouaziz, Microstructure based modeling for the mechanical behaviour of ferrite-pearlite steels suitable to capture isotropic and kinematic hardening, Mat. Sci. and Eng. A, v.496, 2008, pp. 329-336

[ALLAIN] work of S.Allain to be published

[ARGO75] Argon A.S., Im J., Safoglu R., Cavity formation from inclusions in ductile fracture, Met.Trans. A, v 6A, 1975, pp. 825-837

[AVRA09] G.Avramovich-Cingara et ali, Mater.Sci.Eng.A, 2009, doi:10.1016/j.msea.2009.03.055, 2009

[BALL82] N.K.Balliger, Ductile fracture of dual-phase steels, Advances in the physical metallurgy and applications of steels, 1982, pp. 73-83

[BECK79] J. Becker, E. Hornbogen, Microscopic analysis of the formation of dual-phase steels, Structure and properties of dual-phase steels, 1979, pp.20-39

[BENO87] Benoit D. et ali, Microanalyse par sonde electonique: spectrometrie de rayons X, ANRT, 1987

[BERA96] Beranger G., Henry G., Sanz G. The book of steel, 1996

[BHAD04] H. K. D. H. Bhadeshia, Tempered martensite, University of Cambridge, www.msm.cam.ac.uk

[BHAD99] H.K.D.H. Bhadeshia, The bainite transformation: unresolved issues. Mat. Sci. and Eng. A273-275, 1999, pp. 58-66

[CHOI09] K.S. Choi et al., Met.Mat.Trans. A, v. 40A, 2009, pp. 796-809

[COBO09] S. Cobo, ArcelorMittal internal report, 2009

[COLI07] Colin C., Caractérisation microstructurale d'aciers laminés à froid martensitique revenues à basses températures, Arcelor reseach, 2007

[DAVI78] Davies R.G. Influence of martensite composition and content on the properties of dual phase steels, Met. Trans. A, vol. 9A, 1978, pp.671-679

[DAVI81] R.G. Davies, Tempering of dual-phase steels, Fundamentals of Dual-phase steels. Conference and proceedings. Chicago, February, 1981, pp. 265-277

[DELB03] L. Delbis de Lacerda, DP steel toughness, Arcelor internal report, 2003

[DRIL02] Drillet J., Bouleau D., Caractérisation microstructurale des aciers TRIP à l'IRSID, R&D Arcelor, 2002

[ElSE90] I. A. El-Sesy et al., Effect of intercritical temperature and cold deformation on the kinetics of austenite formation during the intercritical annealing of DP steels. Mat. Tech., 1990, vol.3, pp. 131-135

[EMBU81] Embury G.D., Duncan J.L, Formability of dual-phase steels, Fundamentals of Dual-phase steels. Conference and proceedings. Chicago, February, 1981, pp. 333-345

[FANG03] X.Fang et al., Effects of tempering temperature on tensile and hole expansion properties of a C-Mn steel. Journal of materials processing technology, vol. 132, 2003, pp. 215-218.

[FRAN04] François D., Endommagements et rupture de matériaux, Ecole centrale de Paris, EDP sciences, 2004

[GAU81] J.S. Gau et al., Microstructure and properties of dual-phase steels containing fine precipitates. Fundamentals of Dual-phase steels. Conference and proceedings. Chicago, February, 1981, pp. 47-58

[GOUN05] M. Gouné, P. Maugis, T. Iung, "Application of thermodynamics and diffusion in solids to the development of high strength steels for automotive industry", Materialwissenschaft und Werkstofftechnik, 36 (10), 467-470, 2005

[GRAN77] R.A. Grange, C.R. Hribal, L.F Porter. Hardness of tempered martensite in carbon and low-alloy steels. Met. Trans. A. vol. 8A, November 1977, pp. 1775-1785

[GRIF20] Griffith A.A. Phil.Trans.R.Soc, v A221, 1920, p.163

[HANS81] S.S. Hansen, R.R Pradhan, Structure/property relationships and continuous yielding behaviour in Dual-Phase steels, Fundamentals of Dual-phase steels. Conference and proceedings, Chicago, February, 1981, pp. 113-141

[HASE04] K. Hasegawa, Effects of microstructure on stretch-flange-formability of 980 MPa grade cold-rolled ultra high strength steel sheets, ISIJ Int., v. 44, (2004), N3, pp.603-609

[HAYA77] S. Hayami et al., Recent developments in formable hot- and cold-rolled HSLA including dual-phase sheet steels. Formable HSLA and dual-phase steels, 1977, pp.167-180

[HONE84] Honeycombe R.W.K., the plastic deformation of metals, Edward Arnold edition, London, 1984

[HYUN02] D.Y. Hyun et al., Estimation of hole flangeability for high strength steel plates, Journal of Mat. Proc Tech., 130-131, 2002, pp. 9-13

[IBRA75] N. Ibrahim, J.D. Embury, Mater.Sci.Eng, v.19, 1975, p.147

[ISO06] ISO TC 164/SC 2 N 479, Method of hole expanding test, 2006

[ISO06C] ISO 148-1, Charpy pendulum impact test, 2006

[JACQ07] Jacques P et al., Multiscale mechanics of TRIP-assisted multiphase steels: I. Characterization and mechanical testing, Acta Mat., v55, 2007, pp. 3681-3693

[KORZ82] D.A. Korzekwa et al., Aging susceptibility of retained and epitaxial ferrite in dual-phase steels. Met. Trans. A, vol. 13A, November 1982, pp. 2061-2064

[KRAU01] G. Krauss. Deformation and fracture in martensitic carbon steels tempered at low temperatures. Met. Mat. Trans. A, vol. 32A, april 2001, pp. 861-877

[KRAU71] Krauss G., Marder A.R, The morphology of martensite in iron alloys, Met.Trans., vol. 2, 1971, pp. 2343-2357

[KRAU92] G. Krauss, C.J. McMahon, Low-toughness and embrittlement phenomena in steels. Martensite, February 1992, pp.295-321

[KRAU99] Krauss G Martensite in steel: strength and structure, Mat. Sci. and Eng., A 273-275, 1999, pp.40-57

[KRUP81] R.P. Krupitzer, Strain-aging behaviour in a continuously-annealed dual-phase steel, Fundamentals of Dual-phase steels. Conference and proceedings. Chicago, February, 1981, pp. 315-330

[LAFR99] Lafrance M., Propriétés d'emploi des tôles fortes en acier, Revue de Métallurgie, 1999

[LAND] Landron C., Bouaziz O., Damage nucleation in Dual-Phase steels, to be published in Scripta Materalia

[LAWS80] Lawson R. D. et ali, An etching technique for microaloyed Dual Phase steels, Metallography, v. 13, 1980, pp. 71-87

[LEPE80] LePera F. S., Improved etching technique to emphasize martensite and bainite in High-Strength Dual-Phase steels, J; of Metals, March 1980, pp. 38-39

[LIVC90] Livchits B.G., Metallography, Metallurgy edition, 1990, Moscow. Лившиц Б.Г., Металлография, учебник для вузов, М., Металлургия, 1990

[MAIR08] Maire E. et al., Initiation and growth of damage in a dual-phase steel observed by X-ray microtomography, Acta Mat., v. 56, 2008, pp. 4954-4964

[MAND85] S.Mandziej et al., Dislocations and volume accommodation in dual-phase steels. Strength of metals and alloys (IC SMA7). Monreal, Canada, 12-16 august 1985. pp. 545-550

[MARG81] A.R.Marger, The structure-property relationships in chromium-bearing dual-phase steels. Fundamentals of Dual-phase steels. Conference and proceedings. Chicago, February, 1981, pp. 145-160

[MAZI07] M. Mazinani, W. J. Poole, Effect of martensite plasticity on the deformation behaviour of a low-carbon DP steel, Met. Mat. Trans., v.38A, 2007, pp.328-339

[MEYR01] G. Meyrick, H. Wagoner, Tempering of martensite and the effect of alloying elements, Physical metallurgy of steels, 2001

[NISH81] A. Nishimoto et al., Relation between hole expansion formability and metallurgical factors in dual-phase steel sheet. Fundamentals of Dual-phase steels. Conference and proceedings. Chicago, February, 1981, pp. 447-463

[PERR07] F. Perrard, C. Scott, V precipitation during intercritical annealing in cold rolled TRIP steel, ISIJ International, vol.47, N8, 2007, pp.1168-1177

[PETI99] Petitgand G., Remy B., Observation de l'interface martensite/ferrite par analyse du Mn à la sonde électronique, L'IRSID, 1999

[PORT92] Porter D.A., Easterling K.E, Phase transformations in metals and alloys, 1992

[POTT06] N. Pottore et al., Effect of C, Mn, Si and Al additions on the mechanical properties of 980 MPa tensile strength, cold rolled, advanced high-strength steel. Iron and steel technology. Vol. 3, no. 9, pp. 63-70. Sept. 2006

[RACH77] M.S. Rachid, Relationship between steel microstructure and formability, Formable HSLA and dual-phase steels, 1977, pp. 1-24

[RACH81] M.S. Rachid, Tempering characteristics of a vanadium containing dual phase steel, Fundamentals of Dual-phase steels. Conference and proceedings. Chicago, February, 1981, pp. 249-264

[RENG85] W. Rengen, D.Lanku. Effect of tungsten and molybdenum on the strength and toughness of super-high strength steels. Strength of metals and alloys (IC SMA7). Monreal, Canada, 12-16 august 1985. pp. 1157-1162

[RICE69] Rice J.R, Tracey D.M., On the ductile enlargement of voids in triaxial stress fields, J.Mech.Phys.Solids, 1969, v.17, pp. 201-217

[RIED93] H. Riedel, Plastic deformation and fracture of materials, edited by H. Hughrabi, 1993

[RIGS77] J.M Rigsbee, P.J. VanderArend, Laboratory studies of microstructures and structure-property relationships in dual-phase HSLA steels, Formable HSLA and dual-phase steels, 1977, pp. 56-86

[SCOT99] Scott C. et ali, Quantitative analysis of carbon by Electron Energy Loss Spectroscopy, R&D IRSID, 1999

[SHEN86] Shen H.P. et al., Microscopic deformation behaviour of martensitic-ferritic DP steels, Mat. Sci. tech, 1986, v.2, pp.28-33

[SPEI69] Speich G.R. Tempering of low-carbon martensite, Trans. AIME, v.245, 1969, p.2553

[SPEI81] G.R. Speich et al., Formation of austenite during intercritical annealing of dual-phase steels, Metal. Trans. A, 1981, vol. 12A, pp. 1419-1428

[SPEI81A] G. R. Speich, Physical metallurgy of dual-phase steels. Fundamentals of Dual-phase steels. Conference and proceedings. Chicago, February, 1981, pp. 3-45

[SPEI92] G R Speich, K.A. Teylor, Tempering of ferrous martensites, Martensite, February 1992, pp. 243-275

[STEI88] Steinbrunner D.L., Matlock D.K., Krauss G., Void formation during tensile testing of dual phase steels, Met.Trans. A, v 19A, 1988, pp. 579-589

[STEV77] R. Stevenson, Crack initiation and propagation in thermal mechanically treated sheet steels. Formable HSLA and dual-phase steels, 1977, pp.99-108

[TANA79] T. Tanaka et al., Formation and properties of ferrite plus martensite dual-phase structures, Structure and properties of dual-phase steels, 1979, pp.221-241

[TEIR88] Teirlinck D. et al., fracture mechanism maps in stress space, Acta Met., v.36, N.5, 1988, pp.1213-1228

[THOM79] G. Thomas, J-Y Koo, Developments in strong, ductile duplex ferritic-martensitic steels, Proceedings of Structure and properties of dual-phase steels, New Orlean, February, 1979, pp.183-201

[THUR98] J.L. Thirion, Press forming dual phase high strength steels for autobody structural members parts, 40th Mechanical Working Steel processing Conference, Pittsburg, USA, 25-28 oct 1998

[TOMO81] Y. Tomota, Y. Kawamura, K. Kuroki. On ductile fracture of steels containing the coarse second phase. Bulletin of the JSME, 1981, v. 24, pp. 282-289

[TOTT06] Totten G.E., Steel heat treatment, edition 2, CRC Press, 2006

[VALL06] Valle N., et ali, Study of the carbon distribution in multi-phase steels using the NanoSIMS 50, Applied Surface Science, v.252, 2006, pp.7051-7053

[WATE03] T. Waterschoot, Ferrous alloys: static strain aging and tempering in dual phase steels, PhD work, 2003

[WAYM85] C.M. Wayman. Martensitic transformation and mechanical behaviour. Strength of metals and alloys (IC SMA7). Monreal, Canada, 12-16 august 1985. pp. 1779-1805

[WEIY88] H. Weiyong et al., Effect of micro-alloying titanium on the dynamic recristallization behaviour of steels, Steel Res., 59, 1988, pp. 179-182

[ZHON92] J. Zhonghao et al., Acta Mat., v. 40, N ;7, 1992, pp. 1587-1597

INSTITUT NATIONAL
POLYTECHNIQUE
DE LORRAINE

AUTORISATION DE SOUTENANCE DE THESE
DU DOCTORAT DE L'INSTITUT NATIONAL
POLYTECHNIQUE DE LORRAINE

o0o

VU LES RAPPORTS ETABLIS PAR :
Madame Anna FRACZKIEWICZ, Directeur de Recherche, EMSE, St Etienne

Monsieur Alexandre LEGRIS, Professeur, Université des Sciences et Technologies de Lille, Villeneuve d'Ascq

Le Président de l'Institut National Polytechnique de Lorraine, autorise :

Madame PUSHKAREVA Irina

NANCY BRABOIS
2, AVENUE DE LA
FORET-DE-HAYE
BOITE POSTALE 3
F - 54501
VANDŒUVRE CEDEX

à soutenir devant un jury de l'INSTITUT NATIONAL POLYTECHNIQUE DE LORRAINE, une thèse intitulée :

"Evolution microstructurale d'un acier Dual Phase. Optimisation de la résistance à l'endommagement"

en vue de l'obtention du titre de :

DOCTEUR DE L'INSTITUT NATIONAL POLYTECHNIQUE DE LORRAINE

Spécialité : **« Science et Ingénierie des Matériaux »**

Fait à Vandoeuvre, le 02 novembre 2009
Le Président de l'I.N.P.L.,
F. LAURENT

TEL. 33/03.83.59.59.59
FAX. 33/03.83.59.59.55

Evolution microstructurale d'un acier Dual Phase. Optimisation de la résistance à l'endommagement.

Résumé

Actuellement, l'industrie automobile est à la recherche d'une meilleure solution pour l'allégement de la structure de véhicule afin de diminuer la consommation de carburant et par conséquent diminuer les émissions nocives de CO_2. Les aciers à très haute résistance (THR) mécanique permettent d'obtenir les tôles d'acier à section diminué avec les mêmes ou meilleurs propriétés fonctionnels.
Les aciers Dual-Phase (DP), constitués majoritairement d'une phase ductile, la ferrite, et d'une phase dure, la martensite, occupent une place importante en tant que matériaux de structure destinés au challenge préoccupant l'industrie automobile. Une bonne résistance à l'endommagement est exigée pour leur utilisation en tant que des pièces de structures et de renfort pour l'automobile. Il a été bien établi que la résistance à l'endommagement des ces aciers Dual-Phase est contrôlée par leur microstructure.
Ce travail de thèse s'est inscrit dans une logique de compréhension des mécanismes d'endommagement d'un acier Dual-Phase modèle, le DP 780, en fonction de différents paramètres microstructuraux.
Deux mécanismes d'endommagement ont été identifiés pour l'acier DP 780 : la décohésion de l'interface ferrite/martensite et la formation de cavités autour des carbures, dans la martensite revenue. Un modèle qualitatif de mécanisme d'endommagement a été développé afin de pouvoir prédire l'endommagement de l'acier DP 780. Ce modèle qualitatif, développé pour l'acier DP 780, servira de base d'approfondissement de modèles plus élaborés et quantitatifs permettant la compréhension et la prédiction de l'endommagement des aciers Dual-Phase, de façon générale.

Mots clefs : Aciers à très haute résistance mécanique, Dual-Phase, microstructure, endommagement, interface ferrite/martensite, interface carbure/martensite revenu, décohésion de l'interface, concentration locale en carbone, NanoSIMS, EELS.

Microstructural evolution of Dual Phase steel. Improvement of damage resistance.

Abstract

In the automotive industry current environmental concerns require that the vehicle fuel consumption and CO_2 emissions should be reduced as much as possible. It is therefore advantageous to reduce the weight of body in white components by replacing existing parts with higher strength, thinner gauge alternatives with equivalent or improved functional properties.
Dual Phase (DP) steels are a class of high-strength low-alloy steels characterized by a microstructure consisting of martensite and ferrite. Dual Phase steels combine high strength levels with good ductility. Thus, DP steels are potentially very attractive for the automobile industry. In addition to the required high strength and ductility, DP steel has to be cold formed into complex shapes. It appears that DP steel damage behaviour is very complex and cannot be predicted using existing models based on standard mechanical properties.
This work is concerned with the study of microstructural evolution and investigation of the relation between the microstructure and damage mechanisms in a reference DP 780 steel. Two damage mechanisms have been identified in this DP steel: ferrite/martensite interface decohesion and void formation at tempered carbides. A simple modeling for qualitative description of the observed damage formation mechanisms is proposed. This modeling permits a basic understanding of the experimentally observed trends and could be used as the starting point for a more detailed analysis in future.

Keywords: High Strength Steels, Dual-Phase, microstructure, damage, ferrite/martensite interface, carbide/tempered martensite interface, interface decohesion, local carbon concentration, NanoSIMS, EELS.